Metal Oxide Nanoparticles: Optical Properties and Interaction with Chemical Warfare Agent Simulants

Wesley Odell Gordon

Dissertation submitted to the Faculty of the Virginia Polytechnic Institute and State University in partial fulfillment for the degree of

Doctor of Philosophy
in
Chemistry

Brian Tissue, Chair
Mark Anderson
Karen Brewer
John Morris
Gordon Yee

November 06, 2006

Blacksburg, Virginia

Keywords: lanthanide, energy transfer, Y_2O_3, dimethyl methylphosphonate, size-dependent reactivity, phosphor

Metal Oxide Nanoparticles: Optical Properties and Interaction with Chemical Warfare Agent Simulants

Wesley Odell Gordon

ABSTRACT

Materials with length scales in the nanometer regime demonstrate properties that are remarkably different from analogous bulk matter. As a result, researchers are striving to catalog the changes in properties that occur with decreasing size, and more importantly, understand the reason behind novel nanomaterial properties. By learning the true nature of nanomaterials, scientists and engineers can design better materials for a variety of applications. Inert gas-phase condensation synthesis of metal oxide nanoparticles was used to develop materials to explore the optical and chemical properties of metal oxide nanoparticles.

One potential application for nanomaterials is use in optical applications. The possibility of interparticle energy transfer was investigated for lanthanide-doped yttrium oxide nanoparticles using laser spectroscopy. Experimental evidence collected with this study indicates that interparticle, lanthanide-mediated energy transfer may have been observed. In addition, lanthanide-doped gadolinium oxide nanoparticles were synthesized and investigated with optical spectroscopy to identify the best potential candidates for bioanalytical applications of this material. The influence of particle annealing and dopant concentration were also studied.

Nanoparticle film structure was investigated with scanning electron microscopy. Two different film structures composed of oxide nanoparticles were found to grow under different synthesis conditions. The film structure was found to be determined by the degree of particle aggregation in the gas phase during synthesis. Aggregation of the particles was found to be controlled by a combination of gas pressure and properties.

Chemical properties of metal oxide nanoparticles also are very important. Reflection-absorption Infrared Spectroscopy and vacuum surface analytical techniques were used to explore the chemistry of the chemical warfare agent dimethyl methylphosphonate (DMMP) on yttrium oxide as well as other metal oxide nanoparticles. DMMP was found to dissociate at room temperature on several types of metal oxide nanoparticles. Hydroxyl groups were found to be critical for the adsorption of DMMP onto the particles. Finally, the reactivity of the nanoparticles was found to increase with decreasing particle size. This was attributed to a relative increase in the number of high-energy surface defects for the smaller particles.

Acknowledgements

This dissertation would not be possible without the contribution of many mentors, co-workers, friends, and loved ones. While I can not list everyone, I would like to especially thank the following people who have helped me succeed.

I would like to thank my advisors, Brian Tissue and John Morris, for their support, understanding, patience, and guidance through my graduate career. I am also grateful to the members of my committee, Mark Anderson, Karen Brewer, and Gordon Yee; for their assistance and support of my studies. In addition, I thank Ray and Lee Dessy, who provided support, counsel, and advice, both professionally and personally. I am also heavily indebted to the past and present members of the Morris group for not only providing an enjoyable work environment, but also for providing great friendship. Group members B. Scott Day, James Lohr, Jeff Carter, Larry Fiegland, Mindy Ferguson-McPherson, Allyn Milojevich, Josh Uzarski, Megan Bennett, Erin Davis, Leslie Adamaczy, Jessica Lu, and Will Alexander are particularly acknowledged for their friendship and support. Outside of the Morris group, I would like to thank Stephanie Hooper, David Roach, and André Williams for their friendship.

I also wish to express my appreciation to Steve McCartney, Frank Cromer, Melvin Shaver, John Miller, and Scott Allen for advice and sharing their expertise with me. The faculty, staff, students, and support personnel within the chemistry department also deserve recognition for their part in my experience at Virginia Tech. Outside of the University, I wish to acknowledge the assistance of Uwe Hömmerich from Hampton University, Barbara Reisner at James Madison University, and Kenneth Livi from Johns Hopkins University for their contributions to this work.

I wish to express my gratitude to my parents, Marilyn and Jerry, and my siblings, Amy and Blake, for their love and support. Last but not least, I wish to thank the many family members, friends, and loved ones who have each contributed to this achievement. While not individually listed, you know who you are, and I offer my sincerest thanks.

Table Of Contents

List of Figures

List of Tables

Index of Acronyms

AFM	Atomic force microscopy
BET	Brunauer-Emmett-Teller
CWA	Chemical warfare agent
DMMP	Dimethyl methylphosphonate
ET	Energy transfer
HRTEM	High-resolution transmission electron microscopy
ICP	Inductively coupled plasma
IGC	Inert gas-phase condensation
IR	Infrared
Ln	Lanthanide
NP	Nanoparticle
MS	Mass spectrometry
RAIRS	Reflection absorption infrared spectroscopy
RGA	Residual gas analyzer
SEM	Scanning electron microscopy
TEM	Transmission electron microscopy
TMP	Trimethylphosphate
TPD	Temperature programmed desorption
UHV	Ultra-high vacuum
XPS	X-ray photoelectron spectroscopy

Chapter 1
Introduction and Motivation
Thesis Statement

The goal of this body of work is to gain a better understanding of two key components of the properties of metal-oxide nanoparticles: 1) the optical properties when doped with luminescent lanthanide ions, and 2) the interaction with organophosphorus chemical warfare agent simulants.

1.1 Background

Nanotechnology involves the study of the synthesis, characterization, and properties of nanomaterials, which have at least one characteristic dimension that is less than 100 nm. While the study of nanometer-scale materials has existed for some time, advances in synthesis and characterization techniques have catalyzed the great expansion in nanoscience over the past few decades. Even as several products incorporating nanotechnology are commercialized, the understanding of these novel materials is small compared to analogous bulk species.

Nanomaterials are important because of their small size. One reason for this is the greatly increased surface to area ratios compared to bulk materials. The other is due to more fundamental size effects. As the size of a material is decreased below 100 nm, the scale of features becomes similar to many physical phenomena such as the mean free path of electrons and phonons, the wavelength of light, and energy transfer distances.[2] The result is that properties can diverge from bulk material values, and yet remain distinct from those studied by quantum science. Therefore, the properties of nanoscale materials are not understood by strict use of classical physics or quantum theory, particularly for materials with sizes on the order of 2-10 nm.[3] New properties and the ability to control

them through feature size results in a novel dimension of material control that does not exist for bulk matter. For clarification, nanoparticles (NPs) are defined here as solid particles that are three-dimensional and are less than 100 nm in diameter.[4] Nanoparticles can be noncrystalline, polycrystalline, or single crystalline, and can be produced with a variety of methods.

1.2 Nanoparticle Synthetic Techniques

Several synthetic approaches have been developed for synthesizing nanoparticles over the past several decades. Regardless of the technique, the goal of particle synthesis generally focuses on: 1) minimizing and controlling particle size, 2) maintaining a narrow size distribution, 3) control of particle morphology, and 4) control of crystallinity. The ability to control size enables the variation of particle properties, while the narrow size distribution allows greater precision and is required for studies of size-dependent effects. Particle shape and crystal structure can also influence material properties. Nanoparticle synthesis techniques can generally be divided into two classes: gas-phase methods and condensed phase methods. These two classes of nanoparticle synthesis are characterized by unique advantages and limitations.

1.2.1 Condensed Phase Methods

The first class of nanoparticle synthesis techniques involves manipulation of materials in the condensed (solid or liquid) phases. Solid-phase particle production methods include high-energy ball milling[5] and combustion synthesis,[6] where high amounts of applied energy literally break down a solid precursor. Combustion synthesis enables the production of relatively large quantities of material, and the properties of the product are controlled via the ratio of oxidant to fuel in the mixture. Solution-phase

approaches are more common, and include precipitation[7] and sol-gel[8,9] methods. These techniques rely on control of the solution conditions to retard particle growth after formation, often via capping agents, surfactants, or micelles. Solution phase methods are not well suited for continuous reactors and may require elimination of solvents for some applications; however, they work well for producing core-shell particles and are agreeable with template synthesis and assembly processes.

1.2.2 Gas-Phase Methods

Several gas-phase synthetic techniques have been used to prepare nanoparticles. These methods use both inert and reactive atmospheres at a variety of pressures. Gas-phase nanoparticle synthesis methods include electrospray,[10] flame pyrolysis,[11] vaporization and condensation using lasers and other heat sources,[12,13] laser ablation,[14] and plasma synthesis.[15] These methods feature the rapid cooling of evaporated material to induce nucleation and growth of nanoparticles, typically within a confined region. Depletion of the supersaturated vapor prevents excessive growth of the particles, which tend to show a log-normal size distribution.[16,17] Particle size depends on material properties as well as the evaporation conditions. Coalescence of particles can result in particle growth, or the formation of aggregates which complicate the post-synthetic processing required for some applications. While product control (size, morphology, crystallinity) in gas-phase synthetic methods can be complex, many materials can be synthesized without contaminants such as solvents or stabilizers. In addition, many vapor-phase particle growth methods are adaptable for use in continuous, industrial reactors that are compatible with mass production.

Our research laboratory primarily uses inert gas-phase condensation to produce nanoparticles. This method (which is described in more detail in Chapter 2) is amenable to studies of optically active materials since doped precursor bulk powders are easily prepared. In addition, gas-phase condensation is compatible with vacuum techniques. This enables the use of surface-sensitive techniques (such as XPS) to study novel materials as they are prepared, without the need for pretreatment. These properties of the gas-phase condensation method make it an excellent choice for studying both the optical and chemical properties of nanoparticles.

1.3 Summary of Thesis

This body of work is focused on understanding selected properties of size-restricted matter and learning why nanomaterials have such unique properties. Initially, this thesis focuses on the optical properties of lanthanide-doped oxide particles, and then moves towards understanding the interaction between oxide particles and the chemical warfare agent simulant DMMP. A summary of experimental methods that were utilized in this series of studies is presented in Chapter 2. Chapter 3 discusses a survey study on the optical properties of lanthanide-doped gadolinium oxide particles. The study was focused on the potential for these materials for use in analytical assays. Three lanthanide ions were found to be suitable for use in a gadolinium oxide matrix for host-sensitized luminescence.

After the study of doped gadolinia materials, the optical properties of lanthanide-doped nanoparticles are further investigated in Chapter 4, where energy transfer between doped yttria particles is investigated. No evidence was found for interparticle energy transfer between Er^{3+} and Eu^{3+} ions. However, the investigation yielded evidence

consistent with weak energy transfer occurring from Tb^{3+} to Eu^{3+} ions across a particle boundary. $Tb^{3+} \rightarrow Eu^{3+}$ energy transfer has been observed in bulk materials, and was found to depend strongly on the post-processing of the prepared particles. If this energy transfer could be enhanced, it has potential for use in sensor technology.

After observing optical properties, the focus of the thesis then shifts to learning more about the gas-phase condensation synthetic method in Chapter 5. As-prepared film morphology differed when synthetic conditions were varied, so the cause of this change was investigated. A fractal aggregate-like morphology resulted from agglomeration of particles prior to deposition on a collection substrate under conditions with greater cooling. Under lower gas pressures (with less efficient cooling) aggregation becomes less prominent, resulting in column-like structures that are composed of particles that grow perpendicular to the substrate. These films likely have different physical properties; therefore, control over the film morphology may be important. General predictions for film morphology are formulated based on the properties of the gas used in the synthetic method.

Chapter 6 moves the focus of this thesis to the chemical properties of metal-oxide nanoparticles. Specifically, the interaction between the chemical warfare agent simulant, DMMP, and particles is investigated. First, the sorption and reactive properties of a series of nanoparticles were surveyed under ambient conditions using reflection-absorption infrared spectroscopy. The preliminary results indicate that all of the particles tested adsorbed DMMP, and at longer times, some systems decomposed DMMP under ambient conditions. Following these interesting results, a vacuum system was constructed to enable direct transfer of nanoparticle films into an ultra-high vacuum environment. The

interaction of DMMP with Y_2O_3 nanoparticles was studied in greater detail using surface spectroscopic methods. This study indicates that DMMP adsorbs to nanoparticle surface and dissociates to form bound products. Further experiments probed the role of hydroxyl groups in the interaction between the particles and the simulant, with results pointing to a major role in the initial interaction. Most importantly, reactivity was found to increase with decreasing particle size, emphasizing the influence of size on properties.

Chapter 2. Experimental Methods

2.1 Background

Understanding the physical characteristics of a material is important in any exploration of resulting properties. Characterization is particularly important for materials with length scales in the nanometer regime as a result of the high degree of change in material properties with dimension. Real-world nanostructured materials such as the metal oxide particles that are examined in this work can often have complex structures and present several difficulties in characterization due to the length scales involved. A variety of experimental techniques are used as tools to explore the characteristics of metal oxide nanoparticles to assist in clarifying their influence on properties. This understanding will allow the development and refinement of materials for the applications discussed in the previous Chapter. Initial studies focused on the spectroscopic properties of the nanomaterials, while the later studies on reactivity employed surface-sensitive techniques that required an ultra-high vacuum environment.

2.2.1 Nanoparticle Synthesis

Nanoparticles were prepared by the inert gas-phase condensation method.[18] Starting materials were prepared by grinding dry metal oxide powder along with any dopant followed by cold pressing under 5000 lbs to form a 13 mm diameter pellet. The pellets were annealed at 1273 K overnight unless otherwise noted to enhance the pellet robustness. Pellets were then placed on a rotating platform inside of a stainless steel vacuum chamber that was evacuated and then backfilled to a specific pressure of gas (see Figure 2.1). A 40 W continuous-wave CO_2 laser (Synrad DuoLase) is directed toward the chamber, and first passes through a beam splitter. The beam splitter is used to overlay a visible He-Ne laser beam with the CO_2 beam, and also directs a 1% reflection of the

incident CO_2 beam to a Melles Griot 13PEM003 broadband power meter, which reads a value that is proportional to the true laser beam power. The co-linear CO_2 and He-Ne beams are directed into the vaporization chamber via aluminum mirrors and Zn-Se lenses. A Zn-Se lens (254 mm focal length) outside of the chamber is used to focus the beam to a ~1-mm spot on the target to evaporate material from the pellet, which then cools via collisions with the buffer gas and brings about a supersaturation condition.

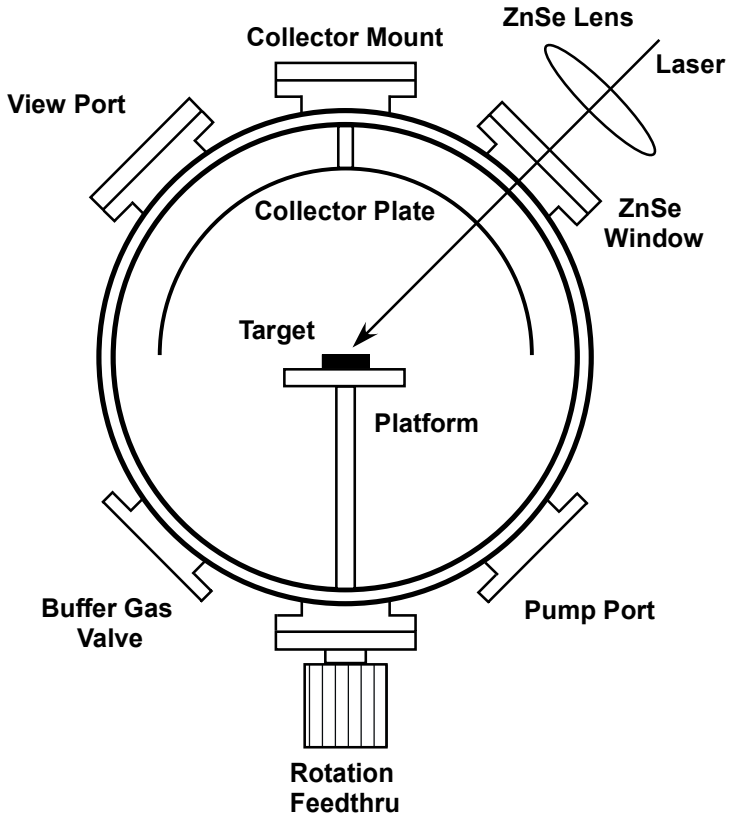

Figure 2.1 Nanoparticle synthesis chamber equipped with a cyndrilical collector plate. This experimental setup was used for the luminescence studies. For other studies, the collector plate is replaced with a substrate mount.

Nucleation of crystals followed by growth occurs until the newly formed particles diffuse out of the supersaturated region. Particles then deposit onto a stainless steel collector substrate that is typically 3 – 4 cm from the pellet. The particles are collected by scraping

the film off of the collector. For SEM and *in situ* exposure studies, particles were collected directly on a suitable substrate that was mounted above the target.

For the initial optical spectroscopy experiments and the survey DMMP exposure experiments, the chamber was evacuated with a mechanical pump. These experiments also made use of a cylinder-shaped stainless steel collector plate to maximize the product yield. Later morphology studies employed the use of a diffusion pump to evacuate the synthesis chamber to lower pressures (~ 5 x 10^{-6} Torr). Clean silicon substrates were suspended 3.5 cm above the oxide target using custom stainless steel mounts. Target-substrate distance dependence studies were performed with a custom stainless steel mount system equipped with screws that enabled fine control of the distance.

2.2.2 Laser Spectroscopy

Optical spectroscopy was performed with a pulsed laser spectroscopy apparatus that is shown in Figure 2.2. Powder and nanocrystalline samples were packed into a depression in a copper sample block, which is mounted inside a vacuum chamber ($3x10^{-2}$ Torr) on the cold head of a closed-cycle helium refrigerator (Cryomech GB 15). The cold head temperature can be controlled (Scientific Instruments 9620-1) from room temperature to 12 ± 3 K. A Nd^{3+}:YAG (yttrium aluminum garnet) pulsed laser (Continuum Surelite II) along with harmonic optics provide a pump beam with wavelengths of 1064, 532, 355, or 266 nm. These different energy pump beams can be directed onto the sample or routed to excite a dye laser (Continuum) to provide a tunable

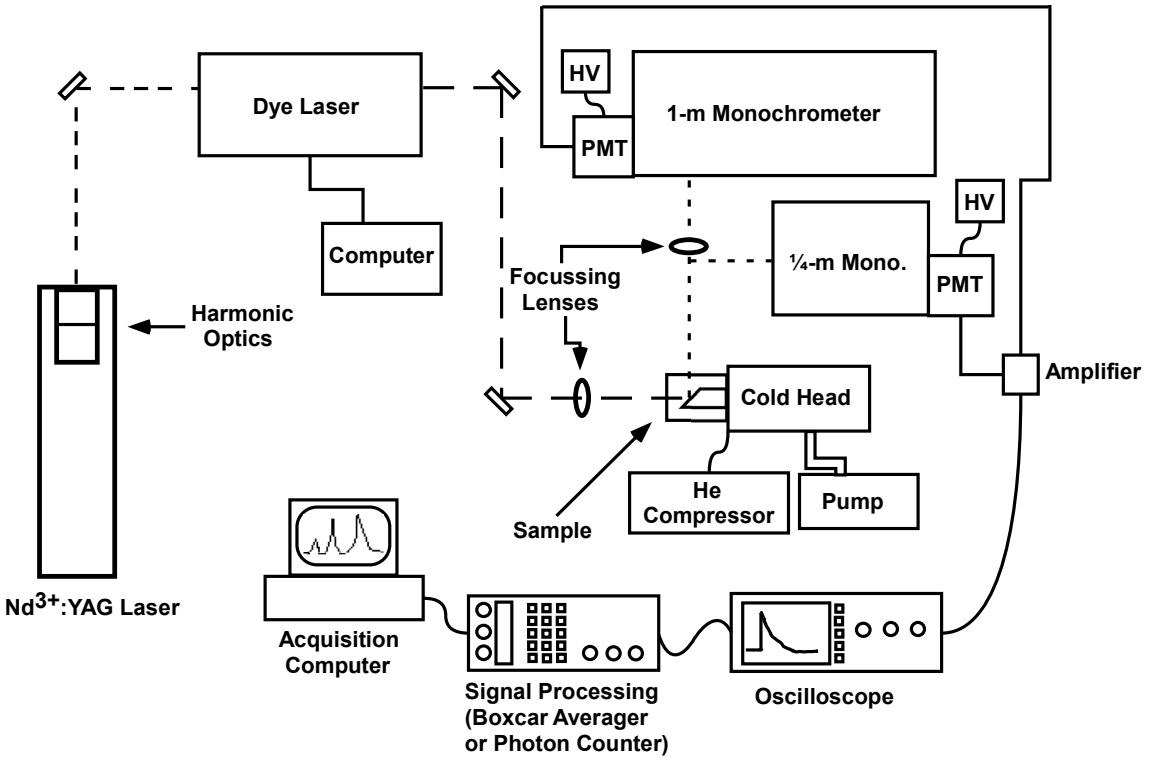

Figure 2.2 Laser spectroscopy experimental apparatus used in luminescence studies. The ¼ –m monochrometer was used for broad band spectra, while the 1 – m monochrometer was used for high resolution studies.

wavelength pulsed laser. A radiometer (DigiRad R752) was utilized to determine the pulse power of the output laser. Excitation light was focused onto the sample through a quartz window. Luminescence light was sampled at 90^{o} with respect to the excitation light and then focused onto the entrance slit of the detection monochromator.

Broad-band excitation spectra were obtained by monitoring luminescence with a ¼ m monochromator with a bandpass of 3 nm and equipped with a photomultiplier tube (Hammamatsu 1P-28A). High-resolution excitation and emission spectra were acquired with a 1 m monochrometer (Spex 1000M) with bandpass values typically < 0.2 nm and a cooled GaAs photomultiplier (Hammamatsu R-636-10). Photomultiplier signals were amplified and processed with either a boxcar averager (Stanford SR250) or a photon counter (Stanford SR400) and captured by an analog-to-digital data acquisition board

(National Instruments Lab-PC+) interfaced with a PC running a custom Lab View® program. Fluorescence transients were obtained with a 350 MHz oscilloscope (Tektronix TDS460), or 500 MHz oscilliscope (Tektronix TDS520A) by averaging at least 200 laser shots or by utilizing the time scanning option on the photon counter. When necessary, optical filters were used to reduce stray light from the source reaching the monochromator.

2.2.3 X-ray Diffraction Characterization

Powder X-ray diffraction is an analytical method used to identify the crystallographic phase of a material that is not in the form of a single crystal. This method uses a monochromatic source of X-rays and measures the pattern of diffracted radiation, which is a result of the constructive interference due to the crystalline structure the powder. In addition to determining crystal phase, the line widths can be used to estimate the mean crystal size of a sample by use of the Scherrer equation:[19]

$$\beta = \frac{K\lambda}{t\cos\theta} \qquad \textbf{Eq. 2.1}$$

Where β is linewidth at half the maximum peak intensity, K is correction factor for particle shape (0.9 for spheres), t is the crystallite diameter, and θ is the angle of incidence for the selected diffraction peak. This broadening arises from crystallite sizes that are small enough that not enough crystal planes are available for the destructive cancellation of reflections that do not occur at exactly the Bragg angle.[20] It is important to note that the size from the Scherrer equation is for crystallites and do not represent correct value if the particles are polycrystalline. Powder X-ray diffraction spectra of nanoparticle powders were obtained on a PANalytical Xpert-Pro Θ-Θ diffractometer with CuK_α (1.5418 Å) radiation by placing a layer of powder on a quartz slide that was coated

with a thin layer of petroleum jelly. Patterns were then compared to a database and the literature to determine the phase of the nanoparticles.

2.2.4 Surface Area Analysis

Surface area is one physical characteristic that is important for materials that are to be used as sorbants. High surface areas imply a larger number of adsorption sites, leading to higher total adsorbate loadings as well as faster sorption kinetics. The most common method used to measure surface area of solid materials is the Brunauer-Emmett-Teller (BET) method[21] where the sample is cooled to liquid nitrogen temperatures and exposed to a gas adsorbant (typically nitrogen) and the BET equation is applied:

$$\frac{1}{W\left[\left(P_0/P\right)-1\right]} = \frac{1}{W_m C} + \frac{C-1}{W_m C}\left(\frac{P}{P_0}\right) \qquad \textbf{Eq. 2.2}$$

where W is the weight of the gas adsorbed at a relative pressure P/P_0 (true equilibrium pressure/equilibrium pressure if no gas were adsorbed), W_m is the weight of a monolayer of adsorbate, and the term C (the BET constant) is related to the energy of adsorption of the first adsorbed layer. When using nitrogen as the adsorbate gas, a linear plot is constructed of $1/W[(P_0/P) - 1]$ vs P/P_0 over an appropriate range (P/P_0 = 0.05 – 0.35). W_m is obtained from the slope and intercept of the plot, and the specific surface area is calculated using this number and the molecular cross-sectional area of the adsorbate molecule.

Specific surface area of Y_2O_3 nanoparticles were determined with a Quantachrome NOVA 1000 gas sorption analyzer. 20 – 30 mg of particles were massed and placed in a quartz cuvette. Samples were allowed to degas for 12 hours under vacuum at 523 K and then were transferred to the analysis port, and immersed in liquid N_2 (77K). The instrument then admitted nitrogen into the cuvette while measuring

equilibrium pressures to measure P/P_0. Single point (measured at P/P_0 = 0.3) and six-point BET measurements were performed after correcting for gas adsorption to the cuvette walls.

2.2.5 ICP-ES Analysis

Inductively Coupled Plasma Emission Spectrometry (ICP ES) is a trace elemental analysis method that was used to quantitate the mass of yttria films produced on the reflective gold substrates. ICP uses a high-frequency alternating field to transfer energy to a flowing gas of argon to form a plasma of ions and electrons. The plasma is propagated when ionization of neutral atoms occurs as a result of collisions with the ions and electrons. Argon is chosen because polarization of its electrons requires less energy than smaller gases.[22]

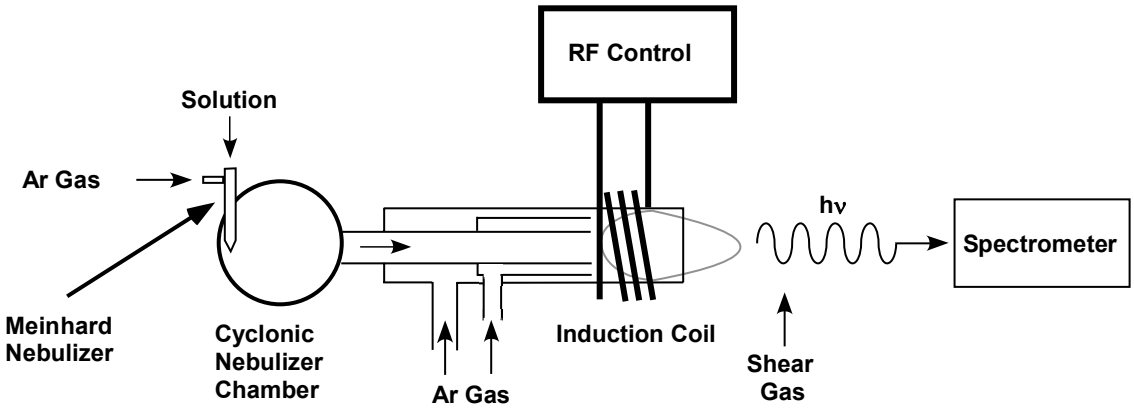

Figure 2.3 Schematic of ICP spectrometer. Analyte solution is nebulized and larger droplets are eliminated from the stream before traveling into the RF field, where a plasma is maintained. UV photons then are analyzed with a high resolution spectrometer. The entire apparatus is maintained under an inert gas purge.

Temperatures in the resulting plasma torch typically reach 10,000 K, where an aerosol containing analytes is introduced.[23] At these temperatures, the aerosol material is vaporized, atomized, and can be ionized by loss of electrons. Additional energy can excite an outer electron of an atom or ion, which will fall back to a lower energy orbital

in about 10^{-8} s. Energy from the relaxation process is released as a photon, which can be detected with a high-resolution spectrometer. Emission lines of atomic and ionic species are remarkably narrow (< 10 pm) and are characteristic of elements, allowing atomic identification.

Figure 2.3 shows a representation of the apparatus used. For these experiments, gold substrates containing the nanoparticle films are placed in a known volume of 10% nitric acid diluted with 12 MΩ water to dissolve the nanoparticle films. Solutions were drawn up at 1.5 mL/minute using a peristaltic pump into a concentric or Meinhard nebulizer and combine with a flow of argon gas to form an aerosol. This flow of droplets enters a cyclonic spray chamber, where the centrifugal force of the gas flowing in a cyclone pattern to force larger droplets to hit the surface. Smaller droplets follow the flow of carrier gas into a quartz tube, where the induction coil provides the excitation energy to form the plasma. A high flow shear gas "cuts" the plasma, eliminating a cooler region of the plasma where adsorption of the analyte signal can occur so that emission can be directed to the spectrometer from down the axis of the torch via a water-cooled optics interface. For experiments presented here, the 40 MHz RF generator was operated at 1250 W, with a nebulizer flow of 0.5 L/min. Quantitation of the analyte signal was performed by use of a series of yttrium calibration standards prepared from a commercial 1000 ppm standard.

2.2.6 XPS

X-ray photoelectron spectroscopy (XPS) or electron spectroscopy for chemical analysis (ESCA) is a well-known analytical technique that is used to determine the chemical composition of a surface in addition to the local chemical environment of a

given atom. Experiments using XPS require that a sample be under vacuum, where it is bombarded with X-ray photons (200 - 2000 eV) and relies on the photoelectric effect described by Einstein in 1905 where electrons are ejected from a sample after interacting with these high energy photons. X-ray photons will interact with a sample by exchanging enough energy with core-level electrons near the surface of a material to cause electron ejection. Ejected core electrons have a specific kinetic energy (E_k) that is related to the energy of the exciting photon ($h\nu$), the binding energy of the electron to the atom (E_b) and the characteristic work function of the material (Φ) by the relation:

$$E_k = h\nu - E_b - \Phi \qquad \textbf{Eq. 2.3}$$

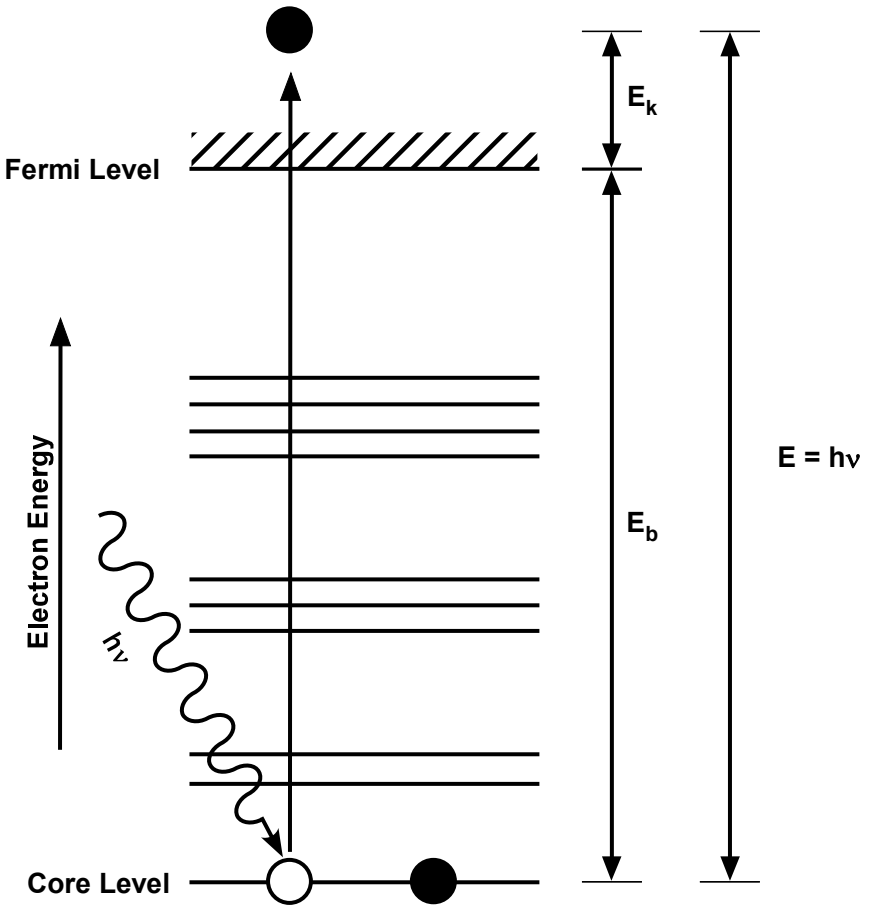

Figure 2.4 Representation of the generation of an X-ray photoelectron.

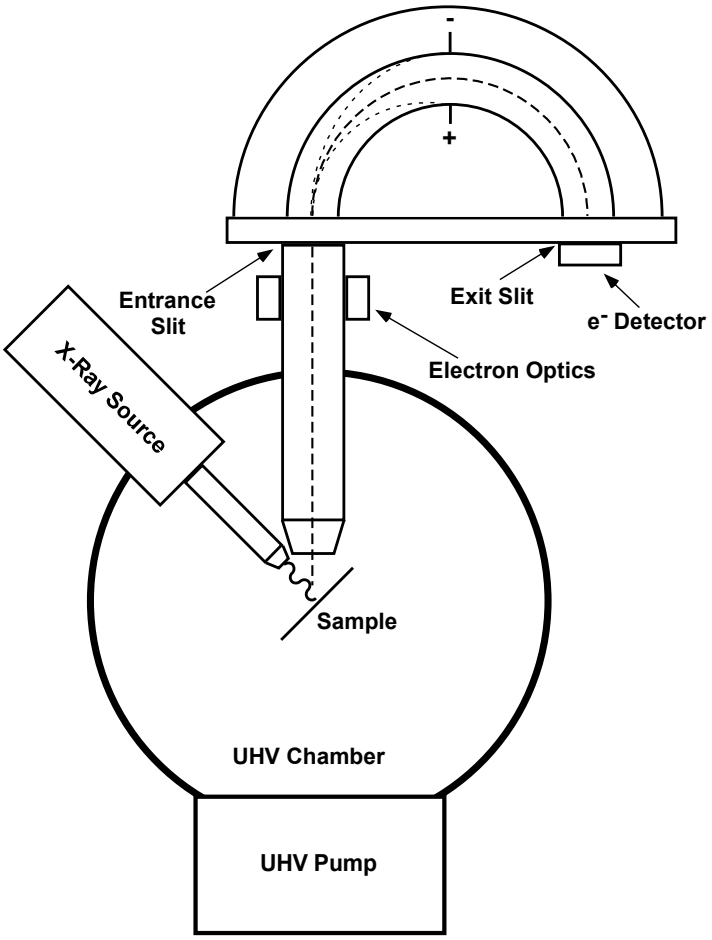

Figure 2.5 Schematic of a typical X-ray photoelectron spectrometer equipped with an X-ray source and a hemispherical analyzer. The dashed line represents the path of a photoelectron through the analyzer, where only electrons with a certain energy will pass through the field created by the charged plates to be detected.

Binding energy is used to determine the oxidation state of elements, and the integrated electron signal can be used to quantitate the elemental composition of a surface.

For *ex situ* experiments, XPS was performed on a Perkin Elmer 5400 X-ray Photoelectron Spectrometer coupled with a Mg(Kα) or Al(Kα) source and a position sensitive, multi-channel plate detector. Electrons were detected at a 45^{o} take-off angle under high vacuum conditions (~1 x 10^{-7} Torr). Survey spectra were taken with a pass energy of 44.75 eV with a 1 mm x 3.5 mm spot size and a power of 250 or 300 W. Higher resolution multiplex spectra were collected with longer scan times and a lower

pass energy. When observable, the C(1s) binding energy was adjusted to the reference value of 284.6 eV. *In situ* experiments in the UHV chamber were performed with a SPECs XR50 Mg(Kα) source operated at 250 W and a SPECs Phiobos 100 hemispherical analyzer with a single-channel electron multiplier. Data was collected with pass energies of 15 – 50 eV and at a take-off angle of 90^{o} with entrance slits set at 7 x 20 mm. Both the analyzer and the X-ray source are equipped with bellows-sealed linear translators (McAllister) that enable retraction of the equipment when not in use.

2.2.7 Scanning Electron Microscopy

Scanning electron microscopes (SEM) can be used to obtain three dimension-like topographical images of a wide variety of samples. This versatile method allows sample images to be quickly collected in the magnification range of 10-250,000X. In SEM, a finely focused electron beam (5 – 20 keV) is directed onto the examined area in a high vacuum environment, and may be rastered to form images or held on the area for static analysis. The interaction of the electron beam with the sample can yield backscattered electrons, secondary electrons, X-rays with characteristic energies, or photons. These emitted electrons and photons can be analyzed to determine the surface topography, crystallinity, and chemical composition. The volume of the sample that interacts with the incident electron beam is on the order of a cubic micrometer and varies with beam energy and sample composition.

Backscattered electrons (BSE) are beam electrons that interact with the sample (usually at the surface) and escape the specimen. These electrons escape the surface by trajectory changes from the initial beam path via multiple elastic collisions and therefore retain most of their incident energy. Production of BSE increases with the average atomic

number, which can be used as a contrast mechanism to qualitatively study sample surface composition. Secondary electrons (SE) are loosely bound outer shell

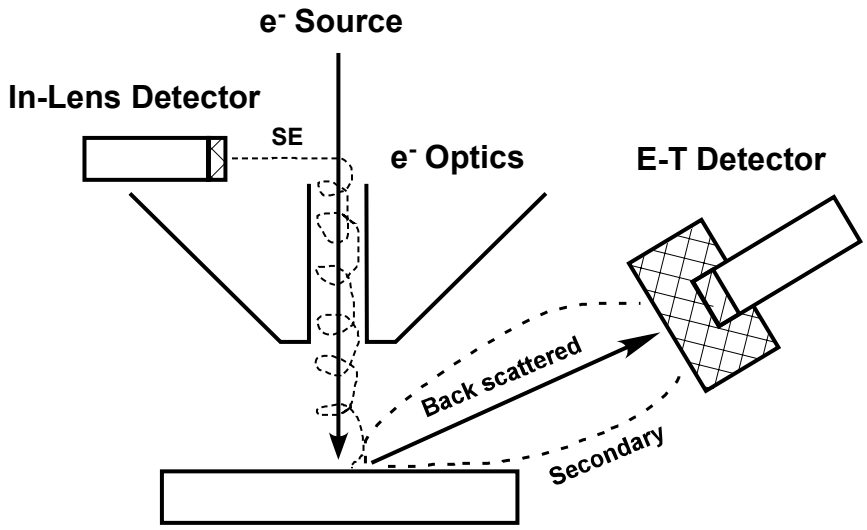

Figure 2.6 Representation of a scanning electron microscope with two detectors. Note the in-lens detector will detect electrons from the same perspective as the source beam, while the E-T detector observes electrons from a different angle. This difference in perspective leads to the differences in the images captured with the detectors.

electrons from the sample that are given enough kinetic energy from inelastic collisions of beam electons to be ejected from the sample. These electrons have relatively low energy (< ~50eV)[24] and therefore have a surface escape probability which decreases exponentially with depth. SE provide much (but not all) of the topographical information about a sample, and some are detected by an Everhart-Thornley (E-T) detector. The detector collects SE with a positively charged faraday cage (+100V) and then accelerates them to collide with a scintillator that is biased to + 12 kV. Electrons colliding with the scintillator coating generate photons, which are detected by a photomultiplier. It is important to note that the E-T detector will also have a signal component due to BSE and SE due to interactions of BSE with chamber walls.

A second type of detector also used in this study is the in-lens detector. The magnetic field that radiates from the beam lens to the sample traps SE coming from the surface. These electrons will spiral up the magnetic field through the lens bore, and

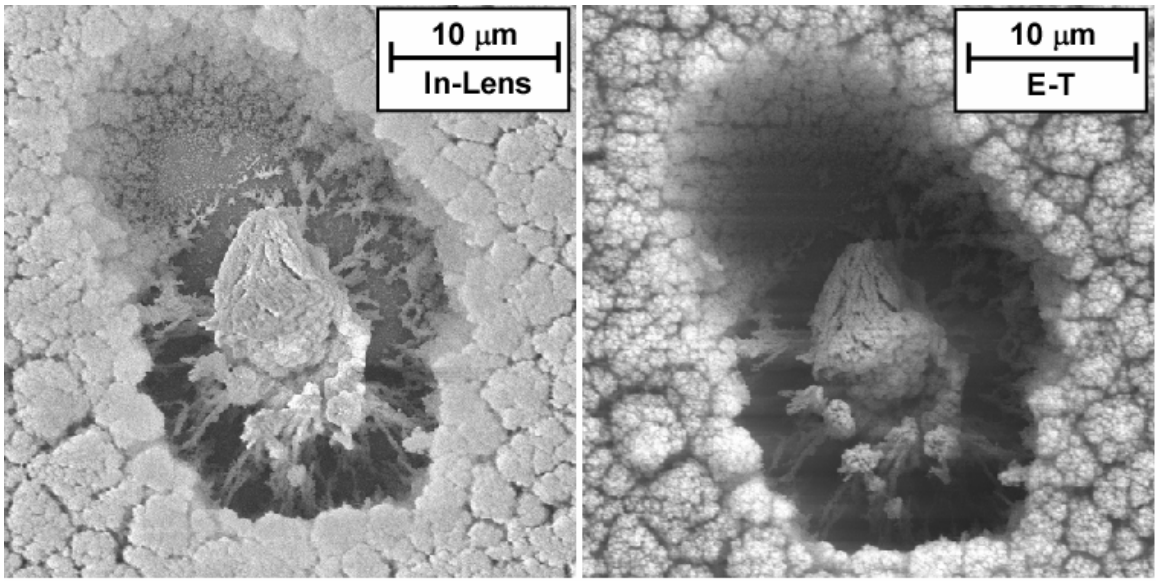

Figure 2.7 Micrographs captured of the same feature within a film but with the In-Lens and E-T Detector. Note that the In-Lens image shows a greater depth of field, but the image appears more flat than the micrograph captured with the E-T detector. This is due to the different perspectives of the detectors.

are detected by a scintillator that is maintained with a high bias (+ 10 kV). As opposed to the E-T detector, the in-lens detector discriminates against both BSE and SE that are produced by BSE collisions with the chamber walls.[24] Qualitatively, the in-lens detector has a greater depth of field (see Figure 2.7) and is better for high resolution images (> 100,000X) than the E-T detector. This greater depth of field is due to the different location of the detector with respect to the probe electron beam, and reduces the 3 dimensional character of the image when compared to the E-T detector. Both of these detectors were used for this study of film morphology.

X-rays are produced by higher energy electrons “falling” to the lower energy shell that is left vacant by an ejected secondary electron. The energy released in this process

can be emitted in the form of X-rays, which are characteristic of the source atom. These X-rays may be detected by an energy-dispersive spectrometer (EDS), which is composed of a liquid N_2-cooled Si(Li) crystal held under a bias that ejects a photoelectron upon exposure to a X-ray. The energy of the photoelectron is given up in the form of an electron-hole pair, which forms a charge pulse that is converted to a signal by a charge-to-voltage converter. This voltage pulse is proportional to the energy of the incident X-ray photon, and can be correlated to a particular atomic species as a result. EDS analysis allows the chemical identification of areas as small as a square micrometer and typically can detect atoms that are up to a micron in depth.[24]

In SEM, the current into the sample due to the impinging electron beam must be offset so the electrical neutrality is maintained. While some of the charge balance is offset by emitted secondary electrons and photons, a large portion of this current is passed through the sample by electrical grounding of the sample stage. For this reason, silicon wafers were used instead of the gold-coated glass slides for the SEM studies presented here. Insulators such as metal oxides have high resistivities and can generate potentials as high as 1kV under a typical electron beam. Such potential buildup leads to severe image distortion with a general phenomena referred to as charging.[24] Y_2O_3 is an insulator and will not conduct current, therefore each film was sputter coated with gold (2.5 nm) to allow a conductive path to the grounded sample stage. Control experiments confirmed that the gold coating as well as the change in substrate from gold to silicon did not influence the results presented here.

2.2.8 Transmission Electron Microscopy

Transmission electron microscopy or TEM is another electron-based technique used to study materials. TEM uses a beam of electrons that transmit through a thin sample and are detected on the other side, while SEM uses non-transmitted electrons as a basis for image formation and uses electronics to scan the beam in a similar method as used in a conventional television. TEM uses a heated pointed filament to thermionically produce electrons which then pass through an anode and into condenser lenses to vary the electron beam spot size. After passing through scan coils, the electron beam will pass through a sample and then an objective lens and aperture that eliminate highly-scattered (> 0.5 ^{o}) electrons.[25] Enlargement of the beam is achieved with a projector lens, and the beam strikes a phosphor screen for viewing or a photographic plate for data collection.

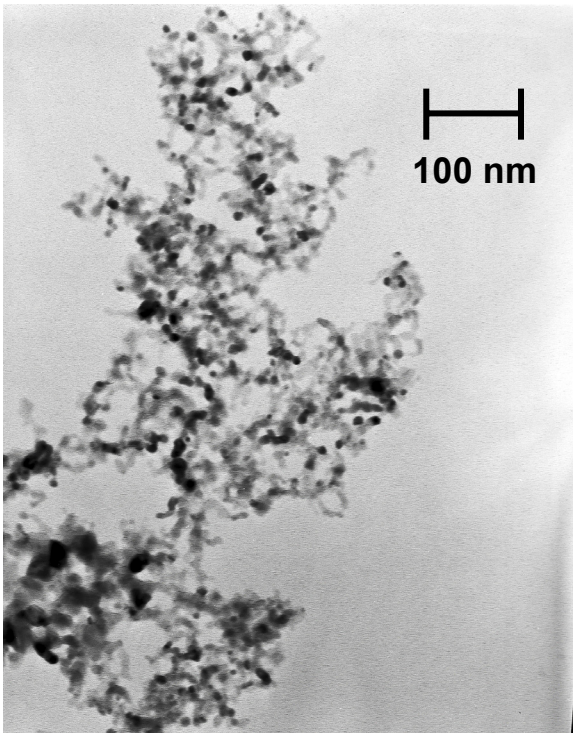

Figure 2.8 Typical transmission micrograph of metal oxide nanoparticles. The particles shown are MgO particles that were synthesized under 10 Torr of O_2 and annealed 6 hours at 873 K.

Electrons interact very strongly with matter, giving rise to the ability to use contrast for detection.[26] Dark areas in the image represent regions where electrons do not transmit through, while lighter areas are those that are more electron transparent.

TEM results were used to compare particle size results with those of AFM. For these experiments, a Philips EM420 TEM/STEM was used operating with a 100 kV accelerating voltage. Nanoparticle samples were dispersed in absolute ethanol, dropped onto a carbon-coated copper grid using a pipette and allowed to air dry. Particle size was measured manually from the negative micrograph (see Figure 2.8 for a typical image) with calipers and converted to actual size with the appropriate magnification factor. At least 75 particles were counted from each sample, and at least 3 regions were scanned to assure representative results.

2.2.9 Atomic Force Microscopy

Atomic force microscopy (AFM) yields an alternative method for determining particle sizes of samples discussed in this paper. AFM is a form of scanning probe microscopy (SPM) where a sharp probe is rastered over a sample and its interaction with the probe is monitored. Two main types of AFM are most commonly used: contact mode and tapping mode. Tapping mode was used in this study because it features reduced forces exerted on the sample, which for small particles might lead to error in the measurements.

Tapping mode involves a sharp probe tip attached to an oscillating cantilever being scanned across the surface. Typical amplitudes for this oscillation are in the range of 20 – 100 nm and lead to the tip “tapping” the surface at the bottom of the oscillation amplitude. This light tapping contact allows force measurements of the sample, without

causing tip damage or dulling, and minimizes force applied and therefore damage to the sample surface. A split photodiode detector monitors a laser beam that is reflected off of the cantilever, giving a measure of the oscillation of the cantilever. Using a feedback loop, constant oscillation amplitude is maintained and the vertical position required to maintain this oscillation is recorded as a height (Z) measurement for a particular (X,Y) coordinate.

An atomic force microscope operated in tapping mode is shown schematically in Figure 2.8. A laser shines onto the cantilever and is reflected onto a photodiode detector. Electronics coupled with a controller for the X,Y,Z stage and cantilever act as a feedback loop as they maintain the root mean square (RMS) amplitude of oscillation. X, Y, and Z movement is independently performed via a piezoelectric tube scanner, operating on the principle that piezoelectric materials will reproducibly contract or expand proportionally to a supplied voltage. The oscillation of the cantilever is also enacted by a piezoelectric material.

Tips and cantilevers for tapping mode AFM are produced by etching a single piece of crystalline silicon. Cantilevers are typically ~ 150 μm in length and have a spring constant in the range of 20 – 100 N/m and a resonant oscillation frequency of 200 – 400 kHz.[27] Tips have a pyramidal shape and have a radius of curvature of approximately 5 – 10 nm, which is the limiting factor for the X and Y resolution as a result of using tip-surface interaction to map the surface. Therefore, the X and Y measurements are greatly exaggerated by this tip curvature for the small (< 5 nm) particles that are measured in the present experiments. However, the Z measurement remains very accurate and is used as a measure of particle diameter with the assumption that particles are roughly spherical.

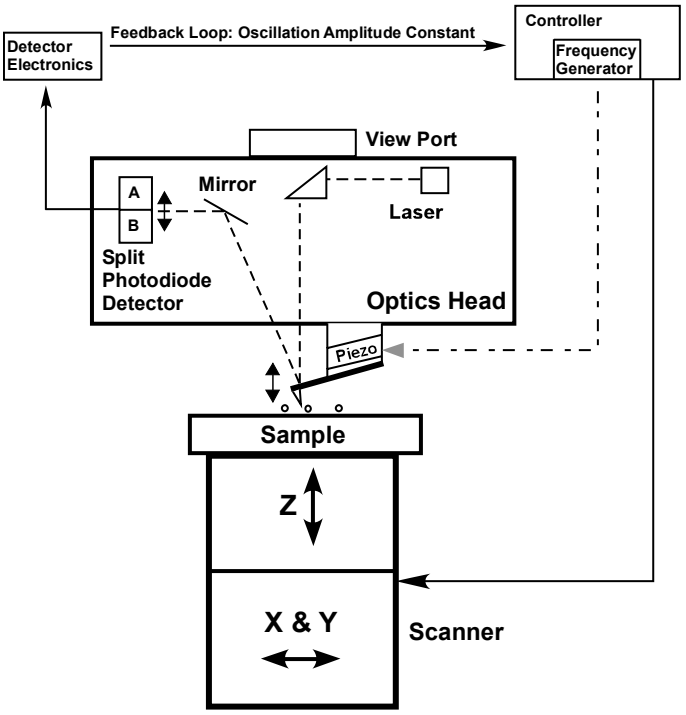

Figure 2.9 Diagram of the AFM instrument used for tapping mode image generation. Note that the sample is mounted on the piezo electric scanner, and the AFM cantilever and optics are held immobile over the sample substrate.

Most of the AFM images collected were collected on a Veeco Multimode™ scanning probe microscope operated in tapping mode with Nanoscope IIIa controller and a 12 μm "E" scanner head. Some images were also captured using a Molecular Imaging PicoPlus AFM operating in magnetic AC mode. For imaging, particles were dispersed in absolute ethanol that had been filtered with a 25-μm syringe filter. Sonication was occasionally used (< 5 min.) to assist in dispersal. Silicon wafer was cut to appropriate dimensions using a diamond-tipped cutter and then cleaned in piranha solution for 20 minutes before rinsing with filtered absolute ethanol. Immediately prior to analysis, a small drop of the dilute particle dispersion was placed on the silicon surface and then promptly removed under a stream of ultra-high purity nitrogen. Failure to do this would

result in the capillary forces of the evaporating solvent drawing the particles together into aggregates, making accurate measurements more difficult.

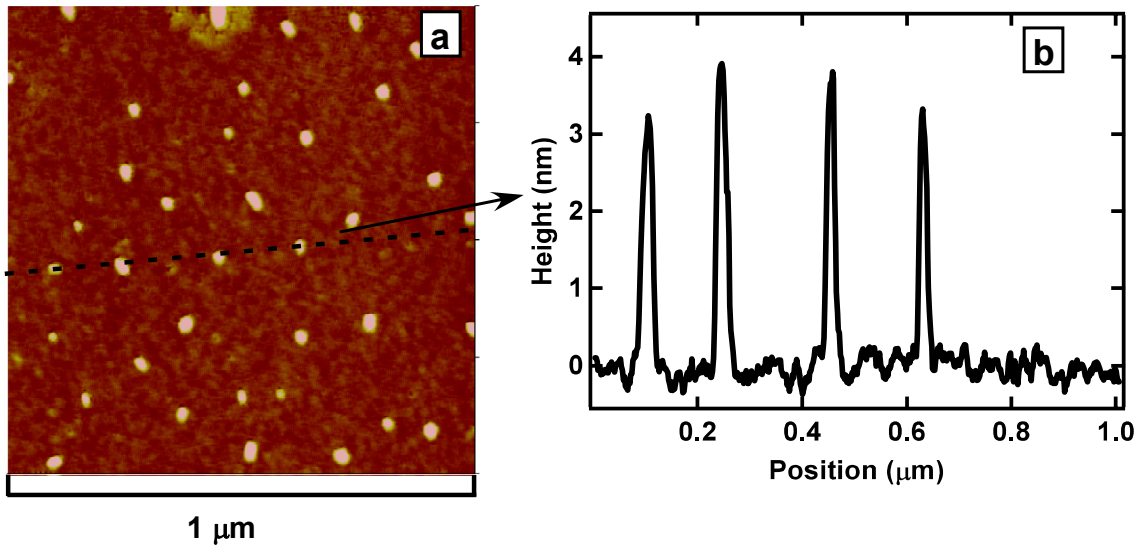

Figure 2.10 AFM data showing a) typical image of dispersed Y_2O_3 nanoparticles and b) plot of the Z cross section of the dotted line segment. The horizontal and vertical segment of the micrograph depicted in a) both have a length of 1 micrometer.

A representative image of dispersed nanoparticles on a silicon surface is shown in Figure 2.10a. Note that the X and Y scale is much different than the Z scale of the false color image that is used to illustrate the height or Z readings of the sample. As seen in the figure, particles are well dispersed when the above procedure is followed. If a line is drawn across the image, a cross section of the Z-value is obtained as seen in Figure 2.10b. Particle diameters are taken to be the height difference between the peak Z value and the baseline. A 3D image that yields itself to easier interpretation of the same data is shown in Figure 2.11. For all Y_2O_3 particle sizes presented here, at least 200 particles were counted in multiple sample regions for at least 2 independently prepared samples.

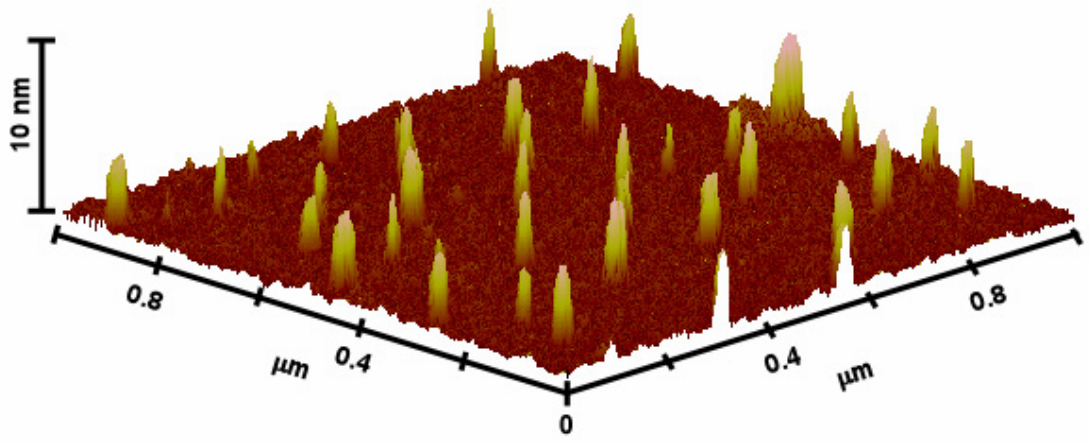

Figure 2.11 AFM data seen in Figure 2.10 rendered as a 3-D image. Note that the particles are well dispersed and can be easily quantified.

2.2.10 UHV Apparatus for DMMP Exposure to Nanoparticles

Ultra-high vacuum conditions are critical for many surface analytical techniques such as XPS and are excellent for low-level exposure experiments. A custom 112 L stainless steel chamber (see Figure 2.12) with a variety of conflat® flanges for UHV compatible seals was used for the present experiments. Components mounted on the chamber include pumps, KBr windows for IR transmission, gauges, a load-lock chamber, a cold-head, electrical and thermocouple feedthrough flanges, viewports, leak valves, X-ray source, and electron analyzer.

A 2,000 L s^{-1} magnetically levitated turbo pump (Osaka 2003 M), that is backed by a rotary vacuum pump (Edwards E2M30, 9 L s^{-1}), evacuates the chamber to a base pressure of ~ $5x10^{-10}$ Torr. In addition to the RGA mass spectrometer, KBr infrared windows, and the X-ray source and electron analyzer described elsewhere, several other pieces of equipment are mated onto the chamber. Pressure is monitored by cold cathode

gauge (Pfeiffer IKR270). The cold head of a helium compressor (APD cryogenics HC-2) is mounted in the chamber and cools the copper block sample mount by connecting copper braiding. Simulant-saturated carrier gas is introduced into the chamber via a sapphire plate precision leak valve (Varian) that enables a controlled exposure rate. Windows allow viewing of the sample and the chamber components during experiments. A manual 6" gate valve (HVA) separates the main UHV chamber from the load lock chamber.

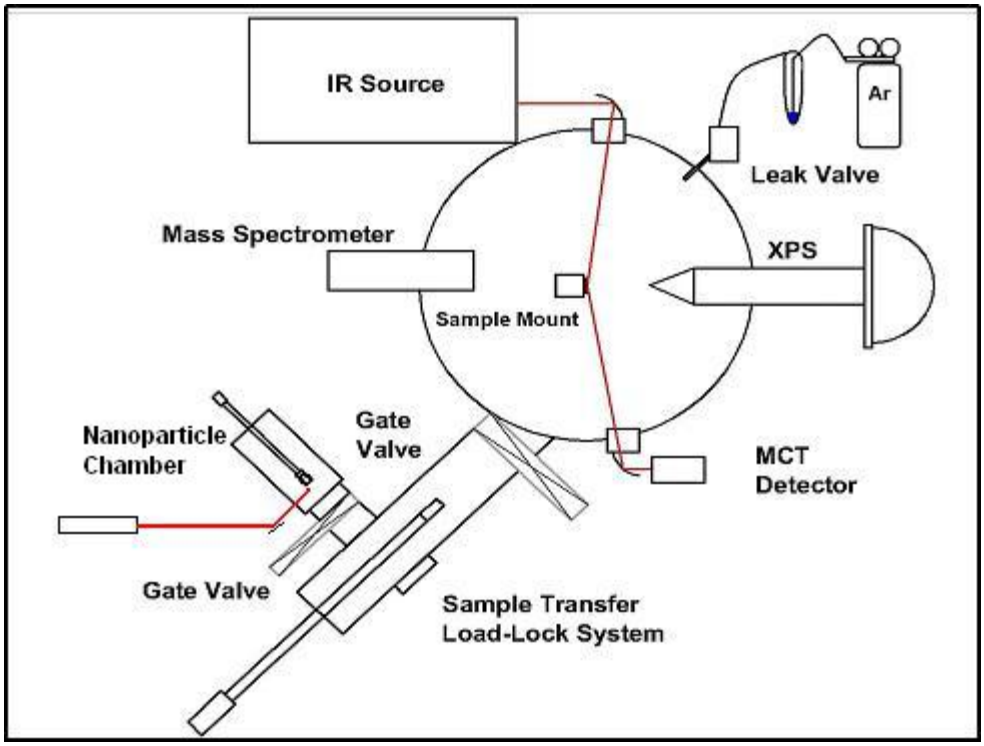

Figure 2.12 Schematic of the nanoparticle synthesis chamber attached to an UHV chamber used for the described experiments.

The sample is mounted on a copper block that is itself mounted onto a stainless steel rod that may be manipulated using a precision XYZ manipulator (McAllister MA1000). Rotation of the sample is controlled with a differentially pumped rotary platform (McAllister DPRF600). The copper block is designed so that the custom-built

sample holder can screw in, maximizing thermal contact and bringing the sample mount flush with the shielded UHV button heater (HeatWave Labs, Inc.) that is capable of reaching temperatures of 1473 K. In order to monitor the sample temperature, K-type thermocouple wire is spot-welded to the copper block, and is connected to a thermocouple display via an electrical feed-through flange.

Sample introduction into the UHV environment is performed with a linear rotary precision magnetic manipulator (Transfer Engineering DBLRP) that has a custom-built stainless steel key piece to secure the sample during transfer. The sample transfer manipulator is housed within a load lock chamber that is roughed with a liquid N_2 sorption pump and brought down to base pressures of ~ 5 x 10^{-8} Torr with an ion pump. Pressures in the load lock chamber are monitored by a compact full range gauge (Pfeiffer PKR251). The turbopump, foreline valve, gate valves, ion pump, and mass spectrometer are controlled using an interlock program.[28] A custom designed Labview® program along with FieldPoint modules prevents damage to UHV equipment due to power losses or unexpected pressure bursts.[28,29]

The nanoparticle films in this study are created in a nanoparticle synthesis chamber (MDC Inc.) that is mated to the load lock chamber through a 2 ¾" flange and is isolated by a gate valve (MDC Inc.). A sorption pump provides an oil-free rough pumping capability, and the ion pump on the load-lock chamber is used to bring the vaporization chamber to a base pressure of ~ 1 x 10^{-7} Torr. A nitrogen-calibrated Pirani gauge (Granville-Phillips) was used for precise measurements of backfill pressures in the ranges under which vaporizations were performed. 1 cm^2 gold-coated substrates were mounted on a stainless steel sample holder for depositing nanoparticle films. A stainless

steel fork mounted on a differentially pumped linear rotation arm (Thermionics) was used to manipulate the sample between the vaporization position and transfer to the sample manipulator-mounted key in the load lock chamber. Pellets for evaporation, prepared as described in Section 2.2.1, were placed on a stainless steel platform with height-adjustable legs.

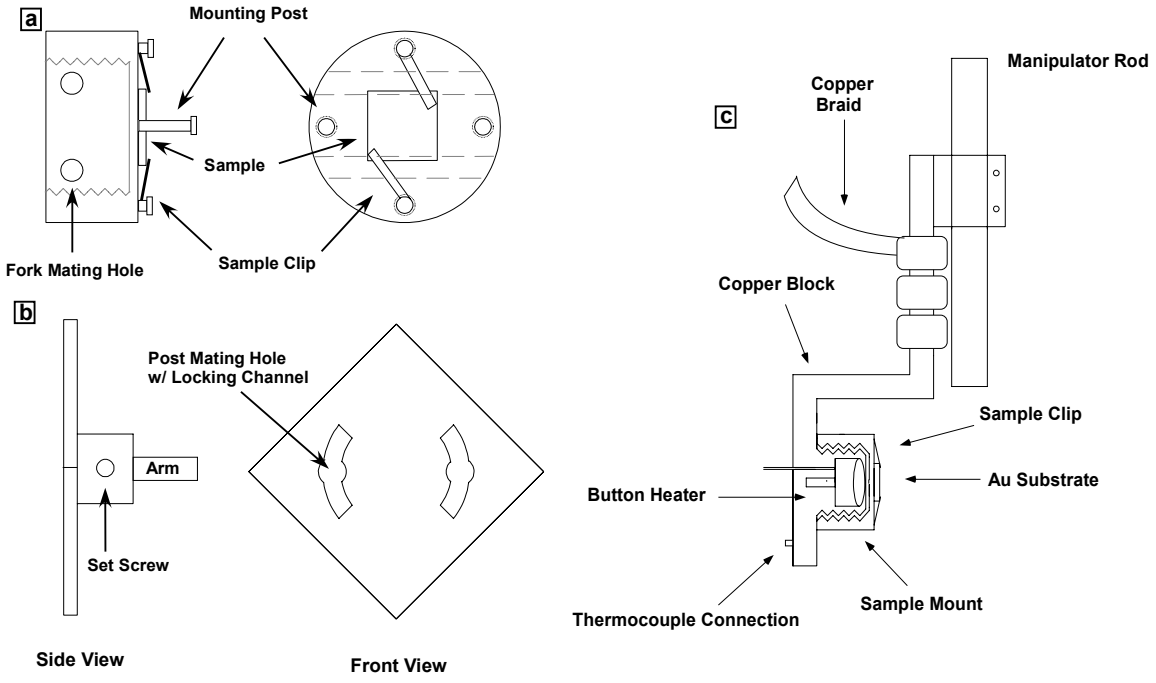

Figure 2.13 Custom devices for sample control: a) Mount for gold substrate, b) Load lock arm transfer key, c) Copper block on precision manipulator in UHV chamber equipped with heating and cooling capabilities.

A Melles Griot 0.5 mW He-Ne laser is reflected using a mirror and beamsplitter to be co-linear with a Synrad Duo Lase cw-CO_2 laser (output 40W). The CO_2 laser is directed by mirrors and focused by a ZnSe lens (focal length 254 mm) to strike the target at a 50^o angle and with a 1 mm spot size. The He-Ne laser enables the user to visually confirm the beam path of the infrared CO_2 laser.

A typical study was performed as follows: the load lock and vaporization chambers were vented with N_2 to load the sample mount with clean gold substrate onto

the forked transfer arm. A pellet was quickly removed from the 1273 K oven and transferred from the Pt crucible to the vaporization platform. The chamber was immediately evacuated to ~ 5 x 10^{-4} Torr via sorption pump, then the load lock chamber ion pump was used to bring the chamber down to base pressure. Laser alignment was checked and the substrate was positioned over the vaporization platform 3.5 cm above the target. The vaporization chamber was isolated from the load lock chamber (and ion pump) via the gate valve and then was backfilled to the desired pressure. Nanoparticle synthesis was then performed (typically for 4 minutes) and the chamber was roughed down again with the sorption pump, after which the gate valve to the load lock chamber was opened. The sample mount was transferred to the precision manipulator while under vacuum, and then the load lock chamber is isolated from the vaporization chamber. Once an acceptable pressure (< 1 x 10^{-7} Torr) is reached, the sample is transferred into the UHV chamber, with care taken to allow an acceptable IR beam path. Any pre-exposure XPS was performed, and then the sample was manipulated into grazing incidence with the IR light beam. The sample is then ready for exposure to simulants.

2.2.11 RAIRS

Reflection Adsorption Infrared Spectroscopy (RAIRS) is the primary analytical method used in this study to investigate the interaction of organophosphonate molecules and metal oxide nanoparticles. Vibrational spectroscopy has been widely used to study the structure-property relationships of simple chemicals and even polymers on surfaces.[30] Infrared spectroscopy is valuable because it is sensitive to bonds as opposed to atoms, so the nature of the functional groups on a surface may be probed. Thus, the chemical environment, identity, and molecular geometry of surface-bound species may be

determined with this vibration spectroscopic method. In the studies here, a reflective gold substrate is used to support the film of nanoparticles, enabling the use of reflection infrared techniques to study the adsorption and decomposition of the CWA simulants on sorbants.

In RAIRS, a beam of infrared photons impinge on the surface at a grazing angle and interact with the supported nanoparticle film along with any adsorbed species. Photons that are not absorbed are reflected by the metallic substrate and directed to the infrared detector. A Michelson interferometer collects all the wavelengths of light simultaneously and is used to generate an interferogram, which is digitized by the spectrometer electronics and then converted into a spectrum by the Fourier transform mathematical operation. The resulting absorbance spectrum is shown as a plot of absorbance intensity versus wavelength (μm) or energy (cm^{-1}). While Francis and Ellison were among the first to validate the use of reflection infrared methods to study adsorbates on metal surfaces,[31] Greenler articulated some of the theoretical aspects of using this powerful experimental technique.[32,33]

An IR beam of light that strikes a reflective planar surface at angle θ (with respect to the surface normal) can be simplified into electric vector components that are resolved into s-polarized (E_s) or p-polarized vectors (E_p), that are respectively parallel and perpendicular to the plane of the surface as seen in Figure 2.14. The phase change for the s-polarized vector upon reflection from the clean metal surface is near 180^o, while the amplitude ratio of the impinging (E_s) and reflected (E_s') is near 1. As a result, the combination of the two opposing vectors with equivalent magnitudes leads to a resultant that is very close to zero at the surface, meaning that there is practically no s-polarized

electric field strength and therefore no interaction between s-polarized light and the dipoles of adsorbed molecules. Due to the relatively long wavelength involved in IR spectroscopy, this phenomenon holds for relatively thick films, as illustrated by the lack of an adsorption spectrum for s-polarized light reflected from a 22-nm thick film of copper oxalate by Poling.[34]

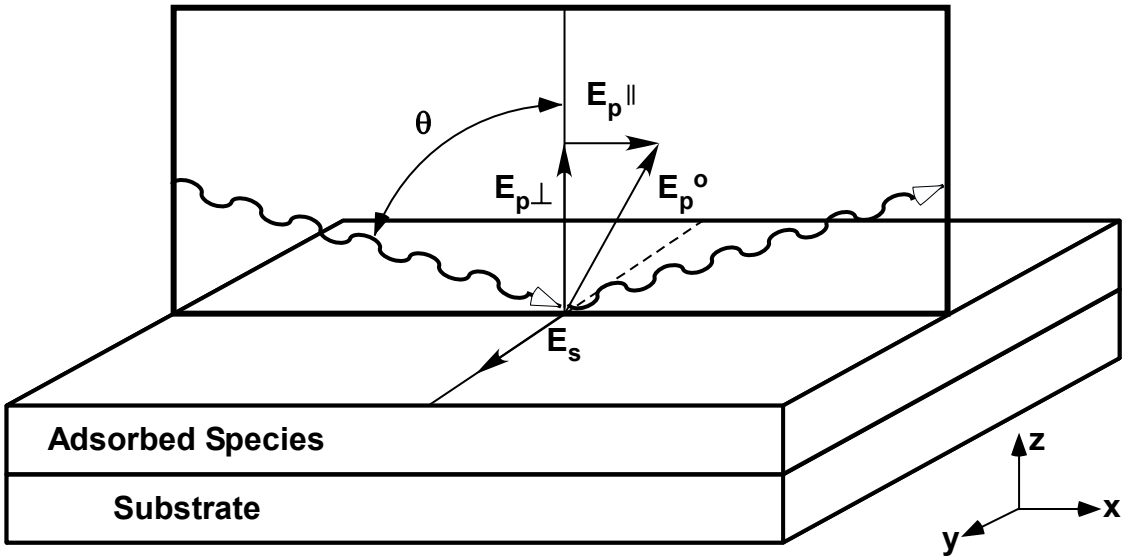

Figure 2.14 Representation of infrared radiation reflecting off of a metal substrate at a glancing angle. The electric dipole is resolved into two parts.

The situation is different for p-polarized light, where application of Maxwell's equations show that the impinging electric vector amplitude (E_p^o) gives rise to a normal ($E_{p\perp}$) and tangential ($E_{p\|}$) fields. As the angle θ nears 90^o or a grazing incidence, the resultant for the tangential field is small, however the resultant for the normal field is enhanced.[35] This gives rise to the surface selection rule for reflection infrared methods: only vibrational modes that have dipole oscillation with some component normal to the surface are observable. In addition, modeling the absorption of p-polarized light for a thin film supported on a reflective copper, it is shown the use of a grazing angle of 88^o yields a 25-fold improvement in absorbance intensity when compared to normal incidence.[32]

For gold metal, the optimal angle is near 86°, which is the approximate angle of incidence used in the current experiments.

For the UHV exposure experiments performed here, RAIRS was performed with a Bruker IFS 66v/S spectrometer, depicted in Figure 2.15. Light is emitted from a SiC glowbar middle infrared sources (A) and passes through a 2.5-mm aperture (B) and a Zn-Se wire grid polarizer before entering the interferometer. A movable mirror (D) is placed to either allow light to pass on to the internal analysis chamber and detector (H and I) or reflects the light through KBr windows, passing into the UHV analysis chamber. The p-polarized IR light strikes the sample surface (F) at an incident angle of 86° and enters the external liquid N_2 cooled MCT (mercury-cadmium-telluride) detector (G). Spectra were taken as difference spectra with the spectrum of the clean nanoparticle surface as the background unless otherwise noted. Each spectrum was collected with a resolution of 2 cm^{-1} and is the average of 256 scans.

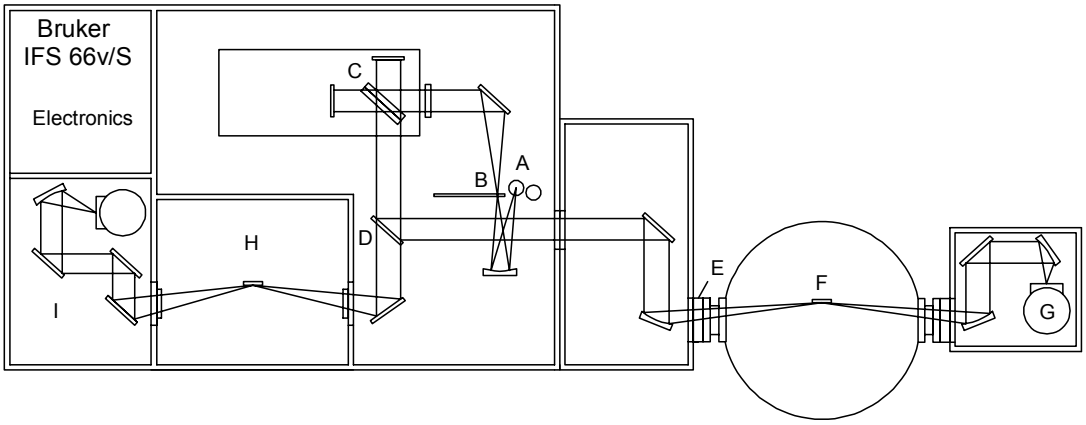

Figure 2.15 Schematic of Bruker IFS 66v/S spectrometer setup for RAIRS: (A) IR Source, (B) Aperture wheel, (C) Interferometer, (D) Movable Mirror, (E) KBr Window, (F) Sample in UHV chamber, (G) External detector, (H) Internal sample compartment, (I) Internal detector chamber.

The Bruker instrument is designed so that infrared spectra may be taken of samples in the internal sample compartment for routine analysis or UHV experiments

may be performed using the external UHV analysis chamber and independent external detector. A Vacuubrand diaphragm MD4 pump (1.04 Ls^{-1}) is used to maintain a vacuum in all compartments of the IFS 66v/S to eliminate interference from gaseous CO_2 and H_2O in the chamber, as well as to maximize the lifetime of the hydroscopic IR optics. The movable mirror within the interferometer operates with flowing N_2 to serve as an air-bearing, so the base pressure of 3 mbar will increase to approximately 18 mbar when the spectrometer is operating.

For *in situ* exposure experiments in the UHV chamber, IR light is directed from the interferometer to the sample at grazing angles using a gold-coated parabolic mirror (focal length 250 mm). A Vacuubrand MD1 diaphragm pump (0.32 Ls^{-1}) evacuates the detector box to approximately 6 mbar, where a series of mirrors reflect the light to the MCT detector. KBr windows (55 mm φ x 5 mm, wedged 0.33^o) that are positioned in flanges (McAllister) that have differential pumping capabilities separate the UHV chamber from the IR components.

2.2.12 Mass Spectrometer

For dosing experiments a Stanford Research Systems (SRS) Residual Gas Analyzer (RGA) 300 mass spectrometer was utilized to monitor the partial pressures of the analyte as well as atmospheric species in the chamber. In addition, the RGA 300 was invaluable for identifying the presence of a leak in the chamber and was used to check for contaminants prior to the experiment. The mass spectrometer works by first ionizing molecules with an electron impact ionizer, and then selecting ions based on a mass-to-charge (m/z) ratio using a standard quadrupole mass filter. Quadrupole probes consist of four rods held parallel to each other that are driven with a combination of direct current

and radio frequency voltages in such a manner that the positively charged ions with a m/z value other than the selected one will have an unstable trajectory through the filter and will not pass through the filter. Ions with the selected m/z value will then be detected with a Faraday cup that is shielded from the intense fields of the quadrupoles. For greater sensitivity during low pressure operation (~ 1 x 10^{-9} Torr), a four-channel continuous dynode electron multiplier is used to collect the ions and amplify the signal before processing.

During experiments, the Faraday cup detector was used to estimate the partial pressure of DMMP in the chamber by taking the ratio of the intensities of the dominant mass fragment of the carrier gas and DMMP. This ratio is then normalized to the absolute pressure reading given by the pressure gauge to give an approximate pressure of the analyte. Typically, scans were collected from m/z values of 1 to 140 with the ionizer electron emission current set to 1.75 mA, a 70 eV electron energy, and a focus voltage of 90 V. If the electron multiplier was used, it was typically set to a gain of ~ 4000 and a potential of ~ 1400 V.

2.2.13 Doser

Exposure of the nanoparticle samples to the low vapor pressure simulants used in this study was performed via a glass doser attached to a leak valve (see Figure 2.16). A few mL of simulant is placed in the O-ring sealed glass apparatus. Inert gas at ~ 760 Torr flows into the doser and is bubbled through the simulant via the glass tube. Gas-entrained vapor then flows out of the apparatus into the leak valve where it is controllably introduced into the UHV chamber. Prior to use, the bubbler is evacuated and then raised to atmospheric pressure with the inert gas. Rotaflow valves are used to control the gas

flow through the apparatus. The bottom of the doser is placed in a heated sand bath (348 K) to increase the partial pressure of the simulant.

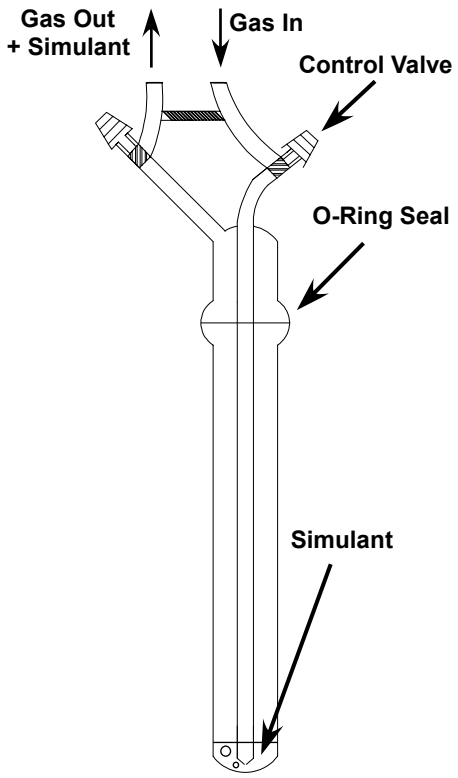

Figure 2.16 Glass bubbler apparatus used for exposing samples to simulant. Control valves are used to vary the flow of inert gas down the straw, bubbling through the simulant.

2.2.14 Experimental Considerations for UHV experiments

Several experimental issues must be taken into consideration for the successful conclusion of exposure experiments performed here. First, one must consider the nature of the nanoparticle samples that are under study here. As demonstrated later (Chapter 5), yttrium oxide is known to be hygroscopic and to react with atmospheric CO_2. High surface area nanoparticles are even more reactive, so exposure to these gases must be minimized before transfer of the sample into ultra-high vacuum conditions. To minimize the amount of CO_2 and H_2O introduced into the vaporization chamber, pellets of Y_2O_3 were transferred directly from the 1273 K oven to the platform, after which the chamber

was promptly evacuated. Even with this precaution, carbonate and hydroxyl groups still populate as-prepared particle surfaces. Upon transfer into ultra-high vacuum, surface bound species undergo changes. Physisorbed and weakly bound species desorb from the surface, and often changes in the structure or bonding of the carbonate groups were detected in the RAIR spectra. These changes are not great when observing the direct RAIR spectrum of particle films, but are substantial when observing difference spectra. Equilibrium was typically reached 30 - 45 minutes post sample introduction, so this amount of time was allowed to pass prior to the initiation of any experiment.

Another concern is the extreme sensitivity of these long experiments to changes in the partial pressure of CO_2 and H_2O in the evacuated spectrometer and detector boxes. Exposure experiments often required very steady partial pressures of these gases for periods greater than 8 hours. To minimize interference, the infrared spectrometer and detector box must be continually under vacuum for several hours prior to the start of an experiment, and care must be taken to prevent any change in the partial pressures during data acquisition. If either has been open to atmosphere, at least 12 hours of uninterrupted pumping must be performed prior to the experiment. The MCT detector remains stable after cooling with liquid N_2 for approximately 7 – 8 hours, however some changes in the detector box occur after filling the detector dewar. Therefore, the detector was initially cooled 2-3 hours prior to the onset of spectrum collection. Once the detector is cool, further additions of liquid N_2 can be performed carefully, minimizing atmospheric changes within the detector box.

Infrared spectra taken with experimental conditions used here are extremely sensitive to the position of the sample, which can be disturbed by external movement or

vibrations or by pressure fluctuations during sample dosing. The latter occurred very often when higher levels of exposure were sought to allow further experimentation within the ~ 8 hour stable lifetime of the IR detector. It was found that once movement of the sample occurred, the background scan for RAIRS was no longer satisfactory for further acquisition, even if manual manipulation of the sample was attempted. Therefore, when dosing at a higher flux (with total pressure of the chamber > 1 x 10^{-7} Torr) it was sometimes necessary to collect a new background spectrum after exposure began to maintain the stable background.

Final consideration must be made of the dosing process. When initially dosing a new simulant, all of the surfaces (such as Teflon® tubing and the leak valve) will be saturated with the simulant before equilibrated vapor passes into the UHV chamber. It was found that mild heating of the leak valve and tube surfaces reduced the loss of simulant on surface walls due to condensation. As a consequence of the saturation of the lines and leak valve, care had to be taken when switching simulants. Even high vapor pressure simulants such as methanol would require days of dosing with dry inert gas to remove contamination. Stainless steel tubing was used to enable bake-out of the lines, but contamination remained a significant problem. Future use of a dosing system with multiple parallel valves will reduce the difficulty in changing simulants.

2.3 Summary

The properties of metal oxide nanoparticles are of great interest due to the many potential applications of these materials. Throughout this series of studies a wide variety of experimental techniques and instruments were utilized to investigate the luminescent properties and surface chemistry of a series of nanoparticles. Laser spectroscopy is used

to probe the effects of doping particles with luminescent lanthanide ions, as well as using these ions as indicators of the particle properties themselves. XRD, TEM, and AFM analysis allow characterization of the physical properties such as size and size distribution, which are critical factors. SEM and BET analysis are used to understand the structure and surface area of bulk films of nanoparticles. XPS and RAIRS are used to probe the surface chemistry of particles when exposed to atmosphere and when exposed to CWAs. Each technique has its own advantages and disadvantages and characteristics which must be understood in order to accurately interpret results and draw conclusions.

Chapter 3. Interparticle Energy Transfer

3.1 Introduction

Lanthanide-doped phosphors are materials that have a wide range of uses, and therefore are the subject of considerable study. One of the newer phosphor classes involves nano-scale optical materials. These ultra-small materials often have different optical properties than their bulk analogues, and therefore are the subject of study by many researchers. One important phenomenon in these materials is energy transfer between lanthanide ions, which can have a strong effect on the optical properties of the phosphor. Many studies have been performed on the properties of lanthanide-doped nanoparticles, including the nature and effect of interparticle energy transfer. However, there is no known example of lanthanide-lanthanide coupled interparticle energy transfer. This technology could enable an expansion of applications of the nanophosphors, particularly within multi-dimensional assays. It is therefore natural to wish to expand knowledge of lanthanide nanoscale materials to heterogeneous or multi-nanoparticle systems. Here, a study was performed to determine if interparticle energy transfer (ET) could occur between two lanthanide ions doped into nanoparticles.

3.1.1 Lanthanides

Lanthanides or the Rare Earths have found increasing use in the past 100 years. Applications of the lanthanides include use in display phosphors for TVs and computer monitors, phosphors in fluorescent lights, as probes to determine the structure of biomolecules, as dopants in fiber optic cable decrease losses, as strengtheners in metals, in materials for solid state lasers, and as luminescent materials for many products.[36] In

lanthanides, the energies of the $4f^n$ transitions correspond mostly to the visible region of the electromagnetic spectrum, resulting in their use for optical applications.[37]

Lanthanides most commonly exist in the trivalent form, and have the characteristic of a partly filled 4f shell, that is less extended than the 5s and 5p shells. The 4f shell is therefore shielded from gross effects such as bonding with the surrounding anions,[38,39] resulting in the same general spectrum as the free ion, with some perterbations caused by the symmetry and crystal-field strength of neighboring ligands.[38] Another result of 4f orbital shielding is that the parabolae representing the ground and excited states in the coordinate diagram are horizontally aligned and do not cross, consequently, spectral bandwidths are narrow, and Stokes shift is eliminated.[37] These 4f orbital characteristics result in sharp, strong spectral characteristics when lanthanides are doped into a solid with a constant crystal field[38,40] This simplicity of the spectrum of lanthanides greatly eases spectral analysis of these compounds.

3.1.2 Properties of Lanthanide-Doped Nanoparticles

In particular, lanthanide-doped nanoparticles have several properties which differ from bulk or micron-sized particles. These changes are typically observed as the particle size is reduced below 50 nm. Previous work in our laboratory showed that the linewidths of the 4f-4f transitions are broadened with decreasing size of Eu^{3+}:Y_2O_3 particles.[41] This phenomenon is attributed to inhomogeneous broadening due to a decrease in the order of the crystal with diminishing size. In addition, the fluorescence yield has been observed to decrease with particle size, which is attributed to quenching caused by surface defects instead of an innate particle size effect.[42,43] Loss in efficiency is coupled with reduced concentration quenching, which could be associated with reduced energy migration

induced by particle boundaries, or due to size-dependent energy transfer dynamics.[44] Luminescent lifetimes are also generally shorter in nano-phosphors than micron-scale or bulk material, likely due to greater non-radiative ET. However, dispersal of nano-phosphors in low-refractive index material can increase the radiative lifetime.[45]

While some of these properties may seem to make nanocrystalline phosphors unappealing for some optical applications, other properties of these materials are advantageous. For example, lanthanide-doped nanoparticles often have less broad emission compared to quantum dots. This makes discrimination between different "colors" of dot emission more difficult, and results in a lower intensity at the λ_{max}. In addition, lanthanides have the capability of excitation by near infrared (NIR) light to eliminate biological sample autoflourescence, while emitting visible light.

Lanthanide-doped nanocrystals also have size-dependent phonon density of states, which can change energy transfer and luminescence dynamics.[46] Nanoparticles also have properties such as a high degree of scattering, low thermal conductivity, and a high degree of light trapping in multilayer systems. These properties could all be advantageous for certain applications such as random lasers, [47] where the high degree of scattering in the disordered gain medium replaces the optical cavity of more traditional lasers.[48] Finally, doping lanthanides into nanostructures can yield information about the material itself. For example, Eu^{3+} emission is sensitive to the surrounding crystal structure, so different Eu^{3+} sites (such as a surface ions) can be detected spectroscopically.[49]

In summary, changing the size scale of phosphors from the bulk to the nanometer scale influences the optical properties of the new material in several ways. Changes in the crystal structure and optical properties of the host material that accompany changes in

size can influence the efficiency and nature of the emission. In addition, the significant increase in defects (at surfaces or due to increased strain) result in changes in emission rates and the energy transfer properties within the particles. Properties such as absorption efficiencies, the phonon density of states, energy transfer efficiencies, quenching by defects, and electron-phonon interactions will influence important optical parameters such as radiative and non-radiative rates, lifetimes, and luminescence efficiencies.

3.1.3 Energy Transfer

One physical phenomenon that has been of great interest to scientists is energy transfer, where an excited molecule or ion transfers its excitation energy to another ion or molecule which may undergo radiative or non-radiative decay. ET is a useful concept because one may excite an ion in a solid mixture and have energy transfer to another ion, which can emit a photon at a different energy compared to the excitation photon.[50] Energy transfer is featured in numerous current applications such as fluorescent lighting, lasers, and displays via excitation of donors followed by transfer to visible-emitting acceptors. ET can therefore give flexibility in the design of emitting devices that is not seen in systems where direct excitation of the emissive species is used.

Since ET is such an important topic, it is critical to understand how and why it happens. ET can involve an intermediate photon (radiative) or not (nonradiative); the former does not exist in the systems studied here because the emission and absorption range do not overlap. Nonradiative excitation energy transfer between ions or molecules in solids has been studied widely.[51] In this type of transfer, the ion that is excited initially (via light energy) is known as the donor (D) or sensitizer. This excitation energy transfers to an acceptor (A) without any corresponding light emission. The excitation energy can

migrate among many D ions until it reaches a D ion that is near an A ion.[52] This migration may lead to concentration quenching as discussed below. Three types of interactions between ions cause energy transfer. These interactions are electrostatic coupling, magnetic coupling, and exchange coupling.

In solid state materials, the interaction or energy transfer between centers in general depends on the separation between the D and A ions, the energy-level structure of each ion, the local crystal field, the number of A ions in the coordination shell of a D ion, the dimensionality of the transfer, and on the population of phonon modes. In real systems, these parameters are not single numbers, but instead are random distributions which can be averaged with some difficulty. The most important of these parameters is the average distance between the active ions, which can be used to identify the interaction that is the cause of ET due to known distance dependences.

3.1.4 Dopant Concentration

When working with solids with energy transfer, it is rare for materials to be composed entirely of the optically active material. If this is the case, the sensitization is termed as host sensitization. Most of the literature instead deals with impurity sensitization, where the donor is a species that is doped into the host. Doping lanthanides into optically and magnetically inert materials has three advantages over the use of the pure materials. First, the signal from the lanthanide ion is not so strong that optical saturation occurs, which results in band broadening. Secondly, doped lanthanides will incorporate into crystal structures that do not occur with the pure lanthanides. This opens up a wider variety of materials to study by lanthanide probes. Finally, concentration quenching due to energy migration among donors to traps is greatly reduced.[40]

3.1.5 Lanthanide Energy Transfer

Lanthanide ET is utilized in many applications, one of which is Fluorescent Resonance Energy Transfer (FRET), where lanthanide ions are used to probe the structures of biomolecules. FRET involves dipole-dipole interactions, and therefore the ET rate falls off with the 6^{th} power of the distance between the D and A. The trivalent lanthanides serve as an isomorphous substitute for the spectroscopically inert calcium ions in biological samples.[53] While we are only considering lanthanide ions in solids, the biological applications indicate that trace amounts of water might not fully quench the luminescence in our compounds.[54]

One of the most studied lanthanide-lanthanide energy transfer is Tb^{3+} sensitizing Eu^{3+} emission. Tb^{3+} is favored as the Eu^{3+} sensitizer because of its good absorption properties and its characteristic green emission[55]. ET between these two ions has been observed in glasses[55], thin films[56], and in polymer matrices.[57] Energy transfer can occur from the $^5D_4$ level of Tb^{3+} to the $^5D_1$ and $^5D_0$ levels of Eu^{3+} (see Figure 3.1). The energy difference between these levels can be accounted for by phonons. It has been found that the most likely type of interaction that causes this ET is the electric dipole-dipole interaction based on the concentrations of the donors and acceptors and the ET probabilities. As expected, all of these studies found that concentrations of the donors and acceptors are important in finding optimal ET.

In addition to the previous examples, some Tb^{3+} - Eu^{3+} ET studies have been performed when the two ions are doped into crystalline Y_2O_3. In one such study, both $Tb^{3+} \rightarrow Eu^{3+}$ and $Eu^{3+} \rightarrow Tb^{3+}$ transfer were observed. The ET was attributed to phonon-mediated, nonresonant cross relaxation at low temperatures, and anti-Stokes, resonant

cross relaxation at higher temperatures.[58] As with the previously mentioned studies, the ET was affected by the acceptor concentration.

In addition to the well-studied Tb^{3+} - Eu^{3+} ET system, energy transfer has recently been observed from $Er^{3+} \rightarrow Eu^{3+}$ in Y_2O_3 waveguides[59] and tellurite glasses.[60] This energy transfer occurs from the Er^{3+} $^4I_{11/2}$ level to the Eu^{3+} $^7F_4$ level. Er^{3+} has been studied as an active component of optical amplifiers for telecommunications purposes, utilizing the 1540 nm stimulated emission from the $^4I_{13/2}$ of the ion. Stimulated emission at 1540 nm is achieved via pumping the higher energy Er^{3+} $^4I_{11/2}$ level with 980 nm light. However, problems have been discovered with excited-state absorption and cooperative upconversion, resulting in energy loss via excitation of higher energy level states.[59] Therefore, energy transfer has been studied as a means to enhance the 1540 nm emission via transferring the population of the Er^{3+} $^4I_{11/2}$ to the $^4I_{13/2}$ level. $Er^{3+} \rightarrow Eu^{3+}$ energy transfer. Up to a 60% depopulation of the Er^{3+} $^4I_{11/2}$ level was achieved in Y_2O_3 waveguides with 0.44% Eu^{3+} doping,[59] however a simultaneous depopulation of the $^4I_{13/2}$ Er^{3+} level was observed in tellurite glasses,[60] which underscores the complicated results of doping a system.

Another type of lanthanide-lanthanide ET that is commonly found is $Eu^{3+} \rightarrow Eu^{3+}$ ET. This transfer has been studied in 1, 2, and 3 dimensional lattices and for $Eu^{3+} \rightarrow Eu^{3+}$ ET between different crystallographic sites. Su et al. reported $Eu^{3+} \rightarrow Eu^{3+}$ ET from the S_6 to C_2 crystallographic sites in Y_2O_3 co-doped with Bi^{3+} and Eu^{3+}. This system was of interest because it would emit blue, green, and red light simultaneously. The wavelength of emitted light in this phosphor was found to depend on temperature and excitation wavelength.[61]

3.1.6 Energy Transfer in Lanthanide Nano-scale Systems

Nogami et al. reported energy transfer from nanocrystals of SnO_2 to Eu^{3+} ions in SiO_2 glasses. Remarkably, fluorescence from the Eu^{3+} ion was 150 times greater in the presence of the SnO_2 nanocrystals than without. It was found that the size of the nanocrystals was important, in addition to the concentration of these donor nanocrystals.[62] Fujii et al. have reported energy transfer from Si nanocrystals to Er^{3+} [63,64], Nd^{3+} and Tm^{3+} [65], and Yb^{3+}.[66] All of these systems emit from the 4f-4f transitions of the lanthanides. The Er^{3+} transfer mechanism is relatively well studied and is attributed to electron-hole generation in Si with the recombination energy being transferred to the Er^{3+}. The use of nanocrystalline Si is critical because quenching at ambient temperatures is very strong in the bulk Si system due to phonon-mediated back transfer. In these systems, the size of the nanocrystals was very important in determining the degree of temperature quenching, with smaller (< 3 nm) sizes having higher efficiencies. Finally, Okamoto et al.[67] have reported energy transfer from CdS nanocrystals to Eu^{3+} ions with the corresponding 4f-4f emission. As in the previous example, the size of the nanocrystals was a major factor in the energy transfer. While these studies all involved transfer to lanthanide ions that were doped into nanocrystals, they indicate that size may play a critical role in any interparticle energy transfer.

One example of ET in colloidal lanthanide NPs was reported by Riwotzki and Haase. They found that ET occurred from vanadate to Eu and among vanadate groups in colloidal YVO_4:Eu NPs. $YP_{0.95}V_{0.05}O_4$:Eu was studied to investigate ET in the absence of vanadate → vanadate transfer. Based on their data, they found that emission from Eu ions

at the surface was quenched and that the ET to Eu was mostly coming from nearby vanadate groups and that the ET was not strongly dependent on temperature.[68]

Another interesting study that does not directly deal with energy transfer is a theoretical investigation of the suitability of Yb^{3+}:Y_2O_3 nanoparticles for a laser-cooling device.[46] Since the phonon spectrum is critical for material performance, the phonon density of states was calculated for Y_2O_3 nanoparticles to compare with bulk materials. The results show that the phonon spectrum is broad and ill-defined as opposed to the sharp modes that are visible in the spectrum for the bulk, that are attributed to the long range crystal structure. However, the phonon spectrum for the 3 nm particles has tails at both the low and high energy range, belonging to phonon modes that do not exist in the bulk. The broad nature of the phonon density of states in the nanoparticles is attributed to the lack of long-range order, and the high energy tail is assigned to surface ions. These results support the concept that a particle size effect influences the available phonon energies of a material, meaning these must be understood to design a material with the optimal phonon spectrum for a given application such as ET.

3.2 Experimental

The gas-phase condensation method was used to prepare pure and doped nanoparticles as described in Section 2.2.1. Doped particles are labeled by the initial molar concentration of the dopant, although dopant enrichment or depletion is possible due to preferential vaporization. The chamber was equipped with a cold finger, which served as a mount for a collector surface for this study. Particles were synthesized under a pressure of 10 Torr N_2, with a laser power of 45 W, and collected as prepared from the cold finger and collector surface. Mixing particle samples was performed by either 1) dry

grinding the mixture with a mortar and pestle, or 2) wet grinding with the aid of ethanol to help disperse particles. Particle annealing or mixing were performed if noted, and particles were then ready for optical studies.

Tb^{3+}-doped nanoparticles required special treatment procedures in order to maintain the terbium in the +3 oxidation state. Trivalent terbium is less stable than the other lanthanides used in this study, and readily oxidizes under the temperatures encountered during nanoparticle synthesis. To counter this effect, terbium was introduced as an oxalate complex into the yttria target. Decomposition of the oxalate results in a reducing atmosphere, which suppressed oxidation of the Tb^{3+}. Annealing of these particles was performed in a tube furnace under a reducing atmosphere (5% H_2 in N_2). These steps allowed the synthesis of green-emitting terbium phosphor nanoparticle materials.

For spectroscopic analysis, the NPs are packed as prepared into wells in a copper block. This block is mounted on the cold finger of a temperature-controlled, closed-cycle, He gas cryostat (capable of reaching 12 K). Unless under ambient conditions, sample temperature will be noted as results are discussed. Excitation is performed by a Continuum Nd:YAG-pumped dye laser using coumarin 480 and 481 for Eu/Er and Eu/Tb experiments, respectively. Laser pulse energy typically fell between 60 and 250 μJ. Light from the sample is detected by PMT equipped monochromators (1/4 and 1 m). The PMT signal is measured by a photon counter or boxcar integrator. Luminescence spectra for the Er/Eu experiments were typically collected with a 250 ns delay and 250 μs gate, while Tb/Eu experiments were collected with a 5 μs delay 500 μs gate. Appropriate optical

filters were used to reduce stray light entering the spectrometer. Data collection is performed by a PC equipped with a Labview data acquisition program.

A set of experiments was also performed in the laboratory of Dr. Uwe Hömmerich at Hampton University. For these experiments, the tunable source was a 10-ns Nd:YAG-pumped optical parametric oscillator (OPO). Luminescence was recorded with a PMT-equipped, ½ m monochromator.

3.3 $Er^{3+} \leftrightarrow Eu^{3+}$ Energy Transfer

3.3.1 Introduction

Initial exploration of interparticle energy transfer was performed with a mixture of Er^{3+}-doped Y_2O_3 and Eu_2O_3 nanoparticles. While Er^{3+} $^4I_{11/2} \rightarrow Eu^{3+}$ $^7F_4$ energy transfer has been observed in solid bulk materials,[59,60] this study focuses on other potential energy transfer processes that can be detected in other important (visible) regions of the spectrum (see Figure 3.1). Following initial characterization of the two materials, Er^{3+}:Y_2O_3 and Eu_2O_3 were mixed then tested for energy transfer. These materials were chosen based on analysis of the energy levels that suggest possible energy transfer from Er^{3+} resulting in the excitation of the $^5D_{2,1,0}$ levels of Eu^{3+}.

If energy transfer occurred in a sample, there are two results one would expect to see in the spectrum. In the emission spectrum, the emission corresponding to the level(s) of the D ion that are involved in transfer would decrease in intensity. Simultaneously, the emission peak(s) for the A ion that are involved in emission of transferred energy should increase in intensity (assuming the ET results in a radiative process). The second indicator would be the time-resolved fluorescent decays. A decrease in lifetime would be expected for the D ion and an increase would be expected for the A ion if ET occurred.

Under ideal conditions, ET could be observed by selectively exciting the donor ion, followed by observing emission of the acceptor, which is not excited by the source. This situation would yield a much greater level of sensitivity to energy transfer, and lifetime analysis would be simplified. Before looking at mixtures of doped particles, the spectral characteristics of the individually doped particles were recorded.

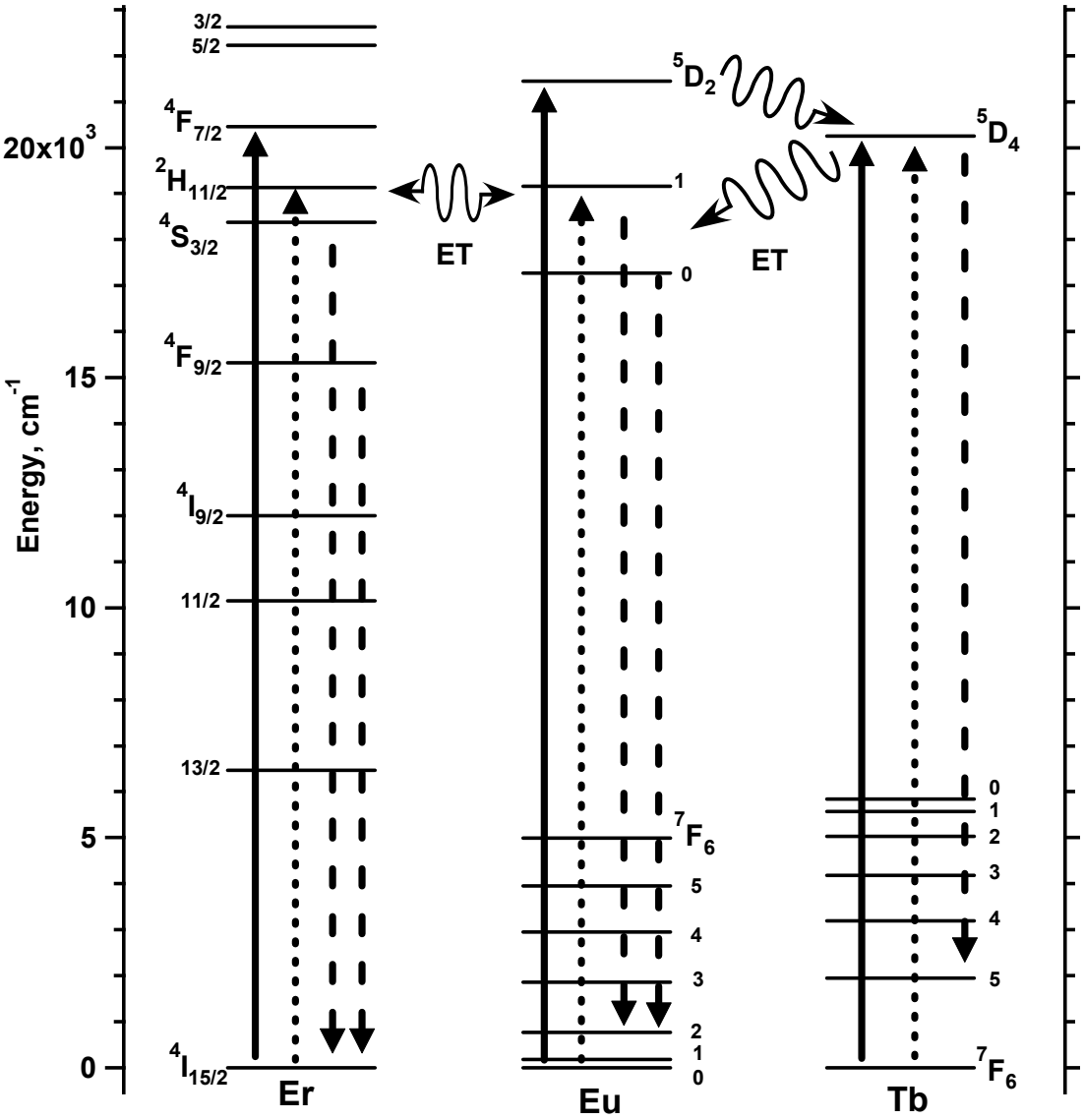

Figure 3.1 Energy level diagram demonstrating the transitions that may be involved in energy transfer between Er^{3+} and Eu^{3+} as well as Tb^{3+} and Eu^{3+}. The solid lines represent the excitation energy of the dye laser in this study, the dotted lines represent possible excitation via energy transfer, and the dashed lines represent the main emission lines analyzed in this study. Possible energy transfer pathways are indicated by curvy arrows.

3.3.2 Characterization of ET Candidate Materials

Before looking for ET, candidate materials that were doped with Er or Eu were studied spectroscopically in order to obtain reference spectra and lifetime values for comparison to the mixed samples. Time-resolved fluorescence data were taken for all major excitation and emission peaks. Initial characterization of the Er^{3+}-doped Y_2O_3 is shown in Figure 3.1. The Er^{3+} ions are excited via the $^4I_{15/2} \rightarrow {}^4F_{7/2}$ transition, and emission from the $^4S_{3/2}$ and $^4F_{3/2}$ levels are clearly observed. Figure 3.2 displays typical spectral data obtained for the Eu_2O_3 nanoparticles, where excitation is achieved using the $^7F_0 \rightarrow {}^5D_2$ transition, and luminescence is observed from the $^5D_0$ level.

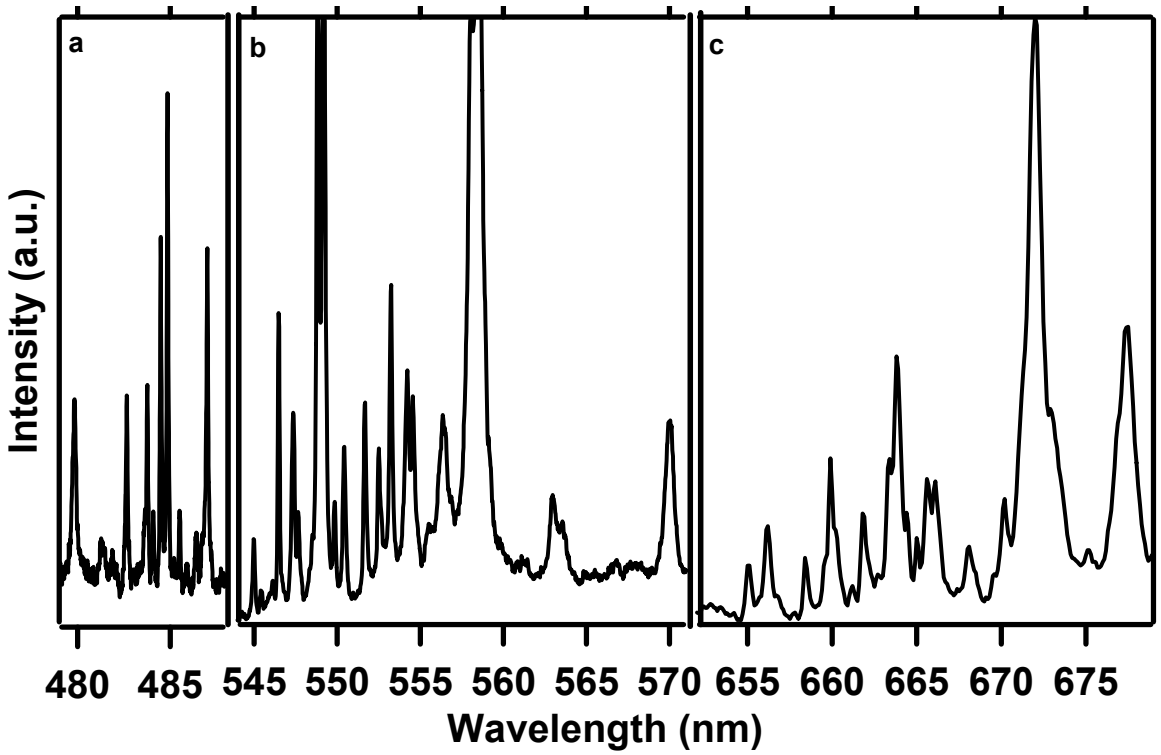

Figure 3.2 Luminescence spectra of 10% Er:Y_2O_3 nanoparticles showing a) $^4I_{15/2} \rightarrow {}^4F_{7/2}$ excitation spectrum monitoring emission from the $^4S_{3/2}$ level, b) $^4S_{3/2} \rightarrow {}^4I_{15/2}$ emission spectrum exciting the $^4F_{7/2}$ level, and c) $^4F_{3/2} \rightarrow {}^4I_{15/2}$ emission spectrum exciting the $^4F_{7/2}$ level.

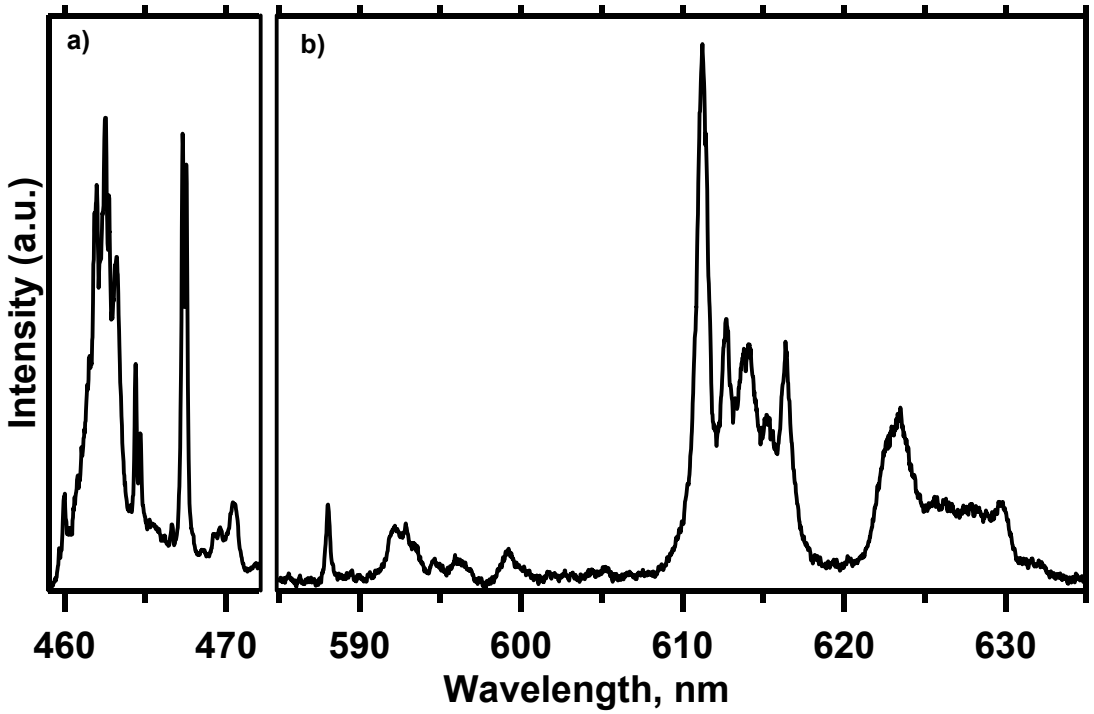

Figure 3.3 Luminescence spectra of Eu_2O_3 nanoparticles showing a) the $^7F_0 \rightarrow {}^5D_2$ excitation spectrum, and b) the emission spectrum from the $^5D_0$ level.

3.3.3 $Er^{3+} \leftrightarrow Eu^{3+}$ Interparticle Energy Transfer Results

After collection of reference spectra of the single-lanthanide materials, experiments were performed with mixed Eu_2O_3 nanoparticle / Er^{3+}:Y_2O_3 nanoparticle samples to search for evidence for energy transfer. 50 / 50 mixtures of the samples were prepared, and then packed into the sample mount for analysis. Spectroscopy was performed to find all of the peaks in the available excitation and emission range. Excitation and emission spectra were examined for any indications of ET at 20 K, 60 K, 120 K, and 298 K. For example, see Figure 3.3, where no apparent change in the Er^{3+} emission spectrum is observed and no Eu^{3+} luminescence is detected when Er^{3+} is excited. Time-resolved data were collected for all peaks and checked for major deviation from the single-lanthanide materials lifetimes. Unfortunately, no evidence for ET was observed.

To enhance the probability of $Er^{3+} \rightarrow Eu^{3+}$ ET, a second mixture of nanoparticles (25/75 Er:Y_2O_3/Eu_2O_3) and annealed the sample at 773 K with the hypothesis that the Eu^{3+} and Er^{3+} ions would be closer together to facilitate ET. As with the previous mixed sample, all emission and excitation lines were recorded and lifetime measurements were collected at four temperatures. No evidence was obtained that would provide evidence for interparticle energy transfer.

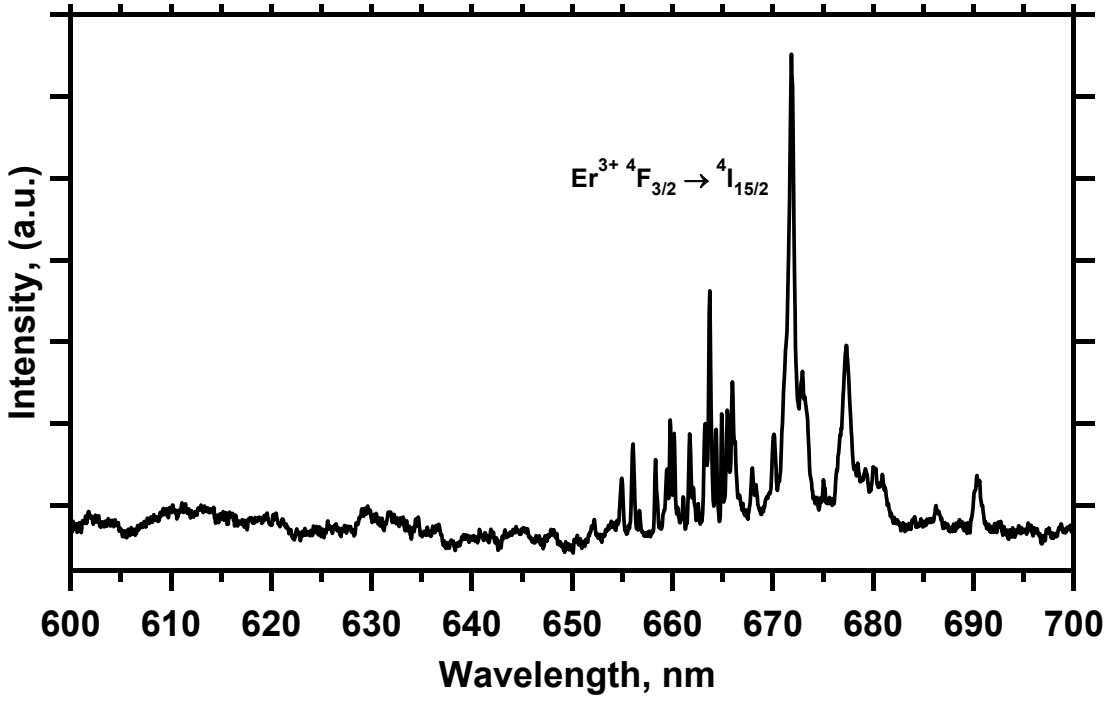

Figure 3.4 Luminescence spectrum of a mixture of annealed 10% Er^{3+}:Y_2O_3 and Eu_2O_3 nanoparticles (25% and 75% by weight, respectively) exciting the $^4I_{16/2}$ level of Er^{3+}. Note the lack of Eu^{3+} emission (see Figure 3.2).

3.3.4 $Er^{3+} \leftrightarrow Eu^{3+}$ Bulk Solid Energy Transfer Results

Once it was clear that no ET was observed in the NP mixtures, the study was expanded to include investigation of the equivalent bulk solid powders. This could provide insight into the possibility of ET occurring without the effects due to the use of nanoparticles. Dried Er:Y_2O_3/Eu_2O_3 as well as annealed Er:Y_2O_3/Eu_2O_3 powders were

studied initially. Once these materials yielded no evidence for energy transfer, further studies were undertaken to test whether a specific crystallographic phase (i.e. cubic or monoclinic) could induce energy transfer. Yttrium oxide exists in the cubic phase in the bulk, but may be converted into the monoclinic phase with high pressures and high temperatures, while Eu_2O_3 may be converted to the monoclinic phase via elevated temperature alone.[69] Each phase will result in slightly different spectral properties due to the change in the environment around the optically active ions. For this reason, bulk samples of cubic Er:Y_2O_3/monoclinic Eu_2O_3 and cubic Er:Y_2O_3/cubic Eu_2O_3 were studied for evidence of ET. No features in the spectra of these bulk materials were attributed to energy transfer.

In summary, no evidence for energy transfer was found for either the mixed bulk or nanoparticulate oxides in the visible region of the spectrum. It should be noted that these experiments did not probe the possibility of Er^{3+} $^4I_{11/2}$ → Eu^{3+} $^7F_4$ transfer that has been documented in the IR region of the emission spectra. After this series of experiments, efforts to develop interparticle lanthanide energy transfer turned to a more well known and studied energy transfer system (Tb^{3+} → Eu^{3+}).

3.4 Tb^{3+} ↔ Eu^{3+} Energy Transfer

3.4.1 Introduction

Following the absence of energy transfer in the previous Er^{3+}/Eu^{3+} study, the focus of the project shifted to the more well-known Tb^{3+}/Eu^{3+} system. Energy transfer is known to occur from the $^5D_4$ level of Tb^{3+} to the $^5D_1$ and $^5D_0$ levels of Eu^{3+}. This energy transfer should be readily observed in the visible region of the spectrum, and have the additional benefit of involvement of the most intense transitions of Tb^{3+} and Eu^{3+}. The

combination of these two features enhances the probability of detection of any energy transfer.

3.4.2 $Tb^{3+} \leftrightarrow Eu^{3+}$ Energy Transfer Experimental

To test for energy transfer, 0.5% Tb^{3+}:Y_2O_3 and 2.5% Eu:Y_2O_3 nanoparticles were prepared. Unless otherwise noted, all samples were annealed at 773 K for 4 hours, which should improve spectroscopic properties of the nanoparticles without resulting in substantial particle growth or necking processes. All spectra were collected at room temperature, and mixing of the samples was performed prior to annealing, unless stated otherwise. To begin the study, the spectral characteristics of the individual Tb^{3+} and Eu^{3+} - doped yttria nanoparticles were collected.

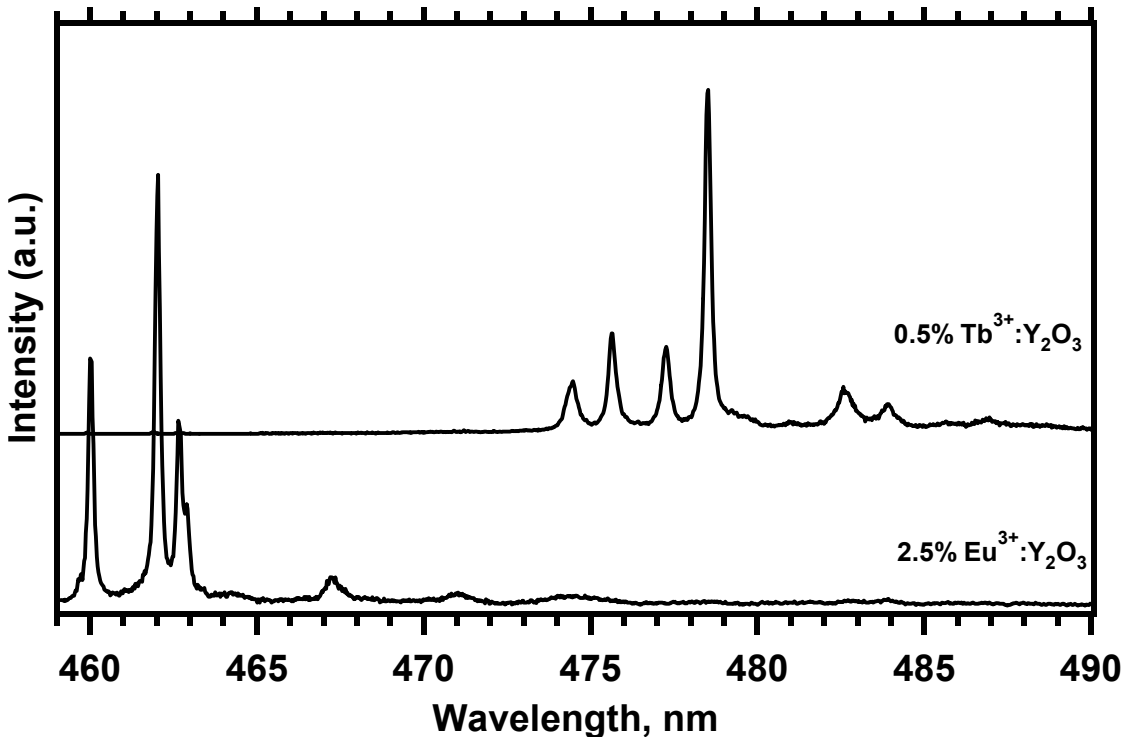

Figure 3.5 Excitation spectra of (top) Tb^{3+} $^7F_6 \rightarrow {}^5D_4$ transition, monitoring the $^5D_4 \rightarrow {}^7F_5$ line at 542.2 nm, with a slit width of 125 µm and (bottom) Eu^{3+} $^7F_0 \rightarrow {}^5D_2$ transition, monitoring the $^5D_0 \rightarrow {}^7F_1$ emission at 611.35 nm, with a slit width of 100 µm. Both spectra were collected at room temperature with all other settings the same. The intensity of the spectra have been adjusted for viewing.

3.4.3 $Tb^{3+} \leftrightarrow Eu^{3+}$ Energy Transfer Results – Luminescence Spectra

Excitation spectra for these two samples are shown in Figure 3.5. For the 2.5%-doped sample, Eu^{3+} is excited via the $^7F_0 \rightarrow {}^5D_2$ transition (~ 461 nm), and the characteristic red emission of the $^5D_0 \rightarrow {}^7F_1$ level is monitored at 611.35 nm. Tb^{3+} is excited via the $^7F_6 \rightarrow {}^5D_4$ transition near 478 nm, and the characteristic 542 nm green emission is observed emitting from the same excited level ($^5D_4$) to the $^7F_5$ level. Note that there is no excitation overlap for either the Eu^{3+} or Tb^{3+} ions at the most intense excitation peaks (461.83 and 478.54, respectively).

After excitation spectra were collected, the emission spectra of the doped particles were recorded while exciting the different peaks seen in Figure 3.5. The emission spectra for the Eu^{3+} and Tb^{3+}-doped nanoparticles (exciting the maximum peak intensity from Figure 3.5) are shown in Figure 3.6. The emission spectrum of Eu^{3+}:Y_2O_3 (see Figure 3.6 a) is dominated by the red emission at 611.35 nm that corresponds to the $^5D_0 \rightarrow {}^7F_1$ transition, while the Tb^{3+} emission spectrum is characterized by the green $^5D_4 \rightarrow {}^7F_5$ line at 542.2 nm (see Figure 3.6 c). It is important to note that there is no Eu^{3+} emission that overlaps with the green Tb^{3+} luminescence, and conversely, no Tb^{3+} signal observable at the same position as the 611 nm red Eu^{3+} light.

The lack of overlap for the most intense excitation and emission transitions of the two lanthanide ions in Figures 3.5 and 3.6 provides good conditions for detection of energy transfer. Absence of conflicting signals means that the background "noise" level is low, and greatly increases our sensitivity to energy to a level of detectable luminescence, instead of relying on significant changes in relative signal intensities or time-resolved emission. Spectrum b in Figure 3.6 shows an emission spectrum recorded for Eu^{3+}:Y_2O_3

nanoparticles while exciting at 478.54 nm, which would excite Tb^{3+}. Absence of any emission at 611.35 further indicates that Eu^{3+} cannot be excited at this wavelength. This fact will become important in the discussion below, where spectral characteristics of mixed samples of Eu^{3+} and Tb^{3+}-doped particles are presented.

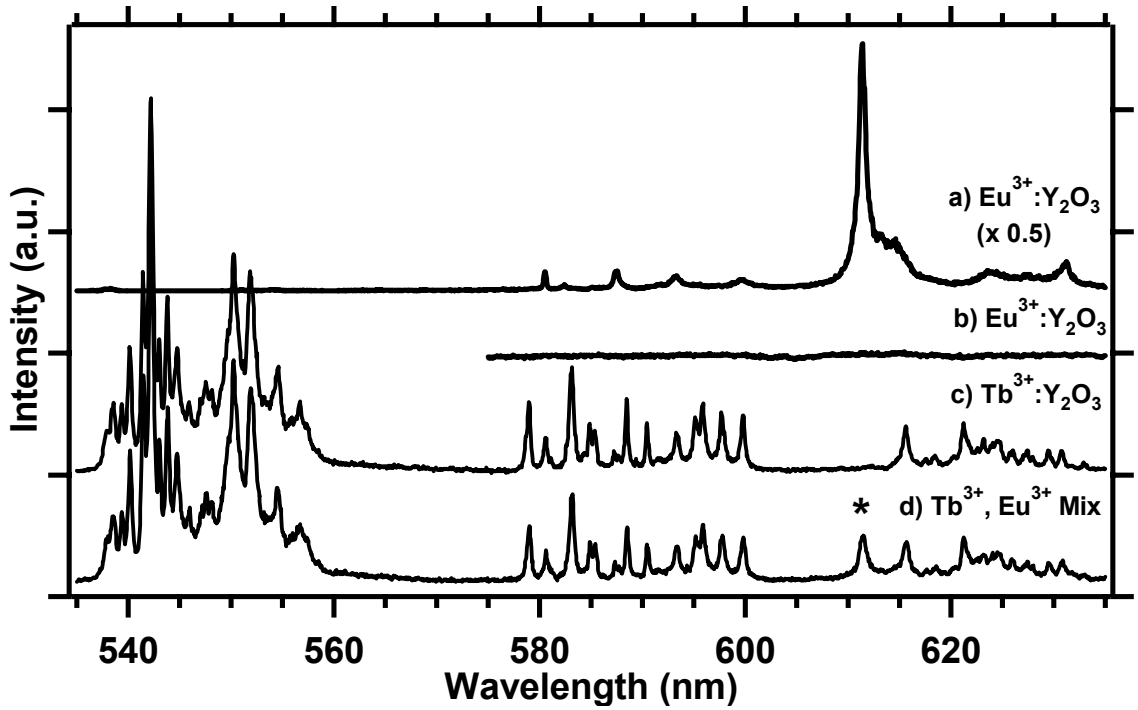

Figure 3.6 Emission spectra of a) Eu^{3+} doped Y_2O_3 NPs exciting the Eu $^5D_2$ level at 461.83 nm b) Eu^{3+}:Y_2O_3 exciting the Tb^{3+} $^5D_4$ line at 478.54 nm c) Tb^{3+}:Y_2O_3 exciting at 478.54 nm, and d) premixed Tb^{3+} and Eu^{3+} doped Y_2O_3 NPs exciting at 478.54 nm. Note that Eu^{3+} is not excited by 478.54 nm light (see b) , and there is no emission peak at 611.35 nm for pure Tb^{3+} doped NPs.

3.4.4 $Tb^{3+} \leftrightarrow Eu^{3+}$ Energy Transfer Results – Mixed Sample Spectra

Upon thorough examination of the spectral properties of both Tb^{3+} and Eu^{3+} doped Y_2O_3 particles, samples of the two were ground together and annealed at 773 K for 4 hours. Room temperature spectra were acquired. No emission from Tb^{3+} was observed upon exciting the Eu^{3+} ions, however, exciting Tb^{3+} at 478.54 nm resulted in spectrum d of Figure 3.6. Spectrum d is similar to spectrum c in the figure with the exception of the

emission peak at 611.35 nm. The appearance of this red emission, which is identical in position to the most intense light from Eu^{3+} cannot be from Tb^{3+}, and is therefore assigned to Eu^{3+}. However, spectrum b clearly shows that the europium is not itself excited by 478.54 nm excitation. These results indicate that energy transfer from excited terbium ions is likely the cause of europium emission.

To further investigate this peak, excitation spectra were obtained while monitoring red europium emission at 611.35 nm. The excitation spectra is shown as spectra b of Figure 3.7. Spectrum c, collected from Eu^{3+}:Y_2O_3 particles with identical settings, is shown for comparison. The excitation spectra b and c both show a large peak at 474 nm, which correspond to a weak Eu^{3+} excitation that is attributed to the weak hot band $^7F_1 \rightarrow {}^5D_2$ excitation that is available at room temperature. However, this band has no excitation intensity above the baseline above 476.5 nm, and spectrum b shows two peaks which match both the wavelength and position of the two Tb^{3+} excitation lines at 477.25 and 478.54 nm (compare to spectrum a). The fact that the red emission of Eu^{3+} shows the characteristics of the Tb^{3+} excitation spectrum provides evidence that the europium is being excited by the terbium ions. These results indicate that energy transfer appears to be occurring between terbium and europium in nanoparticle samples. Lifetime measurements are required to provide more conclusive evidence of energy transfer.

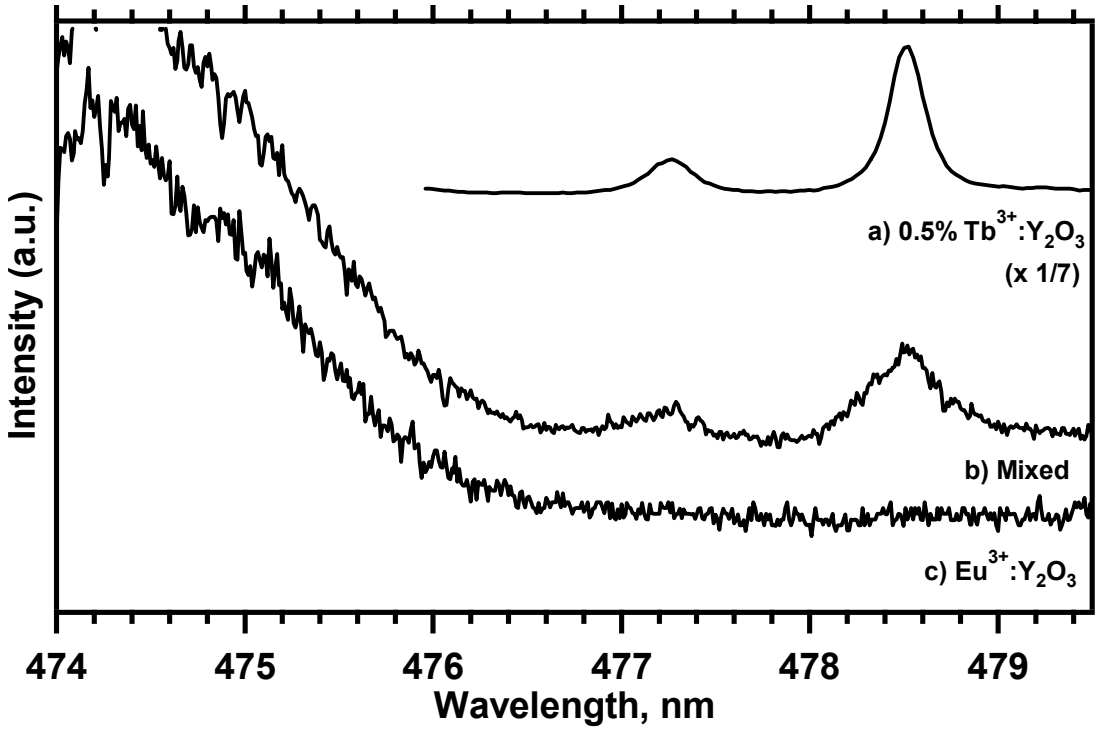

Figure 3.7 Excitation spectra: a) reference Tb^{3+} excitation spectra monitoring the Tb^{3+} $^5D_4 \rightarrow {}^7F_5$ line at 542.2, and monitoring the Eu $^5D_0 \rightarrow {}^7F_1$ emission at 611.35 nm while exciting the Tb $^7F_6 \rightarrow {}^5D_4$ transition for b) a mixture of Tb^{3+} and Eu^{3+}-doped NPs and c) pure Eu^{3+}-doped NPs. The slit width for the bottom two spectra is 300 µm.

3.4.5 $Tb^{3+} \leftrightarrow Eu^{3+}$ Energy Transfer Results – Lifetime Analysis

In addition to the excitation and emission spectral characteristics, time-resolved emission may be analyzed to investigate the dynamics of luminescence. For a luminescence signal with given excitation and emission wavelengths, the intensity versus time profile of the luminescence provides information about the nature of the transitions involved in the emission. The time profile of the emission is controlled by the rates of the population and depopulation of the emitting level, which can be expressed in terms of a lifetime value. In a system using a pulsed laser as an excitation source, the usual time-resolved intensity profile shows a sharp increase to a maximum value, followed by a decay that is characteristic of the emission lifetime. For any emission that is preceded by energy transfer, one would anticipate two features to be evident in the time-resolved

emission data. The first is that the characteristic lifetime of the excitation will be longer since it requires the excitation of the donor followed by energy transfer to the acceptor. Viewed at the correct time scales, this would materialize as a rise in the emission intensity instead of an immediate decrease. In addition, the lifetime of the emission should be longer than the same transition directly excited due to the time required for energy-transfer mediated excitation. The nature of the suspected energy transfer emission peak was investigated using time-resolved methods to see if the results support the conclusions from the above luminescence data.

Figure 3.8 displays the time-resolved luminescence data for three peaks for an annealed mixture of Tb^{3+} and Eu^{3+}-doped yttria particles: 1) Excitation of Eu^{3+} at 461.83 nm while monitoring the 611.35 nm Eu^{3+} emission, 2) Excitation of Tb^{3+} at 478.54 nm and monitoring the Tb^{3+} emission at 542.2 nm, and 3) the proposed energy transfer peak exciting at 478.54 nm (Tb^{3+}) and monitoring the Eu^{3+} 611.35 emission. The three plots are normalized to the maximum intensity, and have been smoothed to help visualization. The initial spike at $t < 20$ μs is due to electrical and optical noise from the laser pulse. Time profiles are similar for both the lines that are due to the Tb^{3+} and Eu^{3+} excitations and transitions, however, the emission for the energy transfer peak decays at a slower rate, indicating this emission line involves different excitation or emission dynamics. Looking closely at the initial ~ 200 μs, one can also see a rise in the emission intensity for the energy transfer peak, while the profiles for the Eu^{3+} and Tb^{3+} emission peaks decrease from an initial maximum. This is more clearly seen in Figure 3.9, which shows data collected under the same conditions but with 25-fold greater time resolution. At this scale, the emission lifetimes cannot be determined, however it is clearly seen that the

Tb^{3+} and Eu^{3+} emission lines have a maximum immediately after the laser pulse, while the energy-transfer line has a maximum 100 – 150 μs after the pulse. Qualitatively, these two features indicate that the excitation and emission lifetimes are greater for the energy transfer peak.

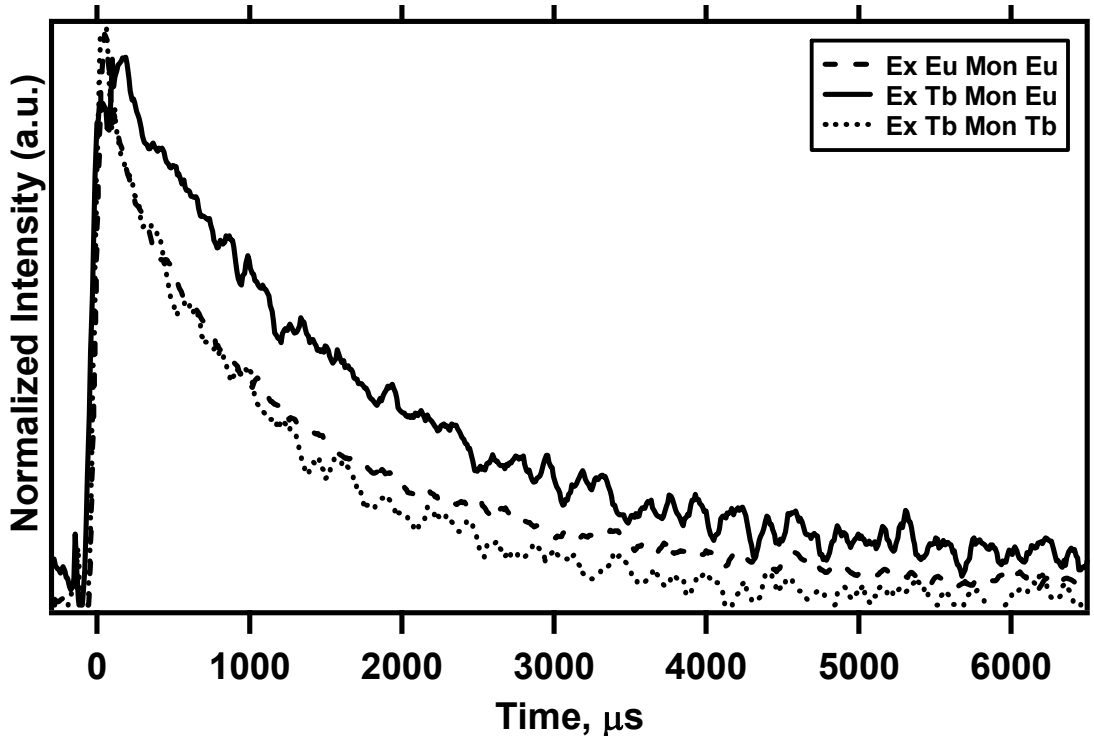

Figure 3.8 Time-resolved emission spectra for directly-excited Eu^{3+} (dashed line), Tb^{3+} (dotted line), and the emission observed from Eu^{3+} upon excitation of Tb^{3+}. Note the longer emission time for the energy transfer peak. For this experiment, the sample was a mixture of Tb and Eu-doped Y_2O_3 particles that were annealed at 973 K for 4 hours. The slit width was 70 μm for the directly excited Eu^{3+} line, 200 μm for the directly excited Tb^{3+} line, and 400 μm for the energy transfer line. Spectra are normalized to the maximum emission intensity and smoothed for presentation. Similar results were observed when the mixture was annealed at 500 K but intensity was reduced.

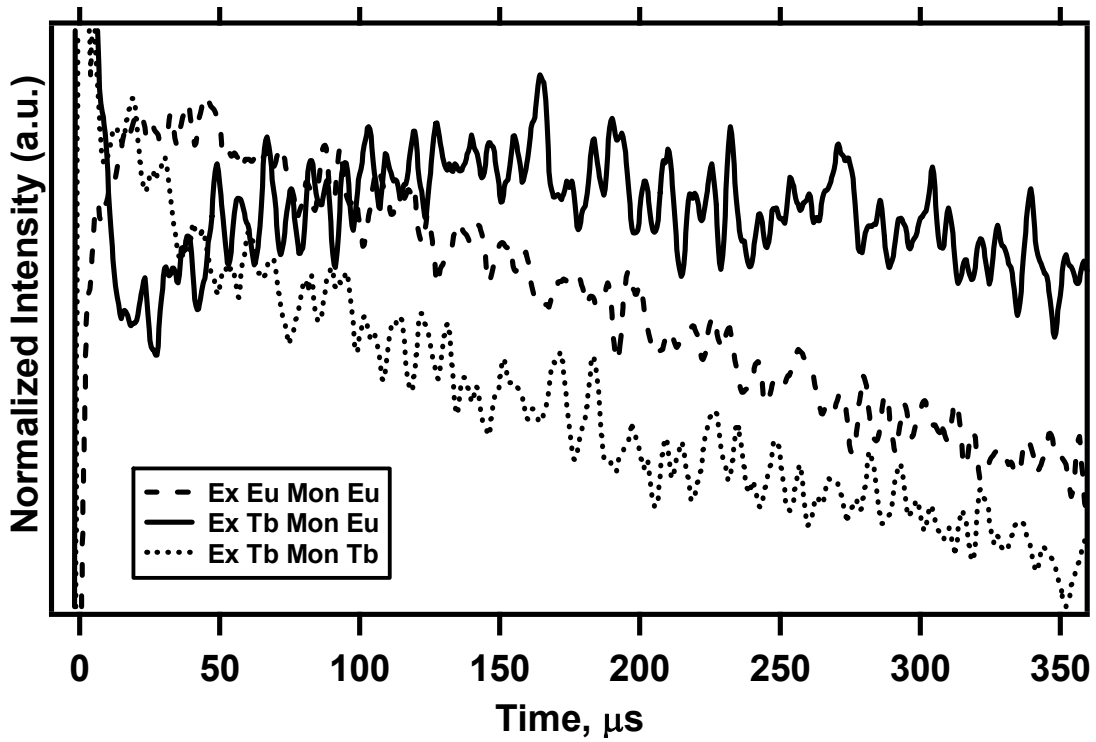

Figure 3.9 Time-resolved data collected at a higher time resolution. Experimental conditions identical to those in Figure 3.8 (intensity range has been narrowed for clarity). This plot clearly shows the rise in intensity of the energy transfer-mediated emission between 20 and ~125 μs.

In order to quantitate the time profile of these three emission lines, non-linear least-squares fits were acquired from time-resolved intensity data using the relationship:

$$I_t = I_0\left(e^{-(t-t_0)/\tau_1} - e^{-(t-t_0)/\tau_2}\right) + b \qquad \textbf{Eq. (3.8)}$$

where I is the intensity, t is the time, t_0 is the time of the laser pulse, τ_1 is lifetime of the excited state population, τ_2 is the lifetime of the emission from the excited state, and b is the baseline correction factor. Table 3.1 displays the excitation/population and emission lifetimes for the three signals. For both direct excitation and emission signals of Eu^{3+} and Tb^{3+} it is seen that the population lifetime (τ_1) is low. The value of near zero for the Tb^{3+} is expected since the emitting state ($^5D_4$) is being directly excited, so no relaxation will occur. For Eu^{3+}, τ_1 reflects the timescale of vibrational relaxation from the excited $^5D_2$ state to the emitting $^5D_0$ state. In contrast to these very short times, the population time

for the energy transfer peak is 50 μs, which tells us excitation of the emitting $^5D_0$ level of Eu^{3+} takes much longer than when the ion is directly excited. This correlates with the rise in intensity observed in Figure 3.9 and is consistent with an energy transfer excitation mechanism. The emission lifetime also is consistent with an energy transfer mechanism. τ_2 is near 1200 μs for both directly excited Eu^{3+} and Tb^{3+} emission, but this value increases to 2000 μs for the energy transfer peak. This can be explained by the fact that energy transfer from Tb^{3+} continues to excite Eu^{3+} after the laser pulse. Finally, measurements on a sample of pure Tb^{3+}:Y_2O_3 particles (denoted in Table 3.1 with a star), results in the same lifetime parameters as for the Tb^{3+} in the mixed sample. If ET were happening to a large degree, the lifetime value for the pure sample should have been greater lifetime due to reduced quenching. However, as clearly seen in Figure 3.6, the ET is weak, therefore, the quenching effect of the ET is not observable in the lifetime data. In summary, the combination of a longer excitation lifetime and emission lifetime both are consistent with an energy transfer-mediated excitation of Eu^{3+} by excited Tb^{3+} ions.

Table 3.1 Lifetimes calculated by linear-least squares analysis of the data in Fig 3.8 with Eq. 3.8 (for a mixture of Eu and Tb-doped particles). The last column (*) represents measurements on pure Tb:Y_2O_3 particles.

	Ex. Eu Mon. Eu	Ex. Tb Mon. Tb	Ex.Tb Mon. Eu	Ex. Tb Mon Tb*
Excited Level	$^5D_2$	$^5D_4$	$^5D_4$ (Tb^{3+})	$^5D_4$
Emitting Level	$^5D_0$	$^5D_4$	$^5D_0$ (Eu^{3+})	$^5D_4$
τ_1 (μs)	10	0.1	50	0.1
τ_2 (μs)	1250	1200	2000	1200

3.4.6 $Tb^{3+} \leftrightarrow Eu^{3+}$ Energy Transfer Results – Annealing

Annealing the particles is important to optimize the optical properties of nanophosphors made with our method. Previous work in our group has shown that annealing to temperatures near 773 K is needed to sharpen the spectra of Eu^{3+}-doped

Y_2O_3.[70] These results are similar to other results discussed in Chapter 4, where Eu^{3+}-doped Gd_2O_3 particles showed good optical properties after annealing to 973 K for one hour (see Figure 4.2).[71] Based on previous work, little grain growth is expected for the samples that were annealed at 773 K for four hours in air.[70] To investigate the role of annealing conditions on the observed energy transfer, a series of experiments was performed.

Figure 3.10 shows the results of the annealing study. The figure displays emission spectra of four samples of 50/50 dry ground mixture of Eu^{3+} and Tb^{3+}-doped yttria particles. All emission spectra are taken when exciting Tb^{3+} (478.54 nm) showing the region that includes the red Eu^{3+} emission (611.35 nm) that results from ET. Starting with spectrum a, no Eu^{3+} signal is observed when the "as prepared" particles are mixed, indicating that ET is undetectable. However, when the particles are separately annealed at 973 K and then mixed, Eu^{3+} emission is detectable, implying weak energy transfer (see spectrum b). Spectra c and d show that the intensity of the ET-mediated emission increases when particles are pre-mixed followed by a four hour anneal. Elevated temperatures also seem to increase the degree of energy transfer.

It is clear that annealing particles after mixing them enhances ET. There are three main possibilities for the enhancement of ET with stronger annealing conditions. The first is diffusion of active ions between neighboring particles, which would enhance energy transfer by eliminating the particle interface. The second is actual fusion of Tb^{3+} and Eu^{3+}-containing particles by grain growth. The third possibility is that annealing particles results in a higher degree of intimate contact between Eu^{3+} and Tb^{3+}-doped particles. The fact that ET is observed when particles are mixed after annealing indicates that

interparticle energy transfer does occur without grain growth processes. However, annealing the particle samples before mixing them probably results "harder" and larger aggregates that, when mixed, are less likely to break up to form a good mixture with a small mean particle distance. This could be the explanation for the greater ET when the particles are mixed prior to the 773 K anneal. When the particles were mixed and then annealed at the higher temperature, particle necking is likely to occur due to observed grain growth under these conditions.[70]

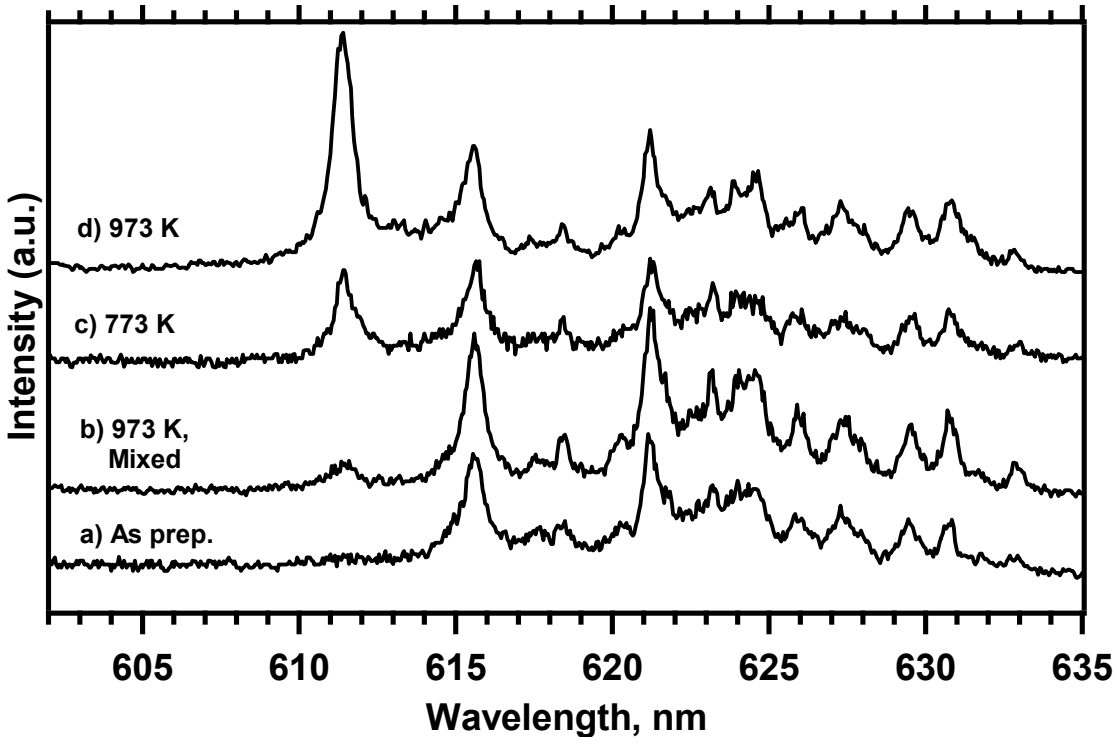

Figure 3.10 Emission spectra of a mixture of Eu^{3+} and Tb^{3+} doped Y_2O_3 nanoparticles when exciting the Tb^{3+} $^7F_6 \rightarrow {}^5D_4$ transition (478.54 nm). a) particles mixed as-prepared (no annealing), b) Particles are separately annealed at 973 K and then mixed, c) particles are mixed and then annealed at 773 K, and d) particles are mixed and then annealed at 973 K. Spectra are normalized to the intensity of the green emission at 542.2 nm. The slit width range for these experiments was 150-200 µm. Note the lack of the apparent energy transfer Eu^{3+} emission at 611.35 nm when the particles are not annealed.

3.4.7 $Tb^{3+} \leftrightarrow Eu^{3+}$ Energy Transfer – Reproduction

Experimental difficulties shortly after the above experiments were completed prevented reproduction of these results and precluded further investigation into energy transfer. However, an attempt to reproduce these results was made using spectroscopy facilities at Hampton University. Particles were prepared under identical conditions as the previous experiment and separately annealed at 973 K for four hours. Particles were stored in a desiccator and spectra were collected three days after annealing.

Figure 3.11 displays the emission spectra of the 2.5% Eu:Y_2O_3 and 1% Tb:Y_2O_3 particles in addition to a mixture of the two. The emission spectra of Eu^{3+} shows evidence of two crystallographic sites. Spectrum b is consistent with the C_2 site of the cubic structure,[72,73] while spectrum a appears to could be indicative of the monoclinic phase.[4,73] Previous studies in our group have indicated that Eu^{3+}:Y_2O_3 particles prepared under similar conditions (10 Torr N_2) contain monoclinic and cubic phase material, and found that a 24 hour anneal at 973 K and higher converts the material to the cubic phase.[70] Therefore, the shorter 4 hour anneal does not completely convert the material to the cubic phase.

Spectrum c in Figure 3.11 shows the emission spectrum of Tb^{3+}, showing the dominant $^5D_4 \rightarrow {}^7F_5$ green emission after exciting the $^5D_4$ level. The figure also shows emission after exciting the Tb^{3+} $^5D_4$ level in a sample of mixed Eu^{3+} and Tb^{3+}-doped particles (spectrum d). Comparison to spectra a and b show that Eu^{3+} emission appears, which could indicated energy transfer. To further investigate this potential energy transfer from Tb^{3+} to Eu^{3+}, a series of excitation spectra were collected.

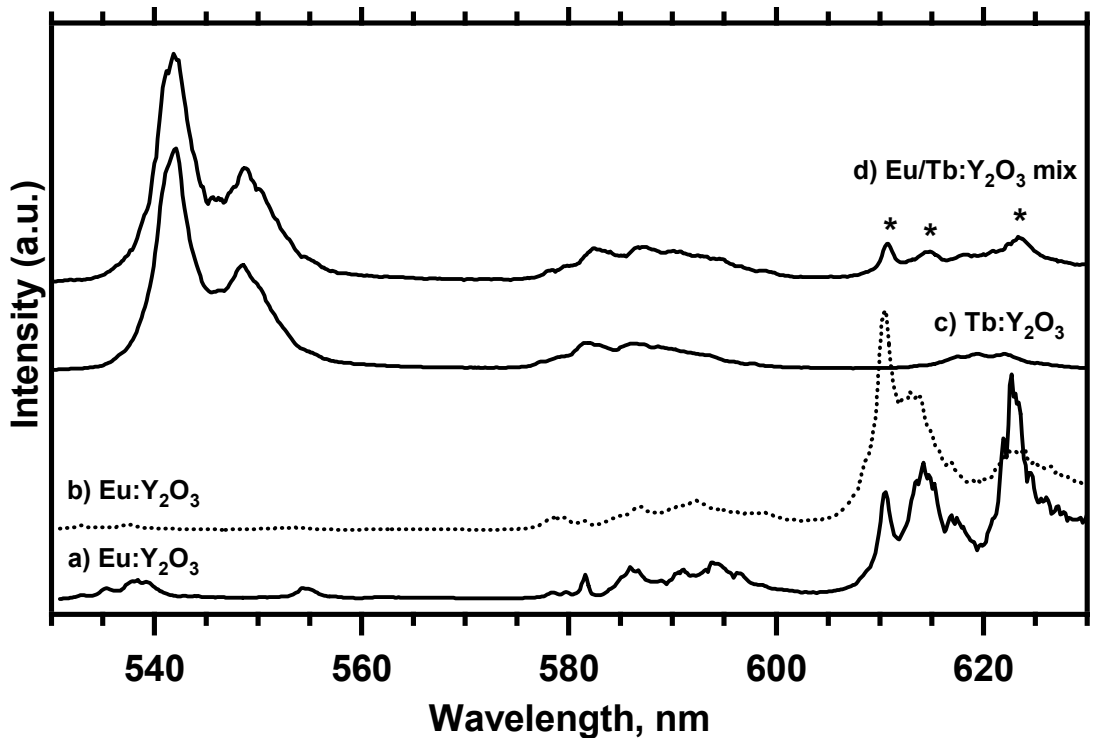

Figure 3.11 Emission spectra of: a & b)Eu:Y_2O_3 particles exciting at 462.35 and 459.9 nm respectively, c) Tb:Y_2O_3 particles exciting at 484.2 nm, and d) a mixture of Eu and Tb:Y_2O_3 particles exciting at 484.2 nm. The slit width was 250 µm and the delay was 14 µs with a gate of 300 µs for all spectra, which have been scaled for viewing. Potential Tb^{3+} → Eu^{3+} energy transfer peaks are denoted by stars.

Excitation spectra of the same samples are shown in Figure 3.12, where spectrum a shows the excitation spectrum of Eu^{3+} while monitoring the $^5D_0$ → $^7F_1$ red emission at 612 nm, and is similar to spectrum in Figure 3.5. This spectra is similar to the one in Figure 3.5 with a change in relative intensities. However, another scan (spectrum b) exciting in the region of the Tb^{3+} excitation and monitoring Eu^{3+} $^5D_0$ emission shows a signal that was not observed in the previous set of experiments, and that overlaps the excitation that was used to produce the potential energy transfer peaks observed in Figure 3.11. These two peaks are assigned to a hot band $^7F_2$ → $^5D_2$ excitation.

The Tb^{3+} excitation (Figure 3.12, spectrum d) is significantly different from the one shown in Figure 3.5. Instead of several well-resolved lines from 474-480 nm, a broad

band appears from 485-495 nm. The cause of this change is unknown, but is a likely indicator of a less crystalline environment for the Tb^{3+} ions. Spectrum c shows the excitation spectrum of the mixed Eu and Tb-doped particle sample while monitoring the possible Eu^{3+} emission at 612 nm. This excitation spectrum clearly matches the one for pure Eu^{3+}-doped particles (spectrum b) and has no feature that correlates with the excitation spectrum of the Tb^{3+}. Therefore, the Eu^{3+} emission observed in this experiment from the mixed particle sample in Figure 3.11 is due to a direct hot band excitation of Eu^{3+} instead of ET from excited Tb^{3+}.

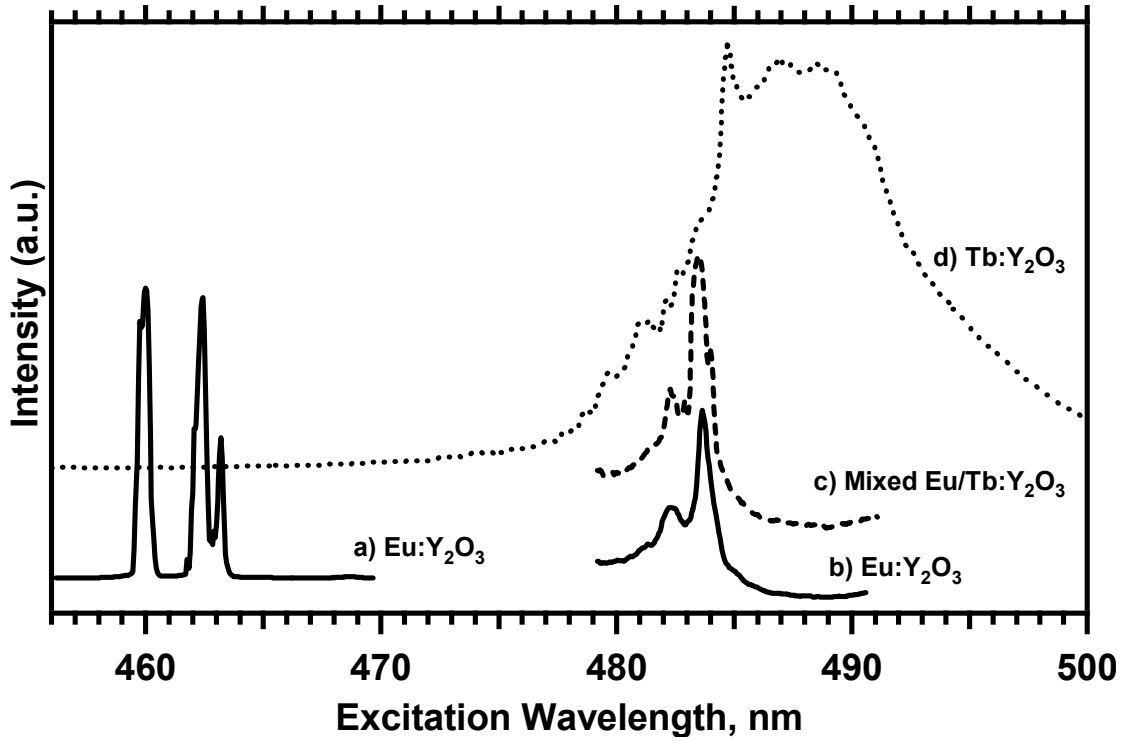

Figure 3.12 Excitation spectra collected at Hampton University for a & b) Eu-doped Y_2O_3 particles monitoring Eu emission at 615 nm, and slit width of 200 and 300 µm, respectively; c) Mixed Eu and Tb-doped Y_2O_3 particles monitoring suspected energy transfer peak at 615 nm with a slit width of 300 µm; d) Tb:Y_2O_3 particles monitoring the Tb^{3+} emission at 542.5 nm with a slit width of 250 µm. All spectra were recorded with a delay of 14 µs and gate of 300 µs. Note the overlap between the Eu and Tb excitation, and the fact that the suspected ET peak follows the profile of Eu, and not Tb^{3+}, implying direct Eu-excitation.

While this second set of experiments on Tb^{3+} and Eu^{3+}-doped particles revealed no evidence for energy transfer, this data does not contradict the previous set of experiments in out laboratory. For example, one important aspect to keep in mind is the reduced resolution and sensitivity for the experiments at Hampton University (compare the resolution of the emission spectra in Figures 3.11 and 3.6, for example). The substantially different structure of the Tb^{3+} excitation spectrum (comparing from Figures 3.5 and 3.12) indicates that there is some difference between the two Tb^{3+} samples tested. With these considerations in mind, the data set collected at Hampton does not indicate ET exists, but does not rule out the possibility that ET occurred for the previous experiments.

3.5 Conclusion

This Chapter has detailed a series of experiments with the goal of investigating the possibility of lanthanide-mediated interparticle energy transfer. This technology could be used for a variety of applications such as biomedical assays. No evidence was observed for energy transfer between Er^{3+} and Eu^{3+}-doped particles that results in changes in the visible region of the spectrum. However, data collected in subsequent experiments is consistent with interparticle energy transfer between Tb^{3+} and Eu^{3+} ions. Attempts to reproduce this data were unsuccessful due to obfuscating signals and unidentified differences in for the Tb^{3+} spectrum.

The results from this work imply that while ET is reduced, the surface interfaces between particles do not completely prevent energy transfer. Annealing was found to enhance transfer of energy between particles, likely due to shorter particle-particle distances or more intimate contact. However, annealing samples prior to mixing probably results in aggregates that do not mix well, which would reduce the number of donors and

acceptors within the transfer distance. In addition to enhancement of particle interaction, annealing is important for improving cystallinity of the sample, maximizing intensity of the luminescence from levels involved with ET, and reducing phase heterogeneity for a less complex spectrum.

The transfer observed here is very weak, and must be improved substantially in order to serve in a practical application. The cause for weak energy transfer can be attributed to a few possibilities. If dopants tend to migrate to the bulk of the particles, then ET would be anticipated to decrease. Another possibility is that surface defects (for example, hydroxyl groups) could quench the dopant. Surface quenching is expected to show a critical influence on energy transfer since the surface ions are the ones in proximity with donor/acceptor ions for interaction. In addition to this possibility, any inability to homogenously mix particles (such as breaking up aggregates) would increase the mean D-A distance, and reduce ET.

Possible methods for improvement of ET include introduction of particles into a solution phase (to take advantage of diffusion-related decrease in particle-particle distances) or to use chemical or physical linkers to either provide a coupling between particles or to minimize particle-particle distances.[74] The effect of temperature could also be investigated to see if thermally-populated levels or phonons are involved in the E-T transition. Reduced temperature would also eliminate hot bands, simplifying the spectra and aiding analysis. Finally, particle size and dopant concentration studies could reveal conditions where ET is more favorable due to surface and concentration quenching effects.

3.6 Future Work

While not conclusive, the data presented above provides the motivation to further study the possibility of interparticle ET between Tb^{3+} and Eu^{3+} ions. Studies should initially focus on parameters that enhance ET (temperature, dopant concentration, sample processing to increase particle mixing). Particle size effects could then be investigated to yield insight into the influence of a changing phonon spectrum on the ET. Finally, using lanthanide emission to discriminate between surface and bulk ions might provide information about the influence of surface defects on energy transfer.

Chapter 4. Luminescent Properties of Lanthanide-doped Gd_2O_3 Nanoparticles

4.1 Introduction

Energy transfer represents one potential use of nanoparticle-based luminescent materials, however, additional properties of optically active nanomaterials make them candidates for use in phosphor-related materials. Inorganic luminescent materials convert energy into light for applications such as displays, fluorescent lighting, X-ray imaging, and scintillators.[75] Another promising application for luminescent nanomaterials is their use as reporters for analytical assays and biomedical imaging. Nanophosphor materials may be ideal for these applications due to: (1) small size and (2) size dependent emission and luminescence dynamics properties. This Chapter details a survey study performed to investigate the properties of lanthanide-doped gadolinium oxide nanophosphors.[71] Gadolinia was chosen as the host material because of its ability to be excited by UV light, followed by energy transfer to the dopant lanthanide ions. Several studies on the synthesis and properties of gadolinium oxide host nanophosphors have recently been published, indicating the interest in this material.[76-82]

4.2 Background

The small size of luminescent inorganic nanoparticles allows them to replace fluorescent molecules or complexes in analytical applications.[83] One example is as a luminescent tag or reporter for affinity or immunoassay applications in environmental, food quality, drug, and biomedical testing.[76] In these assays a luminescent reporter is attached to an antibody that binds to a specific analyte or antigen. Detection or quantitation of the analyte is then based on luminescence intensity (or quenching), energy transfer, polarization anisotropy, etc. The long lifetime of lanthanide ions provides a

significant advantage in discriminating against background autofluorescence,[84] and using lanthanide-doped nanoparticles permits the use of NIR-upconversion excitation to avoid autofluorescence completely.[85] In addition, lanthanide-based reporters offer sharp spectra and good photostability.[40]

While long lifetime is important, other considerations for applying luminescent nanoparticles in multi-spectral immunoassays include: (1) finding multiple reporters with distinct emission wavelengths to attach to different antibodies, (2) having a common excitation wavelength for the different reporters, and (3) keeping the particles sufficiently small or soluble to not alter the activity or solubility of the antibodies. Despite the advantages of luminescent nanoparticles, there are several challenges to their use in analytical applications: (1) inherent size effects can cause inhomogeneous spectral broadening due to disorder, metastable structures, or heterogeneous dopant distribution, and (2) the luminescence dynamics can be sensitive to changes in the electron-phonon interaction, phonon spectrum, surface quenching, metastable population, and spontaneous transition rate. This Chapter presents our first survey experiments to find multiple lanthanide-doped nanoparticles that will be suitable as immunoassay reporters. We use Gd_2O_3 as the host to take advantage of the common excitation in the ultraviolet ($^8S_{7/2} \rightarrow {}^6D_{9/2}$) with efficient energy transfer to the dopant: Pr^{3+}, Dy^{3+}, Eu^{3+}, Tb^{3+}, and Tm^{3+}.

Gadolinium oxide is a material that has been studied for its properties as a host for optically active species, and has been developed as a contrast agent for medical imaging,[86] and as a scintillator.[87] Unlike many other lanthanides, Gd^{3+} features a lack of 4f-4f transitions between the ground state to ~ 32,000 cm^{-1}, which is in the UV region.[88] As a result, no energy in the infrared or visible regions can be back-transferred from

optically active dopants back to the Gd^{3+} ions, making Gd_2O_3 an attractive host for the lanthanides. In addition, the host Gd^{3+} ions may be excited in the UV region, and efficiently transfer energy to optically active ions in the host as shown in Figure 4.1. While many radiative pathways exist for these excited ions, the strongest visible ones are indicated by down arrows in the figure. Gd_2O_3 may also serve as a better host than more common materials, as presented in one study that found upconversion luminescence from Sm^{3+} ions increases when a Gd_2O_3 host is used instead of the more traditional Y_2O_3.[89] This result was attributed to more efficient energy migration in the lattice and transfer to the Sm^{3+} ions, and would likely apply to other optically active ions as well.

Other recent studies have underscored the use of Gd_2O_3 as a host in nanophosphor materials. In one example, 200 nm Eu^{3+}:Gd_2O_3 phosphors have demonstrated a 25% enhancement relative to micron-sized Eu^{3+}:Y_2O_3 commercial phosphor material.[90] A 34% enhancement over the commercial phosphor was reported with annealing temperatures high enough to induce agglomeration.[91] While the authors did not investigate the mechanism of size enhancement, these results validate the concept that size enhancement effects may result in better optical properties for nano materials.

In addition to size-related variables, the influence of post-synthetic processes that are often necessary for optical materials must be investigated. Nanoparticle annealing is a common necessity to optimize optical properties, so this process was tested during the current study. Annealing is often used to process nanophase phosphor material to convert the material to a single phase or improve crystallinity. This enhances the luminescent intensity at the peak wavelength and can be used to convert the material into a desired phase that is accessible through the annealing process. However, annealing will induce a

degree of grain growth, and can also result in sintering particles. These processes need to be minimized for some applications that require disperse, small particles.

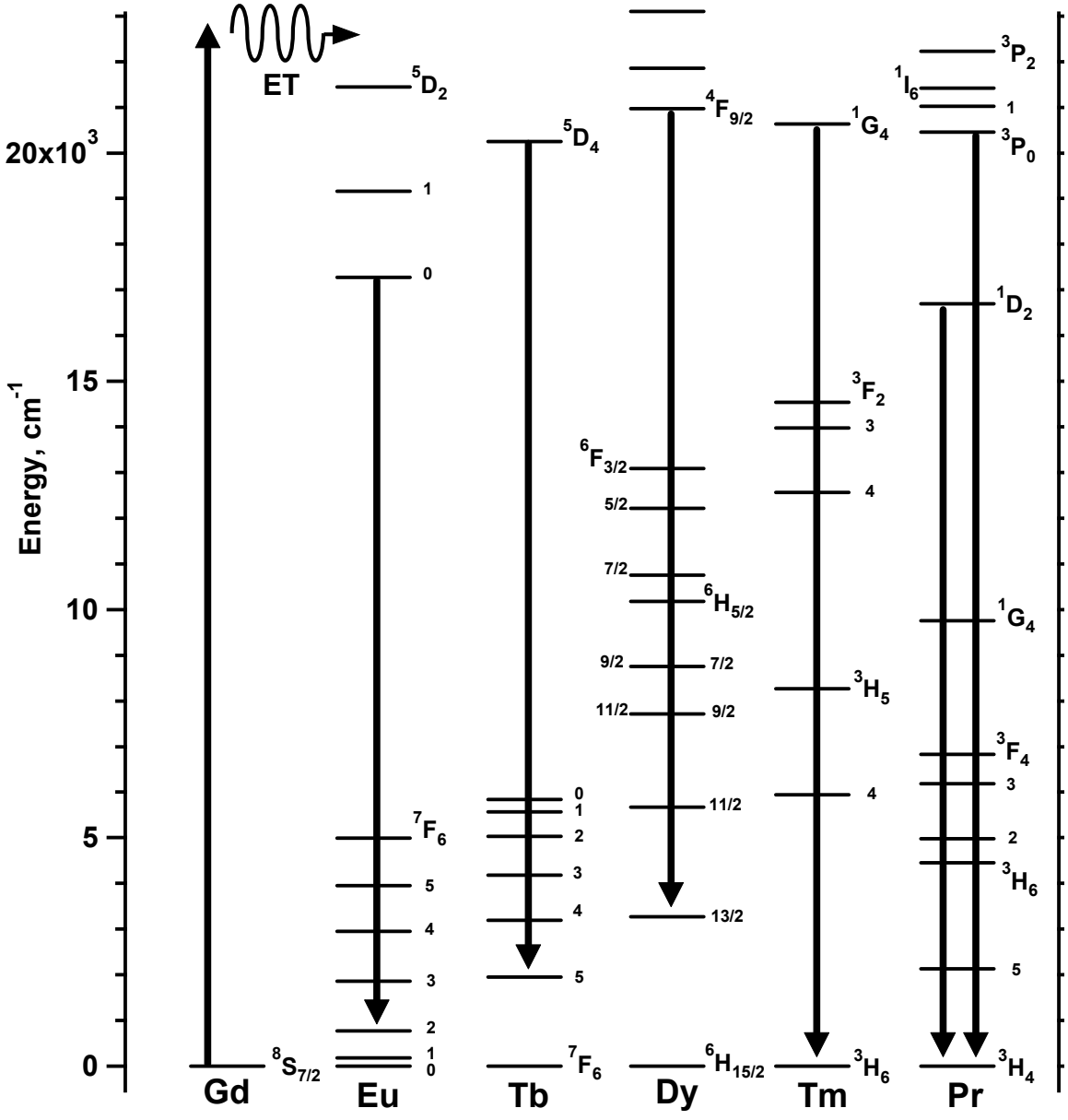

Figure 4.1 Energy level diagram for the trivalent lanthanides used in the present study. The Gd^{3+} of the host was excited in the UV (off scale) and energy transfer occurs to the dopant, resulting in the visible-region emission lines shown.

4.3 Experimental

Mixtures of Gd_2O_3 and Ln_2O_3 (Ln = Eu, Dy, Tm) were pressed into a pellet and sintered overnight at 973 K. [It should be noted that the Eu-doped samples were made with 99.9% Gd_2O_3, which was found to have some europium contamination (all other samples were made with 99.999% Gd_2O_3)]. Tb and Pr were introduced into Gd_2O_3 as the oxalate ($Ln_2(C_2O_4)_3$) to maintain the 3+ oxidation state. The oxalate is synthesized by mixing 50 mL of 0.2 M aqueous oxalic acid at 353 K with 100 mL of 0.025 M $Ln(NO_3)_3$ also at 353 K. The resulting $Ln_2(C_2O_4)_3$ precipitate is rinsed, filtered and dried before pressing with Gd_2O_3 and sintering at 773 K for 5 hours. During vaporization of these samples, the presence of residual oxalate provides a reducing atmosphere to maintain the Ln ions in the 3+ oxidation state.

The nanoparticles were prepared by inert gas-phase condensation[92] under a 1 Torr N_2 atmosphere and using platform rotation. Nanoparticles deposited on a stainless steel collector. The as-prepared nanoparticles had a fluffy morphology and were white for Eu, Dy, and Tm, but were tinted brown for Tb and Pr. This discoloration is likely indicative of oxidized dopant ions, which are dark brown in color. Unless otherwise noted, nanoparticles were placed in platinum crucibles and annealed at 973 K for 1 hour to improve the crystallinity and to obtain single-phase material. The dopant concentration is assumed to be the same as the target material although there may be depletion or enrichment of the dopant ions. Transmission electron micrographs were obtained to estimate particle diameter.

For optical spectroscopy, powder was packed into a pit in a copper block mounted inside a vacuum chamber. All spectra were taken under vacuum (~ $3x10^{-2}$ Torr) at room

temperature with pulsed excitation at 266 nm (Nd^{3+}:YAG laser with quadrupling crystals installed). Luminescence spectra and decay transients were recorded using the 1 m monochromator and the gated photon counter. Some transients were also recorded by signal averaging (> 500 shots) with the 500-MHz digital oscilloscope.

4.4 Results

4.4.1 Annealing

The spectra of the as-prepared (unannealed) nanoparticles showed broadened peaks characteristic of multiple disordered phases[70] with less efficient emission at the desired wavelength (see Figure 4.2). As-prepared nanoparticles had a mean particle size of 7 ± 2 nm. Annealing in air at 973 K for one hour increased particle size to 10 ± 2 nm and annealing for four hours at 1073 K increased the particle size to 22 ± 5 nm. Figure 4.2 shows that the one hour anneal at 973 K produces the desired spectral changes while minimizing grain growth, while annealing for longer times and at higher temperatures has little further effect on the spectra (however changing the lifetimes) and needlessly increases nanoparticle size.

4.4.2 Eu^{3+}:Gd_2O_3

Annealed Eu^{3+}:Gd_2O_3 nanoparticles show a strong emission at 611 nm as seen in Figures 4.2, which corresponds to the $^5D_0 \rightarrow {}^7F_2$ transition of the cubic phase. The lifetimes of this emitting state for as-prepared 0.1, 1, and 5 mol-% Eu-doped Gd_2O_3 were 200, 290, and 170 μs, respectively. Those lifetimes increased to 1650, 900, and 670 μs after annealing at 1073 K for 4 hours. Lifetimes of the unannealed samples are shorter than expected, but probably reflect the presence of Eu_2O_3 in the samples. This would increase the likelihood of Eu-Eu energy transfer, which enhances quenching processes.

The as-prepared sample shows broad peaks that indicate the presence of disordered phases.

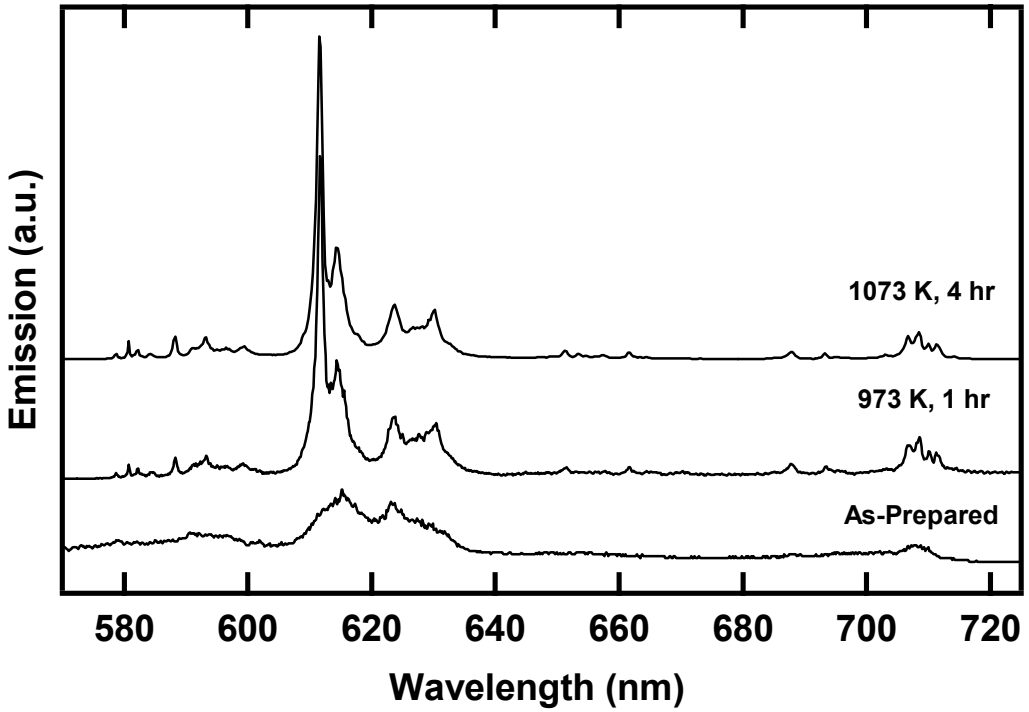

Figure 4.2 Comparison of the emission spectra of 0.1% Eu:Gd_2O_3 before (lower trace) and after annealing (upper traces) for the times and temperatures listed. Spectra were collected with a 5 μs delay and 300 μs gate

Annealing for one hour at 973 K greatly improves crystallinity and intensity of the emission peaks and, for the 1 % sample, increased the lifetime from 290 to 850 μs, which is close to the 900 μs after a stronger anneal. Increasing the concentration also changes the characteristics of the emission spectrum. This is demonstrated in Figure 4.3, which compares the luminescence spectra of 0.1 and 5 % Eu-doped Gd_2O_3. The emission spectrum for the dilute sample reveal signals that represent the $^5D_1 \rightarrow {}^7F_n$ transitions, while concentrated sample does not show these peaks.

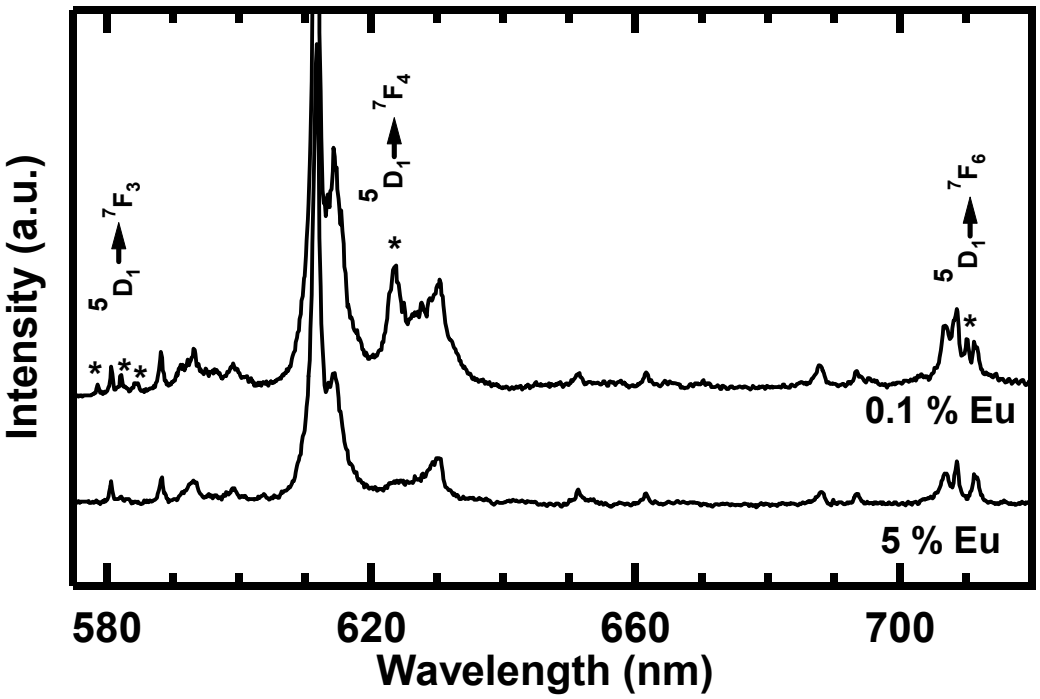

Figure 4.3 Emission spectra of 0.1 % (top) and 5 % (bottom) Eu:Gd_2O_3 nanoparticles. Intensity of the two spectra are scaled for comparison. The delay and gate was set to 1-ms. $^5D_1 \rightarrow {}^7F_n$ transitions are denoted with stars and are observable in the dilute sample but not the more concentrated sample.

4.4.3 Tb^{3+}:Gd_2O_3

Tb^{3+} doped ceramics with concentrations of 0.1%, 3%, and 5% were vaporized. The trivalent terbium has characteristic green emission at 544 nm corresponding to the $^5D_4 \rightarrow {}^7F_5$ transition as shown in Figure 4.4. Of the other lanthanide-doped samples tested, the terbium had stronger secondary lines relative to the most intense peak. Even so, the intensity of the green line was strong. The annealed 0.1%, 3%, and 5% Tb:Gd_2O_3 nanoparticles had main line lifetimes of 920, 330, and 250 μs, respectively. While the lifetime of the 0.1% sample is the most ideal, the relative luminescence intensity was lower than the 3% sample due to a smaller population of emitting ions, so an intermediate concentration might prove to be optimal.

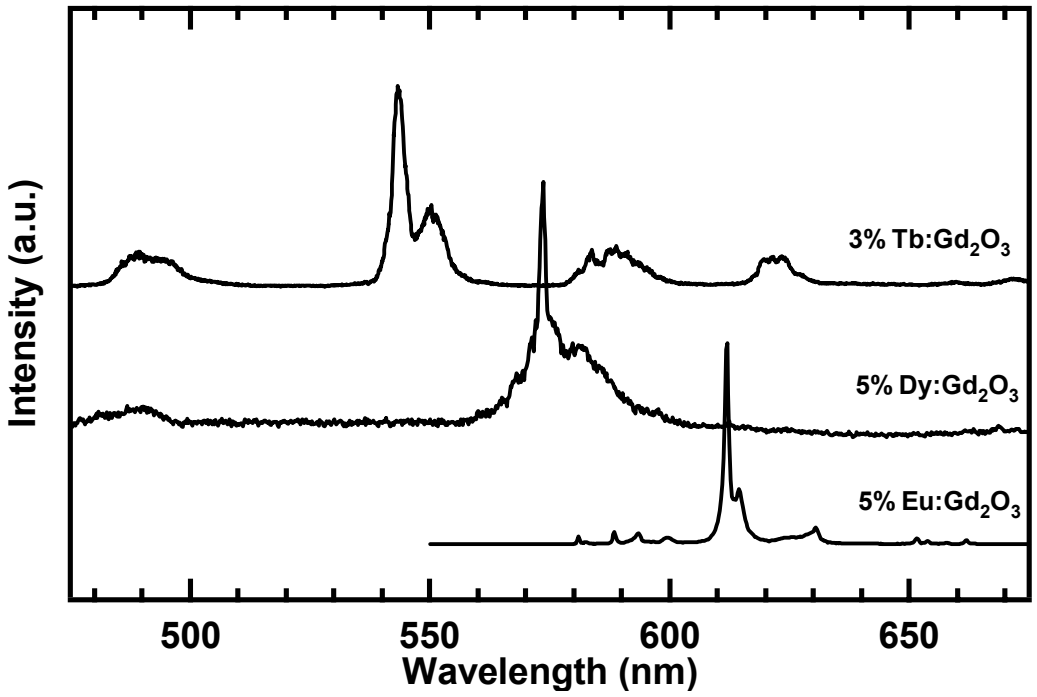

Figure 4.4 Luminscence spectra of annealed Gd_2O_3 nanoparticles doped with Tb^{3+}, Dy^{3+}, and Eu^{3+}. Note the separation between the dominant emission bands (green, yellow, and red). Spectra were collected with a 5 μs delay and 300 μs gate.

4.4.4 Dy^{3+}:Gd_2O_3

The luminescence spectrum of dysprosium doped into Gd_2O_3 showed its strongest emission at 573 nm, corresponding to the $^4F_{9/2} \rightarrow {}^6H_{13/2}$ transition (see Figure 4.4). Analysis was performed on 1%, 2%, and 5% dysprosium doped samples. The annealed 1% sample had a lifetime of 120 μs, but the 2% and 5% samples were strongly quenched with a lifetime of 45 and 20 μs, respectively. The dysprosium samples have somewhat lower luminescence intensity than the corresponding terbium or europium samples, however has greater intensity than the other lanthanide ions studied.

4.4.5 Pr^{3+}:Gd_2O_3

Praseodymium doped into Gd_2O_3 nanoparticles had spectra, shown in Figure 4.5, that were characterized by a weak green emission at 510 nm ($^3P_0 \rightarrow {}^3H_4$ transition) and a

broad red emission with peak intensity at 620 nm ($^1D_2 \rightarrow {}^3H_4$ transition). This red emission overlaps with the emission of europium, and the green emission is too weak for use, unlike emission observed with micron-sized particles.[93] In addition, the lifetimes of both the green and red lines were very short (~ 4 μs and 45 μs, respectively in the 0.1 % sample).

While Pr^{3+} has been determined to be an unlikely candidate for further use in nano-gadolinia phosphors, another interesting result has been observed. Our results indicate that the green Pr^{3+} emission is suppressed in our nanoparticles, possibly due to size effects. This explanation is reinforced by an observation during particle collection. Occasionally, the CO_2 laser beam is reflected from the target platform towards the collection plate, with the effect of heating the nanoparticles and therefore causing grain growth and particle aggregation. The "annealed" nanoparticles on regions on the collector plate that had been struck by the laser reflection showed a visibly yellow emission when excited with a handheld UV light (254 nm), while nanoparticles not annealed by stray laser reflections demonstrated a red-dominated emission. The specific reason for the suppression of the green emission is not known, however, a recent study of Eu^{3+}:Gd_2O_3 nanophosphors found that the luminescence intensity fell as particle size decreased below 30 nm. The intensity followed a power law, and was attributed to increased quenching at the surface of the particles.[82] Our results may also be due to preferential quenching of the $^3P_0$ state, leaving the red emission dominant. This observation underscores the often strong influence that particle size may have on phosphor performance.

4.4.6 Tm^{3+}:Gd_2O_3

Blue luminescence was observed in one 5% Tm^{3+} sample, but not in other samples (5%, 1%, 0.1%). The thulium luminescence, displayed in Figure 4.5, was characterized by several weak peaks from 460-520 nm with short lifetimes (20-30 μs) associated with the $^1G_4 \rightarrow {}^3H_6$ transition, all of which had similar intensities. We believe that the thulium does not vaporize as well as the gadolinium or other lanthanide oxides. Regardless, the lack of a single, strong emission line and the short lifetimes of the Tm^{3+}-doped sample makes this lanthanide an unfavored candidate for further use in this study.

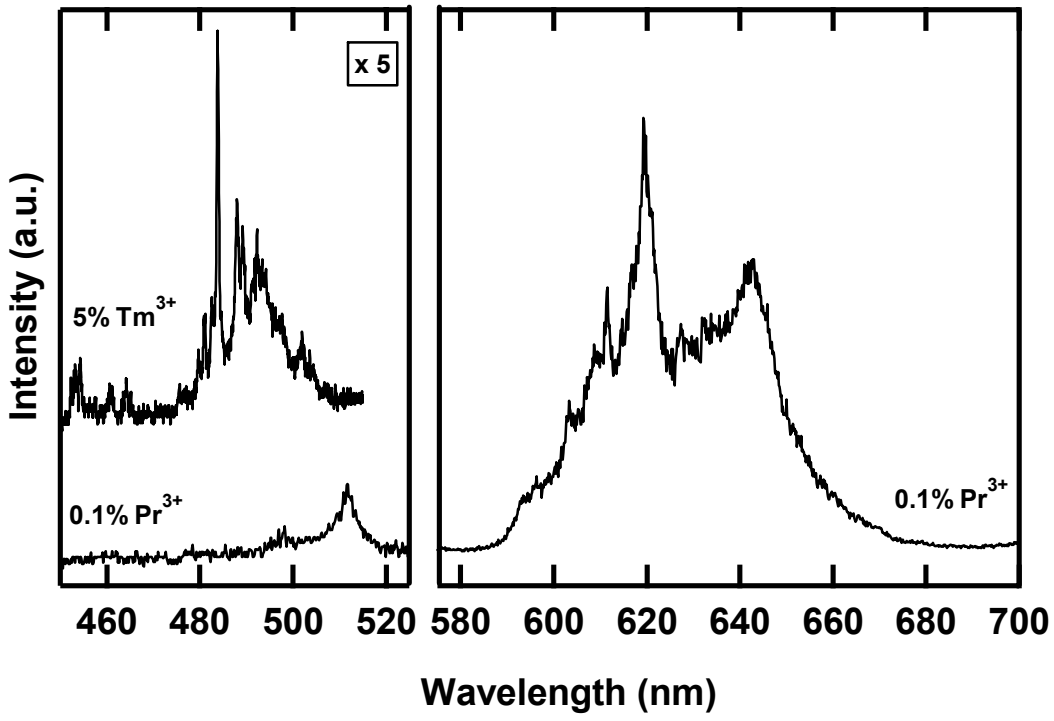

Figure 4.5 Luminescence spectra of Tm^{3+} and Pr^{3+} doped into Gd_2O_3 particles. The higher energy region of the spectra is magnified to assist viewing. The spectrum for Tm^{3+} was collected with a 1μs delay and 50 μs gate, while the Pr^{3+} was collected with a 1 μs delay and 100 μs gate

4.5 Conclusion

These survey experiments have looked at five different lanthanide ions doped into gadolinium oxide nanoparticles to identify suitable dopants for multicolor immunoassays.

This study demonstrates that Tb^{3+}, Dy^{3+}, and Eu^{3+} in Gd_2O_3 can be excited with a common wavelength and emit at different wavelengths, in addition to having sufficiently long lifetimes. The lifetimes of the particles after annealing are summarized in Table 4.1. It has been found that the optimal dopant concentrations are approximately 1% for Tb^{3+} and Dy^{3+} and 0.1% for Eu^{3+}, and that a 1 hour anneal at 973 K is sufficient to give single phase material to enhance lifetime and luminescence intensity of the peak wavelength. As opposed to the three better candidates, Pr^{3+} has preferential emission in the red region, which overlaps with the emission of Eu^{3+} in addition to short lifetimes. Tm^{3+} emission is also very weak (presumably due to depletion of the ion in the particles) but also has a short lifetime, making this candidate unappealing. In addition to identifying ideal lanthanide dopants for nano-phosphors, this study might have uncovered a size-dependent luminescence effect with the relative weak green emission of Pr^{3+} compared to micron-sized materials.

Table 4.1 Measured lifetime values for annealed Ln^{3+}:Gd_2O_3 nanoparticles as a function of the target dopant concentration. For all samples, strong quenching is observed at concentrations greater than 1%. Lifetimes denoted with a † were annealed at 1073 K for 4 hours. Otherwise, annealing was performed for 1 hour at 973 K.

Dopant	Wavelength (nm)	Concentration (mol %)	Lifetime (μs)
Tb^{3+}	544	0.1	920
		3	330
		5	250
Dy^{3+}	573	1	120
		2	45
		5	20
Eu^{3+}	611	0.1	1650 †
		1	900 †
		5	670 †
Pr^{3+}	510	0.1	~ 4
		1	~ 3
	620	0.1	45
		1	20
Tm^{3+}	480	5	~ 20

These phosphors represent a class of nano-materials that might find use for assays and bioanalytical and medical assays. The initial investigation presented here emphasizes the need to further assess candidate materials via lifetime, solubility and chemical modification studies. In addition, the possibility of using NIR-upconversion should be investigated.

Chapter 5. Nanoparticle Film Morphology Dependence on Synthetic Parameters

5.1 Introduction

Comprehension of the dynamics that occur during a synthetic process is crucial for control of product properties. This understanding is even more critical when producing nanomaterials because a small change in the material (for instance, particle size) can induce a large change in properties. While the gas-phase condensation synthetic method is conceptually simple, complicated dynamics occur during the growth, aggregation, and deposition of the synthesized nanomaterials. These dynamics become even more complex if the condensation method involves chemical reactions, so reactive condensation methods are less appealing for use in fundamental studies of the synthetic method. Inert gas-phase condensation (IGC) provides a straight forward system with which to study the dynamics of nanoparticle synthesis and subsequent film growth. A complete understanding of these dynamics will allow finer control of the physical properties of both individual nanoparticles and assembled films.

As-deposited nanoparticle film morphology is an important factor for the preparation of materials with desired properties for specific applications. For example, the morphology and microstructure of nanoparticle films is expected to influence diffusion and adsorption of gases, light absorption and scattering, electron transport, as well as the density and transparency of compacted materials;[94-97] all of these properties may be considered for potential application. It is also likely that other properties such as film adhesion, modulus, robustness, and even catalytic activity[98] will be influenced by this structure. Film morphology may also be important for synthetic consideration in device manufacturing. For instance, an initial nanoparticle film with extensive void areas

could allow subsequent manufacturing of a composite material with a high level of contact between the initial nanoparticles and second material. These considerations provide motivation for understanding growth processes that determine nanoparticle film structure.

This Chapter discusses a study of the influence of synthetic parameters on the morphology of deposited Y_2O_3 nanoparticle films produced with the laser-heated IGC method. Pressure, gas, and target-substrate distance were found to influence the nanoparticle film morphology. Experiments indicate that aggregation of nanoparticles in the gas occurs at higher pressures, resulting in a different film deposit structure. Nanoparticle films were synthesized in a variety of gas atmospheres in an attempt to gain a better understanding of the parameters that influence the film growth mechanism. These results may help predict the microstructure of nanoparticle films synthesized under given conditions.

5.2 Background

5.2.1 Aggregation of Particulates

One of the parameters that will influence the morphology of films is the aggregation of particles prior to deposition on the substrate. Studies of particle aggregation in fluids have been important to the understanding of the gelation of materials in solutions,[99] the coagulation of residue particles in industrial smokestacks,[100] atmospheric soot aerosol dynamics,[101] in addition to nanoparticle synthesis. An important concept for quantifying the morphology of aggregates is fractal dimension, which was introduced by Mandelbrot.[102] Fractal dimension is a representation of the morphology of an aggregate, which can substantially influence the physical and chemical properties of

the cluster.[103,104] The fractal nature of aerosols was discussed by Forrest and Witten[105] and may be expressed by the equation:

$$N = k_0 \left(\frac{R_g}{a} \right)^D \qquad \textbf{Eq. (5.1)}$$

where N is the number of spherical particles in the aggregate, k_0 is the fractal prefactor, D is the fractal dimension, a is the mean particle radius, and R_g is the radius of gyration.[106] The radius of gyration describes the distribution of particles and is defined as:

$$R_g^2 = \frac{1}{N} \sum_{i=1}^{N} \left(r_i - r_0 \right)^2 \qquad \textbf{Eq. (5.2)}$$

where r_i and r_0 are the positions of the ith particle and cluster center of mass, respectively. Fractal dimension, D, varies from 1 for a tightly packed ball of particles to a value of 3 for a linear chain. Most aggregates formed from aerosols have a fractal dimension of 1.5 – 2.0.[106] A significant body of work has been dedicated to develop models for aggregation of particles in fluids, and more recently, work has investigated aggregation of particles in laser-induced plumes.

5.2.2 Fractal Cluster Growth Modeling

While significant understanding has been developed into the aggregation of particles in a fluid, evolution of particle film morphology on the micrometer length scale is not clearly understood. However, some theoretical studies have been performed on the morphology of small particulate films under simple conditions. Witten and Sander introduced the diffusion-limited aggregation (DLA) model in 1981 to study the aggregation of metal particles.[107] This simple two-dimensional, cell-based model ignored cluster interactions, and assumed a particle sticking probabilities of unity, but successfully demonstrated the fractal nature of particle aggregates. Meakin modified the

DLA model and changed the particle to a disk shape in order to study the deposition of particles on fibers and surfaces under diffusion-controlled regimes.[108,109] Results from these two models show relative agreement for predicting the fractal nature of aggregates, however, they only consider aggregation growth for very dilute systems. To answer this deficiency, a cluster-cluster aggregation (CCA) model was developed, which accounts for concentrations of isolated particles and the aggregation of growing clusters.[110,111] Aggregation modeling was further enhanced when particle sticking probabilities were considered. Previous models assumed that all particle-particle collisions resulted in coalescence, but the reaction-limited cluster aggregation (RCLA) model introduced a finite sticking probability.[112] The reduced sticking probability results in greater penetration of the growing aggregate by particles, resulting in a more composite fractal.

Along with the DLA and CCA models, the RCLA model assumes diffusion is the dominant transport method, and that the particles and clusters demonstrate Brownian motion through the fluid. For small particles in a fluid, Brownian motion describes the results of a random number of impacts from random directions of the fluid molecules with the small particle. Since the particle is small enough to be influenced by collisions with individual molecules, its motion exhibits a random, erratic nature. In 3-dimensional space, the mean squared displacement (r^2) of a particle may be described by:

$$\left\langle r^2 \right\rangle = 6kT\beta t \qquad \textbf{Eq. (5.3)}$$

where t is time and β is the mobility of the particle (in units of m^2/s), which is inversely proportional to the fluid viscosity and size of the particle. Brownian motion of small particles occurs in the free molecular regime, where the Knudsen number (K_n, the ratio of the fluid mean free path to the mean particle radius) is greater than 10.[113] When the

Knudsen number is less than 0.25, the collision-dominated regime controls transport, and the gas can be treated as a continuum.[114] Diffusion transport based models were modified by Krinke et al., who expanded these models to account for particle-substrate and particle-deposit interactions in addition to an electric field force.[115] Influences of thermophoretic forces and particle sintering were included by the model of Kulkarni and Biswas.[94,116]

Arunachalam et al. studied the inclusion of long-range van der Waals forces on the morphology of aggregates, finding that inclusion of these forces in the model resulted in more open aggregate structures with fewer branches. Increasing the gas temperature from ambient to 1500 K resulted in a collapse of the open structure.[114] This body of work has yielded a good general model for particle aggregation under strict diffusion-based transport conditions. Further advances were made by Lee and colleagues by developing time-dependent size distribution models for particles undergoing Brownian motion in both the free-molecular[117] and continuum[118] regimes. These models follow the time evolution of particle size distribution and the decay in particle number concentration with aggregation. An interesting result from this study is the determination that particle shape and size influences aggregation rate.

In addition to diffusion-dominated transport, it is also possible to have a ballistic-type transport mode, where particle collisions with a fluid do not strongly influence the particle trajectory. This would be expected for higher vacuum (lower pressure) conditions, or where the particles are large enough to not be influenced by individual collision events with the fluid molecules. The ballistic deposition, or Eden model describes the fractal dimensions of aggregates under these conditions.[119,120] Rosner and

co-workers introduced a study of aerosol particle films formed under ballistic deposition conditions and compared them to films formed under diffusion-dominant techniques.[121] Under the limiting case of a diffusion-controlled deposition of particles, films had relatively low densities and were found to have fractal-like structure. Ballistic deposition occurs when relatively high-energy particles collide with the film and can deposit deeper within the structure, yielding a more uniform and higher density film structure.

One factor that has not been closely evaluated is the influence of particle size on transport dynamics. A series of studies have found that two different mechanisms of gas-nanoparticle collisions occur. These two mechanisms have different energy transfer characteristics, and therefore have a different influence on nanoparticle transport. It has been proposed that these gas-nanoparticle collision dynamics will depend on particle size and a transition between dominant collision dynamics occurs in the particle diameter range of a few nm.[122,123]

While some of the newer models explain many of the factors to consider when studying film growth and are more robust than the simple diffusion or ballistic models, there are a few limitations of these simulations when comparing them to results presented here. Limiting many of these models is the assumption that the density of particles is sufficiently low that no interaction occurs between the particles in the fluid. This assumption is probably valid for some flowing reactor systems and solution-phase processing methods, but is may not be valid for IGC methods where a higher density of material is expected near the laser spot. Plume dynamics and convection could also influence aggregation in a manner not investigated in these models.

The models discussed above have investigated the effects of many variables on film morphology, including different particle-surface and particle-film interactions, Brownian motion, fluid and substrate temperature, convection, in addition to particle size and size distribution. Resulting film properties such as density, fractal number, mean coordination number, deposition rates and deposit thickness have been studied. Several of these theoretical results have been confirmed by experimental studies, providing evidence of their validity. In some cases, knowledge gained from this body of work can be applied to the experiments performed here. The more advanced diffusion-based models are expected to be the most relevant in interpreting the results presented below in Section 5.6. This is because the gas densities are great enough to preclude ballistic-like transport, but low enough to qualify for the free molecular regime (i.e. $K_n > 10$) and therefore induce a more Brownian-like motion. In addition, the models that included the van der Waals and thermophoretic forces are anticipated to have validity for the current experiments, in which convection is a major factor.

5.2.3 Experimental Studies

Substantial effort in modeling particulate aggregation has been augmented by some experimental studies using pulsed laser evaporation and combustion particle synthetic techniques. Forrest and Witten were among the first to study particle agglomeration when they investigated the structure of metal nanoparticle aggregates synthesized under a He atmosphere.[105] Aggregation was observed to occur within a shell that formed within ~ 1 cm of the evaporation filament, and aggregates collected at a distance greater than 3 cm from the filament showed no difference in size or shape.

Aggregates were observed to be larger at higher gas temperatures and at higher pressure (which compressed the aggregation shell).[105]

Lee and Hyun investigated the ability for titania nanoparticles to capture gas-phase elemental mercury in a simulated combustion flue gas.[104] Particles that were synthesized using a thermal gas-phase oxidation technique with increasing temperature were found to have a lower fractal dimension with a more open structure, and larger aggregate sizes. The increase in free space observed with increasing temperature resulted in aggregates that contained a greater number of particles, higher fractal dimension, and a more open structure, leading to a higher mercury capture efficiency.[104] This result is particularly significant, because it demonstrates the importance of aggregate morphology (as opposed to particle size) in applying new materials to real-world situations.

Friedlander and co-workers compared literature data for metal oxide nanoparticles made under pulsed-laser evaporation and flame combustion synthesis conditions while applying aerosol dynamics to analyze the results.[124] The authors concluded that the maximum temperature and quench rate are two of the main factors influencing the particle size and the structure of agglomerates.

Several workers have used spectroscopic methods to monitor the evolution of the plume during pulsed-laser ablation. These are valuable in illustrating the influence of gas pressure and species on the plume. Pakhomov et al. studied the aerosol-aerogel transition of aggregates formed with laser ablation of metal targets in ambient air with photography.[125] Shortly after the laser pulse, individual particles were observed in the chamber, which aggregated to needle-like filaments under the influence of an electric field, or a chaotic web-like structure in the absence of the field. The results clearly

demonstrate that fractal-like aggregates (large enough to bridge the dimensions of the chamber) form in the buffer gas, instead of on the deposition substrate.

Other groups have used laser spectroscopic imaging techniques to study pulsed-laser ablation plume dynamics under a variety of conditions. Geohegan and Puretzky found that ablation of yttrium metal under low oxygen pressures results in a fast component of material forming a shock wave which retards the expansion of a slower component, forming the compressed plume where particles nucleate.[126] Geohegan and co-workers later studied the dynamics of Si ablated into He and Ar at 10 and 1 Torr, respectively.[127] Ablation into the heavier Ar resulted in a vapor plume whose velocity rapidly fell from 2 cm/μs to 0.01 cm/μs within 20 μs of the laser pulse. The plume became uniform and stationary after 300 μs, and particles were observed after three ms. Replacing the 1 Torr Ar buffer gas with 10 Torr of He resulted in significantly different plume dynamics. Instead of a uniform, stationary plume, a shell of nanoparticles morphs into a "smoke ring" at 500 μs as it propagates away from the laser target. The ring halted just above the collection substrate, where aggregation appeared to occur. Nanoparticles formed in the He buffer gas within 0.15 - 0.2 ms, which is an order of magnitude faster than in the N_2 gas.[127] This study underscores the greatly varied plume dynamics (both temporal and spatial) that occur in different buffer gases. For both gases, the nanoparticles synthesized under these conditions deposited in the form of small aggregates and isolated particles after a few laser shots, and grew into larger web-like aggregates after hundreds of laser shots.[128]

Maeda et al. used re-decomposition laser-induced fluorescence methods to study SiO_x nanoparticles forming in 10 Torr of He, finding the clustering of Si atoms began at

0.2 ms, correlating with the measurements of Geohegan and co-workers.[129] Further work by the same authors expanded the study to other gases (all at 10 Torr) to compare plume dynamics.[130] The onset of clustering of Si atoms was observed at 200, 250, 300, and 800 μs after laser ablation of a Si target in He, Ne, Ar, and N_2. In addition to this, the time difference between the onset of clustering and the appearance of larger clusters (measured by different spectroscopic methods) also varied from 50 to 400 μs, indicating that the growth rate of clusters varies in different gases, following the trend He < Ar < Ne < N_2. A final result from this study is the discovery that the spatial distribution or shape of the plume varies with different gases. Ablation into a He, N_2, or O_2 atmosphere resulted in a mushroom-shaped plume, while ablation into Ne and Ar results in a column-shaped plume.[130]

Niklasson investigated the role of gas pressure on the aggregation of Co nanoparticles synthesized under Ar using thermal evaporation.[131] The pressure of the buffer gas was found to have a strong influence on the structure of Co aggregates collected on TEM grids. At pressures below 0.6 Torr, small and dense aggregates were produced, while increasing the pressure resulted in more open, web-like aggregates with higher fractal dimension. This result was attributed to the change in magnetic properties with particle size, however no evidence was provided to corroborate this claim.[131]

Other studies have found that the characteristic collision times of particles can be independent of material properties and only weakly dependent on temperature, while coalescence time is strongly influenced by both material properties and temperature.[132] This is critical, because the balance between coalescence time and collision time is a

major factor in determining if particles aggregate or coalesce to form larger or necking particles.[133,134]

Another study was performed to investigate the role of laser pulse length on the efficiency of fractal aggregate structure. In this work, a 10 ms laser pulse laser was used instead of the much shorter pulses (ns to μs) commonly found in the rest of the literature.[135] The authors pointed out that experimental results using (single) short pulses result in aggregation on the second timescale ($> 10^2$ s), while increasing the pulse duration by an order of magnitude results in agglomerate detection at $\sim 10^{-2}$ s. In this study, the buffer gas pressure (~ 50 – 20000 Torr) influenced the efficiency of fractal formation, plume size, and plume shape. Fractal formation efficiency was found to increase with pressure until a critical value was reached, where the efficiency fell to a minimum value. Critical pressures for maximum aggregate formation varied greatly for different metal oxides. Influence of the buffer gas species was also found to influence critical pressure values: when Ar was replaced with He, the critical pressure increased by a factor of two.[135]

A final variable that may influence aggregation of particles is convection currents within the chamber. In IGC, convection varies with the thermal properties of the evaporation source and collection substrate, geometric parameters of the chamber, and process variables such as buffer gas species and pressure.[136] An experimental and theoretical study on convection currents in IGC found that higher pressures resulted in slower convection velocities and smaller deposition area.[137] The study also highlighted the importance of chamber size and internal geometry to optimize product yields.

It has been shown through several studies that particles can indeed interact before encountering a substrate in many vapor-phase synthetic methods such as IGC. In particular, coalescence, growth, aggregation, and aggregate restructuring may occur under typical synthetic conditions. These processes have seen significant exposure in the literature, and their influence on particle and particle aggregate features have been studied.[12,95,97,138-145] Theoretical and experimental evidence suggest that aggregates with small primary particles are likely to compact by coalescence while aggregates made of larger primary particles will compact by rearrangement of particles.[142] Aggregation of particles has been found to vary with physical properties of background gases[97,139] and possibly due to reactivity.[141] These studies all reveal information about the dynamics of nanoparticle aggregation, sintering, and restructuring in the gas media, but the influence of these processes on deposited film morphology has not been systematically studied in the literature.

5.3 Experimental

The external high vacuum laser vaporization chamber described previously was used in these experiments. Evacuation of the chamber to ~$5x10^{-6}$ Torr prior to backfill and synthesis was achieved with a liquid N_2 trapped oil diffusion pump. Images of the films were obtained with a LEO 1550 field-emission scanning electron microscope (SEM) with an accelerating voltage of 5 kV to analyze microscopic film structure. Nanoparticle films were coated with 25 Å of gold using a sputter coater to provide a conductive path for electrons, reducing charging effects. Specific surface area of Y_2O_3 nanoparticle samples were determined with a Quantachrome NOVA 1000 gas sorption analyzer described previously. TEM and AFM measurements were obtained to determine

particle size distributions. Powder XRD measurements were also obtained to provide information about the crystal structure. Finally, ICP measurements were performed to quantitate the mass yield of particles collected onto substrates. To do this, the nanoparticle films were dissolved in an aqueous 5 % HNO_3 solution and diluted to 10.00 mL and then analyzed for yttrium concentration, which can be converted into a mass of oxide dissolved into the solution.

5.4 Results and Discussion

5.4.1 BET Results

Particle characterization results are shown in table 5.1 below. Surface areas of Y_2O_3 nanoparticles synthesized under 1 and 10 Torr N_2 were found to be 185 and 153 m^2/g, respectively. Similarity between the single and six point measurements, linearity of the BET plot (not shown), and value of the surface area (> 0.1 m^2) all indicate that the results are reasonable. It should be noted that the mass used for the particle sample was measured prior to degassing, so any loss of H_2O or CO_2 from the sample would lead to a lower mass and therefore an artificially low BET surface area value. If surface adsorbates account for 10% of the mass of the particles, the result would be an underestimate of the surface area by the same percentage. This uncertainty is expected to be greater for the smaller particles, which have a greater surface area/mass ratio, and could also cause a small (~ 5%) overestimate of the surface area obscured by grain boundaries.

Table 5.1 Summary of BET, TEM, and XRD results.

Y_2O_3 Sample	1 Torr N_2	10 Torr N_2
Mass	0.0289 g	0.0214 g
1 – pt BET	184.9 m^2/g	152.8 m^2/g
6 – pt BET	186.8 m^2/g	154.6 m^2/g
Size – Microscopy	2.5 nm	4.6 nm
Size – BET Calc.	6.3 nm	7.6 nm
% SA taken by Boundaries	60.4%	38.8%
Crystallite Size – XRD	2.4 nm	3.6 nm

5.4.2 Analysis of BET Results

Several calculations can be performed using the BET results. First is the estimated particle diameter from the BET surface area, assuming spherical particles and bulk density. This calculation yields values of 6.3 and 7.6 nm for particles made in an atmosphere of 1 and 10 Torr N_2 respectively. While the trend in particle size from BET measurements increases with pressure as anticipated, the values are significantly different from the observed particle sizes in TEM and AFM data. This discrepancy can be accounted for by recalling that there is substantial aggregation of particles in these samples, so a significant amount of particle surface will be "masked" by grain boundaries. An approximation of the surface area that is masked by these grain or particle boundaries may be made by assuming spherical particles with the mean diameter as determined by TEM and AFM. As seen in table 5.1, an estimated 60 and 39 % of the theoretical surface area is taken up by these grain boundaries for particles made under 1 and 10 Torr N_2, respectively. The higher fraction of theoretical surface area masked by particle boundaries for the 1 Torr N_2 sample indicates a higher density within the film, correlating with the SEM observations discussed below, as well as the HRTEM images shown in Figure 5.1.

5.4.3 XRD and TEM/AFM Results

Samples of particles produced under 1 and 10 Torr of N_2 were characterized to compare the particle sizes and crystal structure of the two materials. AFM and TEM measurements of dispersed particles indicate that the mean particle diameters for Y_2O_3 made at 1 and 10 Torr are 2.5 nm and 4.6 nm, with standard deviations of 1 nm and 0.5

nm, respectively. This is consistent with the positive dependence of particle size with synthesis pressure and with previous data.[70]

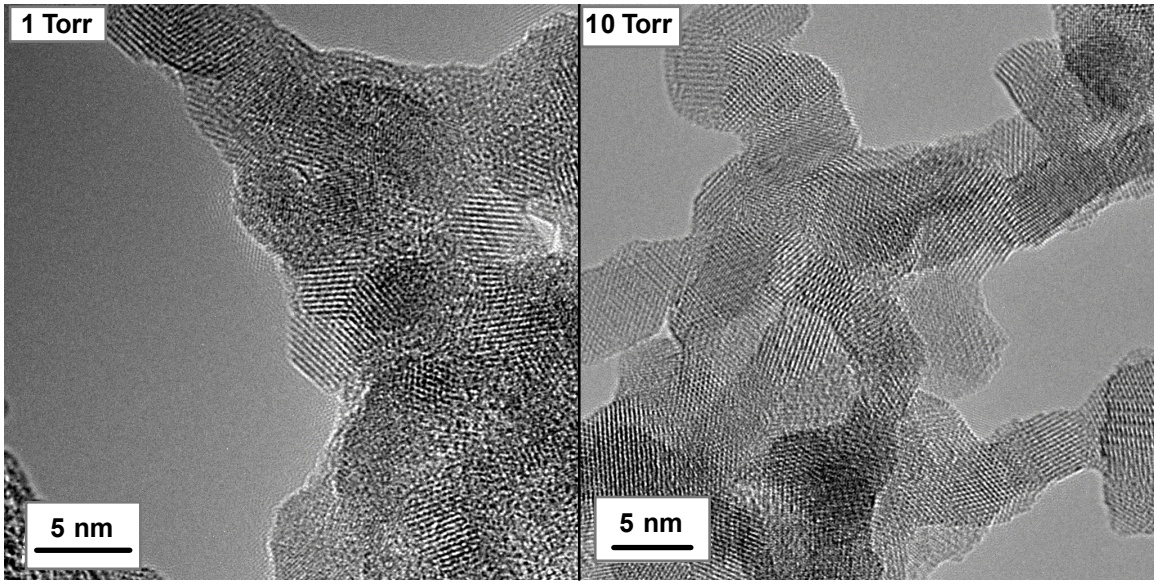

Figure 5.1 HRTEM images of Y_2O_3 nanoparticles synthesized under (left) 1 and (right) 10 Torr. The sample produced under the lower pressure has a more compact aggregate structure, and therefore a higher degree particle surfaces obscured by grain boundaries.

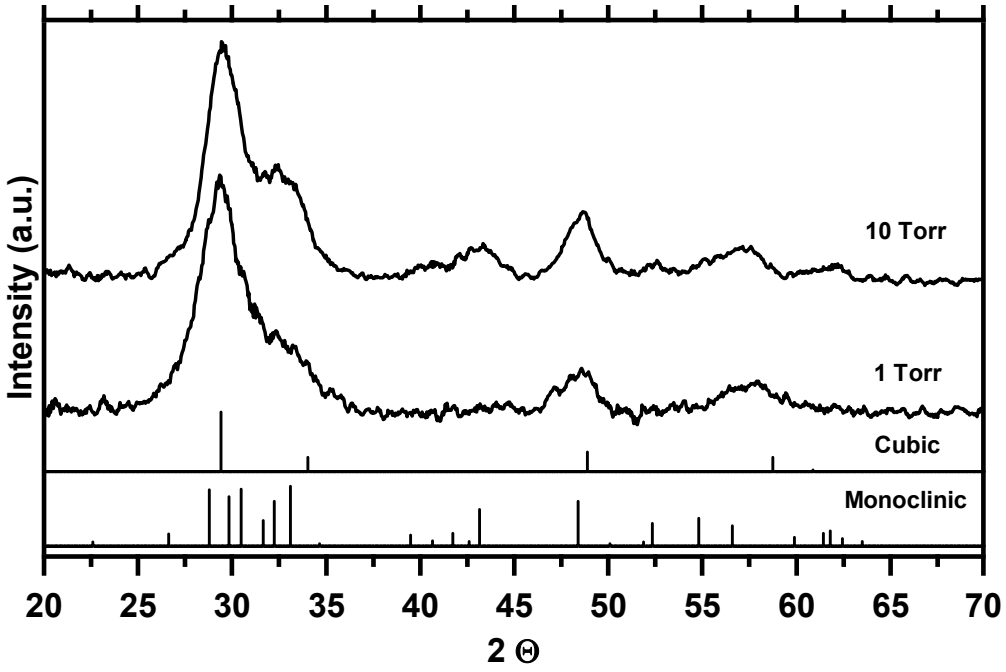

Figure 5.2 Powder X-ray Diffraction data for Y_2O_3 particles synthesized under 1 and 10 Torr N_2, along with reference peak positions for the cubic and monoclinic phases of Y_2O_3.

Powder X-ray diffraction measurements seen in Figure 5.2 indicate that the larger particles have both monoclinic and cubic phases (JCPDS files 43-661 and 44-399) present. Peak fits using reference data for the two phases of Y_2O_3[15,146] show that the particles synthesized under 1 and 10 Torr N_2 are greater than 95 and 75 % cubic phase material, respectively, with the balance of the sample existing in the monoclinic phase. Using the Scherrer equation (see Section 2.2.3) for the predominantly cubic reflection at $2\Theta = 29.15^{o}$, the crystallite size was estimated to be 2.4 and 3.6 nm for the particles made at 1 and 10 Torr, respectively. Broadening of the cubic line due to contribution by the overlapping monoclinic phase reflection of the particles leads to a decrease in the value calculated for the 10 Torr sample.

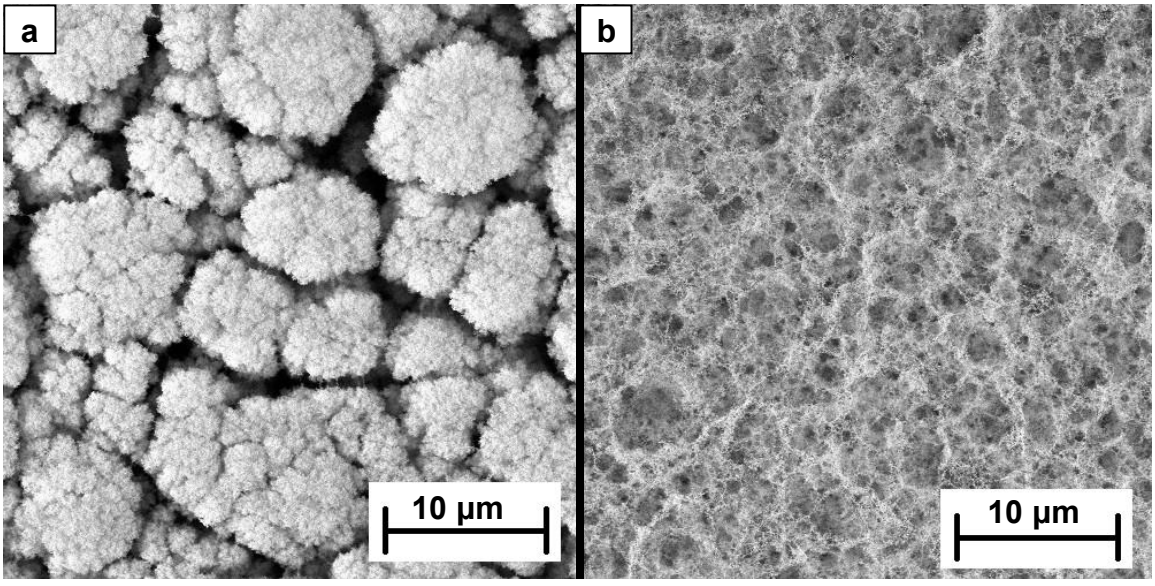

Figure 5.3 Y_2O_3 nanoparticle films synthesized under a) 1 Torr and b) 10 Torr N_2

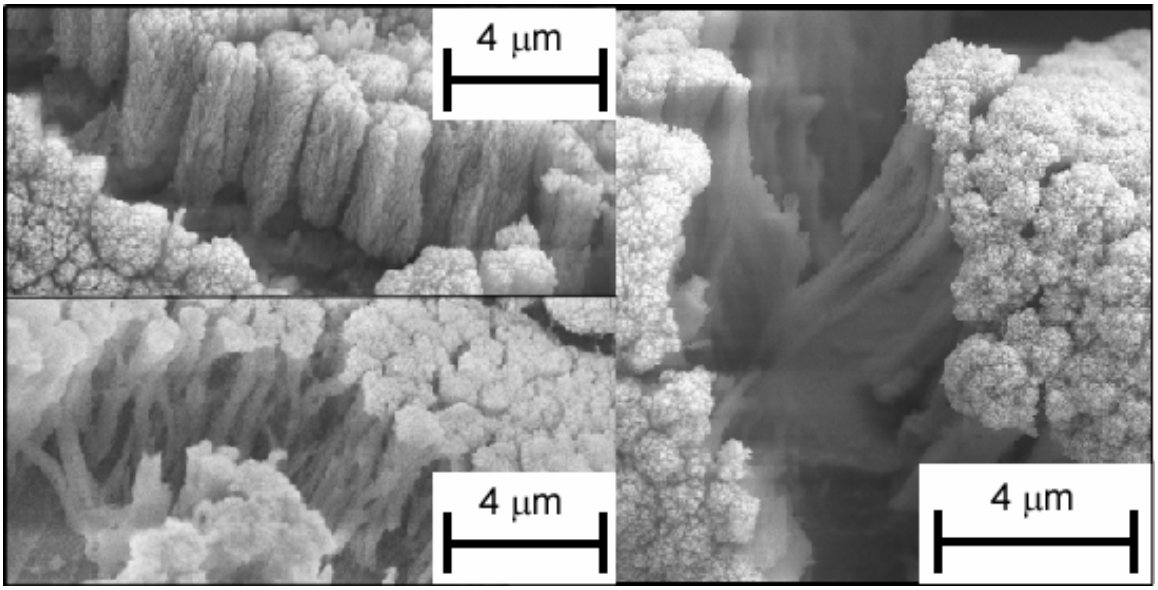

Figure 5.4 Columnar aggregate structures observed at defect sites for the low pressure morphology.

5.5 SEM Analysis and Results

5.5.1 SEM Studies of Film Morphology – N_2

Figure 5.3 shows scanning electron micrographs of Y_2O_3 nanoparticle films that were grown under 1 and 10 Torr of N_2. The micrographs show clear differences between the morphology of films grown under the different pressures. The morphology of the 1 Torr sample leads to a compact, powder-like appearance when scraped, while the 10 Torr sample scrapings come off in larger flakes that appear less dense, more translucent and fluffy. This apparent density difference is consistent with the BET surface area measurements discussed previously.

The film made under 1 Torr of pressure consists of column-like structures of densely packed nanoparticles that are roughly cylindrical. Structure diameter typically falls within the range of 1-10 μm, varying with preparation conditions such as vaporization time, gas pressure, and target-to-substrate distance. Further investigation with SEM revealed that these cylindrical aggregates continue through to the substrate

(see Figure 5.4) in column-like structures that pack in a quasi-hexagonal lattice. We believe the morphology to be the same one that has been reported earlier for Ga_2O_3[147] and Si nanoparticles[148] and the columnar aggregate shape is similar to that of the crystalline nano-nails that have been synthesized from metal oxides.[149,150] Further investigation into the growth of these columns indicate that there are some aggregate connections between the columns, and that growth of the columns begins after some critical surface coverage has been met. This is consistent with the silicon nanoparticle films synthesized by Levoska and co-workers, where "soft agglomerates" formed on the surface followed by development of a regular columnar pattern.[148] The critical surface coverage is on the order of a few layers of small particle aggregates. This process is shown in Figures 5.5 and 5.6, which show films of particles grown at short vaporization times. After 5 s of vaporization (see Figure 5.5a), only small aggregates of particles are present on the substrate. As the time is increased to 30 s (Figure 5.6), more aggregates have deposited on the substrate. Columns are beginning to grow, but have a large amount of free space in between them, where a thin layer of aggregates is seen on the surface. As the film grows, this free space is substantially reduced and eventually smaller columns of material are "outgrown" and blocked from further growth by larger columns. These columns grow perpendicular to the substrate surface, regardless of the substrate orientation with respect to the target. Substrate-directed film growth is demonstrated in Figure 5.7, where a particle film has grown on a foreign object (perhaps a fiber) and the particle structures radiate from the surface instead of forming columns due to the non-planar nature of the object. This film growth is unique at this particular pressure and changes when the pressure is increased during synthesis.

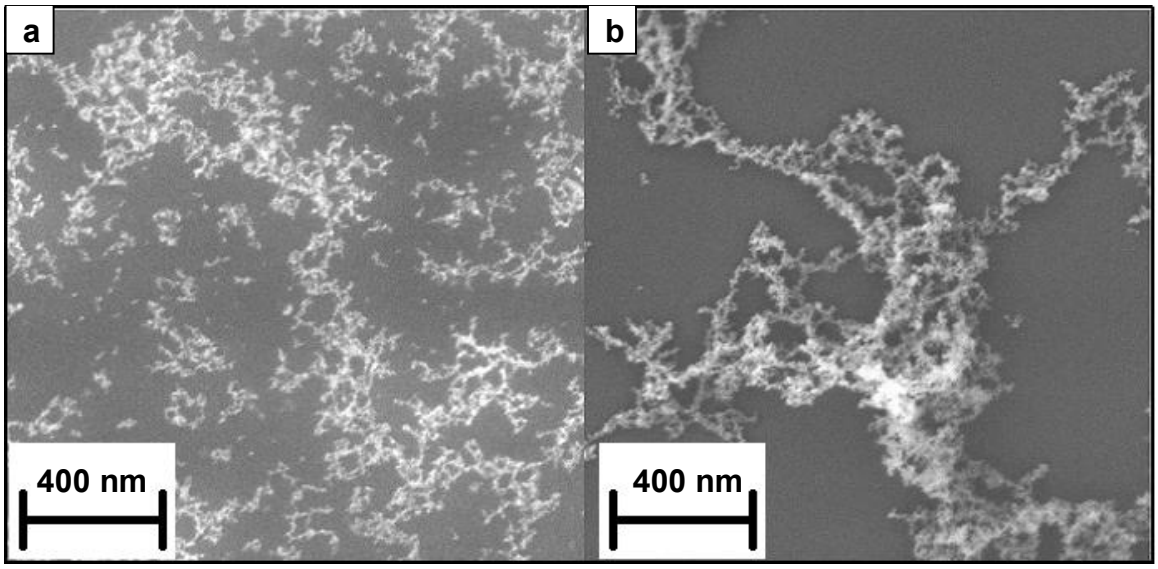

Figure 5.5 SEM images of Y_2O_3 nanoparticle films at 5 s vaporization times a) under 1 Torr b) under 10 Torr N_2.

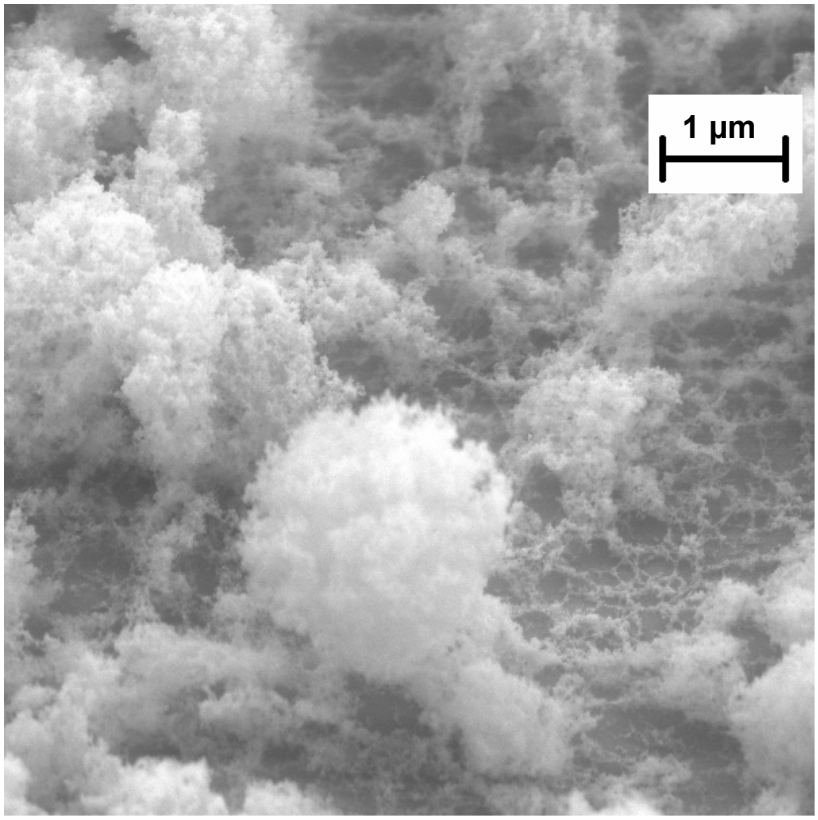

Figure 5.6 SEM image of a Y_2O_3 nanoparticle film grown at short times under 1 Torr. This image is taken with the substrate at a 30^o angle.

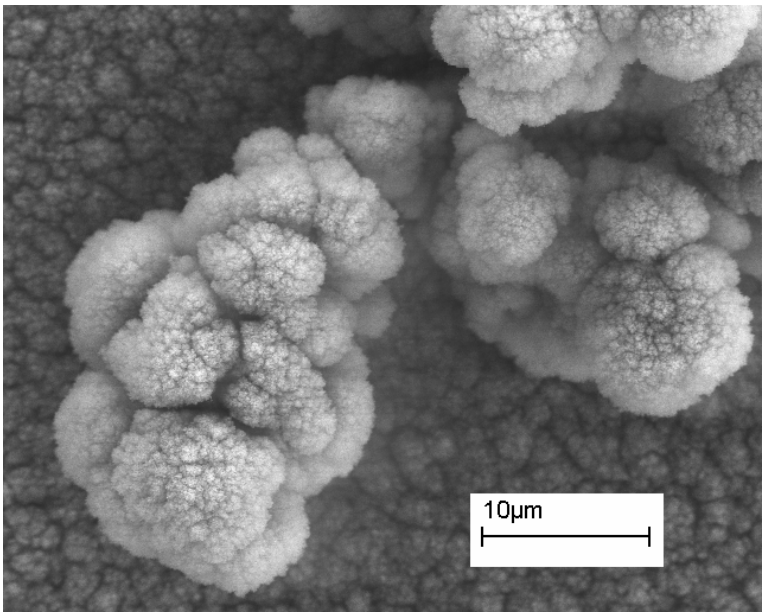

Figure 5.7 Growth of nanoparticle features radially from a non-planar substrate. Note that the features are not oriented facing the target.

At the higher pressures, a morphology that is consistent with more common reports in the literature is seen.[139,140,147,151] Films made at higher pressures are formed of networked aggregates of particles that appear to pack loosely and randomly. The aggregates continue on at micrometer length scales and the packing leaves a considerable amount of void space within the film. Images at defect sites and film edges indicate that this structure persists through the film to the substrate. Further experiments established that the film morphology could be reproducibly controlled with the background N_2 pressure during synthesis. In addition, 3 Torr N_2 was found to be the critical pressure at which a transition between the two morphologies occurred.

5.5.2 Film Growth Mechanism

Several experiments were performed to investigate the growth mechanism of the films. In the first experiment, the distance between the target pellet and the substrate (d) was varied from 0.5 to 8 cm at both 1 and 10 Torr N_2. At these pressures, no distance

dependence was observed in the morphology of the films. However, at 4 Torr the morphology changed from the networked morphology to the columnar morphology as d was decreased to 0.9 cm. These experiments indicate that distance between the target and substrate does have influence on the morphology, but the effect of pressure is more dominant. In addition to distance, the effect of substrate temperature was explored by comparing films grown under 1 Torr of N_2 with the substrate at ambient temperature or cooled to approximately 100 K with a liquid nitrogen cold finger. This experiment was performed to investigate the possibility that thermal diffusion of particles on the film surface was responsible for morphology features. Both films exhibited the column morphology on the surface, but the film grown at lower temperature exhibited cracks (probably due to expansion when warmed) and no other significant morphology differences were observed.

Experimental results indicate that the film growth mechanism is different at 1 and 10 Torr N_2, and is not consistent with nucleation of the particles on the substrate itself. Under the conditions used for this study, a transition region between the two film growth mechanisms occurred at 3 Torr for N_2. The fact that particle size is known to increase with distance between the substrate and target suggests that the different film morphologies is not related directly with particle size and is due to the influence of the gas pressure on the dynamics that occur during particle synthesis. Further investigation of the morphology transition by varying the properties of the buffer gas could shed light on the cause of the different film growth mechanisms for the two morphologies.

5.5.3 Film Morphology Transition in Other Gases

To gain insight into the process of film growth, the critical transition pressure in other background gases was identified using SEM analysis. Table 5.2 lists the gases studied and the approximate morphology growth transition points. It is seen that there is no clear trend between the transition point and molecular weight for the noble gases He, Ne, Ar, and Kr as shown in Figure 5.8, so it can be inferred that mass of the gas atoms is not the only parameter influencing the film growth. In addition, the monatomic gases have similar heat capacities; therefore the heat capacity alone does not influence the growth of the particle film. N_2 and O_2 have similar thermal conductivities and heat capacities, but different masses and viscosities and yet demonstrate only a small difference in morphology transition pressure. Ar and CO_2 have similar masses and thermal conductivities, but different viscosity and heat capacity values which lead to a different transition pressure. Table 5.2 also lists the mean free path values of each gas at the transition pressure, demonstrating there is not a direct correlation between the molecular diameter of the gas and the transition point. It should be noted that the data point for CO_2 may not be reliable for use in determining the relationship between gas properties and transition pressure due to reaction of CO_2 with the nanoparticles. To confirm that the film morphology was not specific to Y_2O_3, HfO_2 nanoparticle films were also grown in different background pressures of nitrogen, showing two different morphologies with a transition point in N_2 around 3 Torr.

Table 5.2 Selected properties of various gases tested at 298 K,[152] the approximate morphology transition pressure for Y_2O_3 nanoparticles, and the mean free path of the gas at the transition.

Gas	Mol. Wt. ($g*mol^{-1}$)	Thermal Conductivity ($W*m^{-1}\ K^{-1}$)	Viscosity (μPa*s)	Cp ($J*mol^{-1}\ K^{-1}$)	Transition Pressure (Torr)	Mean Free Path @ Trans. (μm)
Ar	39.95	0.0179	22.54	20.786	0.75	102.9
N_2	28.01	0.0258	17.79	29.126	3	13.7
CO_2	44.00	0.0166	14.93	37.142	3	6.6
Ne	20.18	0.0481	31.11	20.786	4	29.7
O_2	32.00	0.0263	20.44	29.376	4	10.5
Kr	83.80	0.0095	25.10	20.786	10	3.1
He	4.00	0.1552	19.82	20.786	> 10	< 12.8

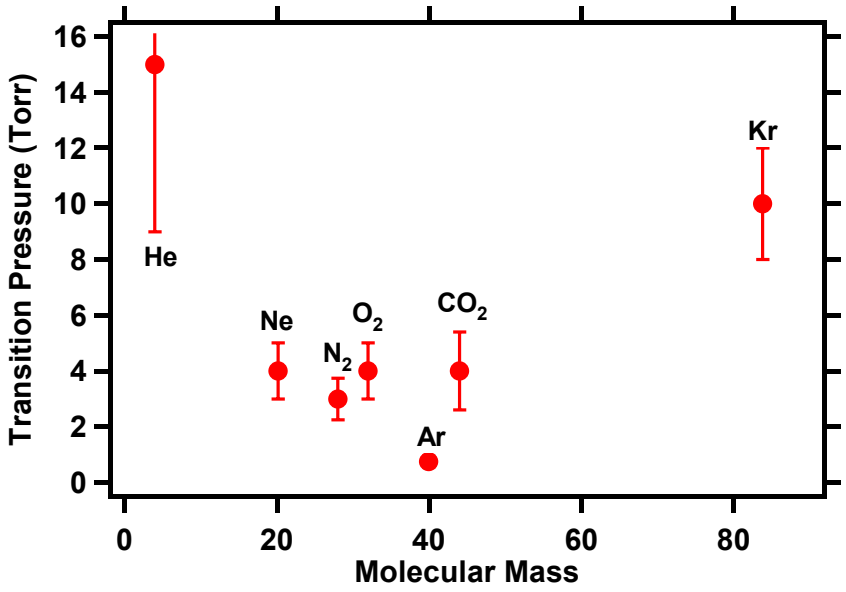

Figure 5.8 Morphology transition pressure of various gases vs. molecular mass. The error bars indicate the estimated uncertainty in the true transition pressure.

5.6 Morphology Discussion

5.6.1 General

It is clear that there is a transition in growth mechanism for films synthesized at different pressures. It has been established that when the target is evaporated with a laser, a dense cloud of evaporated material forms above the surface.[153] As the cloud expands

into the buffer gas, a plume of vapor material forms.[12,127,130,151] The plume is confined by a shock wave that is formed by the collisions of the expanding cloud of evaporated material with the buffer gas. In this spatially confined region, vapor material cools via collisions until a supersaturation condition exists, then nucleation, growth, and aggregation of particles may occur. At the pressures used in IGC (0.5 – 100 Torr), convective currents sweep the particles out of the growth region towards the substrate.[154] Studies have found that plume dynamics such as flow, residence times of particles, and plume shape can strongly depend on the pressure and nature of the buffer gas.[127,130,155,156] Figure 5.8 illustrates the results, which indicate that the nanoparticle film morphology is controlled by the effect background gas pressure has on plume dynamics. Higher pressures lead to a plume where nucleation and growth of particles occurs closer to the target, and therefore a higher loading of particles is found in a smaller area within the plume. The greater pressure also increases the residence time of the particles in the plume and increases the rate of cooling, which is known to influence degree of aggregation of nanoparticles.[139] Higher pressures can also lead to more turbulent convection flow, enhancing particle-particle collision probabilities. This combination of higher particle density, longer residence time, and faster cooling rate, and more turbulent convection means that the particles (and growing aggregates) have higher collision probabilities with other particles. Growing the film under 10 Torr N_2 yields a morphology that results from a higher degree of primary particle aggregation before reaching the substrate where the nanoparticle aggregates deposit randomly when striking the surface.

Conversely, the lower pressures lead to a larger plume with a lower number density of particles. This in turn leads to lower particle collision probabilities and

therefore less aggregation in the gas phase before nearing the substrate. The film is more dense when synthesized under lower pressures, a fact that could be attributed to greater kinetic energy of the particles prior to deposition, but is more likely due to the more compact nature of film growth when small aggregates or isolated particles are the dominant species. Pure ballistic-like movement is ruled out as the cause for the film morphology at the lower pressure because column growth direction did not change with substrate angle. However, it is likely that there is less Brownian or diffusional motion of particles under the lower pressure conditions. Once a critical layer of particles has accumulated on the surface, attractive forces such as van der Waals, electrostatic, or dipole interactions can influence the deposition of the single particles or small aggregates.[94] It is likely that these attractive forces are the cause of the column or filament like growth of the particles on the substrate when the particles are synthesized under lower pressures. At the higher pressures, the particle aggregates are too massive for these attractive forces to have a major influence on deposition of the particles, and therefore only play a role in the particle aggregation.

5.6.2 Plume Density

Figure 5.10 (a) shows a simple geometric model to visualize the influence of plume size and shape. This illustration consists of a square pyramidal plume that starts at a point source (the laser spot) and ends at the 1 x 1 cm collection substrate. The figure shows the plume region divided into 7 regions (each 0.5 cm high) in the 3.5 cm distance between the target and collection substrate. Relative volume of each section is denoted as a percent value, which was calculated using trigonometric and geometric formulas. If the amount of material (both vapor and growing nanoparticles) remains the same in each

section of the plume while moving towards the substrate, the density and thus the particle-particle collision probability decreases dramatically as the growing nanoparticles continue to the substrate.

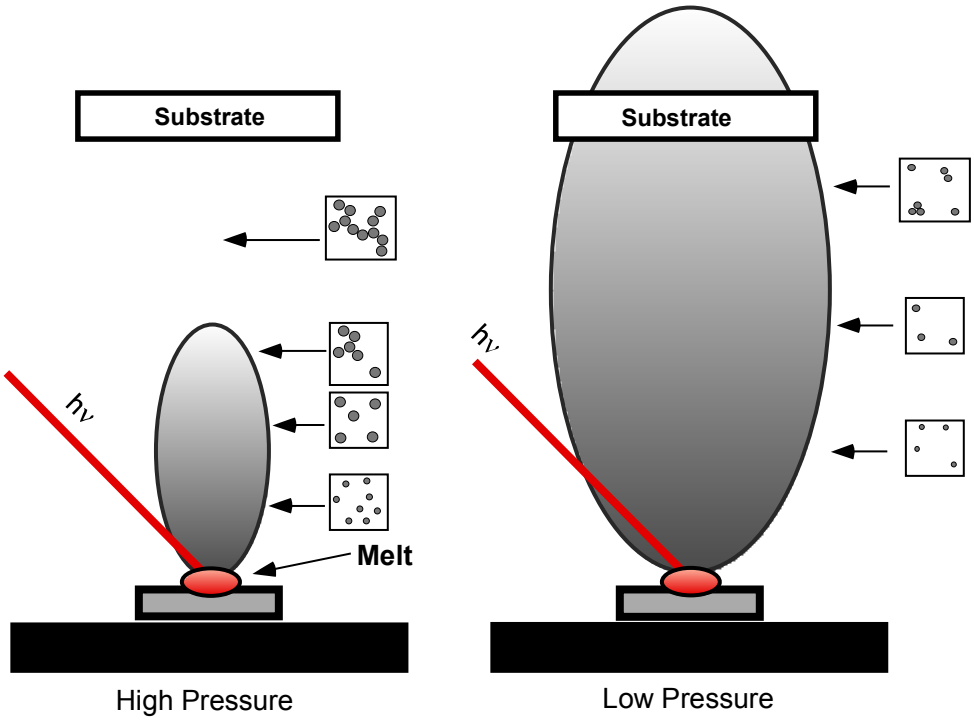

Figure 5.9 Representation of different plume dynamics resulting in different film morphologies at higher and lower pressures. At higher pressures, particles aggregate before striking the substrate. Lower pressures reduce the particle density within the plume as well as increasing plume size and therefore aggregation is kept to a minimum, so particles can build the column-like film structure.

ICP results have been used to estimate the density of particles in the plume. For samples produced under both 1 and 10 Torr N_2, approximately 0.1 mg of yttria particles were deposited on the 1 cm^2 substrate during the four-minute vaporization (see Table 5.3). Assuming spherical particles with the mean particle size (as determined by AFM), and that the material density is the same as bulk cubic yttria (5.14 g/cm^3), the rate of production is estimated to be ~ 2 x 10^9 and ~ 1 x 10^8 particles/μs under 1 and 10 Torr of N_2, respectively. The order-of-magnitude difference in particle number is due to the

relatively small mass of yttria that composes the small versus the large particles since the mass production of Y_2O_3 is similar. Velocity of the material in the plume is expected to decrease from initial speeds as high as ~ 10^6 cm/s[157] to velocities characteristic of convection-based diffusion (~ 10 cm/s)[137] after reaching the shock region (which extends vertically on the order of 1 cm from the target under the present conditions), where the material becomes thermalized by the buffer gas[158] and nucleation of the particles occur.

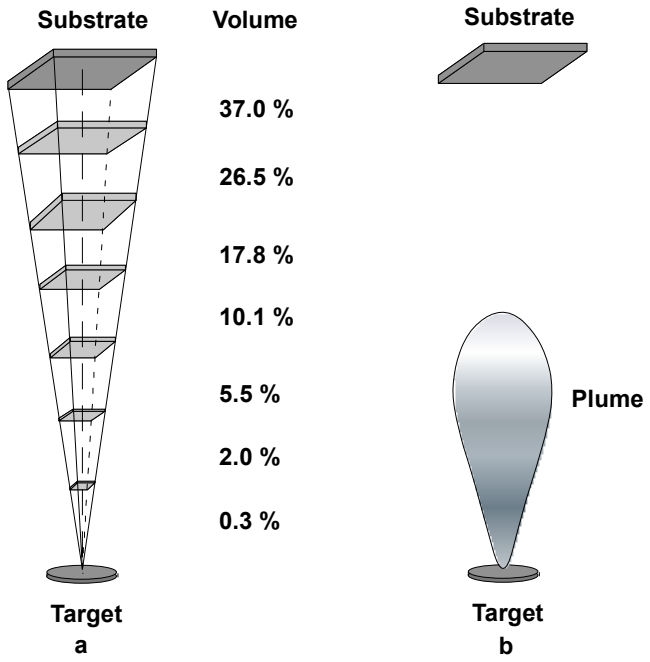

Figure 5.10 a) Model pyramidal plume showing the fast relative increase in volume, resulting in reduced particle/aggregate collision probabilities. b) Representation of the true shape of a typical laser-evaporated plume where nanoparticles grow and aggregate. Convection and diffusion carry the nanoparticles and aggregates to the substrate.

Table 5.3 Results from ICP analysis of dissolved Y_2O_3 nanoparticles. The number of nanoparticles is calculated from the mean particle size and the bulk density of cubic yttria. Relative standard deviation of these values is also shown, highlighting some variability in the mass yield of the particles.

Pressure	mols Y (ICP)	Y_2O_3 mass (g)	Total NPs	NP product rate	R.S.D. (samples)
1 Torr N_2	9.5×10^{-7}	1.1×10^{-4}	5.1×10^{14}	2.0×10^{9} NP/μs	30 % (6)
10 Torr N_2	8.6×10^{-7}	9.8×10^{-5}	2.3×10^{13}	1.0×10^{8} NP/μs	32 % (4)

5.6.3 Buffer Gas

The effect of ambient gas on the transition pressure between the morphologies is explained by the physical and thermal properties of the gas. Oxygen and nitrogen have similar mass and thermal transport properties, so their transition pressure is similar. The experimental results for four noble gases indicate that mass cannot be the sole variable for differences in nanoparticle film formation. These results are consistent with those of Erhart and Albe, who found that molecular dynamics simulations of nanoparticle growth are inadequate when homogenous temperature controls are employed or when random collisions are assumed.[159] Their results show that an explicit model of inert gas cooling and gas-nanoparticle potentials is important, underscoring the complexity of the system under consideration. Argon is heavier than nitrogen and therefore can compress the plume more effectively, leading to a decrease in the transition pressure. Krypton is also heavier than nitrogen, but its very low thermal conductivity reduces the ability of the gas to thermalize the nanoparticles, which leads to an increase in transition pressure. Helium, with a very low mass but high thermal conductivity, is least capable of compressing the plume of the gases tested in this study and therefore its transition point is higher than 10 Torr.

These results are supported by other work in the literature. Geohegan et al. performed in-situ time-resolved spectroscopy of gas-phase synthesized particles and found different plume dynamics in samples produced under 1 Torr Ar and 10 Torr He.[127] Nakata and co-workers also used in-situ time-resolved spectroscopy to study the effect of gas on the plume dynamics and onset of Si nanoparticle formation. It was found that different gases strongly influence the time scale of nanoparticle formation and the spatial

distribution of growing nanoparticles. In their system, the onset of Si particle nucleation was 200, 250 300, and 800 μs when Si was ablated under 10 Torr of He, Ne, Ar, and N_2, respectively. In addition, the plume shape varied significantly in the different gases.[130] Han et al. found that aggregation of nanoparticles made in a reactive gas under flowing conditions in a tube furnace increases with higher residence time and that the gas temperature effects morphology due to differences in Brownian dynamics.[95] Similar results were reported by Sánchez-López and co-workers, whom studied ZnS nanoparticles synthesized in N_2, He, and Ar and found that higher pressures lead to higher gas temperatures that would increase Brownian dynamics and therefore, would favor increased aggregation.[139] Kim and co-workers found that increasing the O_2/He ratio in chemical vapor condensation synthesis of TiO_2 nanoparticles increases the agglomeration of particles while the primary particle size remained the same.[141] This increase in agglomeration was attributed to the increased water production in the gas, but may be due in part to the change in physical properties of the gas mixture.

The experiments discussed above demonstrate that the nature of the gas used in IGC has a drastic influence on the morphology of the film of deposited nanoparticles. Based on experiments in our lab and the results published in the literature, the nature of the gas influences the plume size and shape, the time scales of nanoparticle formation, the density of particles within the plume, and the transport of particles to the substrate. All of these factors can influence the aggregation of particles prior to deposition, which in turn effects the resulting film morphology.

5.6.4 Predicting Film Morphology

One of the goals of this work is to successfully predict the film morphology for a given type of nanoparticles that are synthesized using IGC under a set of conditions. While a quantitative model has not been achieved, several general predictions can be made. These predictions are based upon the influence of the background gas, target-substrate distance, and the vapor material on the plume dynamics, which control the growth of the nanoparticle film.

Pressure of the buffer gas is the most critical value for controlling the morphology of the nanoparticle film. Above a critical pressure, a web-like morphology is created due to aggregation of particles. Below this pressure, an array of columns grows on the substrate. The pressure influences two major features during IGC synthesis: the size, shape, and dynamics of the plume where particles nucleate and grow, and the nature of the convection flow that transports particles from the plume to the substrate. If the gas influence on the plume size is the primary controller of the morphology, then a quantitative understanding of the pressure-plume distance can be developed.

Geohegan published a "blast wave model" for plume propagation during laser-induced ablation, using the relationship:

$$D = \varepsilon_0 (E / \rho_0)^{0.2} t^n \qquad \textbf{Eq. (5.4)}$$

Where ε_0 is a constant, E is the explosion energy, ρ_0 is the gas density (which is proportional to pressure) and t is time. n was found to be 0.4 in the original model, but 0.6 was found to provide a better fit at certain pressures.[160] If we assume that the film transition pressure (and target-substrate distance) correlate with the shock front or plume distance, we can eliminate the time variable to get the relationship:

$$PD^{5(n-1)} = const. \qquad \textbf{Eq. (5.5)}$$

Using the two values for n (0.4 and 0.6) found in the literature, and the transition point observed in nitrogen (D = 0.9 cm, P = 4 Torr), we find that the pressure-distance relationship to be:

$$\left\{\begin{matrix} PD^2 = const. \\ PD^3 = const. \end{matrix}\right\} for \left\{\begin{matrix} n = 0.6 \\ n = 0.4 \end{matrix}\right\} \qquad \textbf{Eq. (5.6)}$$

This relationship is plotted in Figure 5.11, and can provide a prediction of the pressure-distance relationship for the critical morphology transition point.

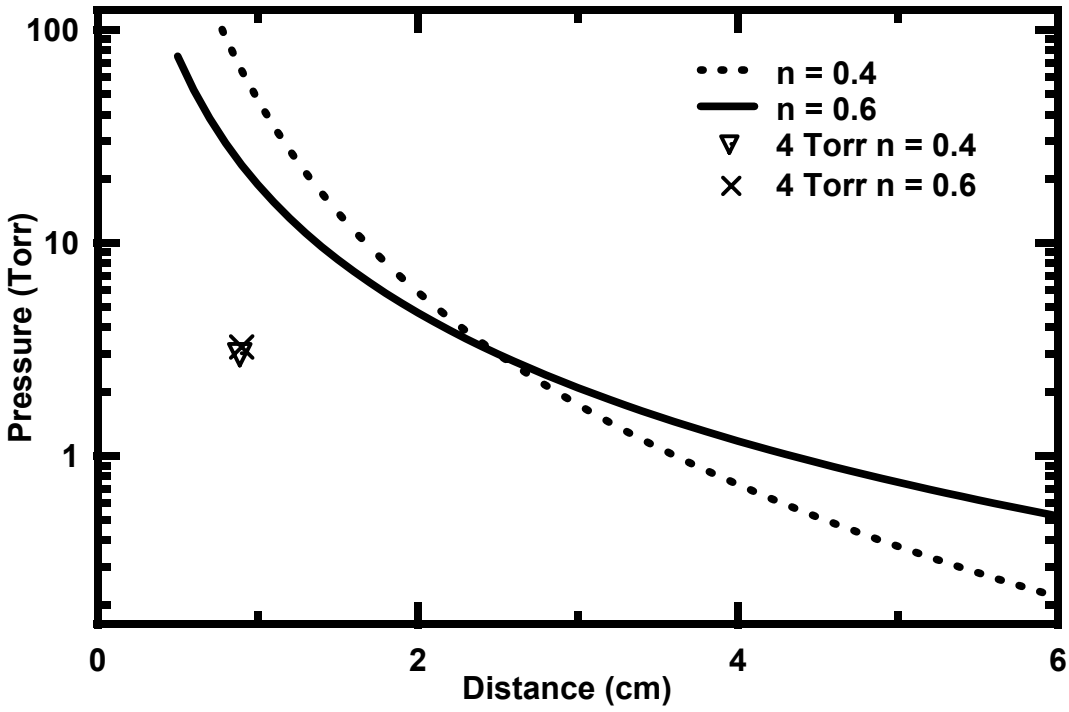

Figure 5.11 Model data for the blast wave model of plume distance versus pressure using an exponent of 0.4 and 0.6. The model is fit to the critical morphology transition point of 2.5 cm, 3 Torr in N_2. The two points plot the data point found from the distance-dependence study (0.9 cm, 4 Torr N_2).

It is clear that the fit for the pressure-dependent study and the data point for the distance-dependent study do not agree well. The poor agreement may be explained by fact that the plume height (or distance) is not the only factor that determines the ultimate

film morphology. This model does not take into account any influence that the particle density or gas convection will have on aggregation of particles prior to deposition. Therefore the results from Figure 5.11 imply that the morphology transition does not solely depend on the plume height. Regardless, the model shows that the plume size varies strongly with pressure. This result agrees with our finding that the morphology is more strongly influenced by pressure than collector height.

Based on the work discussed here, for a system with all other experimental parameters constant, the pressure of the given buffer gas will influence the aggregation of particles prior to deposition, thus resulting in two different film morphologies. For a given gas, a transition point exists where the resulting film structure changes from dense columns to more fractal, web-like features. The transition point is determined by the ability of the gas to thermalize the vapor material, the shape and size of the resulting plume, and the transport dynamics of particles and aggregates to the collection substrate. As the pressure increases, the plume becomes more compressed, reflecting the increases ability for the gas to thermalize the vapor material. This results in greater particle density, and therefore increased collision probabilities.

When changing the buffer gas, the most important properties for predicting the morphology seem to be molecular diameter, mass, and thermal conductivity. Molecular diameter determines the mean free path, or the frequency of collisions of vapor material/nanoparticles. For a given density, increased gas molecular diameter increases the number of collisions, therefore leads to faster thermalization of vapor and greater Brownian motion. These parameters both result in increased particle aggregation. The mass of a gas molecule influences the energy transfer between a colliding particle (or

vapor molecule). Heavier gas molecules will lead to faster cooling rates, which compress the plume and result in higher particle collision properties. Finally, thermal conductivity determines the ability of the gas to dissipate the energy gained from collisions with the energetic vapor material. Increasing the thermal conductivity of the buffer gas will result in more efficient thermalization and therefore greater aggregation.

In addition to the buffer gas, it is also important to predict the change in the critical transition pressure for different target materials. Characteristics of the target material that influence the rate of evaporation should also determine the relative morphology transition pressure. Therefore, the transition pressure for a material should increase with melting point and decrease with the ability of the target to adsorb the laser radiation. Along the same lines of thought, an increase in laser power should increase the quantity of vapor material in the plume and therefore decrease the transition pressure. These results discussed above give us a rough ability to predict the film morphology for a given target material, laser power, and buffer gas.

5.7 Additional Observations

Several other interesting features were found in particle films during this SEM based study. The source of some of these features is explained, however some are unknown. Two types of holes were observed in films of particles. Both are believed to be caused by small molten droplets of material being ejected from the target and cooling in the gas before striking the particle films. Under high pressures (well above the morphology transition point) the impact trenches show that the incoming fragments are not approaching perpendicular to the surface as seen in Figure 5.12 a), and it is inferred that the trajectory of droplets of molten material is influenced by the higher gas pressure.

Vertical holes seen in Figure 5.12 b) caused by ejected matter hitting perpendicular to the surface were found in films with both types of film morphologies. Another defect type that was observed was seen in several low pressure morphology films as shown in Figure 5.13. This defect is characterized by close packing of groups of columns of particle aggregates after growth of the film, resulting in a ring of void space. Pressurization or some mechanical stress could be responsible for inducing this feature, but it appears that attractive forces between the columns allow the contraction within the ring.

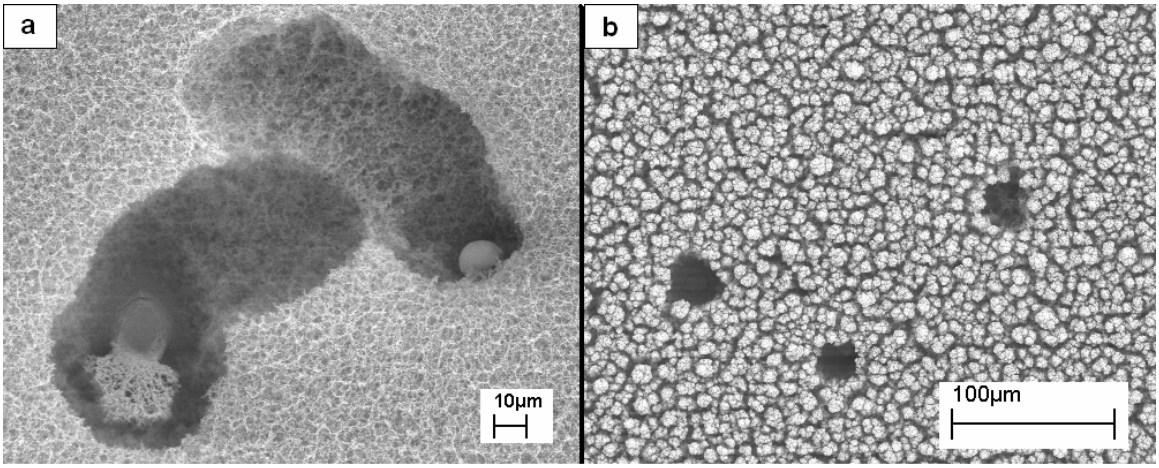

Figure 5.12 Defects caused by ejected droplets of yttrium oxide hitting the surface. Defects such as the ones in a) were only observed at higher pressures while those in b) were seen in both morphologies.

A final film feature that was discovered is the star-like indention seen in Figure 5.14. This feature was only observed in films with the high pressure morphology grown in gases well above the morphology transition point. Characteristic of this defect is a circular shaped pit surrounded by a raised lip of nanoparticle film. Eight to ten trenches radiate from this circular feature to form a star-like pattern seen in the figure. If these star features are close enough to each other, they can share the trenches in a pattern similar to magnetic field lines. It is possible these features are due to impact of macroscopic pieces

of material that do not stay imbedded with the film, but the true cause for this interesting feature is unknown.

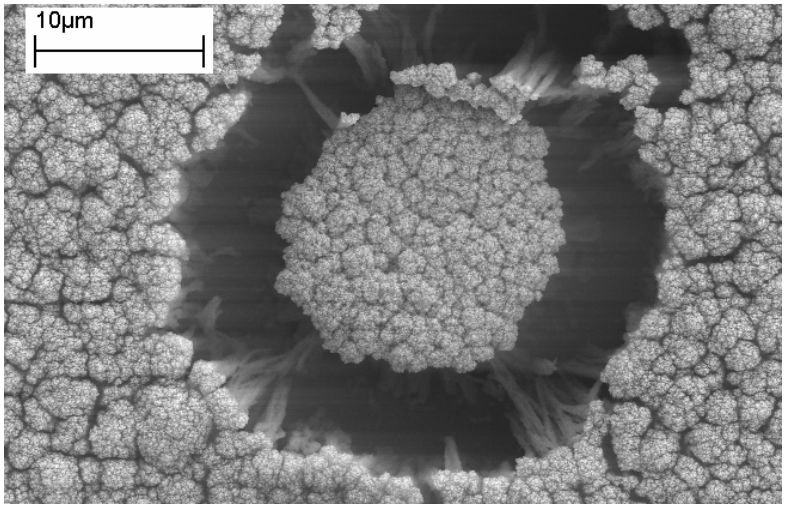

Figure 5.13 Ring defect caused by contraction of columnar aggregates in the film. Note the smaller size of column tops in the "island" compared to the rest of the film.

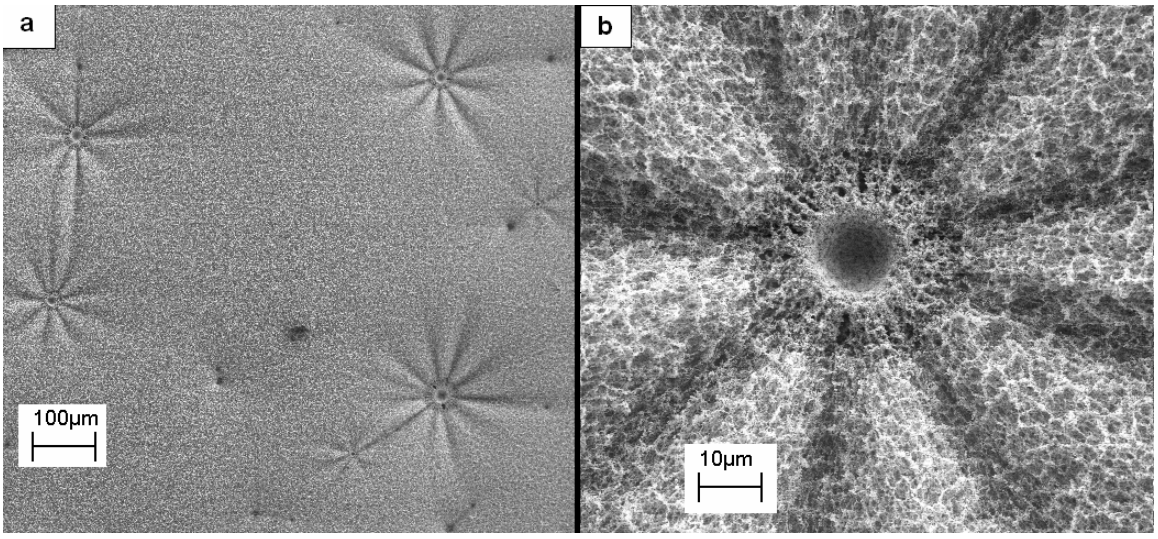

Figure 5.14 a) Star-like patterns seen under high pressure. Note the trenches that are shared by two features. B) A higher magnification micrograph shows the center of the star pattern.

5.8 Conclusion and Suggested Work

The morphology of films composed of nanoparticles may be controlled by the pressure and type of gas used in gas-phase condensation. The difference in the morphologies is believed to be due to aggregation of particles in the gas phase. Variables that impact this aggregation include the thermal conductivity, mass, and molecular diameter of the gas, and the background pressure. These different aspects may influence morphology of deposited nanoparticle films and should be considered in any explicit model of nanoparticle film growth. The ability to control film morphology provides an additional dimension to gas-phase condensation and enhances the product control of this method. Further work is needed to define a quantitative model to predict the morphology in a given system. Future work should focus on building a more quantitative model to increase the predictive power for deposited nanoparticle film morphology.

Chapter 6. Interaction of DMMP with Metal Oxide Nanoparticles

6.1 Introduction

6.1.1 Background

Chemical warfare agents are materials that are intentionally used to injure, incapacitate, or kill people. Chemical warfare agents (CWAs) have been a threat to the military since the modern period of chemical warfare began in World War I, and more recently to civilians with the specter of chemical attacks by terrorist organizations. While the history of chemical warfare stretches back to as early as 2000 BC,[161] the availability of technically skilled workers, the spread of chemical technology, and knowledge of chemical warfare agents has led to an era of unprecedented risk for military and civilian populations worldwide.

CWAs that are designed to affect humans include nerve agents, blood agents, asphyxiates (choking agents), and vesicants (blister agents). Nerve agents are the most toxic class of CWAs, and work by inhibiting the acetylcholinesterase enzyme. This inhibition leads to a buildup of acetylcholine near nerve cells in the body, strongly affecting skeletal muscles and the central nervous system. Sufficient exposure by inhalation or skin contact can result in cardio-respiratory arrest and death within minutes. Development of the nerve agents (refer to Figure 6.1) began in 1936 by Dr. Gerhart Schrader, a German chemist working with organophosphorus insecticides. The substance, tabun, became known as GA, for "German agent A" by the German army. In 1938, Schrader and co-workers, now working on CWAs, developed sarin (GB), which was found to be ten times more toxic on animals than GA.[161] Soman or GD, was discovered by another German researcher, Dr. Richard Kuhn in 1944. These agents, part of the G

class of nerve agents, were relatively unknown to the Allies until the end of World War II.

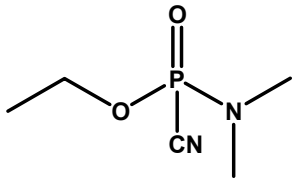

Ethyl N,N-dimethylphosphoro-amidocyanidate (Tabun, GA)

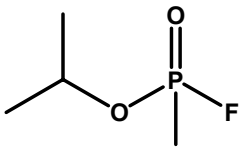

2-Propyl methylphophonofluoridate (Sarin, GB)

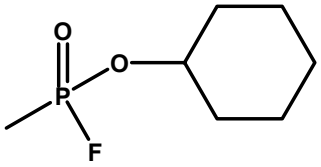

O-cyclohexyl-methylfluorophophonate (Cyclosarin, GF)

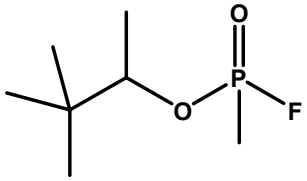

3,3-Dimethyl-2-butyl methyl phophonofluoridate (Soman, GD)

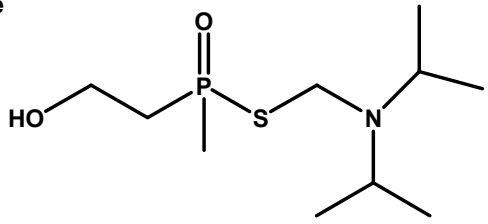

O-Ethyl S-2-(diisopropylamino)ethyl methylphophonothiolate (VX)

Figure 6.1 Common G and V-series nerve agents

Table 6.1 Chemical properties of nerve agents.[162,163]

Name	Molecular Weight	Melting Point (K)	Boiling Point (K)	Vapor Pressure (Torr)	Decomposition Temperature (K)
GA	162.1	223	493	0.037 (@ 293 K)	423
GB	140.1	217	431	2.1 (@ 293 K)	423
GD	182.2	231	471	0.4 (@ 298 K)	403
GF	180.2	261	512	0.07 (@ 298 K)	---
VX	267.4	222	571	0.0007 (@ 293 K)	423

Table 6.2 Toxicological data.[162,163] Dosage noted with a star are values for a 70 kg person with a 15 L/minute respiratory volume and a ten minute exposure.

Route	Exposure	Effect	Type	GA	GB	GD	GF	VX	Dosage
ocular/inhalation	vapor	miosis/rhinitis	EC_{50}	--	<2	<2	--	<0.09	mg-min/m^3
inhalation	vapor	incapacitation	IC_{50}	--	35	35	--	25	mg-min/m^3
inhalation	vapor	death	LC_{50}	2	1.2	0.9	0.5	0.3	mg/m^3 *
percutaneous	liquid	death	LD_{50}	1	1.7	0.35	0.35	0.01	mg *

Fueled by fears of possible Soviet chemical warfare, the United States and Britain continued development and testing of CWAs. In 1952, a British scientist working on pesticides discovered a new series of nerve agents that were even more deadly than the G agents. These compounds, named the V-series for venomous, were given to the Americans, who developed VX, the only significant nerve agent developed after the Second World War. Chemical properties and toxicity data are displayed in Tables 6.1 and 6.2, respectively.

Since the introduction of nerve agents, efforts have been made to develop methods and material for the detection, sorption, and decomposition of G and V-series compounds. The technology needed to effectively deal with this need requires improved insight into the uptake and reactivity mechanisms of CWAs, which can in turn lead to development of more effective strategies to deal with agents.

6.1.2 Solution Phase Decomposition of Nerve Agents

As opposed to the interaction of nerve agents with solid surfaces, the solution-phase chemistry of the agents has been studied extensively. GB, GD, and VX all undergo hydrolysis with water, particularly under basic (pH > 10) conditions. However, the solubility of VX significantly decreases with the increasing basicity of the water, ruling out base-catalyzed hydrolysis for this agent.[164] VX may be hydrolysed at the P-S bond after oxidation of the sulfur, which can be performed with excess exposure to aqueous NaOCl or $Ca(OCl)_2$.[165] In addition, solutions of peroxides with activators such as carbonate or bicarbonate have been found to effectively decontaminate VX and GB, even at temperatures as low as 243 K.[166] Finally, basic solutions containing NaOH and Na_2CO_3 have been found to decompose GD in soil matrices.[167]

These works provide some knowledge of methods to decompose CWAs with solution-phase materials. However, liquid-based decontamination is not a practical answer to the needs of the military or civilian responders to any chemical warfare event. First, decontamination solution is heavy and corrosive, which results in logistical barriers to fast response to a chemical event. For example, the U.S. Army's primary terrain decontamination system is the 5 ton, M12A1 truck.[168] Second, these methods are often not compatible with mission-critical military equipment such as computers, communications gear, sensors, and weapons. Finally, solution phase methods are not a proactive method for protection. These points have led to interest in solid materials that may be easier to deploy, do not destroy electronics, and can be incorporated into protective coatings for equipment or topical skin protectants.[169] Development of these solid materials requires understanding chemistry that occurs at the surface of solids instead of in bulk solutions.

6.1.3 CWA Simulants

High toxicity of CWAs is a major hinderance to any study on the uptake and reactivity of the agents with surfaces. In addition, the varied functionality of the nerve agents makes it difficult to isolate the role of each functional group in the overall chemistry of the molecules. For these reasons, CWA simulants are used by both the military and academic researchers. Simulants, shown in Figure 6.2, feature a reduced level of toxicity while also enabling the selection of specific chemical functionality to probe the chemical influences of each group. Simulant chemical properties are presented in Table 6.3.

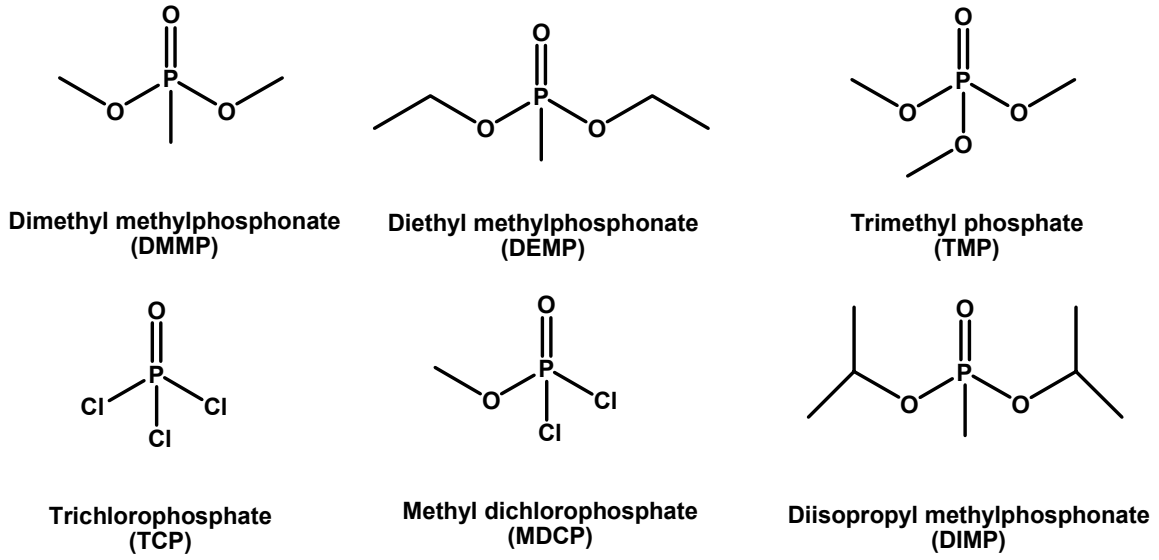

Figure 6.2 Examples of chemical warfare agent simulants

Table 6.3 Chemical properties of nerve agent simulants

Name	Molecular Weight	Melting Point (K)	Boiling Point (K)	Vapor Pressure (Torr)
DMMP	124.08	---	454	0.962
DEMP	152.13	---	467	5.2 (343 K)
TMP	140.08	227	470	---
TCP	153.33	274	378	---
MDCP	148.91	---	336	---
DIMP	180.18	298	---	0.277

6.1.4 Summary of CWA and CWA Simulant Chemistry on Metal Oxides

CWA chemistry on metal oxide surfaces has been studied by observing the surface chemistry of CWA simulants on a wide variety of metal oxide surfaces. Metal oxides demonstrate a superior ability to adsorb and decompose CWA simulants compared to pure metal surfaces.[170-172] This is often attributed to acidic sites on the metal oxide surface through which organophosphonate species can adsorb and subsequently undergo a hydrolysis reaction. Investigations involving the use of simulants to model the surface chemistry of CWAs on metal oxides has been validated by work with the actual agents.[173-176] A wide variety of metal oxide systems have been studied from clean, crystalline surfaces to high surface area nanomaterials. High surface area powders have

been found to offer superior adsorption capabilities, and nanomaterials show enhanced reactivity due to a higher degree of defect sites. Research has focused on several metal oxides, including WO_3,[177-179] TiO_2,[177,178,180-184] Al_2O_3,[177] Fe_2O_3,[185] and SiO_2.[185,186] In addition, the greatest body of work has been the study of CWA simulants on MgO materials.[1,177,187-190] A summary of published results is presented below, but a more detailed account by oxide is presented in the Appendix for reference.

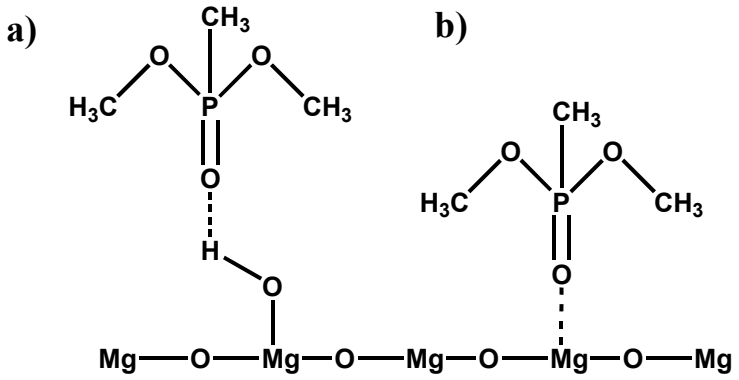

Figure 6.3 DMMP was found to interact with MgO in two ways: via H-bonding interactions to form species a, or through Lewis acid sites, resulting in species b.

Previous work has revealed significant insight into the interaction between organophosphorus CWAs and CWA simulants. DMMP, the most common organophosphonate simulant, has been heavily studied when adsorbed onto metal oxides. A summary of experiments with DMMP (and TMP) on metal oxides is presented in Table 6.4. As demonstrated in Figure 6.3, DMMP and its analogs readily adsorb through the phosphoryl oxygen onto most metal oxides at Lewis acid (metal atom) or at Brønsted base (hydroxyl) sites[1,190] with the exception of silicon oxide, where the interaction is via hydrogen bonding.[186,191] On metal oxides (excluding silica), organophosphates decompose via oxidation or hydrolysis on a surface. The resulting species is typically an O-P-O bridging species, along with either gas-phase methanol or a surface-bound

methoxy group as seen in Figure 6.4. The onset temperature of decomposition has varied in the literature, but room temperature decomposition has been observed for a few metal oxide materials. For DMMP, the O-CH_3 bond is preferentially attacked unless another mechanism is available such as on iron oxide and in photo-induced degradation.[184,185] While the role of water and hydroxyl groups is not completely understood, it is clear that these species are very important in determining the outcome of a CWA simulant–metal oxide encounter. In general, complete decomposition of organophosphates leaves a PO_x species on the surface, poisoning active sites from future reaction. Sample history (preparation conditions) plays a role in the reactivity of the metal oxides, a testament to the rich surface chemistry that can occur on these systems.

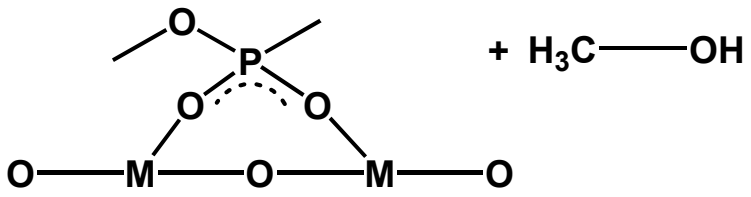

Figure 6.4 DMMP has been found to dissociate on metal oxide surfaces to form a O-P-O bridging species along with gas phase (or surface-bound) methanol.

Forays into nano-scale dimensions demonstrate the superior characteristics of ultra-fine oxide powders compared to their bulk analogs. At times, surface area is the dominant factor in sorbant performance, however enhanced reactivity can be seen with the increase in defect and coordinatively unsaturated sites that occur with decrease in particle dimensions.[192] One important finding is that loose and low density nanopowders can be pressed into a compact powder without loss of the critical surface area and while controlling pore sizes.[193] Further investigation is needed to clarify the mechanism of organophosphonate adsorption and decomposition on metal oxides. In addition, the

expansion of knowledge to more oxide systems coupled with exploration of nano-material properties will likely yield knowledge of these novel materials, which could help lead to the development of enhanced protection capabilities.

Table 6.4 Summary of studies on phosphonate CWAS interaction with metal oxides

CWA / Simulant	Oxide	Products/Observations	Conclusions
DMMP	MgO	O-P-O species @ higher T	Adsorbed through P=O, stiochiometric
DMMP	MgO	Increasing T reduces quantity adsorbed	Multiple adsorption interactions
DMMP	MgO	Little O-P-O species @ RT	Adsorption irreversible
DMMP	Fe_2O_3	Loss of methoxy at 170 K	Oxidize P-CH_3 @ 250 K. P species migrates to bulk at higher T
DMMP	Fe_2O_3	Decomposition	Both P-OCH_3 & P-CH_3 cleaves between 373 and 473 K
DMMP, TMP	WO_3	Phosphate residue above 573 K	Methoxy and methyl groups cleaved at 473 and 573 K, respectively
DMMP, TMP	WO_3	No RT reaction	Adsorbed through P=O group, degree of hydroxylation/hydration important in interaction
DMMP	TiO_2	Hydrolysis > 214 K to form O-P-O bridging species	Adsorption to Lewis acid sites and hydroxyl groups
DMMP	TiO_2	O-P-O bridging species	Methoxy groups lost above 473 K
DMMP	TiO_2	O-P-O bridging species, PO_4^{3-} residue remains after complete reaction	Under UV light, oxidation of both methyl and methoxy groups occur at 200 K
DMMP	TiO_2	MeOH with water	Sorption increases with humidity
DMMP	TiO_2 (110)	O-P-O species @ 500 K	Adsorbed DMMP dominant @ RT, PO_x remained at 1000 K
DMMP	Al_2O_3	O-P-O species & methoxy	Dissociation at 295 K
DMMP	Al_2O_3	O-P-O species	Dissociation at 473 K
DMMP	MgO, La_2O_3	O-P-O species @ 373 K	Second methoxy cleaves @ 673 K
DMMP	Al_2O_3	373-673 K: CO, CH_4, CO_2 bulk phosphonates	More than one C per DMMP released @ 673 K
DMMP	Si_2O_3	DMMP molecularly adsorbed	Desorbtion temperature greater with hydration. Slight reactivity with heavy hydration
DMMP	Si_2O_3	DMMP desorbs by 573 K	No reaction

6.1.5 Introduction to Present Work

Investigation into metal oxide nanoparticle sorption of DMMP began as a screening of a series of materials. After initial survey DMMP exposure experiments, yttrium oxide was chosen for a more detailed study to investigate metal-oxide interaction with the simulant. Y_2O_3 is an insulating material that can host optically active dopants[194] and stabilize ZrO_2 for use in catalytic and ceramic materials.[195] Although the literature is extensive for these applications, the reactive and catalytic properties of yttria have received less attention.[196,197] Yttrium oxide is known to have a large number of basic surface sites[197,198] that could result in similar adsorption and reactive properties to other commonly studied basic metal-oxides such as MgO.

Our approach to investigating the sorption and reactive properties of chemical warfare agent simulants on novel metal-oxide nanoparticle systems combines laser-heated, gas-phase condensation of nanoparticles with ultra-high vacuum (UHV) analysis techniques. By coupling the synthetic method with UHV techniques, one can synthesize particles of various size and transfer them from the synthesis chamber into a clean environment without exposure to air. While some contamination persists when synthesizing nanoparticles under vacuum conditions, experiments show that saturation of active adsorption sites does not occur (see Section 6.4.3), eliminating the requirement for thermal pretreatment and associated concern about changes to the metal-oxide film that thermal pretreatment may cause, such as annealing of defect sites.

6.2 Experimental Details: DMMP Adsorption Study

6.2.1 Materials

Absolute ethanol was obtained from Aaper Alcohol. Dimethyl methylphosphonate (97%), trimethyl phosphate (99%), methyl phosphonic dichloride (98%), anhydrous ethyl ether (99%), pyridine (99%), Al_2O_3 (99%), Y_2O_3 (99.99%), MgO (99%), Eu_2O_3 (99.9%), Er_2O_3 (99.9%), and Tb_4O_7 (99.9%), and 16-mercapto-1-hexadecanoic acid (90%) were obtained from Aldrich. Pressed HfO_2 (99.9%) and ZrO_2 (99.7%) pellets were acquired from Cerac Incorporated. Gd_2O_3 (99.9%) was obtained from Alfa Aesar. The sample of FeO_x was provided by the geology department and used as received. Silver nitrate (99%) was purchased from Sigma. HPLC grade methanol was acquired from EMD. Deuterium oxide (99.9%) and methanol-d_4 (98%) were purchased from Cambridge Isotope Laboratories, Inc.

Synthesis of dimethyl methylphosphonate-d_6 (DDMMP) was performed following a procedure published by Templeton and Weinberg.[199] 6 mL of dry pyridine was added to a solution of 5 g methylphosphonic dichloride in 15 mL anhydrous ethyl ether in a round bottom flask under a nitrogen atmosphere. 5 g of methanol-d_4 was added dropwise, and the solution was left to stir overnight. The product was filtered to remove pyridine salt and washed with anhydrous ethyl ether to yield a tan oil that was then vacuum distilled. Purity was confirmed by ^{1}H-NMR and infrared spectroscopy of the neat oil. For the UHV experiments, TMP, DMMP, and DDMMP were purified by vacuum distillation to remove volatiles followed by standard freeze-pump-thaw (3 cycles) to degas samples prior to use. All other chemicals were used as received.

6.2.2 Preparation of Nanoparticle Films for UHV Studies

Gold substrates were obtained from Evaporated Metal Films. These were prepared by evaporating a 50 Å chromium adhesion layer followed by a 1000 Å gold layer on a 1 cm x 1 cm x 1 mm silica surface. Substrates were cleaned in a 30%/70% mixture of H_2O_2 (30%)/H_2SO_4 (concentrated) at room temperature for 1 hour, followed by copious rinsing in 18 MΩ deionized water (Millipore Purification Systems), and absolute ethanol. Substrates are then dried under a stream of ultra-pure N_2, mounted onto the substrate holder, and placed into the ultra-pure N_2 purged vacuum chamber.

Yttrium oxide pellets were prepared as previously discussed and transferred directly from the sintering oven to the pellet platform in the chamber. The chamber was then pumped down with liquid nitrogen-cooled sorption pumps, followed by evacuation with an ion pump. Pumping continued until base pressure was achieved in the evaporation chamber at 5 x 10^{-7} Torr (typically 1 hr). The evaporation chamber was isolated from pumps and carefully backfilled to the desired pressure, followed by vaporization for four minutes. Immediately after vaporization, the chamber was again pumped by a sorption pump until the pressure was sufficiently low to open to the load-lock chamber (about three minutes). The sample mount was then transferred to the load-lock arm with care to prevent leaks through the differentially pumped transfer arm. After transfer, the load lock chamber was isolated from the vaporization chamber and then evacuated to a pressure low enough for transfer into the UHV chamber to (2 x 10^{-7} Torr). After this pressure was reached, the sample was carefully transferred to the mount inside of the UHV chamber. The entire transfer process typically was completed within 6-15 minutes after vaporization ended. All reflection-absorption infrared (RAIR) spectra were

the average of 256 scans from 4000 to 800 cm^{-1} with a 2.5 mm aperture and 2 cm^{-1} resolution.

6.2.3 Preparation of Cu^{2+}-COO^- - terminated Self Assembled Monolayer

SAMs terminated with a copper ion complex were synthesized following literature procedures.[200] A freshly cleaned gold-coated substrate was placed in a 1 mM ethanolic solution of 16-mercapto-1-hexadecanoic acid for 18 hours. The acid-terminated SAM was then copiously rinsed with absolute ethanol and placed in a 100 mM ethanolic copper sulfate solution for 1 hour. Following an absolute ethanol rinse, the SAM was mounted and introduced into the UHV chamber for DMMP adsorption experiments.

6.3 Survey Study Summary

A survey study was performed to identify candidate oxide materials for the more detailed UHV study. Discussion of the experimental parameters, RAIR spectra, results, and conclusions are presented in Appendix B. In general, all of the nanoparticle samples were found to readily adsorb DMMP molecules from the vapor phase. Figure 6.5 shows the difference RAIR spectra of metal oxide nanoparticles shortly after exposure to DMMP, demonstrating that the simulant adsorbed readily on all of the tested metal-oxide nanoparticles under ambient conditions.

RAIRS confirmed that most of the DMMP remains adsorbed to the particles over the 1-10 day time period investigated. In the RAIR spectra, the P=O mode of DMMP red-shifts substantially from the gas-phase value of 1275 cm^{-1} upon adsorption while other modes are only slightly perturbed by the sorption (see Table 6.5). This shift indicates that the interaction of DMMP with these metal-oxides is predominantly through the P=O moiety of DMMP and not the methyl or methoxy groups. Perturbation of surface

hydroxyl groups is observed in all of the samples by virtue of the loss of intensity in the 3700 cm^{-1} region associated with isolated hydroxyl groups. Several samples show evidence for DMMP decomposition after the exposed nanoparticles were left in an ambient environment for several days, however experimental conditions (such as background problems) precluded analysis of some samples at extended times. A more detailed discussion of results and the RAIR spectra has been included in Appendix B for reference.

Table 6.5 Location of the P=O stretching modes observed for DMMP adsorbed to different metal oxide nanoparticle samples under ambient conditions. The value of the redshift of this mode compared to its value for gas-phase DMMP is listed, along with some literature values.

	ν (P=O) (cm^{-1})	Δ (cm^{-1})	Literature
DMMP Gas	1276	-	
Al_2O_3	1220	56	1217[199]
Eu_2O_3	1215	61	
Fe_2O_3	1205	71	1208[1]
Er_2O_3	1222	54	
MgO	1237, 1188	39, 88	1238, 1184, 1190[1,201]
Y_2O_3	1212	64	
$Tb:Y_2O_3$	1217	59	
Gd_2O_3	1225	51	
ZrO_2	1212	64	
HfO_2	1212	64	

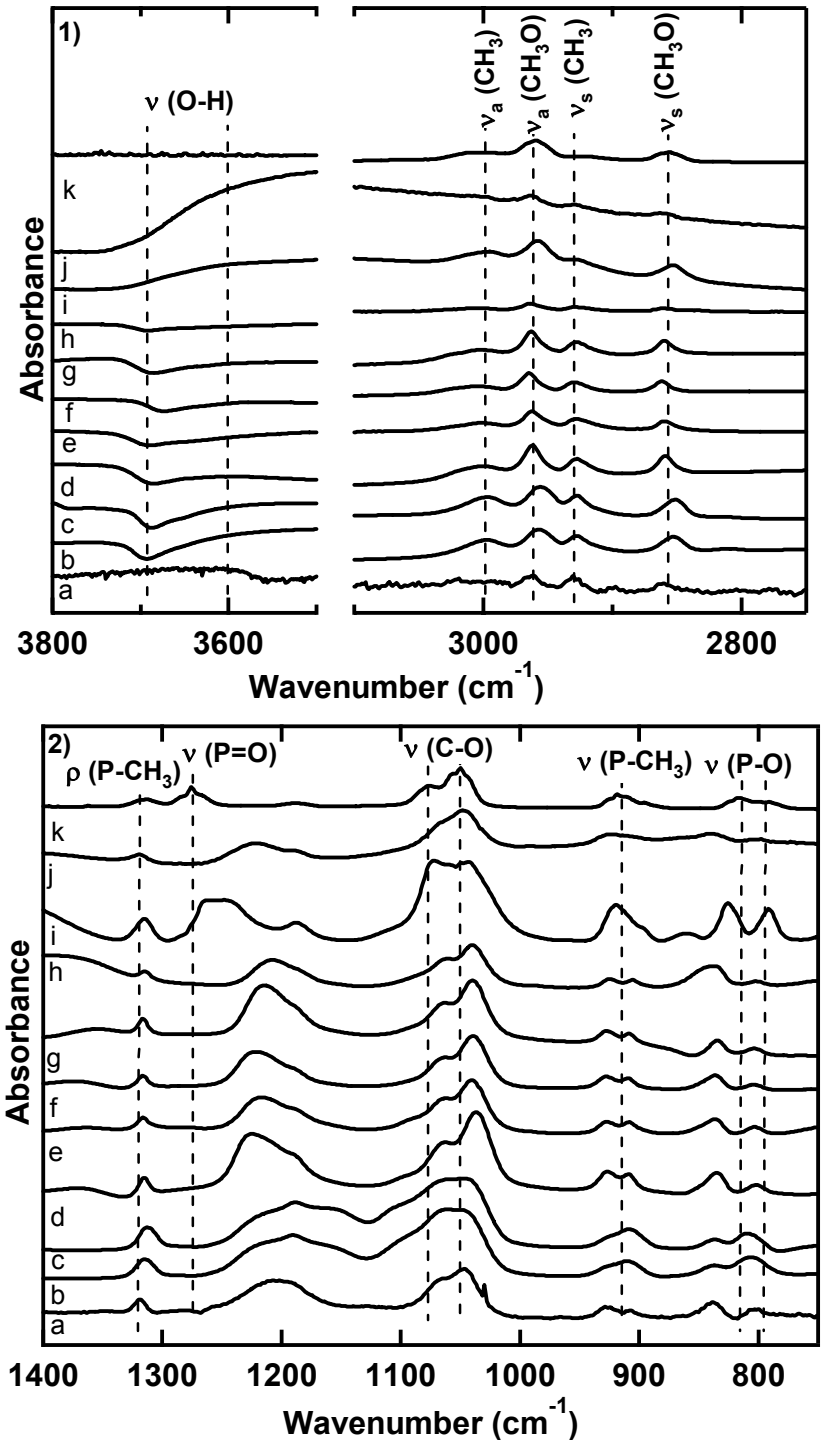

Figure 6.5 Difference RAIR spectra showing the 1) high wavenumber and 2) low wavenumber region for a series of metal-oxides shortly after saturation exposures to DMMP. Scaling of spectra is arbitrary. Oxides: a) Fe_2O_3, b) HfO_2, c) ZrO_2, d) Gd_2O_3, e) 10% Tb:Y_2O_3, f) Er_2O_3, g) Eu_2O_3, h) Y_2O_3, i) MgO, j) Al_2O_3, k) gas-phase DMMP.

6.4 Characterization of HV-synthesized NPs

6.4.1 RAIRS Characterization: UHV study

Nanoparticle films are inspected by RAIR spectroscopy and XPS to determine the purity of the samples under investigation. Pure yttria is transparent in the 4000 – 800 cm^{-1} region,[202] so all of the features observed in the RAIR spectrum are due to surface contaminants. Figure 6.6 displays the RAIR spectrum of freshly made Y_2O_3 nanoparticles, which indicates that a significant amount of background CO_2 and some H_2O are adsorbed during synthesis and transfer of the sample into the UHV environment.

High reactivity of CO_2 with Y_2O_3 is consistent with a high number of basic surface sites on these particles.[203] In the RAIR spectrum of clean Y_2O_3, two sharp peaks at 3708 and 3676 cm^{-1} can be assigned to the O-H stretches for monodentate and multidentate isolated surface hydroxyl groups due to dissociation of H_2O on the surface and a broad band centered at 3200 cm^{-1} is due to the O-H stretch of associated (hydrogen-bonded) hydroxyl groups. Two broad and intense peaks at 1562 and 1343 cm^{-1} are assigned to the asymmetric and symmetric C-O stretches of surface carbonate groups. This assignment was confirmed by RAIR spectroscopy studies of Y_2O_3 nanoparticle exposure to CO_2 (see Appendix C.1) and is supported by the fact that Y_2O_3 is known to form surface carbonate groups upon exposure to atmospheric CO_2.[197,204] The intensity of the RAIR carbonate peaks often decreased slightly under UHV conditions, probably due to desorption of weakly bound or physisorbed species.

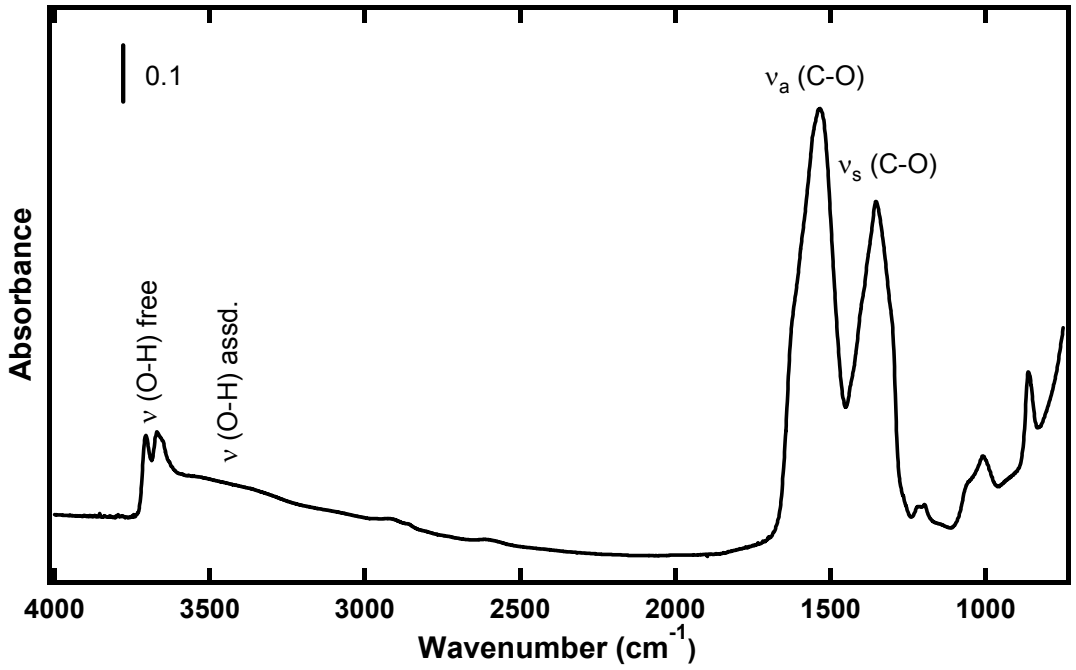

Figure 6.6 Direct RAIR spectrum of freshly prepared 5.8 nm Y_2O_3 nanoparticles synthesized under 10 Torr N_2.

6.4.2 XPS Characterization

XPS was also used to characterize the clean nanoparticle surfaces prior to DMMP exposure as shown in Figure 6.7. The Y($3d_{5/2}$) peak at 157.3 eV matches the literature values of 156.8 eV[205] and 157.1 eV[206] for Y_2O_3 while the O(1s) region features two overlapping peaks at 529.3 eV and 530.5 eV that correlate well with literature peak values of 529.4 eV for Y_2O_3 eV[198,206] and 530.3 eV for $Y_2(CO_3)_3 \cdot 3H_2O$.[207] The higher binding energy O(1s) component likely includes oxygen from surface hydroxyl groups, which would be expected to show a peak at 531.0 eV.[206] This assignment is supported by the reduction of intensity of the high binding energy side of the O(1s) peak after heating nanoparticles to 773 K in vacuum. The C(1s) region shows a peak at a binding energy of 290.5 eV, which is too high for a hydrocarbon, but is near the literature value of 288.2 eV for $Y_2(CO_3)_3 \cdot 3H_2O$[207] and would correlate with the RAIRS assignment of carbonate

groups on the nanoparticle surface. However, this peak in the C(1s) region is located at the right binding energy and has the correct intensity to be assigned to a satellite peak of the Y($3p_{3/2}$) signal. Satellite peaks are due to non-monochromatic X-ray radiation and manifest themselves at known positions and intensities relative to the main peak. The α_3 and the α_4 satellite peaks for a magnesium source would develop at binding energies of 8.4 and 10.1 eV lower than the main peak with intensities of 8 and 4.1%, respectively.[208] The peak at 290.5 eV is approximately 8.9 eV lower in binding energy than the Y($3p_{3/2}$) peak at 299.4 eV and has a relative intensity of 10% to the main peak. However, Y_2O_3 particles prepared in nitrogen but exposed to CO_2 gas prior to analysis show an increase in the relative intensity of the peak at 290.5 to 17% while the higher binding energy component of the O(1s) peak becomes more dominant. These results support the interpretation that the 290.5 eV peak is primarily due to a combination of the α_3 and α_4 satellite peaks of the Y($3p_{3/2}$) photoelectron band in addition to a small component of C(1s) signal from surface carbonate groups. Quantitative analysis of several samples of Y_2O_3 nanoparticles prepared under nitrogen indicate that the clean particles contain ~ 63% oxygen, ~ 37% yttrium, and < 1 % carbon. Stoichiometric yttria would be anticipated to have 60% oxygen and 40% yttrium, therefore the excess oxygen is attributed to hydroxyl and trace amounts of carbonate species.

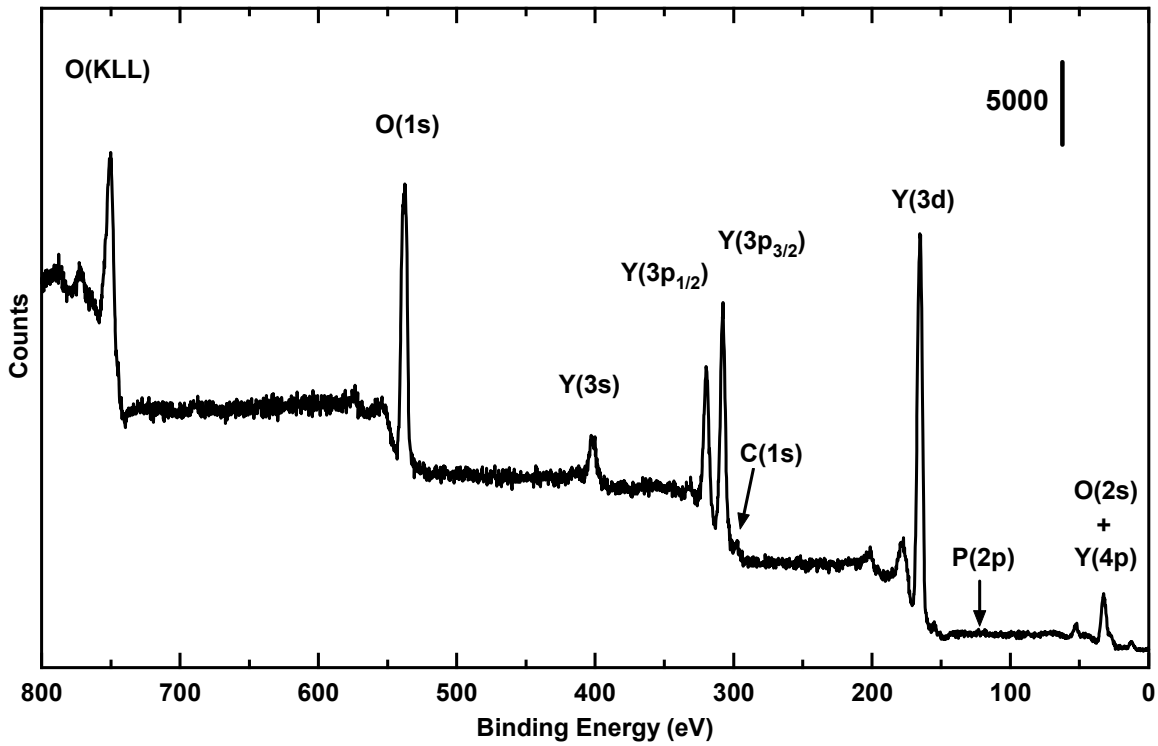

Figure 6.7 X-ray photoelectron spectrum of freshly prepare Y_2O_3 nanoparticles after correction for satellite peaks. Major photoelectron peaks are labeled. Regions for the C1s and P2p signals are labeled with arrows.

6.5 DMMP Adsorption Experiments

6.5.1 Room-Temperature Exposure

Upon completion of the characterization experiments above, enough information about the yttria nanoparticle samples was known to perform DMMP exposures and monitor the results with RAIRS and XPS. Initial studies used as-prepared particle films that were deposited on Au-coated substrates and transferred into the UHV chamber. Analysis by XPS confirmed the existence of the nanoparticles on the surface and was used to check for any elemental contamination. Samples were characterized by RAIRS and then exposed to the DMMP simulant. Figure 6.8 shows a RAIRS difference spectrum of 5.8 nm particles synthesized under 10 Torr of nitrogen after exposure to DMMP. The

gas phase spectrum of DMMP obtained in our lab is given for reference. Significant changes in the infrared absorption demonstrate that the surface of the particles are chemically altered upon exposure to DMMP. Analysis of this data also indicates that DMMP decomposed on the surface of these nanoparticles at room temperature.

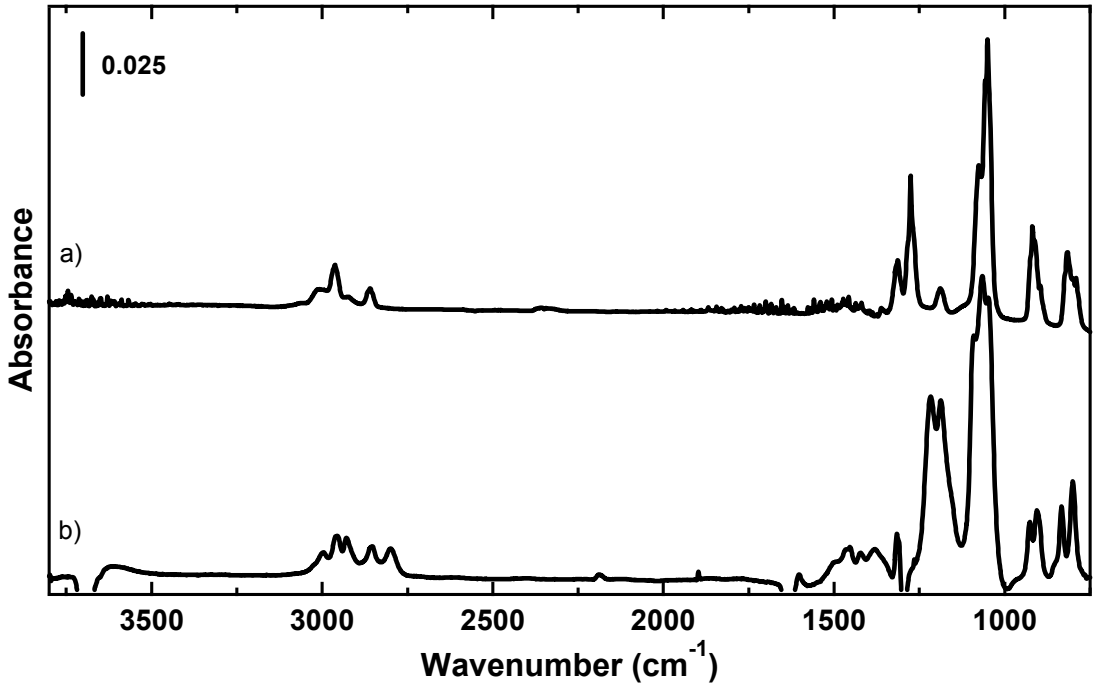

Figure 6.8 RAIR spectra of a) gas-phase DMMP and b) difference spectra of 5.8-nm Y_2O_3 nanoparticles exposed to DMMP.

6.5.2 Peak Assignments

RAIR spectra of the adsorbates in this study give substantial insight into the interaction of DMMP with Y_2O_3 nanoparticle films at room temperature. All peak assignments are made with the aid of a series of absorption experiments that are discussed in Appendix C. As seen in Figure 6.9, DMMP adsorption perturbs the O-H stretching region by causing a loss of the monodentate and multidentate free O-H modes for at 3705 and 3676 cm^{-1} while a broad associated O-H stretching peak grows in at 3200 cm^{-1}, indicating that there could be some hydrogen-bonding interaction between surface

hydroxyl groups and adsorbed DMMP. Degree of hydroxylation and the presence of water has been determined to be important in the reactivity of some metal-oxide surfaces,[190] so it is also possible that a portion of the reactivity of this system is due to hydrolysis of DMMP on the surface.[189,201,209]

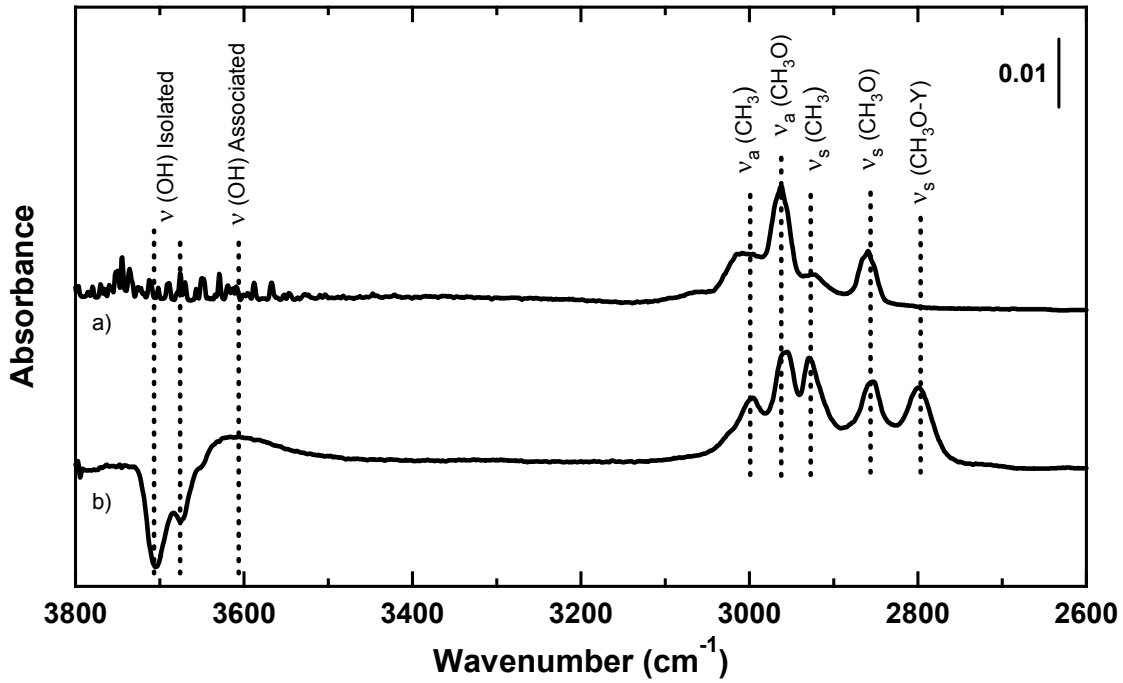

Figure 6.9 High wavenumber region RAIR spectra of a) gas phase DMMP and b) difference spectra of DMMP adsorbed onto 5.8 nm Y_2O_3 nanoparticles. Assignment for the ν_a (CH_3O-Y) stretch at ~ 2927 cm^{-1} is absent for clarity.

The (PCH_3) and (OCH_3) C-H stretches of adsorbed DMMP on Y_2O_3 nanoparticles matches that of other metal-oxides[1,184] and are only slightly shifted from the gas-phase DMMP values. Absence of a significant shift indicates that DMMP does not strongly interact with the nanoparticles through the methyl or methoxy portions of the molecule. This is consistent with most metal-oxides with the exception of silicon oxide, where hydrogen bonding between surface hydroxyls and methoxy groups is observed.[172,186,191,210] A symmetric C-H stretch for a (CH_3O-M) species that appears at

2795 cm^{-1} has been observed on La_2O_3[1] and TiO_2[184] at room temperature and cannot be attributed to intact DMMP, indicating a reaction occurs on the surface.

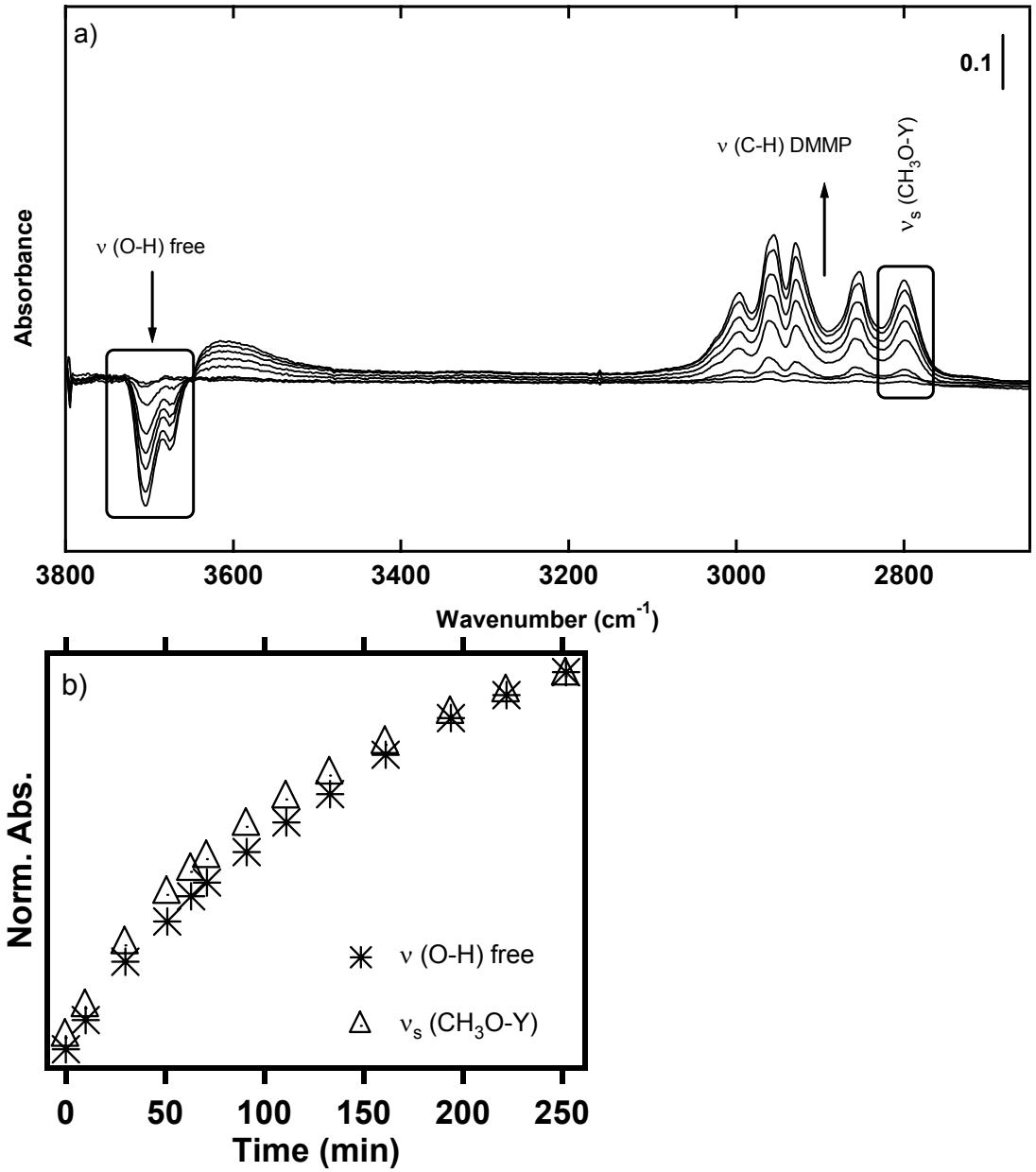

Figure 6.10 a) Sequential RAIR spectra of Y_2O_3 particles being exposed to DMMP. b) Plot of normalized absolute integrated intensities for the free ν(O-H) stretches and $\nu_s(CH_3)O$-Y stretch versus time.

Insight into the importance of surface hydroxyl groups into the adsorption of DMMP may be gained by comparing the relative intensity loss for isolated hydroxyl

groups with the intensity gain for a given DMMP vibrational mode. Figure 6.10 a) demonstrates the change in the O-H stretching region as DMMP is adsorbed onto nanoparticles. By plotting the absolute integrated intensities of the symmetric surface-bound methoxy C-H and isolated O-H stretches as shown in Figure 6.10 b), it can be seen that change in the amount of reacted DMMP is associated with the loss of the free hydroxyl groups. It is therefore possible that hydroxyl groups play a significant role in the reaction of DMMP on the nanoparticles in addition to adsorption.

In the lower frequency region of the spectrum (Figure 6.11), the C-O stretches are not strongly shifted, but the P=O mode seen at 1214 cm^{-1} is strongly shifted from the gas-phase value of 1275 cm^{-1} and is similar to the value reported on Al_2O_3.[1] This strong shift of the P=O stretch coupled with the lack of a shift for the methyl and methoxy C-H modes indicates that DMMP interacts with the Y_2O_3 surface through the (P=O) moiety and not through methyl or methoxy moieties.

Although the gas-phase DMMP spectrum shows a weak signal at 1190 cm^{-1} that corresponds to the O-CH_3 rocking mode, the high intensity of the 1187 cm^{-1} peak of DMMP adsorbed to Y_2O_3 is contrary to this mode being solely responsible for the 1187 cm^{-1} signal. As shown in the experimental evidence below, the 1092 cm^{-1} peak clearly is not due to intact DMMP on the surface. This datum, in addition to the evidence of P-OCH_3 bond cleavage with the 2795 cm^{-1} surface-bound methoxy stretch, supports assignment of 1187 and 1092 cm^{-1} signals to the symmetric and asymmetric modes of a bridging O-P-O species as shown in Figure 6.12. Several authors in the literature have reported spectroscopic evidence for the existence of this bridging species on a variety of metal-oxides at different temperatures.[1,201,211] Kuiper and co-workers have reported a 90-

100 cm^{-1} difference between the asymmetric and symmetric stretches for bridging O-P-O species on a surface,[212] which correlates well with the 95 cm^{-1} difference between those assigned peaks on this system. Evidence reported here indicates that some adsorbed DMMP exists on yttria nanoparticles at room temperature, as well as a bridging O-P-O species (see Figure 6.12) along with a surface bound methoxy group that are products of dissociation.

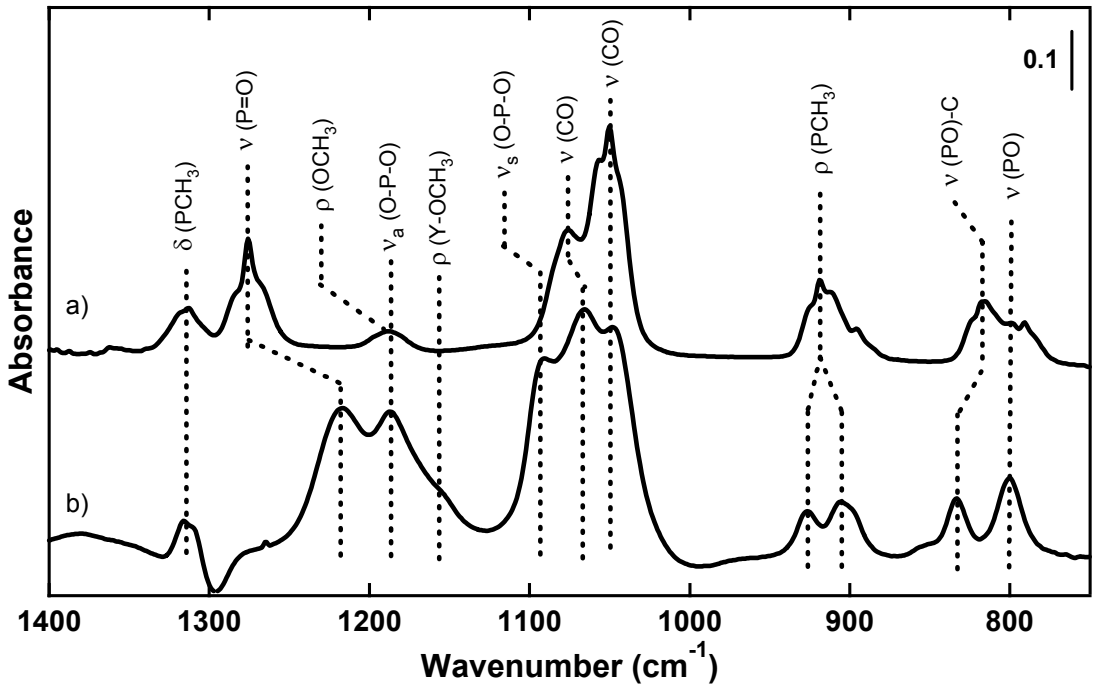

Figure 6.11 Low wavenumber region RAIR spectra of a) gas phase DMMP and b) difference spectra of DMMP adsorbed onto 5.8 nm Y_2O_3 nanoparticles.

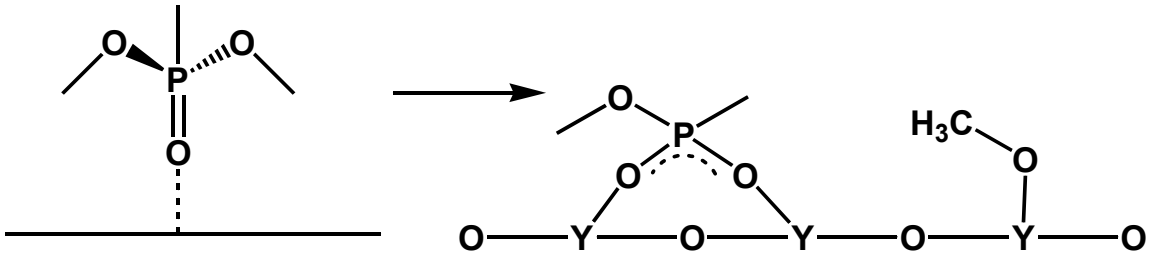

Figure 6.12 DMMP initially interacts with the yttria surface through the phosphoryl oxygen and a substantial amount will dissociate to form the bridging species along with a surface bound methoxy group seen on the right.

6.5.3 Changes with Exposure Time

Inspection of time-resolved RAIR spectra during DMMP exposure to Y_2O_3 also supports the above assignments. Close observation of changes in the C-H stretching region reveals that asymmetric and symmetric ($OC-H_3$) stretching modes are each composed of two pairs of signals at ~ 2961, 2952, and 2859, 2852 cm^{-1} respectively. The higher wavenumber component of these modes is assigned to intact adsorbed DMMP on the Y_2O_3 surface, while the lower wavenumber component is assigned to partially decomposed DMMP on the surface. As exposure increases, the peak wavenumber value shifts towards the lower energy component of the mode. Changes with exposure time are also observable in the low wavenumber region. The O-P-O decomposition product peak at 1187 cm^{-1} increases relative to the undissociated P=O signal at 1216 cm^{-1}. As this occurs, the relative intensity of the O-P-O mode at 1092 cm^{-1} also increases when compared to the C-O stretches as seen in Figure 6.13. The intensity of the $P-CH_3$ rocking mode at 898 cm^{-1} also increases relative to the 914 cm^{-1} $P-CH_3$ rock, while the 800 cm^{-1} P-O stretch increases in intensity relative to the 833 cm^{-1} (P-O)C stretch, suggesting that the 898 and 800 cm^{-1} peaks are better attributed to the dissociated DMMP product. In addition, RAIRS data shows that a small proportion of the adsorbed DMMP dissociates after termination of dosing. This is consistent with a fast initial dissociation followed by a slower dissociation step, which is also observed with VX on nano-sized CaO and MgO and could be explained by diffusion of species on the surface.[173,174]

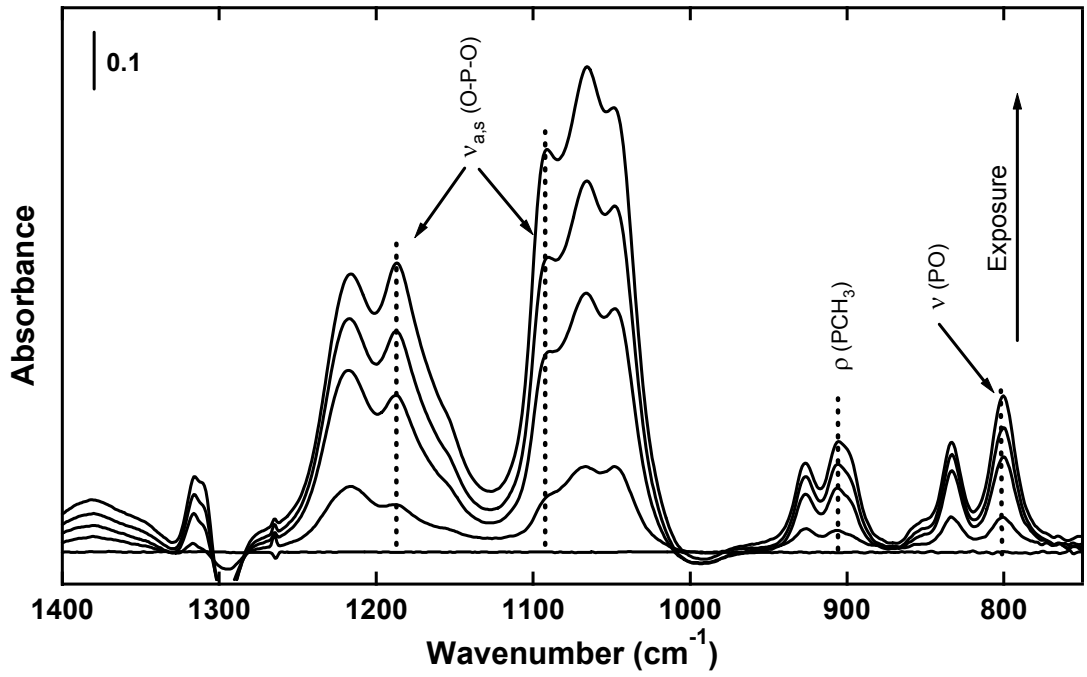

Figure 6.13 Difference RAIR spectra of 5.8 nm Y_2O_3 particles at different exposure times. Approximate exposures are (from bottom to top) 0, 30, 100, 150, and 200 L. Note the relative intensity increase of labeled peaks that are associated with the dissociated DMMP species.

Adsorption isotherms for Y_2O_3 nanoparticles exposed to DMMP as followed by infrared mode peak intensities are shown in Figure 6.14. These graphs show data collected under a constant flux of DMMP molecules. The solid lines are fits to a Langmuir adsorption isotherm:[213]

$$I_t = I_0[1 - e^{(-at)}] \qquad \textbf{Eq. (6.1)}$$

where I_t and I_0 are the infrared absorption intensities at times t and 0, respectively, and

$$a = \left[\frac{1}{4}\bar{\nu} S_0 C_D\right] / L \qquad \textbf{Eq. (6.2)}$$

where $\bar{\nu}$ is the mean molecular velocity (cm/s), S_0 is the sticking probability at time 0, C_D is the concentration of DMMP above the sample (molecules/cm^3) and L is the density of adsorption sites on the nanoparticles (sites/cm^2). C_D (4.6×10^{12} molecules/cm^3) was calculated using the measured partial pressure of DMMP while L (3.0×10^{18}

sites/cm^2) was estimated from the measured BET surface area, the mass of Y_2O_3 in the sample as measured via ICP-ES, and the crystallographic parameters of Y_2O_3. These Langmuir adsorption models fit the data reasonably well and indicate that the particle films are nearing the saturation point of DMMP at the end of the experiments. From the model fits, the initial sticking probability can be reasonably estimated to be 0.7 - 1 given the uncertainty in the model parameters.

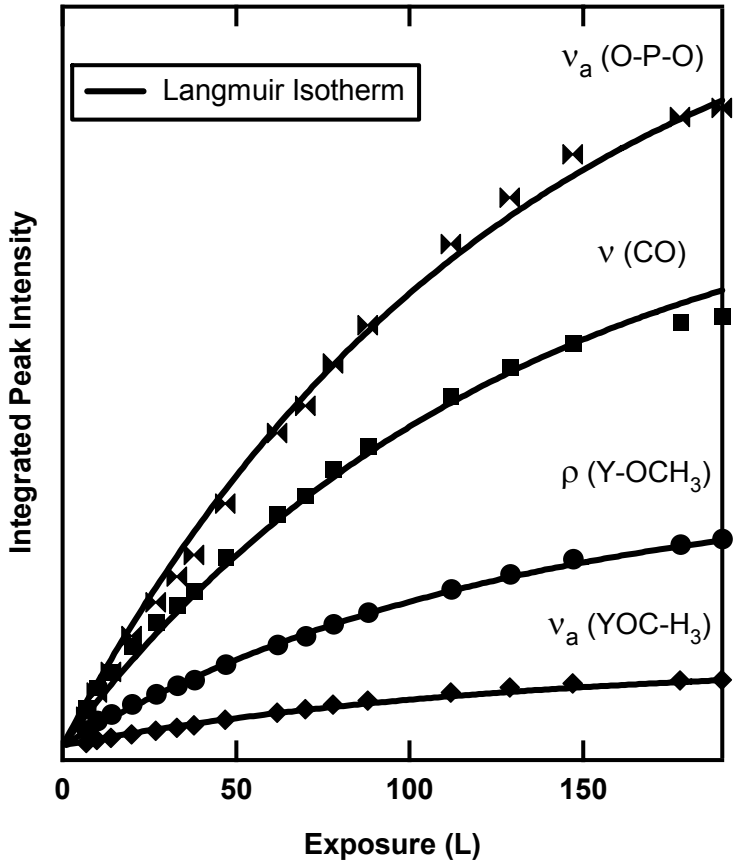

Figure 6.15 Integrated intensities for selected vibrational modes (points) plotted with the fitted Langmuir adsorption isotherms (lines).

6.5.4 Changes After Exposure

Further confirmation of peak assignments may be gained by observing changes in the RAIR spectrum of exposed nanoparticles after exposure is complete. As the time-

resolved spectral differences indicate, reaction of adsorbed DMMP continues to some degree with time. After exposures of ~ 200 Langmuir over several hours, the reaction rate is slow, but great enough to be observed with RAIRS. Figure 6.15 shows the difference RAIR spectrum of exposed 5.8 nm Y_2O_3 nanoparticles 30 minutes after dosing stopped. The background for this spectrum was taken shortly after DMMP dosing was terminated. Mass spectrometer readings indicate that there are detectable levels of DMMP in the chamber, however the partial pressure of DMMP is relatively low (< 1x 10^{-9} Torr). Combining this low partial pressure and the low sticking probability due to many of the available sites already being taken, no significant DMMP adsorption is expected to occur even at these relatively long times. This is confirmed by the RAIRS data that show no evidence for adsorption of new DMMP molecules.

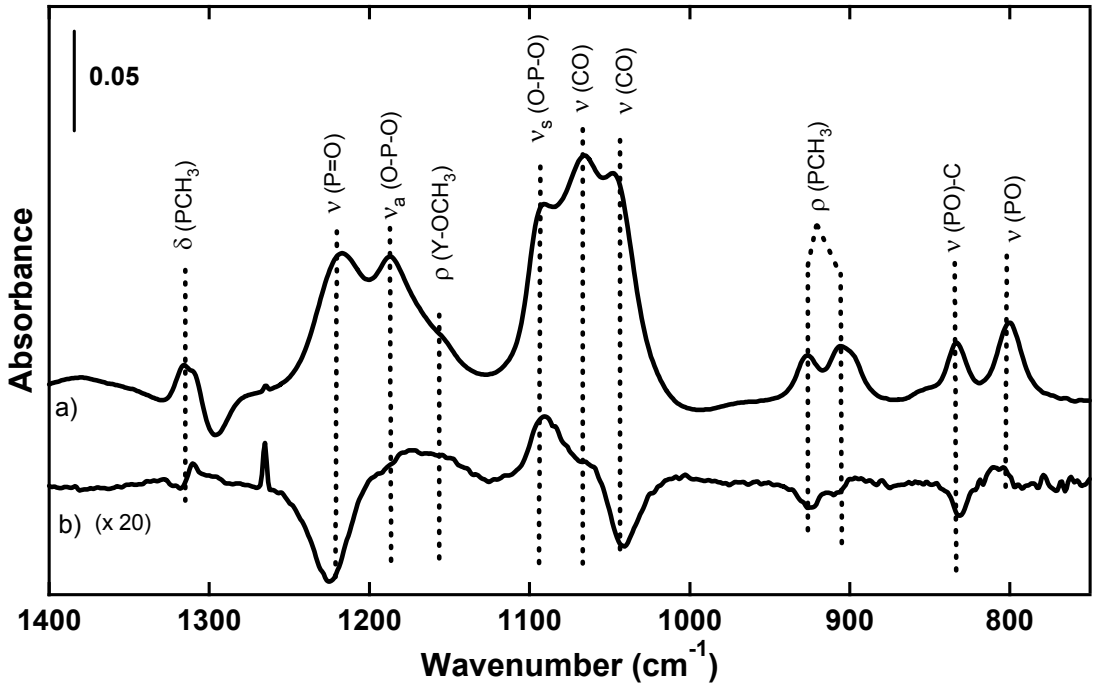

Figure 6.15 RAIR spectra of 5.8 nm Y_2O_3 nanoparticles a) exposed to DMMP and b) difference RAIR spectra of same sample showing changes 10 minutes after dosing was halted.

In the C-H stretching region (not shown), two major changes are visible. The first is "S-shaped" features centered on the symmetric and asymmetric ($OC-H_3$) stretches at 2958 and 2856 cm^{-1}. Negative intensity on the high wavenumber side and positive intensity on the low wavenumber side indicate that these features are due to a red-shift of these modes. This is consistent with the red shift observed in the modes during dosing and these features are attributed to red-shifting of the ($OC-H_3$) stretches upon reaction of the DMMP to form the bridging species. A slight increase in intensity is observed at 2936 cm^{-1} where the asymmetric C-H surface-bound methoxyl stretch is located while the symmetric mode of the bound methoxy at 2802 cm^{-1} clearly grows in intensity. A very subtle loss of free O-H groups is observed at 3706 and 3654 cm^{-1}, but the changes here are not clearly defined above the noise level.

The low wavenumber region of the spectrum also shows changes occurring post DMMP exposure. Another "S-shaped" feature indicative of a red-shifting of the ($P-CH_3$) deformation is observed centered at 1314 cm^{-1}, while a simultaneous loss of intensity is observed at the higher wavenumber $P-CH_3$ rock at 923 cm^{-1}, concurrent with a small increase in the $P-CH_3$ rocking mode at 898 cm^{-1}. The most dramatic change in the post-exposed difference spectra is the strong negative peak at 1220 cm^{-1} while a small increase is noted at 1159 cm^{-1}, indicating loss of P=O species with growth of O-P-O stretches on the surface at 1175 and 1092 cm^{-1}. The large loss of intensity at the P=O feature washes out the high wavenumber side of the asymmetric O-P-O stretch, leading to the appearance of a red-shifted peak. In addition to these changes, the (PO)-C mode at 833 cm^{-1} is depleted while the (PO_2) mode at 800 cm^{-1} increases in intensity. Finally, the (C-

O) stretching peak shows a sharp reduction on the red-shifted side of this multimode peak at 1049 cm^{-1}.

These changes that occur after dosing DMMP onto the surface prove to be valuable in confirmation of peak assignments shown in Table 6.6. Since there is no detectable desorption (or adsorption) of DMMP molecules to the surface, these changes are due to the continuing reaction of the adsorbed DMMP to form the assigned bridging O-P-O species. These results help the refinement of peak assignments, so the (C-O) stretch at ~1050 cm^{-1} can be assigned to intact DMMP, as can the (P-CH_3) rock and (PO)-C stretching modes at 926 and 833 cm^{-1}. Red-shifting of the O(C-H_3) stretching and P-CH_3 deformation modes are also identified. These changes again underscore the observation that there is likely diffusion of species on the nanoparticle surfaces.

6.5.5 Post Exposure XPS Results

Figure 6.16 shows XPS data for the Y_2O_3 nanoparticles after exposure to DMMP at room temperature. There is negligible change in the O(1s) and Y($3d_{5/2}$) peaks due to the high number of Y and O atoms in the sample, however, a second peak appears in the C(1s) region at 286.0 eV, and a P(2p) peak is observed at 133.5 eV that are attributed to adsorbed DMMP. Assignments here agree with reported values of 287.7 eV and 286.3 eV for C(1s) and 134.9 eV for P(2p), for DMMP adsorbed on TiO_2 at room temperature.[181] Using published sensitivity factors, the integrated intensity of the P(2p) signal was used to estimate the amount of DMMP found on the surface. Phosphorus signal was chosen for the lack of interfering satellite peaks as is seen in the C(1s) region as well as the higher sensitivity factor for the P(2p) photoelectrons as opposed to the C(1s) photoelectrons. After exposure experiments, phosphorus was estimated to account for two to seven

atomic percent of the sample, corresponding to DMMP coverages of up to one molecule for every six Y atoms in the sample. These atomic percent numbers are not expected to represent saturation coverages of DMMP, but should be treated as approximations of the value of adsorbed DMMP on the samples.

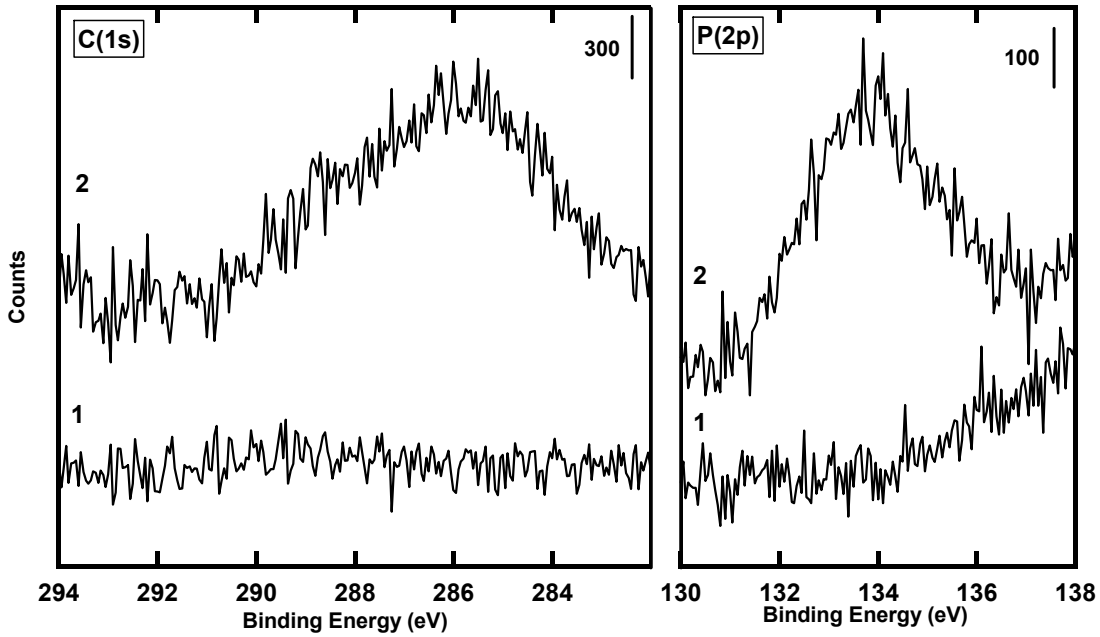

Figure 6.16 Satellite peak corrected X-ray photoelectron spectra in the C(1s) and P(2p) regions of Y_2O_3 nanoparticles 1) before and 2) after exposure to DMMP.

6.6 Influence of Temperature

6.6.1 Exposure to Cold Nanoparticles

Another way of gaining insight into the reactivity of yttria nanoparticles is to reduce the temperature of the substrate prior to adsorption of DMMP. DMMP was exposed to a Y_2O_3 nanoparticle film cooled to 120 K. Perturbations of the O-H stretching modes at 3720 and 3682 cm^{-1} are again indicative of hydrogen bonding of DMMP at the particle surface at these temperatures. Difference RAIR spectra shown in Figure 6.17 demonstrate that the 5.8 nm particles decompose DMMP even at this low temperature as

evidenced by the surface methoxy C-H stretch at 2790 cm^{-1}, the (O-P-O) stretching modes at 1188 and 1092 cm^{-1} as well as the 1154 cm^{-1} surface Y-OCH_3 rock. Inspection of time-resolved data shows that the relative intensity of peaks assigned to the dissociated bridging species increase with respect to the intact DMMP P=O and redshifted C-O modes.

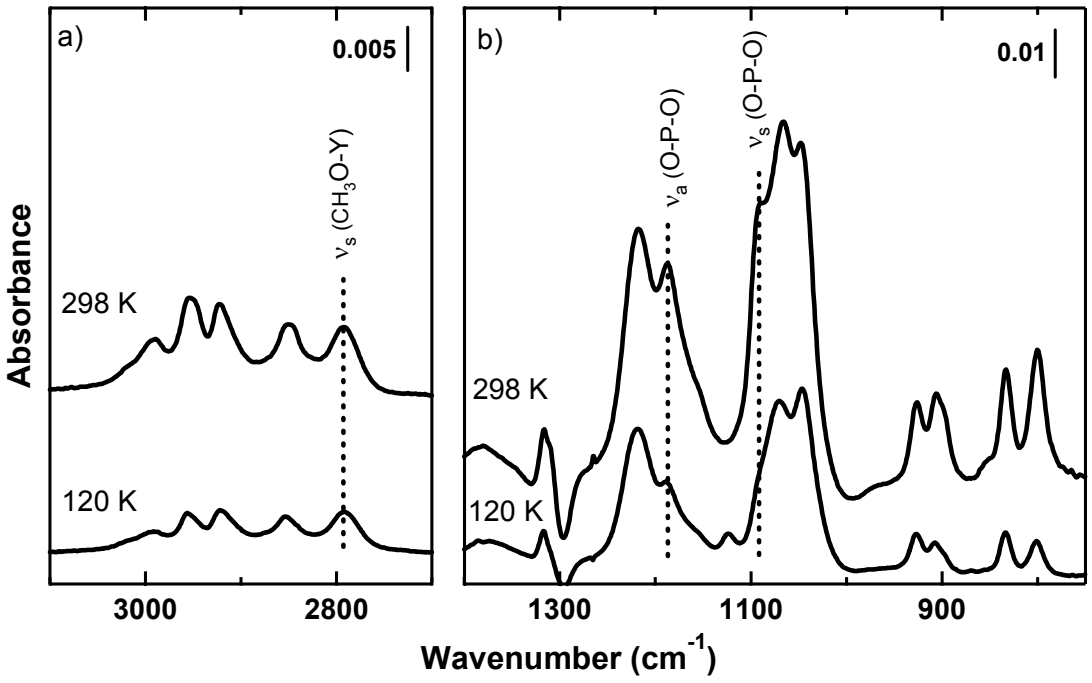

Figure 6.17 Difference RAIR spectra in the a) high wavenumber and b) low wavenumber regions showing DMMP exposed to 5.8-nm Y_2O_3 nanoparticles at 120 K (lower trace) and 298 K (upper trace). The particles still decompose some of the adsorbed DMMP at 120 K.

6.6.2 Heating After a Cold Exposure

Experiments were performed in which DMMP exposed to the cold substrate of the nanoparticles was heated slowly from 120 K to > 370 K at a rate of approximately 3-5 K/scan, or 1-2 K/min. These experiments were performed to determine if a critical temperature for reactivity exists and to provide further confirmation of the peak

assignments to adsorbed and reacted DMMP species. As seen in the time-resolved study, RAIR spectra demonstrate several features that indicate reaction of DMMP on the surface. As observed in the spectra in Figure 6.18, the dissociation of DMMP on the surface proceeds in a continuous manner over the temperature range of 190 – 370 K.

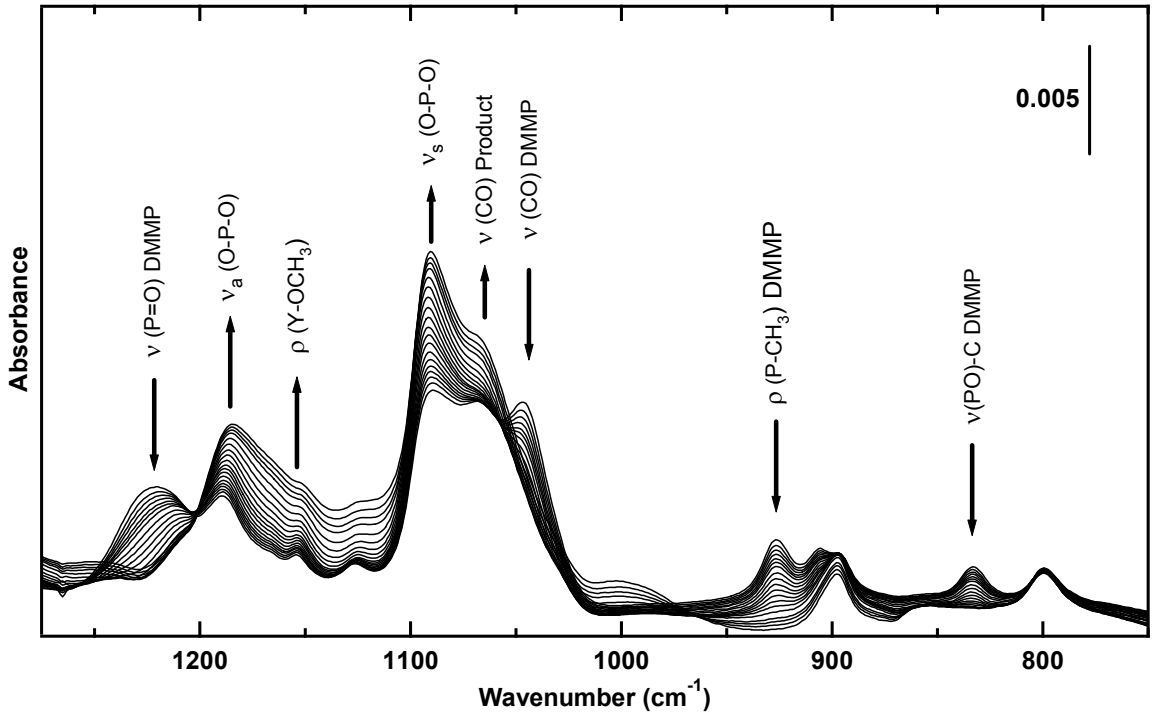

Figure 6.18 RAIR spectra of DMMP adsorbed onto 2.2 nm Y_2O_3 particles at 120 K, followed by heating from 206 to 365 K. Arrows indicate the depletion or growth of vibrational modes.

The clear indicators of the reaction are the loss of intensity for the P=O stretch, red-shifted C-O stretch, blue-shifted P-CH_3 rock, and (PO)C stretching modes associated with molecularly adsorbed DMMP. The formation of the dissociation products is shown by the increase of the O-P-O modes over the slight background increase that is due to thermal expansion. The smooth nature of the transition from adsorbed to dissociated DMMP seen in Figure 6.19 is consistent with a surface that has many reactive sites, each with a slightly different environment instead of a single, critical site.

The higher wavenumber region (not shown) is much more difficult to interpret. A drastic decrease in the associated hydroxyl O-H stretch is observed, but this may be due to sublimation of ice from the sample surface instead of involvement in a reaction with DMMP. The C-H stretching region is strongly influenced by the O-H region perturbations, but clearly shows all of the assigned peaks and the anticipated growth of the surface-bound methoxy C-H modes.

As seen from the data, there is no sharp transition observed with temperature which could be due in part to the thermal gradient that likely exists across the nanoparticle film due to the insulating nature of the oxide and the space-filled structure of the film as discussed in Chapter 5. It is also observed that the 2.8 nm particles almost completely dissociate adsorbed DMMP at around 340 K. This relatively low temperature underscores the reactivity of these metal-oxide nanoparticles.

6.6.3 Increased Temperature after Room Temperature Exposure

The role of increasing temperature on the decomposition of DMMP was also probed on nanoparticles that were pre-exposed to the molecule at room temperature. Larger, 5.8 nm particles were used as the substrate for this experiment so that a significant amount of molecularly adsorbed DMMP would be available for decomposition. After exposure to DMMP, the nanoparticle sample was heated from 295 K to 580 K.

The higher-wavenumber region shows evidence for continuous dissociation of DMMP via a red-shift in the DMMP-bound methoxyl C-H stretches at 2952 and 2858 cm^{-1}, in addition to increasing intensity of the surface-bound methoxy C-H stretch at 2800. Above 350 K, the baseline began to increase unevenly across the full range of the

spectra, presumably due to thermal movement of the sample. In addition, significant dehydroxylation of the surface was observed above 350 K with loss of all OH stretching modes. In addition to these changes, it is clear that the surface-bound methoxy mode stops growing near 410 K, and all C-H stretching modes begin to decrease at 480 K. There is no observed preferential loss of the methyl or methoxy C-H stretches.

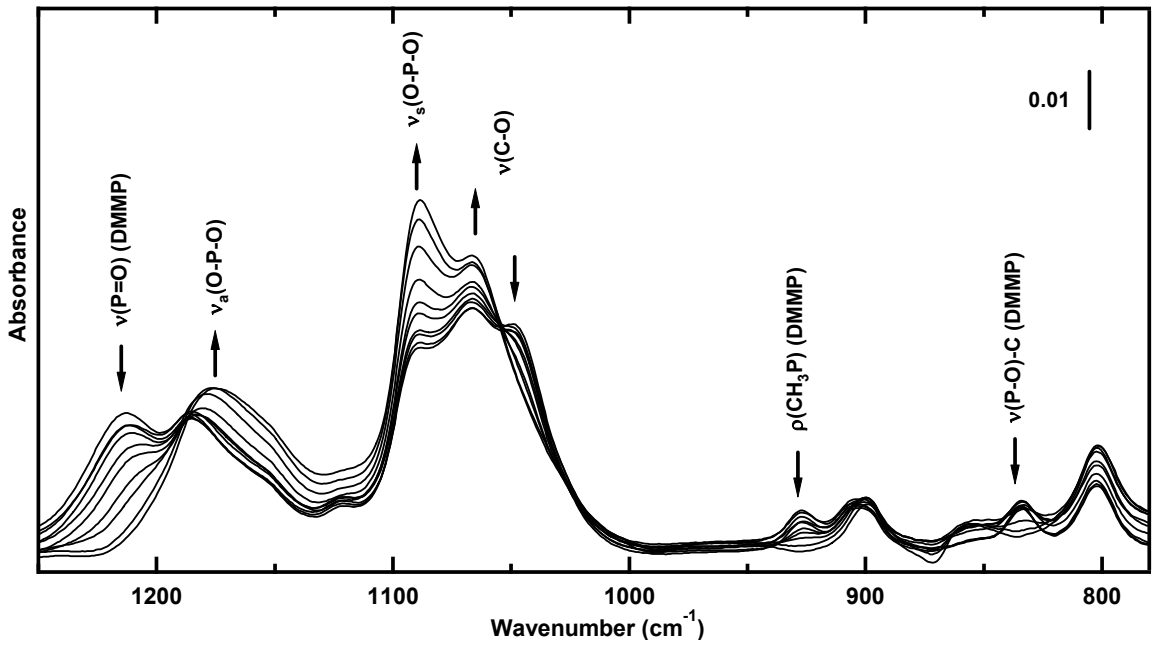

Figure 6.19 RAIR spectra of DMMP adsorbed onto 5.8 nm Y_2O_3 particles at 295 K, followed by heating to 440 K. Arrows indicate the depletion or growth of vibrational modes.

Interpretation of the low-wavenumber region, displayed in Figure 6.19, matches the results seen in the C-H stretching region. Segments of the spectra are muddled by strong background shifts as well as the loss of modes associated with carbonates on the surface. Heating the sample is accompanied by the dissociation of molecularly adsorbed DMMP, indicated by the loss of the P=O stretch, the red-shifted C-O stretch, the blue-shifted P-CH_3 rock, and (PO)C stretching mode. Modes associated with the bridging O-P-O species such as the O-P-O stretches increase simultaneously. Near 440 K, the P=O mode was no longer observable and the growth of the O-P-O modes stopped. Further

heating to ~ 480 K resulted in the red-shifting of the asymmetric O-P-O mode, resulting in the merging of the C-O and phosphorus-oxygen modes. Below 1000 cm^{-1}, loss of the remaining P-CH_3 rock, and PO stretch occurs simultaneously.

The results in the high and low wavenumber regions clearly point to dissociation of DMMP (and elimination of some surface-bound methoxy groups) between 295 and ~ 420 K, at which no molecularly adsorbed DMMP remains. Changes above 440 K indicate that further decomposition of the bridging species occurs, likely forming a surface phosphorus oxide material. No evidence was observed for preferential cleavage of the 2nd methoxy group or the methyl group of the bridging species, so the surface species at elevated temperatures is not clearly identified.

6.7 Influence of Atmospheric Gas Exposure

Pre-exposure of Y_2O_3 nanoparticles to O_2, CO_2, and air was performed prior to introduction of the sample into UHV to determine the influence that these gases have on the uptake and reactivity of the films to DMMP. Outcomes of these experiments might shed light onto the active adsorption or reactive sites on the nanoparticle surface in addition to probing the feasibility of applying Y_2O_3 nanoparticles to real-world environmental work.

2.8 nm Y_2O_3 nanoparticles that were exposed to 10 Torr of O_2 gas for five minutes prior to transfer into UHV conditions and subsequent exposure to DMMP displayed all five C-H stretching modes, including the surface-bound methoxy symmetric C-H stretch at 2792 cm^{-1} in the RAIR spectra. Relative intensities of the O-P-O modes compared to the P=O stretch in the low wavenumber region of the spectra indicate a high amount of reactivity. However, intensity of all the peaks was significantly reduced (~ 10

fold) when compared to particles not exposed to O_2. Uptake of DMMP is therefore significantly reduced upon O_2 pre-exposure of the nanoparticles, while relative reactivity remains roughly similar.

Influence of CO_2 pre-exposure prior to sample introduction into the UHV chamber resulted in more ambiguous results. Uptake of DMMP on this sample is reduced by an order of magnitude, making the signal to noise (S/N) reduced enough to make interpretation of the C-H stretching region more difficult. Four peaks are observed in the C-H stretching region, and all are shifted from expected wavenumber values. The splittings between these peaks indicates that the asymmetric methyl C-H stretching mode is not visible at these S/N levels, and that there is evidence in this region for the formation of some surface-bound methoxy groups. The low wavenumber region, however, shows little sign of the O-P-O stretching modes, indicating little or no DMMP dissociation. The evidence from the C-H stretching region points to DMMP dissociation, but it is likely the quantity of the decomposition species are not highly concentrated based on the evidence from the low wavenumber region.

Additional insight into the influence of atmospheric gases on the reactivity and uptake of the particles can be gained when a DMMP-dosed sample is removed from the UHV environment to be exposed to air for 10 minutes, then re-introduced into the UHV chamber. The extreme sensitivity of RAIRS to the position of the sample with respect to the IR beam as well as the heterogeneity of the surface make the experimental results very difficult to interpret. After exposure to DMMP and then air, a significant amount of DMMP species desorb from the sample as seen with the loss of C-H stretching, (PO)-C stretching, and (PCH_3) rocking mode intensity. However, some DMMP remains on the

surface, and clear evidence is observed for the bridging species with the observation of the O-P-O modes.

These experiments show that the uptake of DMMP is reduced on Y_2O_3 nanoparticles when they are previously exposed to O_2 and CO_2. Some reactivity may remain after oxygen exposure, but CO_2 exposure seems to poison reactive sites in addition to saturating adsorption sites. Air exposure was found to induce desorption of some DMMP from nanoparticles, but the O-P-O bridging product species is more resistant to desorption or any further reaction.

6.8 Influence of Thermal Pre-Treatment of Nanoparticles

6.8.1 Introduction

In vacuo thermal pre-treatment is often performed on metal-oxides prior to exposure to chemical warfare agent simulants to reduce the amount of water or hydroxyl groups on the surface in addition to reducing other surface contaminant species. Thermal pre-treatment may involve temperatures greater than 775 K and treatment with oxygen. While many bulk metal-oxides will maintain structure under these conditions, nanomaterials can often be more sensitive to elevated temperatures due to their unique structure. Thermal annealing could reduce the number of surface defects, induce a change in crystal structure, or provide the energy for grain growth to occur in addition to driving off unwanted contaminants. These potential drastic changes in materials properties mean that any thermal annealing study must be carefully performed to reduce their influence on results.

6.8.2 Influence of Hydroxyl Groups

Thermal pretreatment allows for the investigation of hydroxyl groups in the adsorption and decomposition of DMMP on yttria nanoparticles. Figure 6.20 shows the difference spectra of 2.2 nm Y_2O_3 nanoparticles exposed to DMMP after prior 573 K and 773 K anneal *in vacuo*. Both spectra show characteristic peaks for significant decomposition of the adsorbed DMMP. Comparing the two spectra, the relative intensity of the surface-bound methoxy C-H modes are greater for the sample pre-annealed at 773 K. In addition, the P=O stretching shoulder on the peak at 1250 – 1150 cm^{-1} is less visible and the PCH_3 rocking and (PO)-C stretching modes associated with adsorbed DMMP are not observable over the noise. Modes for the P=O stretching, PCH_3 rocking, and the (PO)-C stretching vibrations are visible for the sample pre-annealed at 573 K. The conclusion from these results is that the sample pre-annealed at 773 K appears to be more reactive than when annealed at 573 K, however these results should be considered as preliminary and this difference may be due to variability in the experiment.

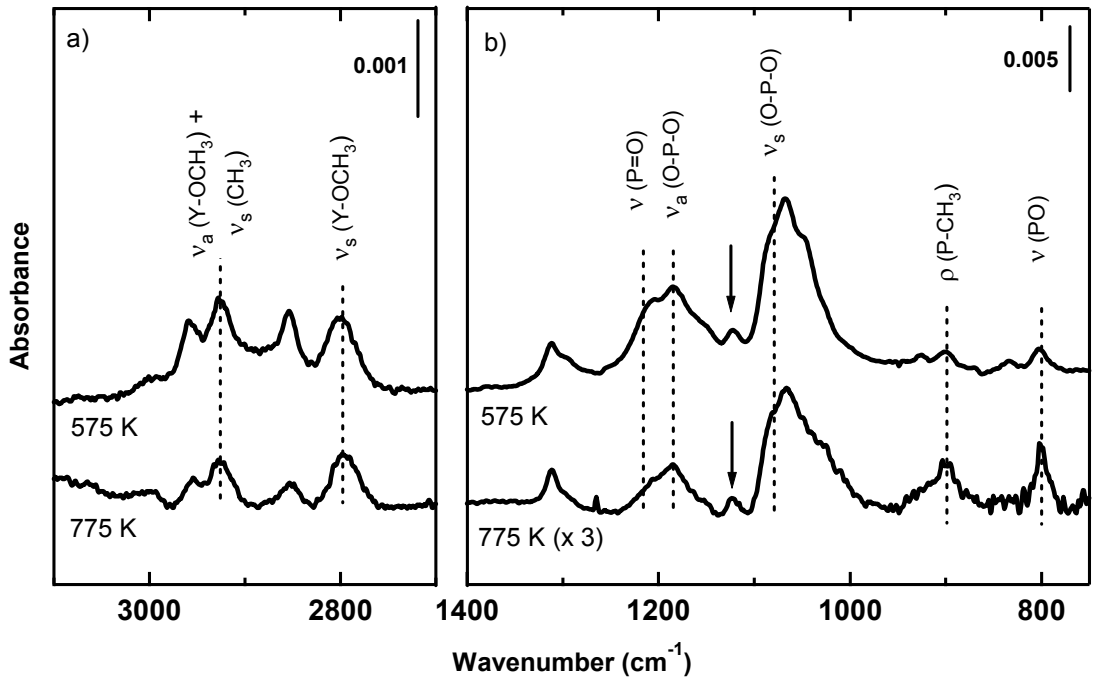

Figure 6.20 RAIR spectra of DMMP exposed to Y_2O_3 nanoparticles annealed at (upper trace) 575 K and (lower trace) 775 K showing the a) C-H stretching region and b) low wavenumber region. The arrows in b) mark a peak due to contaminating CD_3OD but this does not influence the interpretation of the results here.

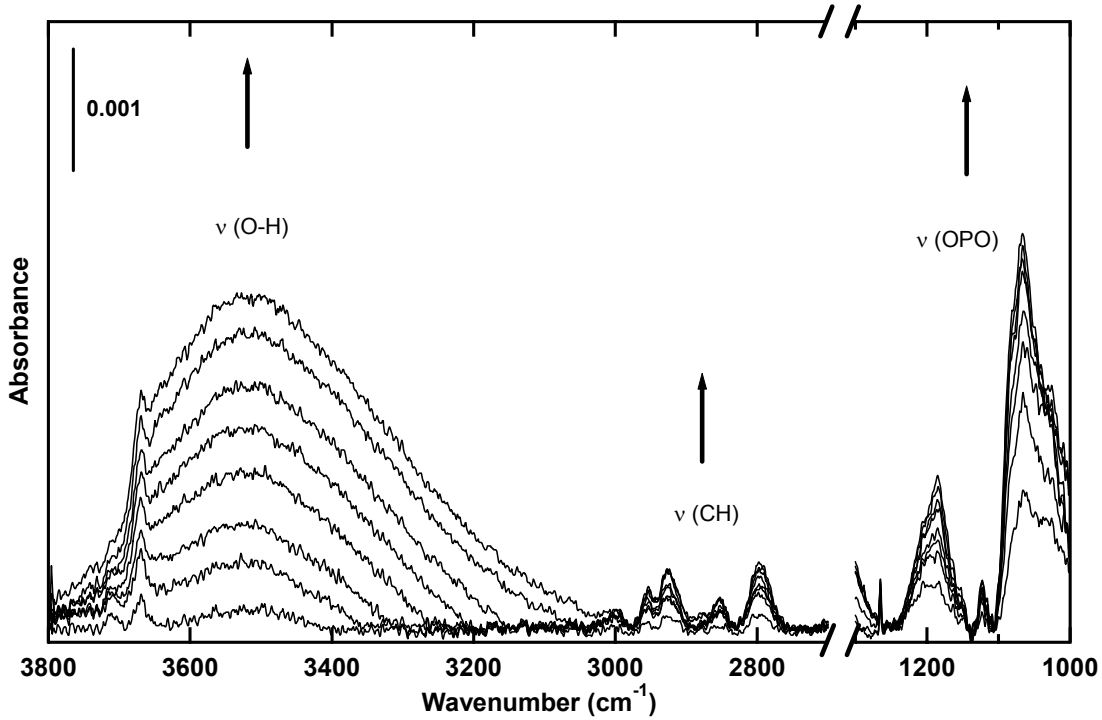

Figure 6.21 RAIR spectra over time of DMMP exposed to Y_2O_3 nanoparticles pretreated at 775 K prior to exposure. Hydroxyl groups (from water contamination in the doser) on the surface increase as DMMP is adsorbed, and may be mediating the adsorption.

One fact that is clear from these results is shown in Figure 6.21, where the sample pre-annealed at 775 K is exposed to DMMP. It is clearly observed that the intensity for RAIR modes associated with O-H stretches of hydroxyl groups rise with the intensity of DMMP. Because DMMP is polar, it is expected that the bubbler reservoir will contain some water, which will enter the chamber with DMMP. The exposure of the dry dehydroxylated surface to water seems to be the limiting factor for the uptake of DMMP during this experiment. Further confirmation may be gained by comparing the uptake of DMMP on this 775 K pre-annealed sample with a similar unannealed sample. At similar DMMP exposure levels, the annealed yttria particles show less than 10% of the RAIR intensity for adsorbed DMMP species than the equivalent unannealed sample. Hydroxyl groups therefore play a major role in the uptake of DMMP on the nanoparticles, as postulated from earlier results.

Other evidence points towards hydroxyl group involvement in the dissociation of DMMP on the surface. After DMMP dosing on the yttria is ended, difference RAIR spectra are used to ascertain the changes that occur. Figure 6.15 displays the low wavenumber region of such a spectrum that yields evidence for reaction, but not desorption of adsorbed DMMP species. Observation of the O-H stretching region for this and similar spectra show a weak and broad negative feature at 3560 cm^{-1}, indicating loss of associated hydroxyl groups concurrent with dissociation of surface-adsorbed DMMP. While the evidence is not beyond doubt, it provides implication of involvement with surface hydroxyl groups with the dissociation of DMMP.

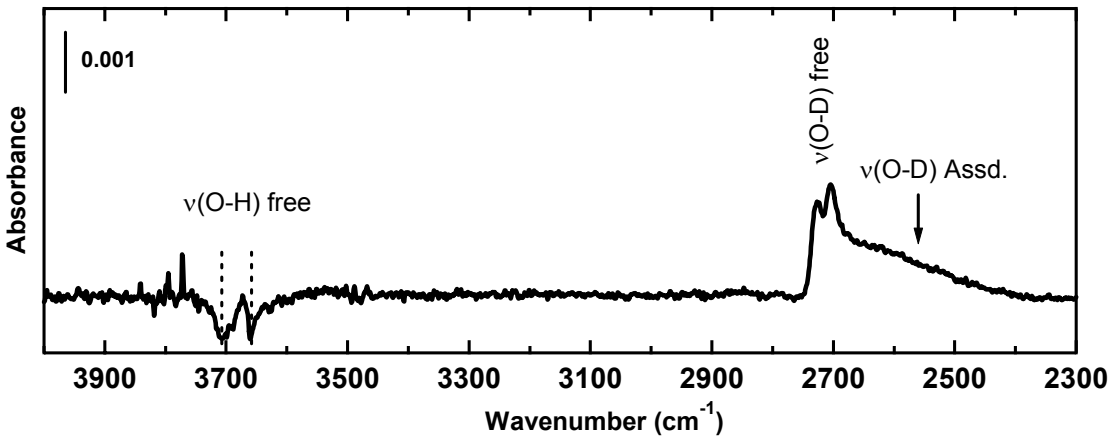

Figure 6.22 RAIR difference spectrum of Y_2O_3 nanoparticles exposed to D_2O.

6.8.3 D_2O Exposure

Further investigation into the role of hydroxyl groups was performed by preparing a yttria nanoparticle sample, annealing to 775 K, exposing particles to D_2O followed by DMMP exposure. After annealing and D_2O exposure (see Figure 6.22), it is clear that OD groups populate the surface by virtue of the O-D stretches visible in the RAIR spectrum at 2726 and 2704 cm^{-1}. The unidentate and multidentate OD stretches of isolated surface OD species are responsible for these peaks. Simultaneously, small negative peaks develop at 3709 and 3660 cm^{-1}, while a broad positive mode grows in at 3600 cm^{-1}, signaling the loss of some of the remaining isolated OH groups on the surface.

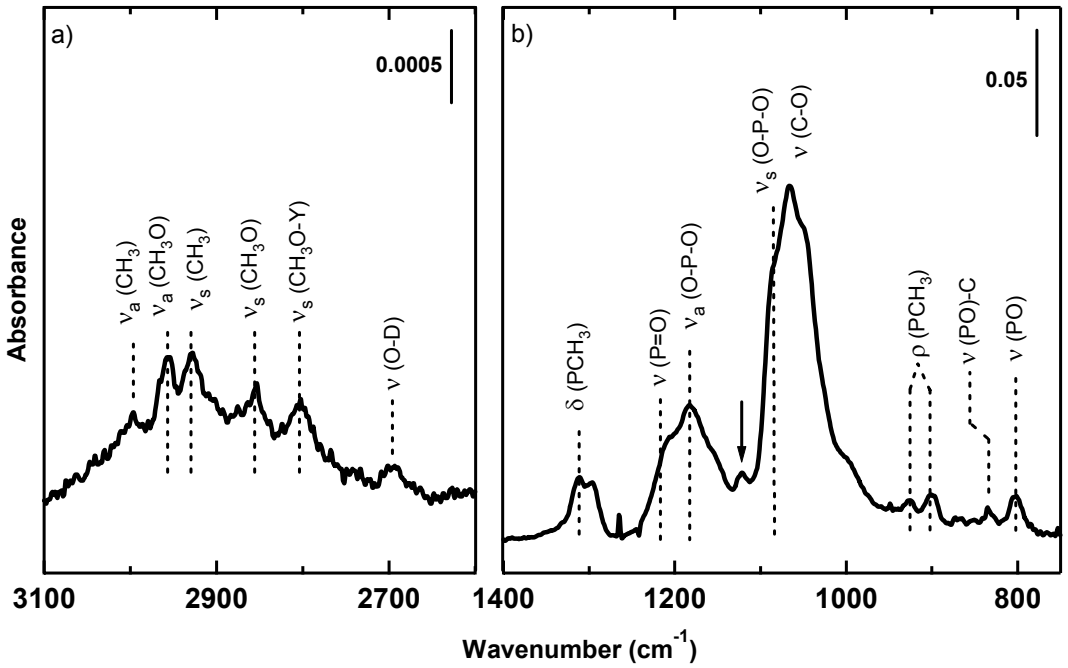

Figure 6.23 RAIR spectra of DMMP adsorbed onto yttrium oxide particles that were previously annealed at 775K for 4 hours and then exposed to D_2O. The peak labeled with the arrow is due to a small degree of CD_3OD contamination.

Upon DMMP exposure (shown in Figure 6.23), it is clear that adsorption and some decomposition occur as evidenced by the surface-bound methoxy symmetric C-H and O-P-O stretches. However, relative uptake of DMMP for the D_2O exposed sample does not appear to be significantly different from a sample that is annealed. One possible explanation for this is physical change induced by the annealing of the sample. Previous work on Y_2O_3 nanoparticles indicate negligible particle size change when annealed in air at temperatures of 775 K for 24 hours,[70] however it is possible that surface defect sites are changed under the conditions of the experiment causing a change in uptake probability.

Table 6.6 Infrared peak assignments (in cm^{-1}) for DMMP, CH_3OH, TMP, DDMMP, and CD_3OD adsorbed on yttrium oxide nanoparticles. Peaks for gas-phase DMMP are included for reference.

	DMMP Gas[214]	DMMP[199]	CH_3OH	TMP[178,179,188,215]	DDMMP[199,214]	CD_3OD[216-218]
$\nu_a(CH_3)P$	2998	2996			2997	
$\nu_a(CH_3)O$	2958	2952		2956		
$\nu_s(CH_3)P$	2924	2926			2930	
$\nu_a(CH_3)O$-Y *			2928	2923		
$\nu_s(CH_3)O$	2859	2858	2873	2854		2854
$\nu_s(CH_3)O$-Y *		2795	2804	2796		
$\nu_a(CD_3)O$					2239 wk	2237
$\nu_a(CD_3)O$-Y					2180	2176
$\nu(CD_3)O$					2138 wk	2134
$\nu_s(CD_3)O$					2082	2083
$\nu_s(CD_3)O$-Y					2036	2044
$\delta_s(CH_3)$	1319	1312			1309	
ν(P=O)	1275	1216		1216	1219	
ν_a(O-P-O) *		1187		1193	1189	
$\delta_a(CD_3)$					1164	1162
ρ(O-CH_3)	1190					
ρY(O-CH_3) *		1154	1152	1152		
$\delta_s(CD_3)$					1119	1126
ν_s(O-P-O) *		1092		1106	1085	
ν(C-O) *	1070	1065	1074	1076	1065	
ν(C-O)	1049	1047		1055	1030	1029
ρ(P-CH_3)	914	926				
ρ(P-CH_3) *		896			896 wk	
ν(PO)-C	816	833		839		
$\nu(PO_2)$ *		799			791 wk	

6.9 Effect of Particle Size on Reactivity

The size of nanoparticles has a critical influence on the reactive properties of nanomaterials. For example, smaller MgO nanocrystallites have been found to adsorb three times more SO_2 and CO_2 gases[219] and are more reactive with DMMP than larger nanocrystals at 775 K.[220] This increase in reactivity has been attributed in part to higher

surface areas in nanoscale materials, but is also due to the higher number of defect sites that are induced by the greater disorder that occurs with decreasing size[221,222] as well as the new crystal morphologies that occur.[220]

Mean nanoparticle size is controlled by varying the background pressure in inert gas-phase condensation. In order to test the effect of particle size on the reactivity of Y_2O_3 nanoparticles, a second series of nanoparticle films were prepared under 1 Torr of N_2. AFM analysis show that the primary particles synthesized in 10 Torr and 1 Torr N_2 have a mean size of 5.8 and 2.2 nm with standard deviations of 1.3 and 0.8 nm, respectively.

Size histograms of the two samples are shown in Figure 6.24. BET analysis indicates that the surface areas of films of the 5.8 and 2.2 nm particles are 155 and 187 m^2/g. These similar surface area values imply different density or packing of the particles, but are similar enough that this factor should not strongly impact the results of the experiments. Powder X-ray diffraction results indicate that the particles have similar crystal structures, and are composed of a mixture of monoclinic and cubic phases as discussed previously in Chapter 5.

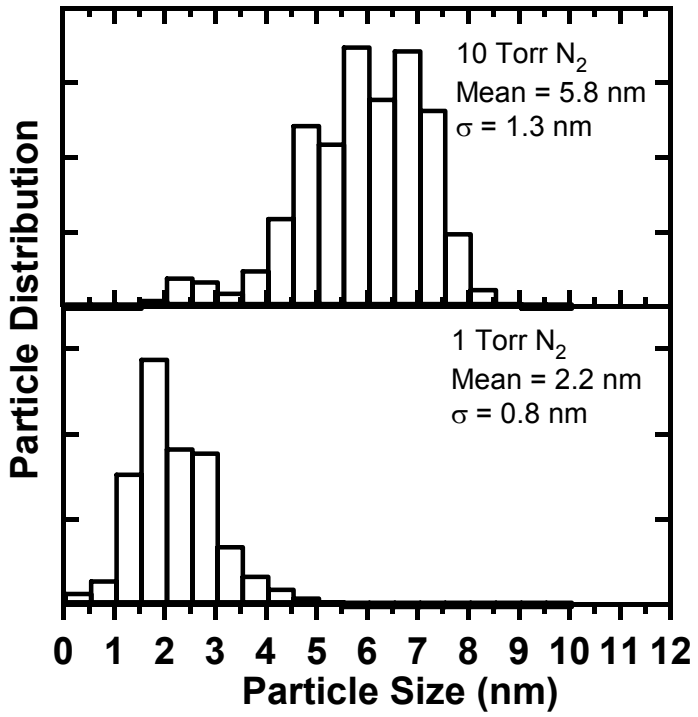

Figure 6.24 Size distribution of Y_2O_3 nanoparticles used to investigate particle size influence on interaction with DMMP.

The RAIR spectrum of DMMP exposed to the 2.2 nm particles is shown in Figures 6.25 and 6.26. Difference RAIR spectra show that the intensity of the peaks that are associated with the surface bound methoxy group (2800 cm^{-1}) is greater than the intensity of the intact DMMP-bound methoxy C-H stretches, and the asymmetric and symmetric bridging O-P-O stretches (1187 and 1092 cm^{-1}) are relatively more intense than the molecularly adsorbed P=O stretching signal in the spectra for the smaller nanoparticles. Comparison of relative intensities rules out the possibility that surface area is the governing factor for reactivity, supporting the conclusion that the smaller particles are intrinsically more reactive than their larger analogues.

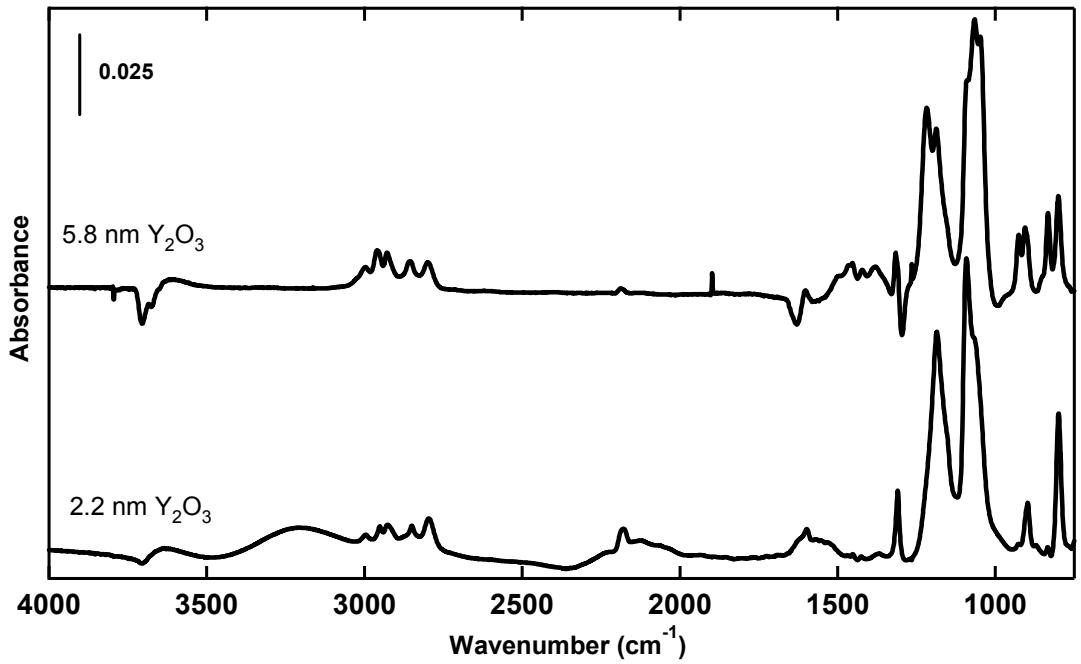

Figure 6.25 RAIR spectra of 5.8 and 2.2 nm Y_2O_3 nanoparticles exposed to similar doses of DMMP.

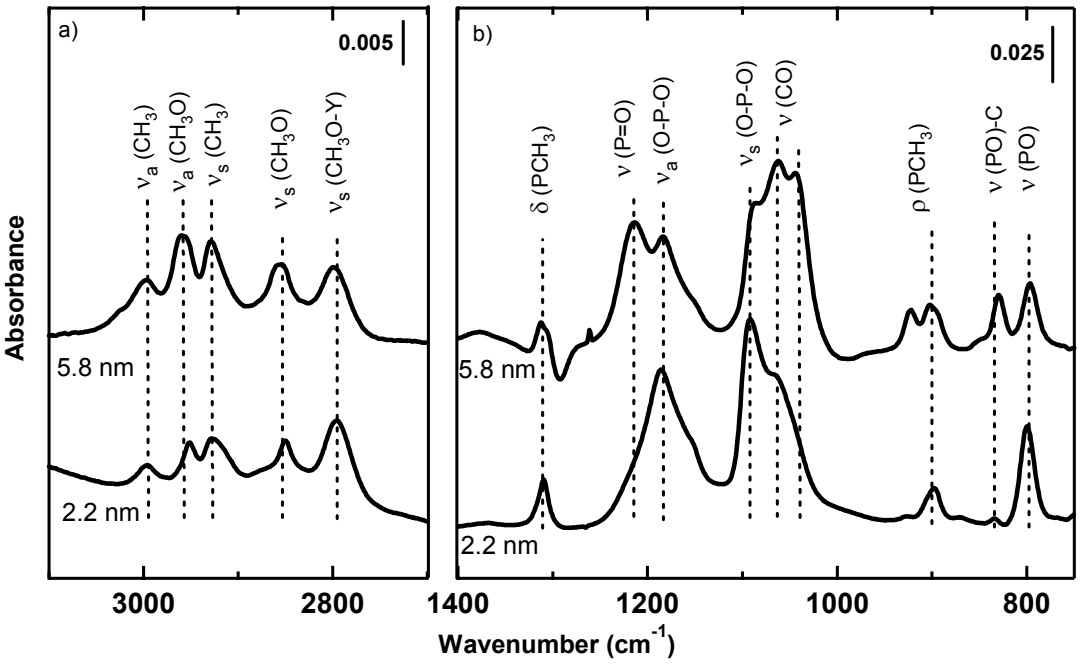

Figure 6.26 Magnification of the RAIR spectra in Figure 6.25 showing the a) high and b) low wavenumber regions.

It is estimated from the relative intensities of RAIR data that the 2.2 nm particles have approximately a 2 – 3 fold higher reactivity towards DMMP than the 5.8 nm particles. Size enhancement of particle reactivity as seen with DMMP was also observed with DDMMP as the simulant, giving confirmation of these results.

The results from post-exposure heating (including the experiments discussed in Section 6.6.2.) also provide evidence for the greater reactivity of smaller particles. While both the 5.8 and 2.2 nm particles dissociate DMMP at temperatures as low as 180 K, elevated temperatures are required to completely react the molecularly adsorbed molecules. Post-exposure heating experiments found that the 2.2 nm particles completely dissociated DMMP by the time the sample reached ~ 370 K. In contrast, the 5.8 nm particles required temperatures near 420 K to fully dissociate adsorbed DMMP.

Particle size influence on reactivity is anticipated and has been observed in several systems previously, particularly in the critical size range below 10 nm. Y_2O_3 particles with diameters of 5.8 and 2.2 nm are estimated to contain 7000 and 380 ions per particle, with a respective 43 and 84% of these ions within 5 Å of the surface. It is known that low coordination sites such as edge and corner ions, vacancies, and other defects can be more reactive than ions that are situated at non-defect sites. Simple geometric arguments show that as particle size decrease for similarly shaped crystals, the relative number of ions in low coordination (edge and corner) sites increases significantly. Hence, if corner or edge ions are more reactive, a great increase in reactivity will be observed in the size range probed during this work. Surface defects should also influence the reactivity of hydroxyl groups, which have been implicated in this study as being major contributors to the reactivity of the system.

6.10 DMMP Adsorption and Decomposition on ZrO_2 Nanoparticles

In order to fully understand the general interaction between DMMP and metal-oxide surfaces, a variety of materials must be studied to learn about the influence of the chemical properties of the oxide on organophosphonate reactivity. For this reason, the UHV study of DMMP adsorption and decomposition was expanded to include ZrO_2. Unlike yttria, ZrO_2 has been studied more extensively as a potential catalyst or catalyst support.[223-226] Experimental procedures were identical for this study as for yttria as described in Section 6.2.2, with exception of the use of purchased ZrO_2 targets.

6.10.1 DMMP Exposure Results

ZrO_2 nanoparticles were synthesized under atmospheres of 1 and 10 Torr N_2 and then exposed to DMMP. Upon exposure, the resulting RAIR difference spectra (see Figure 6.27) were analogous to the spectra of DMMP adsorbed to yttria particles. In the O-H stretching region, two sharp negative features were observed at 3775 and 3680 cm^{-1} which are indicative of the loss of monodentate and multidentate isolated hydroxyl groups, respectively.[195,227,228] The 3680 cm^{-1} band has been normally assigned to a tridentate species,[227,228] but this assignment has been disputed in favor attributing the mode to a bidentate bridging OH species on ZrO_2.[229]

Evidence for DMMP adsorption is observed in the C-H stretching region with bands associated with the methyl (3001 and 2929 cm^{-1}) and methoxy (2957 and 2856 cm^{-1}) C-H stretches. A fifth C-H stretching mode is also observed at 2824 cm^{-1}, indicating the presence of a surface methoxide species. The lower wavenumber region features the methyl rock at 1313 cm^{-1}, an intense and broad absorbance from 1230 – 1000

cm^{-1}, the P-CH_3 deformations at 927 and 910 cm^{-1}, and the P-O stretches at 837 and 809 cm^{-1}.

The results indicate that a majority of adsorbed DMMP on the particles dissociate to form surface-bound methanol and a O-P-O bridging species shown in Figure 6.13. In the C-H stretching region, the intensity of the symmetric stretch of the surface-bound methoxy group at 2824 cm^{-1} implies that a large proportion of the intensity in the 2929 cm^{-1} is due to the asymmetric C-H stretch of the surface bound methoxy, in addition to the symmetric C-H stretch of the methyl group. The assignment to surface-bound methoxy groups is supported by the literature values for dissociated methanol on ZrO_2 of 2926 and 2821 cm^{-1}.[224]

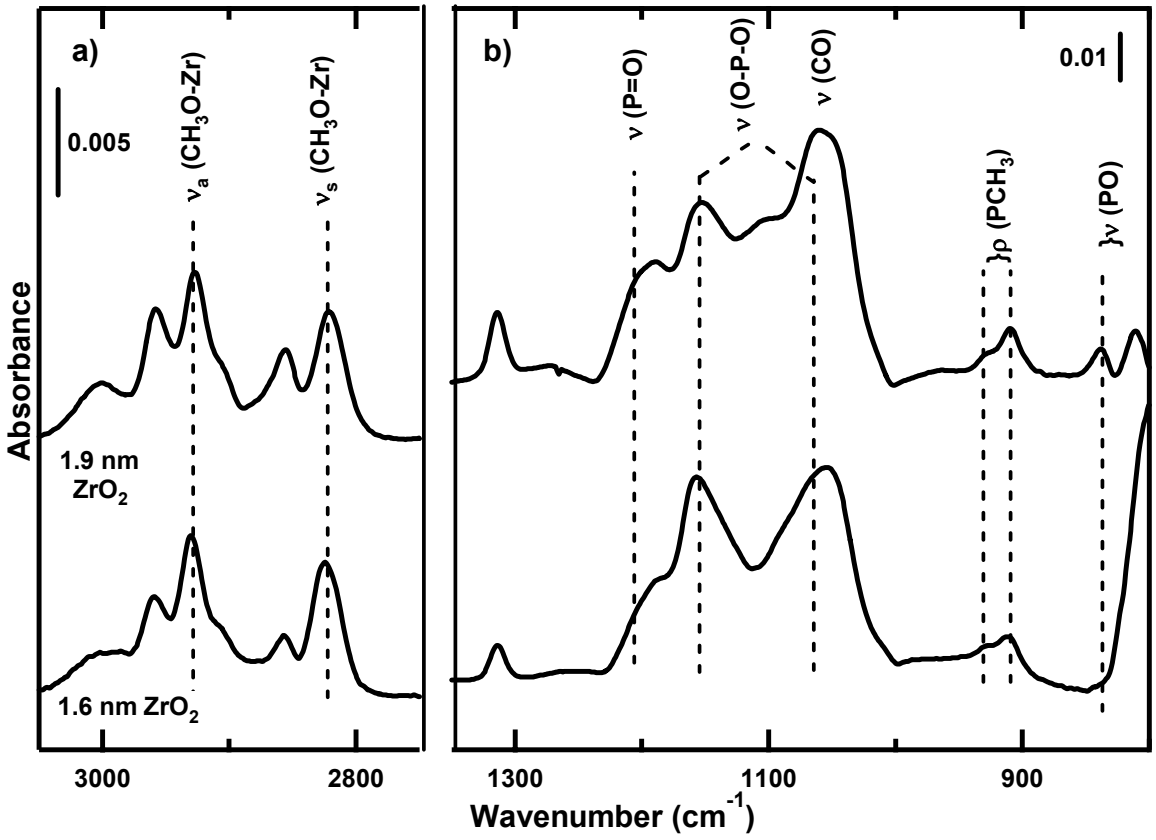

Figure 6.27 Difference RAIR spectra of DMMP adsorbed to 1.9 nm (top) and 1.6 nm (bottom) ZrO_2 nanoparticles, viewing the a) high and b) low wavenumber regions.

In the lower wavenumber region, the P-CH_3 deformation at 910 cm^{-1} and the PO stretch at 809 cm^{-1} are relatively more intense than the higher wavenumber P-CH_3 deformation and (PO)C stretch that are observed at 927 and 837 cm^{-1}, respectively. Similar to the interpretation of the results for yttria, the relative intensities of these modes imply that the dissociated DMMP is the dominant surface species on both samples of ZrO_2 nanoparticles. While other modes can be clearly assigned, the exact location of the P=O, O-P-O, and C-O stretches as well as the OCH_3 rocking modes of DMMP and surface-bound methoxy groups are obfuscated by the broad nature of the peaks in the 1220 – 1000 cm^{-1} region. Based on observation of time-resolved spectra, the P=O stretching mode is located near 1205 cm^{-1}, while the asymmetric and symmetric O-P-O stretches of the bridging species are located near 1155 and 1055 cm^{-1}. The splitting between these two assignments (~ 100 cm^{-1}) is near the expected value of 95 – 100 cm^{-1}.[212] Literature assignments indicate that peaks for surface-bound methoxy groups should appear at 1142 and 1039 cm^{-1}, both of which fall within the more intense regions of the broad absorption peak.

6.10.2 Reactivity and Particle Size Influence

The above peak assignments are reinforced by observation of the spectral changes after ZrO_2 exposure was completed. Difference spectra collected several minutes post-exposure show the growth of surface-bound methoxy groups and the O-P-O species, coupled with the loss of DMMP with negative features assigned to the P=O, (PO)C, and PCH_3 modes of DMMP. In addition, the O-H stretching region shows loss of multidentate OH species, along with a slight increase in monodentate OH groups. This result implies

that the multidentate OH groups may be involved in the dissociation reaction of DMMP (presumably through hydrolysis).

Particle size dependence on the reactivity of DMMP on the ZrO_2 nanoparticles is not as clear as with yttria. DMMP was exposed to ZrO_2 nanoparticles synthesized under 10 and 1 Torr of N_2. AFM analysis of the two particle samples indicated that both have very small sizes, which may partially account for the high degree of reactivity observed on each. ZrO_2 synthesized under 10 Torr of N_2 was determined to have a mean particle size of 1.9 nm, while particles condensed in 1 Torr of N_2 were found to have a mean particle diameter of 1.6 nm, and standard deviation values for both samples around 0.9 nm. The near parity in particle size is reflected in the RAIR spectra of adsorbed DMMP, which shows a slightly higher reactivity on the smaller particles synthesized under 1 Torr N_2. This is shown by the relatively greater absorption peaks for the surface-bound methoxy group in the C-H stretching region, and the relatively higher signal for the P=O stretching mode seen for the larger 1.9 nm particles.

6.10.3 Conclusion

ZrO_2 nanoparticles were found to be extremely reactive towards DMMP upon adsorption at room temperature. Some evidence was observed for the loss of multidentate hydroxyls upon reaction, suggesting involvement of this species in DMMP decomposition. The data shows a particle size dependence on the reactivity similar to the one observed for yttria particles, however this result is not as apparent due to the small change in size between the two samples. Since these particles are very small, most of the atoms will be at or near the surface, which may be a significant factor in the great reactivity of the system.

These results also allow comparison to the reactivity towards DMMP of the particles when compared to the sample of ZrO_2 that was exposed in ambient conditions (see Section B.3.10). The particles from the survey study were synthesized under 1 Torr of N_2, and therefore, should be physically very similar to the particles studied during the UHV study. Two major differences between the survey (air) and UHV study must be discussed. The first is the presence of air for the survey study, which likely results in increased amounts of carbonate and hydroxyl groups on the surface. In addition, the air-exposed metal-oxide particles will have a layer of physisorbed water, which is not present for the sample held under ultra-high vaccum. Another consequence of the continued air exposure is the availability of water and other species to interact with the surface and the DMMP during and after exposure. The second difference is the saturation exposure that was used for the air study, while the vacuum study employed much lower exposures. Under ambient conditions, a saturation exposure may lead to layers of weakly interacting DMMP on the surface, which could influence the infrared spectrum.

It is clear that the nanoparticles that are synthesized and transferred *in vacuo* react much faster with adsorbed DMMP due to the instantaneous nature of the dissociation. Significant evidence was observed for decomposition on the air-exposed ZrO_2 within an hour of exposure to DMMP, however the molecularly adsorbed DMMP was likely the dominant species. However, given time (four days in the study), the sample shows strong capabilities for decomposition of DMMP. One difference observed in the RAIR spectra is the lack of surface-bound methoxy groups for the sample held in air. Methoxy groups are known to be able to be liberated as gas-phase methanol upon interaction with hydroxyl groups, adsorbed water, and atmospheric water. The air-exposed sample therefore has a

virtually limitless supply of these species (provided surface sites are available), therefore, it is likely that methanol was liberated from the surface. The sample held in UHV had only a limited supply of hydroxyl groups to start with, which could be depleted (or made less reactive) upon adsorption and dissociation of DMMP. Therefore, a large portion of the methoxy groups were unable to find a hydrogen source for liberation. The fast rate of decomposition on the UHV sample may be due to the lack of atmospheric species blocking reactive sites. If this is the case, the physisorbed water layer on the air-exposed particles may hinder the diffusion of DMMP to these active sites.

6.11 Summary

The experiments discussed in this Chapter have demonstrated the ability for nanocrystalline metal-oxides to adsorb DMMP under ambient conditions. It is likely that extended exposure (days) to air will passivate these adsorbants. Evidence was uncovered for a slow decomposition of DMMP on these metal-oxides when exposed under ambient conditions. A more detailed UHV study found that yttria nanoparticles will readily adsorb and dissociate DMMP at room temperature and below. Several experiments were performed to confirm peak assignments using analogs TMP and DDMMP. It was found that DMMP will interact initially with the yttria surface through the phosphoryl oxygen, probably through a hydrogen bond with a surface hydroxyl group. Dissociation then occurs to form a surface-bound O-P-O bridging species along with a surface bound methoxy group. No evidence was uncovered for products desorbing in the gas phase at room temperatures. The reactivity of the system was demonstrated by the dissociation of some DMMP at temperatures as low as 120 K. Hydroxyl groups were found to play a important role in adsorption and probably provide the initial interaction between DMMP

and the nanoparticles. Some evidence was also found to indicate that surface bound water or hydroxyl groups are also important in the dissociation of DMMP on the surface, probably involving hydrolysis. Finally, it was found that 2.2 nm Y_2O_3 particles are much more reactive with DMMP than 5.8 nm analogues, likely due to the greater relative number of edge, corner, and other defect sites.

Since the surface characteristics of these particles are not well understood, a specific mechanism for this reaction is not currently identified, however a slow dissociation step may involve diffusion of species under these conditions. One possible reaction pathway is similar to the Mars and Van Krevelen mechanism that has been proposed as a route for the dissociation of DMMP and other phosphonates on alumina.[211,212,230] This mechanism, displayed in Figure 6.28 involves the interaction of the DMMP with a hydroxyl group, destabilizing the phosphoryl group and enabling a nucleophilic substitution to occur at the phosphorus. It is noted for this mechanism to occur, hydroxyl groups must be present, but not necessarily for the initial interaction of DMMP with the surface. This mechanism yields a surface-bound O-P-O bridging species along with a gas-phase methanol, which may then interact with the surface to yield a methoxy group and hydroxyl group.

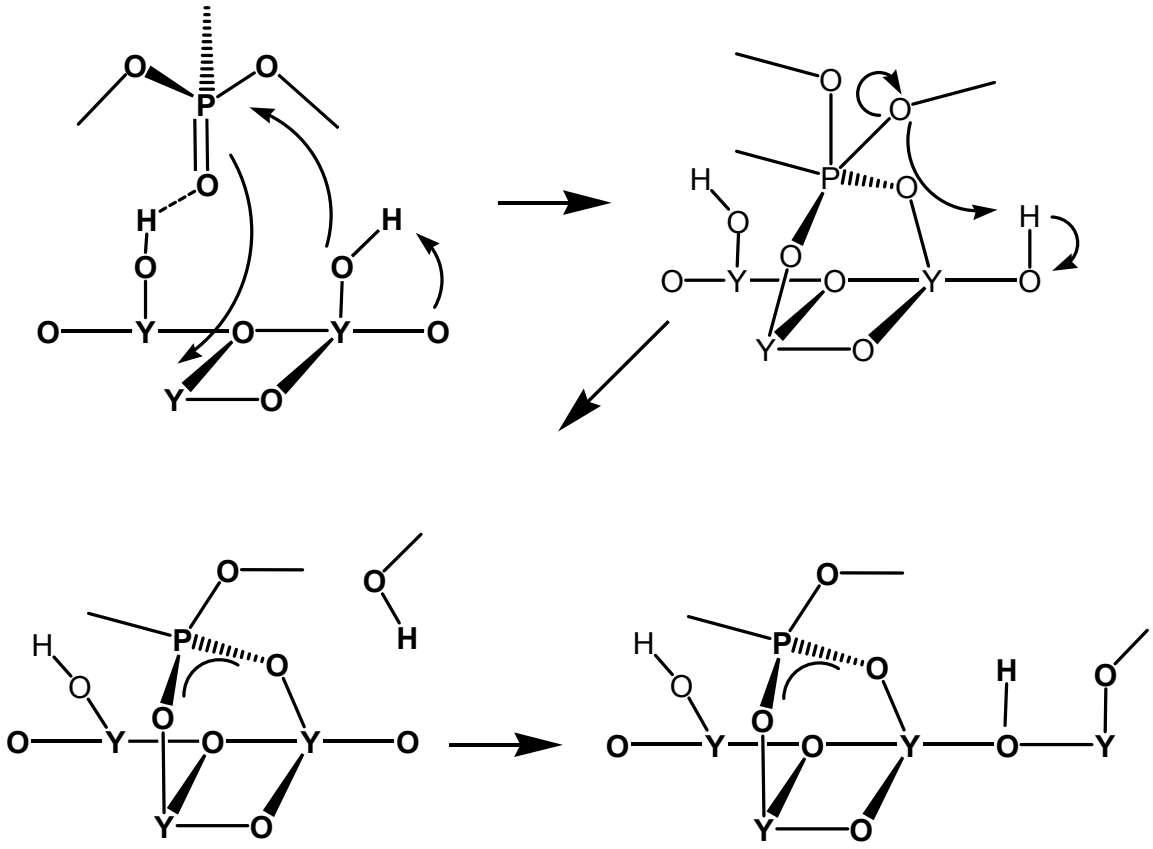

Figure 6.28. Possible mechanism of dissociation of DMMP on yttria nanoparticles.

Zirconia nanoparticles were also found to rapidly dissociate DMMP upon adsorption in a UHV environment. Evidence points towards a similar adsorption and dissociation mechanism as found for yttria particles. The evidence shows that hydrolysis of DMMP by surface hydroxyl groups is also likely a reactive pathway. The zirconia particles seem to demonstrate a slight increase in reactivity when the sizes decreased from 1.9 nm to 1.6 nm, however the relatively small difference (in both particle size and apparent reactivity) points to little change over this size regime.

6.12 Future work

Several questions remain to be answered for the reactivity of DMMP on nanoparticles. One question is the precise mechanism of reaction of DMMP on yttria nanoparticles. It is very likely that hydrolysis through surface hydroxyl groups is a major pathway, yet it is unclear if other sites (such as defects) on the nanoparticles surfaces play a role or not. More controlled heating studies using a thermocouple to monitor actual sample temperature will enable a more thorough study of the role of hydroxyl groups. Dosing samples with labeled water or exposing a dry oxide material that had previously been dried and dosed with DMMP may provide other experimental evidence for identifying the role of water.

In addition, the author believes that many metal-oxide surfaces will be reactive if they are in the form of ultra-small nanoparticles due to the higher energy surfaces available. Survey experiments with a wide variety of metal-oxides may provide evidence for or against this hypothesis. It is not clear how properties of the metal-oxides themselves will influence the reactivity in the 1-10 nm size regime. The other major feature to be probed is the true nature of the surface sites of as-prepared particles. Vacancies, step edges, dangling bonds, and other defects may exist on the particles surfaces and could strongly influence the reactivity. The use of probe molecules could characterize the acidic or basic properties of the surface, and yield insight into the source of reactivity. A series of oxide materials could also be tested to determine if the properties of the metal influence the chemistry of the oxide. Combining the wealth of information about the basic and acidic site properties of metal-oxides and the results from

a survey metal-oxide-DMMP reactivity study, some insight may be gained into the type of reactive sites that are responsible for the decomposition of DMMP.

Further information may be gained by temperature programmed desorption, or TPD. TPD experiments could be used to characterize the products of DMMP decomposition at elevated temperatures and could provide confirmation of surface bound species such as the phosphate species remaining on the surface. In addition, TPD could be used to compare the relative reactivity of different metal-oxides.

Once the fundamental insight about the interaction of metal-oxide surfaces and chemical warfare agent simulants has been gained, researchers will be able to design and test new materials that are aimed at use in real world protection applications from chemical warfare agents. These might involve heterogeneous metal-oxide or other hybrid materials that are less passivated by atmospheric species and yet retain the reactive abilities of the oxides.

Chapter 7. Summary and Concluding Remarks

7.1 Summary of Results

During the course of these studies, the properties of nanometer-scale oxide nanoparticles have been probed. Initial focus of this work centered on the optical properties of doped metal oxide nanoparticles. The first study was on interparticle energy transfer between lanthanide ions doped into Y_2O_3 particles. No evidence of energy transfer between Eu^{3+} and Er^{3+} ions was found. However, when the system was changed to mixed particles doped with Eu^{3+} and Tb^{3+}, the results were consistent with energy transfer. The interaction between the ions was weak compared to energy transfer that occurs in bulk materials such as glasses, and annealing the mixed particles was required to get sufficient signal to measure lifetime values. This leads to some concern that particle necking or interparticle ion migration might result from elevated temperatures, but most likely reflects the better packing of particles when mixed before annealing. An attempt to reproduce these results was unsuccessful, due to differences in the annealed samples.

Nanophosphor materials were further studied by surveying the properties of lanthanide-doped gadolinium oxide nanoparticles. Trivalent europium, terbium, and dysprosium were found to be the best lanthanide candidates by nature of their greater intensity, longer lifetimes, and resolvable emission spectra. Concentration effects were observed for Eu^{3+} samples, where the $^5D_1$ emission diminished at higher doping levels. Annealing was also found to strongly influence the intensity and broadening of emission spectra, reflecting the disorder of the as-prepared samples.

In addition to nanoparticle properties, the particle synthetic method was studied by observing a transition in as-prepared film morphologies. Gas pressure was found to be the dominant factor in influencing the growth of either a fractal-aggregate film or a film composed of columns of nanoparticles. Changing the buffer gas also resulted in a change of the critical pressure, which is attributed to the cooling ability and transport dynamics characteristic of each gas. Increased aggregation under higher pressures resulted in large agglomerates randomly depositing on the surface, while lower pressures resulted in reduced levels of aggregation, causing growth of the column structures. Differences in particle density and connectivity within the film means the films likely have different physical properties.

After studying optical properties and the synthesis of metal oxide nanoparticles, the focus shifted to the chemical properties of metal oxide particles. Specifically, the interaction of the particles with the simulant DMMP was studied. A survey study under ambient conditions found evidence for adsorption and reaction of DMMP on the nanoparticle surfaces, particularly a few days after exposure. Yttria particles were chosen for a more detailed study which was performed under ultra-high vacuum conditions. Y_2O_3 particles were found to be highly reactive towards DMMP, decomposing the adsorbed complex to form a bridging O-P-O species along with a surface-bound methoxy groups. Hydroxyl groups were found to be critical for the uptake of DMMP, and likely play a major role in the surface reaction via hydrolysis. Most importantly, a strong particle size dependence on reactivity was found. These studies have all looked at the properties of nano-scale metal oxide particles. Results from the experiments described in this thesis have implications on the properties and potential uses of nanoparticles.

7.2 Implications and Future Work

7.2.1 Energy Transfer

The study discussed in Chapter 3 provided evidence for energy transfer between europium and terbium ions doped into isolated particles. The energy transfer occurred between the $^5D_4$ level of Tb^{3+} (donor) and the $^5D_1$ or $^5D_0$ level of Eu^{3+} (acceptor). The energy difference between the donor and acceptor levels is approximately 1640 and 3300 cm^{-1} for the $^5D_1$ and $^5D_0$ levels of europium, respectively. Since the phonon energies for yttria nanoparticles have been estimated to be 25 – 800 cm^{-1},[46] energy transfer probably involves a multiple phonon process, and is more likely to occur to the $^5D_1$ Eu^{3+} level. The weak (or absent) energy transfer is most likely due to two possible causes: 1) large donor-acceptor (D-A) distances, and/or 2) surface defects quenching the energy transfer processes.[231,232]

Eu^{3+}-Tb^{3+} energy transfer in bulk materials is known to be due to a dipole-dipole interaction,[55] which has a rate dependence on D-A distance of R^{-6}.[233] In zinc-phosphate glass, the maximum D-A mean distance where energy transfer was observed between Tb^{3+} and Eu^{3+} was 1.79 nm.[233] Assuming our nanoparticles can be represented by two adjacent 6 nm diameter spheres and that the Tb^{3+} - Eu^{3+} interaction distance is 2 nm, 1.6 % of the donors or acceptors are close enough to interact with each other. Assuming an even mixture of spheres with D or A ions that are organized with cubic close packing, the average number of D-doped particles neighboring an A-doped particle is 6. Therefore, even with the best packing, less than 10% of the optically active ions in a given particle are within a distance where energy transfer could occur. This exercise demonstrates one difficulty of using nanoparticles as opposed to lanthanides doped directly into solids.

The doped yttrium oxide nanoparticles studied in Chapter 3 likely has a lower packing density than for ideal spheres, and also has less-than-ideal mixing of the particles. To counter this in the future, a few strategies could be employed. The first is to optimize the dopant concentrations to maximize the number of ions per particle before the onset of concentration quenching.[44] Another option would be to try smaller particles. If particle size or surface-related optical effects are not dominant, then the use of smaller particles would result in a greater percentage of D or A ions within energy transfer distance. Finally, optimizing the mixing/packing of particles would maximize the potential for interparticle energy transfer. One possible way to do this is dispersion of particles in solution followed by mixing and allowing particles to precipitate. Another option would be use of self-assembly methods to build particle structures with optimal packing. Enhancing the mixing and packing of the particles will increase the probability of ET and enable better studies of the phenomenon.

Surface defect quenching is one other possible explanation for the weak energy transfer. Quenching can result from traditional crystalline defects or surface contaminants, and is known to influence the luminescence of bulk inorganic materials like laser crystals and phosphors.[231,232] In another example, lattice hydroxyl groups are known to quench luminescence of Tb^{3+} and Eu^{3+} in bulk materials due to multi-phonon relaxation of excited ions that are coupled to OH groups.[56] Therefore, surface hydroxyl groups (and possibly carbonate groups) on the yttria particles are also capable of quenching the lanthanide luminescence. Since ions that are capable of participating in interparticle energy transfer processes are more likely to be near the surface of the particle, any surface quenching is expected to have a greater effect on energy transfer

processes than luminescence, which can still occur in less-quenched "bulk" ions in the interior of the particles.

Reducing surface defects (by annealing and reducing air exposure), optimizing dopant concentrations, probing smaller particle sizes, and using better particle packing and mixing methods may enhance the degree of interparticle energy transfer occurring for these lanthanide-doped materials. A significant improvement of energy transfer is required before these materials could realistically be used in applications. Success with ET enhancement would enable the use of these particles in a variety of ways, such as complex analytical assays that use selective excitation of one lanthanide, as probes of particle-particle distances in nanostructured materials, or as replacements for quenching and D-A distance studies.[54]

7.2.2 Ln^{3+}:Gd_2O_3 Nanophosphors

The survey study detailed in Chapter 4 identifies three lanthanide candidates for use in nano-phosphor based biological tags or assays. The lifetimes of the Tb^{3+}, Eu^{3+}, and Dy^{3+} emission are long enough to gate out short-lived autofluorescence in biological samples. Further work should be done in a few areas. First, the possibility of NIR excitation of these ions in nanomaterials should be investigated. This would enable the exclusion of autofluorescence in biological samples. One possibility would be the use of Yb^{3+} to excited Dy^{3+} ions. Similar transfer to Er^{3+} and Sm^{3+} has already been observed.[79,89] Another potential application for this material is as a combination contrast agent[86] and luminescent probe. This application would enable dual detection mechanisms for *in situ* and *ex situ* work. One other interesting result from this study that may prove fruitful to study is the relatively weak green emission compared to the red emission of

Pr^{3+}. In Gd_2O_3 microcrystals and particles annealed via laser reflections hitting the collection plate, the green emission has greater intensity.[93] This result implies there may be a particle size-induced preferential quenching of the green emission. Future particle size studies may confirm this observation. Regardless of this result, gadolinium oxide nanoparticles were found to be sufficient hosts for lanthanides for use in luminescent applications when UV excitation is used. Recent work in the literature demonstrates the continued interest in this material.[77,79,80]

7.2.3 Morphology

In addition to the properties of individual nanoparticles, the properties and structure of as-deposited particle films produced by a given synthetic method are important, particularly if the method is to be applied industrially.[95-97,116] Our study has developed a simple understanding of the role that the buffer gas plays on the growth of nanoparticle films. Starting with preliminary results, a general prediction of film morphology can be made for a particular material and set of buffer gas conditions.

In general, the transition pressure where the film growth mechanism changed was found to depend on the thermal and mass transport properties of the gas.[113] Properties of the gas that result in faster cooling rates, greater plume compression, or more turbulent particle transport dynamics decrease the transition pressure. An increase in gas pressure also results in faster cooling and greater aggregation of the particles prior to deposition.[139] One factor which was not probed is the role of the physical properties of the target on the transition pressure. Presumably, properties that influence the rate of evaporation such as laser adsorption coefficient, melting temperature, and other physical parameters also demonstrate some control over aggregation and therefore film morphology.[12]

While this study has uncovered the likely mechanism of control over the film morphology, the influence of gas properties on aggregation is not completely understood. It would be ideal if a model were developed to determine the relationship between gas properties and particle aggregation. Such a model, coupled with experimental data, would enable a user to predict the morphology of a given material for particular conditions. Since some knowledge of the gas on particle size is known, one may be able to independently control particle size and composed film morphology, which would represent a major advantage of the synthetic method.

In addition to modeling work, it may be valuable to map out film properties as a function of film morphology. The large difference between the two film structures should result in significantly different film properties. For example, diffusion of gases is likely to be greater for the fractal-like aggregate film due the free space,[97] while particles within the structures of the column-like film will have greater shielding from the gas stream. Likewise, properties that are enhanced by the greater density of particles such as energy transfer or greater reactivity due to particle interaction at grain boundaries[234] might be improved by producing the columnar films.

Any post-synthetic processing also can be affected by the film structure. For example, scraping the columnar film results in the removal of whole columns of material, while the film produced at higher pressure is removed in the form of larger flakes. This means a film of the column structures could be "machined" to produce features such as trenches, islands, or reservoirs for some purpose. In another example, a very thin film of particles could be produced under higher aggregation conditions, and a second material

vaporized at low aggregation conditions, resulting in a film with a good degree of particle intermixing.

A final point that merits further study is the source of defect sites observed in the films. The ability to control these defects may lead to a new strategy for constructing micron-scale structures. Take for instance the ring defects shown in Figure 5.14. It may be possible to use this defect as a template to deposit a metal (or other material) within the defect void area, and then etch the particles away by sonication or weak nitric acid.

This study has uncovered the underlying cause of the change in film morphology, and enables a rough prediction for new materials and experimental conditions. Further work to investigate the role of individual gas properties on aggregation may result in a model that can yield predictions with higher accuracy, and also may shed light into the dynamics occurring during the gas-phase condensation process.

7.2.4 Reactivity of Metal Oxide Particles with DMMP

Our results from the study of the reactivity of metal oxide particles with DMMP correlate well with previous studies of metal oxides, yet also represent an important advance. Use of deuterated simulants as well as methanol and TMP has increased confidence in vibrational peak assignments made in previous studies. This work also introduced a new material (Y_2O_3) to the environmental decontamination field, and it is hoped other novel materials will also be studied. Under vacuum conditions, the interaction between DMMP and the Y_2O_3 particles is characterized by a high sticking probability, and a good degree of reactivity. Yttria particles dissociate DMMP to a high degree at room temperature under vacuum conditions. While reactivity of DMMP on metal oxides at room temperature is not unknown, this study indicates that decomposition

of DMMP occurs at very low temperatures. If this behavior translates to real nerve agents (which might be anticipated based literature data), then metal oxide nanoparticles could be a good choice for decontamination or sorption in cold climates.

While yttria was studied with the greatest detail, its usefulness for real application is questionable. Yttria particles were found to be very reactive, but the products remain surface-bound and block further uptake. This prevents the material from use as a catalyst. The other primary drawback of yttria is its affinity for CO_2, which appears to block adsorption sites. Since a large portion of Y_2O_3 particles are expected to convert into carbonate species at long time periods, it is not likely that yttria itself is a good choice for an actual decontamination strategy. However, two candidates have been identified that may be more applicable for a decontamination application. Both under ambient and vacuum conditions, HfO_2[235] and ZrO_2 appear to be the best metal oxide material among those tested. In addition to superior reactivity, both of these oxides adsorb much less CO_2 than Y_2O_3, which would make these oxides more robust for use under ambient conditions. I suggest that these nanomaterials be investigated for potential use in CWA-related applications, or as a potential catalysts or catalyst support.

Perhaps the most important result from this study is the observation of reactivity dependence on particle size. Size-enhanced reactivity has been noted in a few studies, particularly those involving small metal nanoclusters.[236-238] Similar studies have found that reducing the size of clusters or nanoparticles will enhance the strength of adsorption of molecules.[238,239] In addition, MgO nanoparticles have been found to show increased reactivity with decreasing size towards DMMP at 775 K.[220] A common explanation in the literature for enhanced reactivity is the increase in defect sites (such as edge, vertex, and

vacancy sites.) Defects are also well-known centers of chemical reactivity on catalysts such as TiO_2[240] and oxide-supported metal clusters.[241] In fact, STM has been used to correlate reactivity of surfaces with defect concentration.[242] At least one paper has used selective passivation of defect sites on nanoclusters to garner more support for this argument.[237] The results presented in Chapter 6 are consistent with the increase of the relative number of surface defect sites driving the greater reactivity of the smaller particles. While the nature of the site that is responsible for enhanced reactivity is unknown, it is apparent that reducing the size greatly increases reactivity. This result, along with the results from the survey study implies that the identity of the metal oxide material may not be as important as particle size when determining the reactivity of the sample. The oxide surface may just be providing coordination sites for the DMMP molecules, while defect sites and hydroxyl groups are responsible for the reactivity at ambient temperatures.[201] With this in mind, it may not be a coincidence that our smallest particles (ZrO_2) also appear to be the most reactive.

Once the nanoparticle surface is characterized and the reactive sites are understood, focus should be moved to developing a new material that has desirable properties of metal oxides. For example, a heterogeneous catalyst could be designed where the oxide domains "crack" DMMP (or a real agent), and diffusion to a domain with less affinity towards the surface species could result in the release of less-toxic gas products. Regardless of the outcome of this future work, it appears that metal oxide nanoparticles have great potential for use in environmental remediation and protection.

7.3 Concluding Remarks

This dissertation has presented a series of studies of the optical, chemical, and micron-scale morphology properties of metal oxide nanoparticles synthesized by the inert gas-phase condensation method. Lanthanide-doped yttrium oxide particles show evidence for weak interparticle energy transfer. This result has significant implications since interparticle energy transfer could be used as a probe for particle distance in nanocomposites or for sensing applications. The author believes that the observed energy transfer can be enhanced by optimizing dopant concentrations and particle packing. Additional improvement may be gained by altering particle size or changing the host material. The observation of lanthanide-mediated, nanoparticle to nanoparticle energy transfer is significant, and to the author's knowledge, has not been reported in the literature. Further investigation into this phenomenon is strongly encouraged.

Lanthanide-doped, gadolinium oxide nanophosphors have also been found to exhibit sufficient luminescence intensity and lifetimes for use in bioanalytical applications. Significant work on gadolinia nanophosphors using lanthanide dopants in the literature since the completion of this study underscores the potential use of these materials. It may also be possible to use lanthanide-doped Gd_2O_3 nanoparticles as a dual luminescent reporter and contrast agent, which would enhance the possibilities of this material. The author suggests the most interesting potential application is the possibility of the use of Yb^{3+} or other dopant to excite the lanthanide ion by infrared light pumped upconversion. This would enable the elimination of autofluoresence from biological samples completely. A final result which the author emphasizes is the possible observation of particle size-influenced luminescence from Pr^{3+}:Gd_2O_3. If this result is

reproducible, it may provide a probe for understanding the changes on phosphor materials induced by decreasing size, such as changes in the phonon spectrum.

In addition to the properties of the individual particles, the characteristics of particle ensembles are also important to understand. The ability to control as-deposited film morphology of nanoparticles is an important aspect to consider for various applications. By controlling the film morphology and structure, bulk film properties may also be influenced. With this in mind, the author suggests further investigation into the physical properties of the particle films, such film adhesion or conductivity. Results from this study indicate that particle size is independent of the film morphology, although conditions that lead to greater particle size also lead to greater particle aggregation). Since particle size and morphology are independent, a specific buffer gas can be chosen to select both the desired particle size and the desired film morphology. For example, if one were using metal oxide nanoparticles to purify a gas stream, smaller particles may have more desirable adsorption characteristics. However, the film structure that is grown under higher pressures will likely have better performance for removing target materials from a gas stream. Therefore, the choice of buffer gas (and pressure) may significantly influence product performance.

Another branch of this work studied the chemical properties of metal oxide particles. It is clear from the present results that hydroxyl groups are critical for the interaction of DMMP with metal oxide surfaces, and probably represent a significant factor in the reactivity of the surface. The formation of the bridging species along with a surface methoxy group is also clearly defined. However, the precise mechanism of this reaction is not understood. Learning what sites are reactive should be the next goal of this

research and understanding the nature of these sites may enable the tailored design of highly reactive materials. The observation of a strong interaction between DMMP and metal oxide nanoparticles agrees with previous studies; however, the unambiguous change in reactivity with particle size does demonstrate the strong control that size has on the properties of nanomaterials. This result represents the most important conclusion from this work. Defect sites that exist in greater numbers on the surfaces of smaller particles are implicated as the source of the enhanced reactivity, and should therefore be studied to identify their nature. The yttria particles tested in the UHV study represent a system that is among the most reactive towards DMMP that has been studied. However, the analogous ambient air study indicates that yttria may be a relatively poor choice for agent decomposition, likely due to surface contamination. Regardless, other materials such as hafnia and zirconia appear very promising as sorbants or decontamination agents for CWAs or other environmental pollutants. Ultimately, the most important feature of these materials may be the particle size as opposed to the oxide that composes them. As stated earlier, the author does not think it is coincidental that our smallest particles show the greatest relative reactivity. As future researchers gain better understanding of the properties of metal oxide nanoparticles, it seems likely that these materials will be incorporated into optical devices and probes, as well as devices for the protection from and decontamination of CWAs and other environmental contaminants.

Appendices

Appendix A: Background CWA and CWA Simulant Chemistry on Metal Oxides

A.1.1 MgO

Metal oxide sorption and reaction with organophosphates has been studied in the greatest detail on magnesium oxide due to its known basic active sites, ease of preparation, and simple crystal structure.[243,244] MgO also is known to have many types of surface defects, which add to the rich chemistry that may occur on the oxide.[245] Studies of DMMP on MgO have mostly been performed by Klabunde and co-workers. Initial studies showed that DMMP and other organophosphates initially interact with MgO through hydrogen bonds to the phosphoryl oxygen, and decomposition via stepwise elimination of the methoxy groups follows at elevated temperatures.[187,188] Klabunde's work indicates that the reaction of organophosphonates with MgO is stoichiometric and that reaction yield increases with surface area.

Adsorption and decomposition of organophosphines R_3P, organophosphites $(RO)_3P$, and organophosphates $(RO_3)P{=}O$, was studied by Lin and Klabunde[187] on MgO that had been pretreated at 573 or 973 K for 14 hours. Adsorption was performed in a vacuum chamber by exposing saturation amounts of phosphorus compounds followed by evacuation to low vacuum. It was found that the amount of phosphorus species adsorbed decreased in the series: phosphites, phosphates, and phosphines. Substitution experiments found that adsorption decreased with increasing size due to steric effects, and also decreased with the lower basicity of the adsorbate. Increasing sample temperature decreased the sorption capability of MgO, leading the authors to conclude that multiple surface interactions exist. This conclusion was supported when it was found that saturated

MgO samples at elevated temperatures would adsorb greater quantities of phosphorus compounds when the temperature was decreased. Surface-bound water was identified as an important factor in the adsorption process when it was determined that MgO pretreated at 573 K adsorbed a much lower amount of $(CH_3CH_2O)_3P$ than oxide treated at 973 K. Other studies (discussed below) have further implicated hydroxyl groups and water as critical actors in oxide-simulant interactions.

Following this work, infrared spectroscopy was used to identify reaction products of triethyl-phosphorus species after exposure to MgO and after baking to 473 K.[187] IR spectra of adsorbed triethylphosphine showed little change from the gas phase spectrum, indicating a weak interaction between this species and the oxide. Decomposition of the triethylphosphite was found to adsorb through the phosphorus atom, and decomposes to an ether upon heating via a nucleophilic substitution at the phosphorus atom followed by a nucleophilic substitution at the secondary carbon atom. IR spectra showed a slight shift in the ν(C-H) peaks and a broadened and red-shifted ν (P-OC) mode, indicating a net gain of electron density. Triethylphosphate was also found to adsorb similarly through the phosphoryl group, but a loss of electron density was proposed due to blue-shifts in the peaks. An electrophilic attack on the oxygen was proposed due to lack of observed ether and the blue-shift of peaks in the spectrum.

DMMP was also studied on a series of metal oxides, including MgO, by Aurian-Blajeni and Boucher.[177] Their study utilized diffuse reflectance-FTIR (DRIFTS) to study the powder metal oxides wetted with liquid DMMP or vapor exposed at a variety of temperatures, 298 – 375 K, and times, 30 minutes - days. The dominant difference between the neat liquid DMMP IR spectrum upon adsorption was the energy decrease in

the phosphoryl mode at 1240 cm^{-1}. A relation was discovered between the isoelectric point of the metal oxide and the peak shift, leading to a proposal that the phosphoryl mode energy depends on the acidity of the oxide. Adsorption of DMMP on the metal oxides was found to be an irreversible process that is influenced by the surface area of the oxide, and is related to temperature in a Arrhenius-like manner. Arrhenius-like behavior was attributed to an activated chemisorption process. No evidence for catalytic activity was found, however it is likely that decomposition of DMMP to form the methyl methylphosphonate bridging species occurred to some degree on the samples.

Li, Schlup, and Klabunde continued previous work with two studies of DMMP and its analogs on heat treated magnesium oxide materials.[188,201] In the first study, heat treated MgO with surface areas of 10 – 390 m^2/g was exposed to DMMP, triethylphosphate (TEP) and trimethylphosphate (TMP) and studied with fourier transform infrared – photoacoustic spectroscopy (FTIR-PAS) using a closed gas cell and an ultra-sensitive microphone. FTIR studies were performed after heat treating the MgO powder at 573 K under a He gas flow, and then exposing the sample to the phosphorus simulant for 1 hour, followed by evacuation for 0.5 hour and transfer to the PAS cell. Further exploration was performed by injecting organophosphorus compound into a He gas stream that flowed through a U-tube with the oxide at 463 K, and then onto a GC column for gas species analysis.

FTIR-PAS measurements of all three phosphorus species adsorbed on MgO demonstrated the following general results in comparison to neat liquid spectra: all peaks broadened, the ν CO-(P) band did not shift, and the ν (P=O) band downshifted in energy by 51 – 58 cm^{-1}. Two possible adsorption structures were proposed as shown in Figure

6.3, one involving phosphoryl group interaction with a metal atom (Lewis acid site) or with a hydroxyl group. To identify this species, MgO was heat-treated at 973 K to reduce the residual hydroxyl groups on the oxide by a factor of 30. Little difference was found between the IR spectra of DMMP adsorbed to MgO treated at 773 and 973 K, implicating domination by the Lewis acid site structure (Figure 6.3 b). Results from this experiment also provided evidence that fresh DMMP molecules can oxidize surface methoxy groups to form a deoxygenated DMMP species and gas-phase formic acid. Evidence for the formation of the bridging species (as shown in Figure A.1) was observed at room temperature, with complete decomposition occurring at 463 K. Investigating the role of surface area, it was found that the amount of DMMP adsorbed correlates with the raw surface area, but no difference in the FTIR-PAS peak shapes was observed, implicating surface area and not specific defect sites in the adsorption of DMMP.

Several studies have used temperature-varible stainless steel U-shaped tubes that are packed with solid powder, placed in line with a controlled gas flow source, and flow into a GC or GC/MS for analyzing gas-phase products. Studies of MgO powders using the U-tube GC reactor[201] found that volatile products of DMMP decomposition at elevated temperatures were formic acid (major product) with small amounts of methanol, dimethyl ether, and ethane. Decomposition capacity of sorbants was found to increase with contact time (lower reactor flow rate) and temperature. At lower temperatures, volatile products were released slowly, due to a strong product-substrate interaction. As in other studies, the decomposition was found to be stoichoimetric, and no phosphorus-containing species were observed in the gas phase, instead remaining on the MgO

sorbant. Saturation coverage of DMMP and its decomposition product on the MgO sorbants were determined to be 1 DMMP per 2 Mg surface atoms.

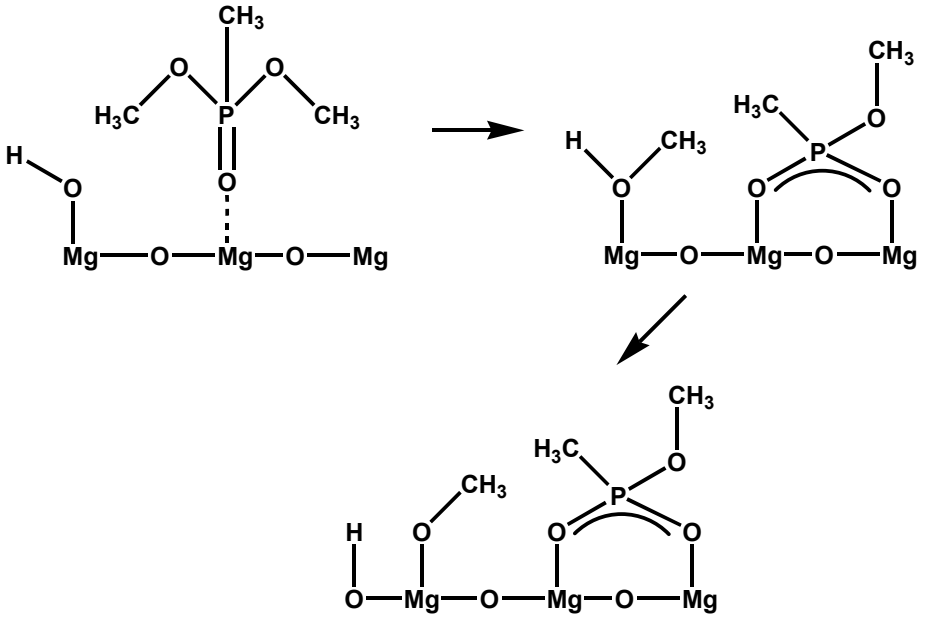

Figure A.1 Adsorption of DMMP followed by formation of the bridging species and surface methoxy group.

Klabunde, Zhanpeisov, and co-workers studied a theoretical model of DMMP on magnesium oxide surfaces in order to solidify the understanding of the decomposition species proposed in the previous experimental studies.[189] Dissociative adsorption of DMMP was found to be thermodynamically favored over molecular adsorption to a single Lewis acid Mg^{2+} site on a 24 atom, two-layer model of the MgO (001) plane via a MINDO/3 computational method. The authors also considered a molecular adsorption pathway involving two Mg^{2+} sites, finding this interaction to be unfavorable. Further tests were performed to identify the fate of the surface-bound methoxy groups. This species could be oxidized by the phosphoryl oxygen of another DMMP molecule to produce formic acid and $(CH_3O)_2PCH_3$ (see Figure A.1), or could react with a surface hydroxyl or

water to form methanol. Calculations also indicated that ions with reduced coordination are thermodynamically more favorable sites for molecular and dissociative adsorption of DMMP. This result implies that ions found at edge and corner sites will more readily serve as sorption sites in addition to possessing greater reactivity. Findings from this study support the results of the Klabunde group's experimental work, and also reinforce the hypothesis that molecular adsorption occurs through the phosphoryl oxygen, and dissociation then occurs if the temperature is high enough.

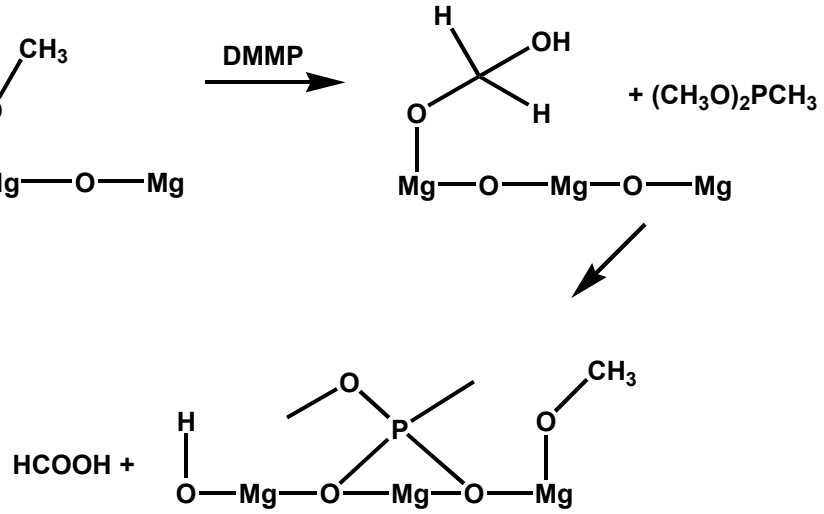

Figure A.2 Surface methoxy groups from DMMP dissociation can be in turn oxidized by a new DMMP molecule. Formic acid is released, and the deoxygenated DMMP molecule is free to dissociatively adsorb.

A.1.2 Magnesium Oxide Nanoparticles

Klabunde and co-workers focused on nanoscale particles after studying CWA's interaction with magnesium oxide. In an initial study, Li and Klabunde[201] studied MgO nanoparticles as potential destructive adsorbants for CWAs. Using a U-tube coupled with a GC, followed by FTIR-PAS, nanoscale MgO was found to be superior in adsorbing DMMP. The decomposition was stoichiometric, with 2 surface MgO moities required to decompose 1 DMMP molecule. Capacity of the MgO particles to decompose DMMP was influenced by the temperature of the sample due to volatilization of some products, which

liberates MgO surface for further reaction. In addition, the immobilized decomposition products were not found to be crystalline in XRD data, indicating that the reaction does not require a specific defect site on the MgO surface.

An extension of this work by the Klabunde group was performed to further investigate nanocrystalline MgO as a reactive sorbant material.[190] As before, a pulsed GC-MS microreactor with similar conditions as previously discussed was used. DMMP, trimethyl phosphite, trimethylphosphine, triethyl phosphate (TEP), and triethyl phosphate were used as simulants in this study. In the empty stainless steel U-tube, triethyl phosphite and TEP decomposed to yield C_2H_4 as well as phosphorus oxide species. For the other simulants, decomposition products were not observed until the blank cell temperature was raised to 1023 K, and further decomposition pathways were discovered at 1123 K. When the same experiments were performed under the presence of water, hydrolysis products were observed for trimethyl phosphite and DMMP at 773 K, but little effect was noted for TEP, triethylphosphate, and trimethylphosphine. The reduced decomposition temperature for trimethyl phosphite and DMMP in the presence of water underscores its important role for destructive CWA materials.

Investigating the ability for nanoscale MgO to decompose these phosphorus compounds, samples with surface areas of 130 and 390 m^2/g were tested.[190] For all of the phosphorus compounds except trimethylphosphine, decomposition began at 443 K and was complete at 473 K on 130 m^2/g MgO. Formic acid was the initial major product for DMMP and trimethyl phosphite, while ethanol was the first decomposition product for the ethoxy-substituted compounds. The products composition altered at 773 K for DMMP and trimethyl phosphite, and at 573 K for the ethoxy-substituted compounds.

Trimethylphosphine began decomposition on this material at 873 K. No phosphorus-containing species were observed in the gas-phase when the reactor was heated to 973 K, confirming Klabunde's previous hypothesis that phosphorus-containing species remain on the oxide. When water was exposed to the oxide bed along with the phosphorus compounds, no influence was noticed for the ethoxy phosphorus compounds; however, water reduced the decomposition temperature of trimethylphosphine. The presence of water changed the dominant decomposition product of DMMP and trimethyl phosphite from formic acid to methanol, and reduced the temperature of the formation of secondary products (CO, H_2O, and CH_4) by 100 degrees to 773 K. Water also was found to regenerate the sorbants by causing the release of non-phosphorus containing volatiles, and increased the capacity of MgO decomposition of DMMP by 30 % at 773 K. 390 m^2/g MgO was found to have higher capacity to adsorb and decompose the phosphorus compounds, providing further evidence that surface area is a critical factor for sorbant design. In addition, the higher surface area sample demonstrated a decreased decomposition temperature for trimethylphosphine, however no significant difference was observed for the other phosphorus compounds. The latter result does indicate the particle size may influence the reactivity of a metal oxide material.

Most of the studies discussed above identify the bridging O-P-O species shown in Figure A.1 and surface-methoxy groups as products of the initial dissociation of DMMP on metal oxide surfaces, but do not investigate the subsequent oxidation of the $–OCH_3$ group to formic acid. Li et al.[190] performed a labeling experiment where $Mg^{18}O$ was used as the reactive bed. Upon DMMP exposure, the formic acid product included one ^{18}O atom, indicating oxygen exchange occurs on the surface. Klabunde proposed that the

bridging O-P-O species is likely mobile on the surface and that oxygen scrambling occurs as shown in Figure A.2. Another pathway for surface $–OCH_3$ group is formation of methanol after interaction with water, confirmed by the release of CH_3OD from DMMP-exposed MgO upon the addition of D_2O.

A.1.3 CWA interaction with MgO

Researchers have also used parallel studies with actual chemical warfare agents to validate the use of simulants on metal oxides. Interaction of the CWAs VX, GD, and HD have been studied on MgO nanoparticles at room temperature by Wagner, Bartram, Klabunde, and co-workers.[173,176] Multi-element solid-state magic angle spinning (MAS) NMR was used to study the interaction of neat liquid agents to the nanopowder. Particles had been exposed to air prior to study, therefore the degree of hydroxylation is unknown.

Similar to the organic phosphorus molecules, VX and GD were found to hydrolyze on MgO to form less toxic, surface-bound species. The first-order half-life for VX was found to be very short at 28 minutes, while hydrolysis of GD was slower, leading to a 68 hour first-order half-life. For both of these agents, further decomposition occurred to form surface-bound methyl phosphonic acid (MPA) on the surface. The authors were surprised that an anticipated toxic hydrolysis byproduct (S-(2-diisopropylamino)ethyl methylphosphonothioate) was not found upon GD decomposition on MgO. HD was found to undergo hydrolysis and elimination of the chlorine groups, yielding surface-bound thiodiglycol or gas-phase divinyl sulfide. The ratio of hydrolysis to elimination was found to vary on different metal oxide nanoparticles, indicating some influence of the metal chosen.

As with the organophosphorus simulants, decomposition of V and G agents resulted in a strongly bound phosphorus residue (see Figure 6.6) on the oxide surface, blocking the site from further reaction. Room temperature reaction was stiochiometric as with the simulants discussed previously, and the chemistry was also found to be analogous to solution-phase hydrolysis chemistry of these agents.

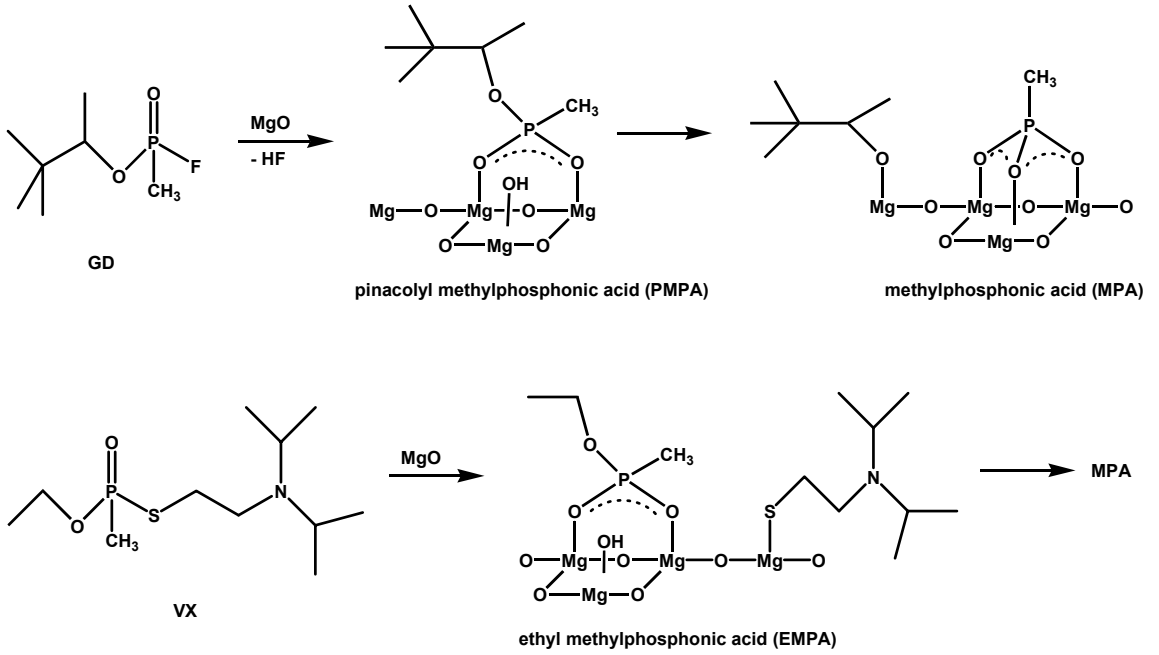

Figure A.3 Decomposition of nerve agents on sol-gel MgO nanoparticles. Products were non-toxic phosphate complexes. GB decomposes in a similar manner as GD.

Kinetic investigation of the decomposition found a fast step followed by a slower steady-state decomposition. The fast step was attributed to liquid agent spreading over the porous surface, implying the influence of viscosity and surface tension of the liquid. The slow steady-state reaction that follows the fast step is due to the evaporation and diffusion of gas-phase agent to remaining virgin MgO. Since the gas diffusion coefficients of the agents are roughly similar, evaporation was assigned as the limiting step. Indeed, the steady-state half-life was found to correlate with the vapor pressure of the agent.

Interaction of CWAs with MgO was also investigated in a theoretical study of GB on MgO nanoparticles.[192] Two-atom thick $Mg_{16}O_{16}$ and Mg_4O_4 cluster models were developed using B3LYP/6-31G(d) and MP2/6-31G(d) levels of theory to compare the GB's response to adsorption on crystalline or defect (edge or step) sites. Hydroxylation of the small cluster model was also performed to contrast "dry" and "wet" nanocrystal surfaces.

Adsorption of GB (Sarin) on the $Mg_{16}O_{16}$ model resulted in some redistribution of electronic density associated with an internal polarization. However, the results indicate that Sarin is molecularly adsorbed in a way characteristic of physisorption and does not decompose on the dehydroxylated MgO cluster. The smaller cluster model shows a much stronger interaction with GB that is more characteristic of chemisorption, that is similar to the molecularly adsorbed species shown in Figure A.1 and correlates with experimental results for DMMP on MgO. Four types of interaction were observed for the small particles: molecular adsorption at hydroxyl or Mg ion sites; (Figure 6.3) and decomposition on both hydroxylated and unhydroxylated MgO. Decomposition occurs by transfer of the F atom to a Mg ion on dry Mg_4O_4, while HF is formed on hydroxylated MgO fragments. Physisorption was attributed to the creation of hydrogen bonds and to ion-dipole and dipole-dipole interactions between GB and the surface. In the case of decomposition, covalent bonds formed between the surface and GB. Sarin adsorbed onto hydroxylated Mg_4O_4 fragments were found to be less stabilized than when adsorbed onto dry Mg_4O_4, regardless of whether the adsorption site was at a hydroxyl group or a Mg ion. These results provide evidence of the importance of hydroxylation on metal oxide

surfaces when considering CWA interaction. More importantly, this work provides more evidence of the superior reactivity of nanoscale materials due to edge and corner sites.

A.2 WO_3

The interaction of tungsten oxide with CWAS was first studied by Aurian-Blajeni and Boucher using reflectance infrared methods to confirm adsorption of DMMP on low surface area WO_3.[177] This exploratory study resulted in evidence for adsorption but was not focused on observing decomposition. Interaction of CWAS with this metal oxide was further studied by the Tripp group.[178] A high surface area WO_3 powder was exposed to DMMP, TMP and DMHP at room temperature and then heated to study the decomposition of the simulants. It was concluded that the phosphonates adsorbed through a hydrogen bond via the P=O functionality at room temperature and the methoxy and methyl groups were cleaved above 473 and 573 K, respectively. Above 573 K, a stable phosphate species was observed that poisoned the catalysts site, reducing the effectiveness of the material as a sensor.

Further work by the Tripp group studied DMMP, TMP, and the chlorinated organophosphorus compound MDCP adsorbed to WO_3 nanopowders that were pretreated at different temperatures.[179] This allowed comparison of the influence of adsorbed water and hydroxyl groups on adsorption of the simulants. In a manner similar to TMP and DMMP, MDCP was adsorbed through the P=O functional group to surface Lewis acid groups and through molecularly adsorbed water as well as Brønsted acid hydroxyl groups. Importantly, the relative number of molecules bound to these three sites varied with pretreatment, implying that the degree and type of hydroxylation or hydration of the metal oxide influences the adsorption of the simulants. The chlorinated MDCP was found

to readily hydrolyze with surface water in a similar manner to other G-agents,[175] prompting the authors to suggest halogenated simulants for investigating the influence of environmental levels of moisture on sensors.

A.3 TiO_2

Rusu and Yates[184] published the first detailed study of DMMP on TiO_2. Using reflection infrared methods, the adsorption of DMMP was studied on the thermally pretreated metal oxide at 160 K and decomposition was studied at temperatures up to 486 K. Below 160 K, DMMP condensed in an ice phase on the metal oxide, and diffused along the surface and began to interact with hydroxyl groups as the temperature was raised to 200 K. In this range, isolated hydroxyl groups were replaced with associated groups and the ν (P=O) mode simultaneously redshifted from the ice phase value by 32 cm^{-1}. Evidence was found for adsorption both to Lewis acid sites as well as hydroxyl groups via hydrogen bonding. Above 214 K, hydrolysis was observed, yielding a surface-bound methoxy group and a bridging O-P-O species seen in Figure 6.4 while surface hydroxyl groups were consumed. The hydrolysis bridging species remained on the surface at elevated temperatures while the surface methoxy groups desorbed as gaseous methanol. Similar results were observed by Kim et al. on TiO_2, where it was found the methoxy groups of DMMP were lost at about 473 K.[178]

Rusu and Yates also studied the photooxidation of DMMP on TiO_2 powders, finding that both the P-CH_3 and P-OCH_3 groups oxidized under UV-irradiation at 200 K leaving a P=O surface bound species.[183] Hoffmann and co-workers[180] confirmed these results, and also found that sample pre-treatment influences the adsorption and reactive properties of the metal oxide. Results indicate that dissociative adsorbtion of DMMP at

room temperature occurs at isolated instead of associated hydroxyl sites, and thermal dehydration reduces the reactivity of the sample, while light-assisted dehydration does the opposite by forming reduced Ti sites. DMMP adsorption was associated with a loss of isolated hydroxyl groups and formation of associated hydroxyl groups. Ultimately, a PO_4^{3-} species was found to remain on the surface after complete reaction.

Trubitsyn and Vorontsov studied the photocatalytic oxidation of DMMP on TiO_2 while varying the relative humidity of the environment.[182] Untreated TiO_2 was found to hydrolyze a submonolayer coverage of DMMP under ambient conditions and 1% relative humidity. Hydrolysis was found to involve only one methoxy group, leaving the previously mentioned bridging species and methoxy group on the surface. At saturation exposure levels, multilayer adsorption was observed, with hydrolysis occurring for $1/5^{th}$ of the adsorbed DMMP molecules. For this higher exposure level, it was found that the surface methoxy groups were displaced to form gas phase methanol.

Performing the same experiments at 50% relative humidity levels resulted in identifying water as a reactant in the hydrolysis reaction, as the amount of gas phase methanol released increased. In addition, the TiO_2 adsorbed significantly more DMMP when in the more humid environment, but some DMMP desorbed as the surface-bound water was depleted via hydrolysis. Trubitsyn and Vorontsov concluded that that polylayers of DMMP will form in a water layer adsorbed to the surface under humid conditions.[182]

Chen and coworkers also studied DMMP decomposition on TiO_2, focusing on a pretreated single crystal (110) surface under UHV conditions.[181] TPD and detailed analysis of XPS spectra indicated that molecularly adsorbed DMMP was the dominant

species at saturation exposures. Two linearly independent surface species were noted in both the C(1s) and P(2p) regions from room temperature to 700 K. At about 500 K, molecular DMMP desorbed from the surface, while carbonaceous decomposition products were observed to desorb at temperatures up to 800 K. As observed in other studies for metal oxides, phosphorus oxide species remained on the surface at 1000 K. Furthermore, it was discovered that significant cleavage of P-CH_3 bonds occurred before the P-OCH_3 bonds were completely eliminated. This result stands in contrast to the work of Rusu and Yates, and was attributed to the completely dehydroxylating pretreatment conditions.

The Chen group also studied well characterized Cu[246] and Ni[247] clusters and films supported on TiO_2 (110). The copper structures were found to enhance irreversible adsorption and reactivity compared with the bare TiO_2, but no size effects were observed for Cu clusters with diameters from 4 – 14 nm. For Ni clusters, smaller clusters were found to be more active than larger annealed ones, but this was not attributed to an innate size effect. Both of the surfaces were poisoned with PO_x at high temperatures, making the goal of catalysis unlikely for the materials.

A.4.1 Al_2O_3

Templeton and Weinberg published some of the early studies of organophosphorus compounds on aluminum oxide.[199,211] These studies involved alumina exposure to a wide range of simulant levels from 200 – 673 K in an UHV environment. Inelastic electron tunneling spectroscopy (IETS) was the primary analytical method used to study Al_2O_3 surface chemistry for these experiments. Peak assignments in the IET spectra were determined with the aid of spectra of adsorbed deuterated DMMP d_6

(DDMMP), methylphosphonic acid, and methanol d_4. Results indicated that DMMP molecularly adsorbs to Al_2O_3 at 200 K through the phosphoryl oxygen. This interaction was attributed to a Lewis acid/Lewis base complex between DMMP and surface hydroxyls. At 295 K, dissociative adsorption of DMMP occurred via cleavage of a P-OCH_3 bond to form an O-P-O bridging species.[199] DIMP was found to adsorb molecularly while diphenyl methylphosphonate (DPMP) was found to dissociatively adsorb at 295 K. Upon increasing the temperature to 373 K, DIMP dissociated.[211] At elevated temperatures, cleavage of carbon-oxygen bonds was observed.

Mitchell and co-workers studied the interaction of DMMP with alumina surfaces using diffuse reflectance Fourier transform spectroscopy (DRIFTS).[1,248] In the initial survey study, commercial γ-Al_2O_3 was calcined, exposed to DMMP overnight at room temperature, and then diluted to 5 wt% with KBr to reduce the oxide stretching peaks in the infrared spectra. Confirming the results of Templeton and Weinberg, DMMP was found to adsorb at room temperature through the phosphoryl oxygen with the observation of a 30 cm^{-1} redshift of the P=O mode from the diluted liquid value. No evidence was found for dissociation of DMMP until the temperature reached 473K, when a surface bridging O-P-O species was observed, due to loss of methoxy groups from the molecule. MgO and La_2O_3 studied in the same manner were found to be more reactive, with cleavage of the methoxy group occurring at 373 K. At 673 K, the second methoxy group is lost, leaving a phosphorus oxide species on the surface. The latter result correlates with the study of Templeton and Weinberg, where the second methoxy group was lost between 573 and 673 K. Mitchell did not observe evidence for surface-bound methoxy or

formate species, indicating that methanol evolves from the surface, possibly via hydrogen abtraction from surface hydroxyl groups or water.

Sheinker and Mitchell performed another study of DMMP on alumina using a U-tube reactor through which DMMP-saturated He would flow, with post-reactor gas-analysis performed using FTIR. The commercial γ-Al_2O_3 sample studied previously was compared to a sol-gel alumina sample. Both samples released methanol along with a small amount of dimethyl ether at room temperature after an induction time that was attributed to adsorption to the alumina. At 373 K, the induction time was greatly reduced due to thermal desorption of reaction products, and the γ-Al_2O_3 released dimethyl ether first, then methanol dominated the product vapor. Higher temperatures resulted in no induction time for the products, and secondary products (CO, CH_4, and CO_2) were observed prior to methanol and dimethyl ether production. Quantitative analysis indicated that more than one carbon species was released per reactant DMMP at 573 K, indicating cleavage of the second methoxy group.

Comparing the two samples, product branching ratios were similar for both the γ-Al_2O_3 and sol-gel material. However, the sol-gel sample was more reactive initially, although the γ-Al_2O_3 demonstrates better reactivity after DMMP breakthrough when corrected for surface area. This is attributed to the faster conversion of the higher surface area sol-gel alumina to bulk phosphonates, which poisons the catalyst.

A.4.2 CWAs on Alumina

Kuiper, van Bokhoven, and Medema published the first study of the interaction of CWAs on metal oxides when they examined sarin on γ-alumina in 1976.[212] GB was found to adsorb through the phosphoryl oxygen, likely on Lewis acid sites. Hydrolysis of

the P-F bond was found to occur in addition to dealkylation that liberated propene. Fluorine remained on the surface after hydrolysis, in addition to a O-P-O bridging species. The addition of water accelerated the reaction.

More recently, Wagner, Klabunde and co-workers used solid-state magic-angle-spinning (MAS) NMR to study the interaction of liquid VX, GB, and GD with Al_2O_3 nanoparticles that were synthesized via a sol-gel technique. Results indicated that hydrolysis of nerve agents occurs on the surface to yield surface-bound non-toxic aluminophosphonates, similar to the results reported for nanosized MgO. The nanoparticulate alumina was found to be very reactive with all three nerve agents, and were superior to MgO and CaO in this respect. Perhaps the most interesting result from this study is that high loadings of nerve agents led to the formation of bulk aluminophosphonates upon exposure nano alumina, reacting to the core of the particles. This discovery led to the proposal to use aluminophosphonates on aluminum surfaces as a forensic marker of previous nerve agent exposure.

A.5 Fe_2O_3

Iron oxide reactivity towards DMMP was first studied by White and co-workers on Fe_2O_3 powder[185] and oxidized polycrystalline Fe.[249] Decomposition of DMMP was observed at temperatures as low as 170 K. This work also determined that pre-adsorption of water increases the reactivity of the oxide. Iron oxide was found to oxidize the P-CH_3 functional group of DMMP at 250 K. At higher temperatures the phosphorus species remained on the surface and migrated into the bulk, leaving some sites available for further decomposition.

The Mitchell group studied DMMP adsorbed to iron oxide with infrared spectroscopy,[1] finding that some reaction occurs at room temperature, creating a surface bound methoxy group. Confirming the results of White and co-workers, the decomposition occurred by cleavage of the P-OCH_3 and P-CH_3 bonds between 373 and 473 K. The P-CH_3 cleavage decomposition pathway was not observed on four other metal oxides examined in the same method, underscoring the uniqueness of Fe_2O_3 among other oxides. Iron's low energy Fe(II)/Fe(III) couple enables oxidation of the P-CH_3 moiety via a lattice oxygen. This study found iron oxide to be more reactive than other oxides, by nature of the elimination of all carbon-containing species from the surface by 573 K. Mitchell and co-workers further studied iron oxide when impregnated into alumina[230,248,250] finding improved reactivity for these hybrid materials.

A.6 SiO_2

Initial studies of the interactions of CWA simulants on SiO_2 surfaces were performed by Henderson et al.[185] DMMP was dosed onto a thin film of SiO_2 held at 170 K in an UHV chamber with a base pressure of 5 x 10^{-9} Torr. Temperature programmed-desorption (TPD) and Auger electron spectroscopy (AES) were used to study the adsorption and desorption of DMMP from the SiO_2 surface. Two TPD peaks were observed at 210 and 275 K for DMMP adsorbed onto dehydroxylated silica, corresponding to the monolayer and multilayer state. Multilayer formation began prior to saturation of the monolayer state, which occurred at 30 Langmuir of exposure. AES analysis indicated that the DMMP remains in a molecular-like state upon adsorption, leading to the conclusion that DMMP does not decompose on dehydrated silica. A small amount of methanol and methyl phosphonate (corresponding to 9 % of the DMMP

monolayer) desorbed at 650 K from heavily hydrated (by air exposure) SiO_2, but not from a sample that was partially hydrated with D_2O. The authors concluded that SiO_2 molecularly adsorbed DMMP and would only cleave a single O-CH_3 bond in the presence of heavy hydration; and that hydration did not influence the uptake capacity for DMMP.

Kanan and Tripp[186,191] continued the study of organophosphorus interaction with SiO_2 by using infrared spectroscopy. SiO_2 was partially dehydrated, leaving only isolated hydroxyl groups prior to exposure to TCP, MDCP, DMMP, and TMP. All of the organophosphorus compounds were found to molecularly adsorb via hydrogen bonding between surface hydroxyls and the methoxy or phosphoryl oxygen of the simulant (see Figure A.4). DMMP and TMP did not form hydrogen bonds through the phosphoryl oxygen due to steric reasons. The strength of the interaction depended on the number and strength of the hydrogen bonding. TCP desorbed at room temperature upon evacuation, while TMP was completely desorbed at 673 K. Lack of DMMP decomposition and its desorption by 573 K agree with the results of Henderson.[185]

Ferguson-McPherson et al. studied the adsorption of DMMP into multi-layer Langmuir-Blodgett films of trisilanolphenyl polyhedral oligomeric silsesquioxane (POSS) that contain silanol groups.[210] This study used TPD and reflection-absorption infrared spectroscopy (RAIRS) to determine that DMMP strongly interacts with the organic/inorganic hybrid POSS by hydrogen bonding to silanol groups. DMMP desorbed from the material without evidence for reaction.

The results of these three laboratories indicate that silica does not decompose organophosphonates, and interact through hydrogen bonding. DMMP and TMP do not

have a strong interaction between the phosphoryl oxygen and SiO_2, contrasting it to all of the other metal oxides studied. SiO_2 has therefore been proposed for use as a pre-concentrator for organophosphorus CWA sensor devices. The inert nature of SiO_2 also may also make it useful as a catalyst support for thermocatalytic decomposition of CWAs due to its unique resistance to poisoning with PO_x species.[251]

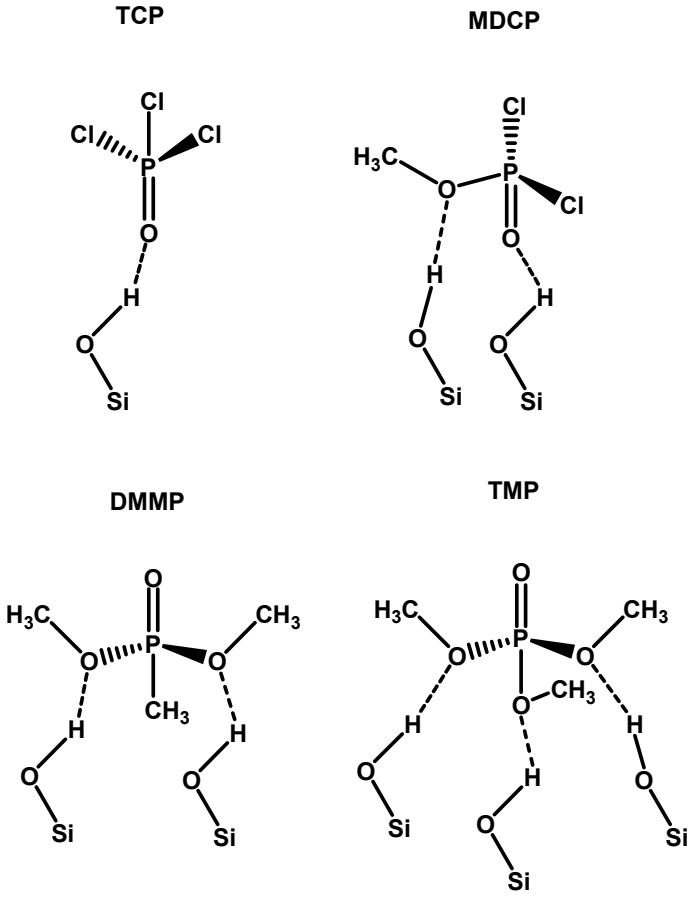

Figure A.4 Adsorption structures of 4 organophosphorus CWA simulants on silicon oxide.

Appendix B: Survey Study of DMMP Interaction with Metal Oxide Nanoparticles

B.1 Introduction

This survey study investigated the interaction of a series of novel metal oxide nanoparticle samples with DMMP to identify candidates for more detailed UHV study. There are several differences between this series of experiments and the more detailed study on yttria nanoparticles described in Section 6.5. Most importantly, these survey experiments were performed with the nanoparticles exposed to air prior to, during, and after exposure. Interpretation of the results from the RAIR spectra must consider atmospheric influence on the uptake and reactivity of the particles. In addition, air exposure permits reactive pathways that are eliminated in the UHV instrument, such as reaction of adsorbed molecules with atmospheric species, or replenishment of surface hydroxyl groups from moisture. Atmospheric exposure makes this study more relevant for determining the real-world suitability of the materials, but increases uncertainty in data analysis. Unlike UHV experiments, samples could be stored in air for several days to determine if any changes occur over longer times. This proved to be very valuable in identifying candidate metal-oxide systems for further study. A final difference between the survey and the UHV studies is the exposure method. These survey studies involve exposure to a saturated vapor of simulant, where the detailed UHV study involves much lower fluxes to allow more detailed understanding of the uptake properties and the kinetics of reactions involved.

RAIR spectra of exposed particles can readily be interpreted to determine if the particles adsorb DMMP via comparison with the gas-phase DMMP spectrum. Evidence for decomposition would be clear if surface species with unique spectral markers such as

methoxy or formate groups are observed; however, the spectral properties of the anticipated decomposition species such as methyl methylphosphonate (MMP) are similar to DMMP, complicating interpretation of the results presented here. Surface-bound MMP is characterized by the appearance of strong symmetric and asymmetric O-P-O stretches in the region of 1200 – 1000 cm^{-1} that are separated by ~ 100 cm^{-1}. DMMP, however, is expected to adsorb through the phosphoryl oxygen on most metal oxides, resulting in a P=O stretch that is shifted to 1260 - 1200 cm^{-1} from the gas-phase 1275 cm^{-1} value.

B.2 Experimental: Nanoparticle Films for Survey Study

Nanoparticle films were prepared by vaporizing metal-oxide targets that were prepared as described previously (see Section 2.2.1) with the exception of ZrO_2 and HfO_2, which were purchased as sintered pellets. Films were made in the stand-alone chamber that was evacuated with a mechanical pump to a base pressure of 20 mTorr. The chamber was backfilled to a pressure of 1 Torr N_2 and the oxide was vaporized for 5-10 minutes onto a 1 $inch^2$ Au-coated glass substrate. RAIR spectra with a 2 cm^{-1} resolution and an average of 512 scans were obtained with a N_2-purged Nicolet 710 FTIR spectrometer. Samples were purged in the IR spectrometer under N_2 for 10 minutes prior to spectrum collection. Background scans were acquired of the nanoparticle samples, and the samples were then exposed to a saturated vapor of DMMP by placing them in a sealed 60 cm^3 jar with 25 μL of DMMP deposited on the jar floor. After 25 minutes of exposure, the nanoparticle samples were placed back into the purged RAIR spectrometer and a scan was taken with the background set as the RAIR spectrum of the fresh particles. Follow-up RAIR scans were taken of some samples 4 or 5 days after exposure to see if any changes had occurred to the sample. For some of the samples, background

subtraction led to spectra that prevented interpretation. Care was taken to prevent the exposure of the nanoparticles to plasticizers and other contaminants which were found to adsorb to the nanoparticles readily.

B.3 Results for Individual Metal-Oxide Particles

B.3.1 Al_2O_3

Aluminum oxide did not vaporize well due to ejection of molten material from the pellet, leaving a relatively small amount of nanoparticles to adsorb the simulants. Al_2O_3 did adsorb DMMP through the phosphoryl group with an observed ν (P=O) shift of 56 cm^{-1} but no clear evidence was seen in the RAIR spectrum for decomposition. The 1220 cm^{-1} ν (P=O) mode observed in this study agrees with the literature value of 1217 cm^{-1} for DMMP adsorbed onto aluminum oxide.[199] Room temperature reaction of adsorbed DMMP on alumina has been observed in some studies,[199] but not others,[1] highlighting the importance of sample preparation and experimental conditions in influencing the decomposition temperature.

B.3.2 Eu_2O_3

Europium oxide showed similar results to the alumina particles. Adsorption of DMMP was observed and only the P=O stretch of DMMP shifted from the gas phase value to 1215 cm^{-1}, indicating adsorption through the phosphoryl group. The C-O stretching modes were slightly red-shifted, but shaped similarly to the corresponding gas-phase peaks. The other vibrational modes match those of gas-phase DMMP very well. DMMP was therefore found to interact with the oxide surface through the phosphoryl oxygen and no indication of dissociation was observed.

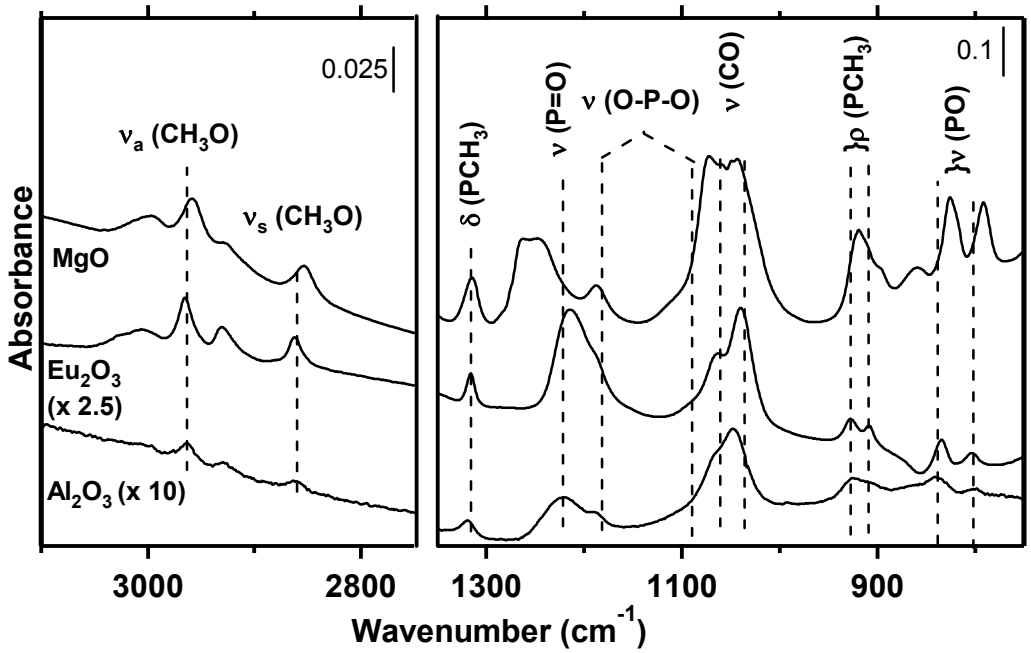

Figure B.1 RAIR spectra of MgO, Eu_2O_3, and Al_2O_3 nanoparticle films exposed to a saturated DMMP vapor in air. Spectra are scaled as noted for viewing.

B.3.3 FeO_x

Iron oxide also did not vaporize well under our experimental conditions, resulting in low signal-to-noise ratios in the C-H stretching region. Adsorption of DMMP led to an unassigned peak in the C-H stretching region at 2900 cm^{-1}, as well as a sharp shoulder at 1029 cm^{-1}. The P=O stretching mode is again strongly shifted to about 1205 cm^{-1}, but the remainder of the spectrum did not show any evidence of reactivity. After 5 days, a new mode at 1264 cm^{-1} grew in and the P=O peak red-shifted to 1192 cm^{-1} while a blue-shifted shoulder appeared at 1095 cm^{-1}, providing evidence for the existence of adsorbed methyl methylphosphonate. Furthermore, the relative intensity of the 808 cm^{-1} P-O vibration becomes greater than the 838 cm^{-1} (P-O)C stretching mode.

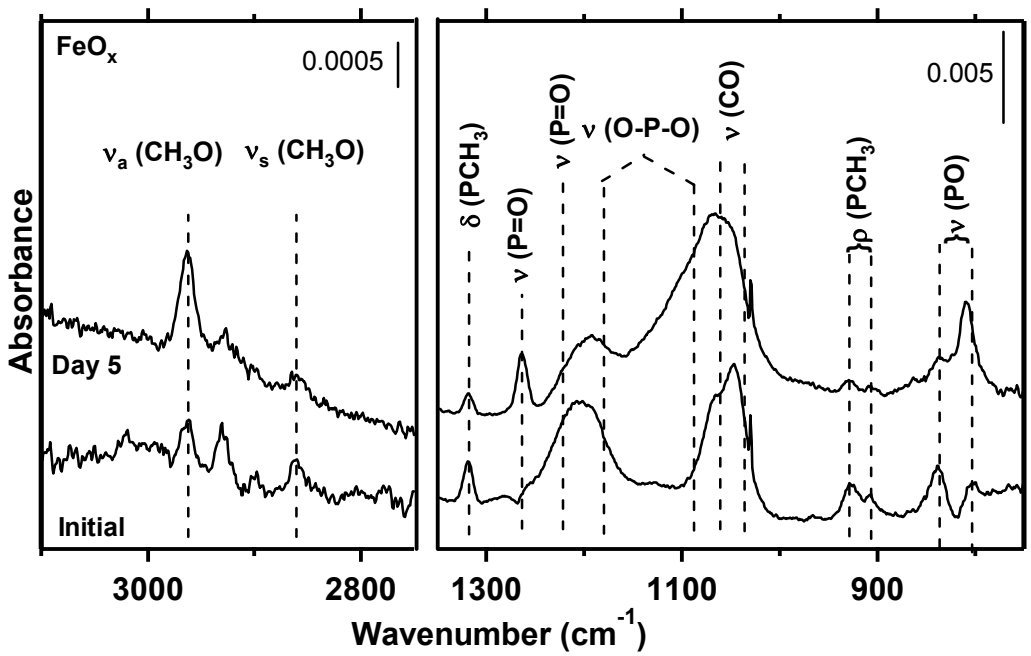

Figure B.2 RAIR spectra of a FeO_x nanoparticle film (bottom) shortly after exposure to a saturated DMMP vapor in air after and (top) after five days sitting in an air-filled jar.

Mitchell and co-workers observed a peak at 1255 cm^{-1} immediately after DMMP adsorption on Fe_2O_3 at room temperature.[1] This mode was observed to blue-shift to 1271 cm^{-1} over 1 hour under a nitrogen purge and to higher wavenumbers as the sample temperature increased. This mode was assigned to a ν (P=O) mode for a DMMP product species that is not observed on other oxides. This species was proposed (see Figure B.3) to result from a nucleophilic attack on DMMP from the surface, leaving a species bound through the methoxy oxygen. Based on this literature precedent, the 1264 cm^{-1} mode is assigned to the P=O stretch of a DMMP molecule chemisorbed through a methoxy oxygen. The results offer significant evidence for decomposition of DMMP on FeO_x over time with two reaction pathways, leaving a surface bound O-P-O species and a DMMP residue bound through the methoxy oxygen.

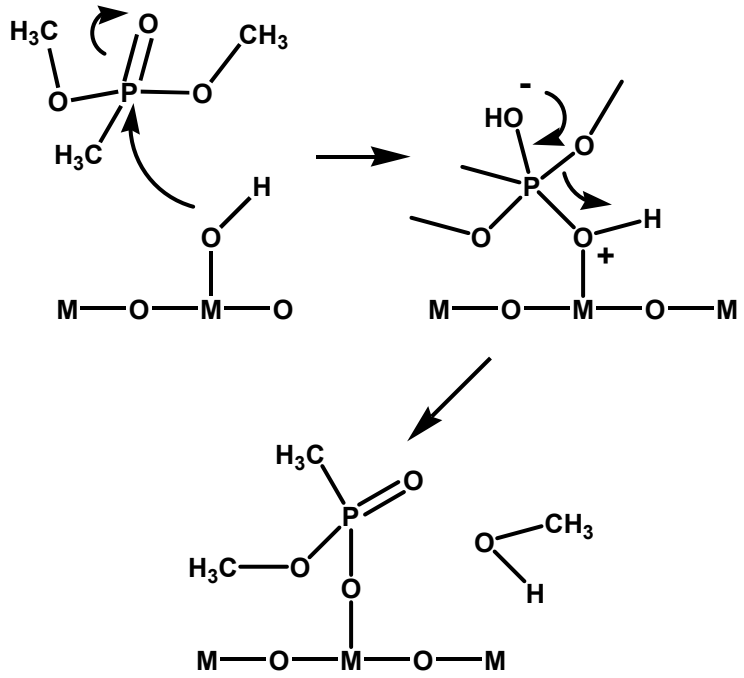

Figure B.3 Nucleophilic attack on DMMP proposed on iron oxide surfaces, leading to the species responsible for the 1264 cm^{-1} mode observed in this study. [1]

B.3.4 MgO

MgO was studied in order to provide some reference since the interaction of DMMP with this metal-oxide is well known in the literature. The shifted P=O stretch is seen with a peak at 1237 cm^{-1} and a shoulder at 1188 cm^{-1}. Comparing to the literature, the ν (P=O) mode has been reported to shift to 1190[1] and 1184 cm^{-1} [188] for chemisorbed DMMP on MgO, while another P=O stretch has been reported at 1238 cm^{-1} for a physisorbed species of DMMP on the same oxide.[188] If this literature assessment is correct, it is possible some chemisorbed DMMP exists on this MgO sample along with layers of physisorbed species that do not interact strongly with the oxide. However, the 1188 cm^{-1} shoulder could also be in part due to an (O-P-O) dissociated species on the surface, especially considering the existence of a 1079 cm^{-1} shoulder. This interpretation is reinforced by literature assignments of the dissociation species on MgO at room

temperature. In addition to the vibrational modes attributed to DMMP, peaks at 1514 and 1435 cm^{-1} that grew in simultaneously with exposure are assigned to the asymmetric and symmetric C-O stretches of a carbonate species. The growth of this species is due to CO_2 uptake on the metal-oxide surface and is not believed to be directly associated with the DMMP uptake on the particles. In this study, MgO particles were found to adsorb and possibly dissociate DMMP.

B.3.5 Y_2O_3

Yttria particles showed similar results to the previously mentioned metal-oxides. The ν P=O mode of DMMP is shifted to 1212 cm^{-1} on Y_2O_3, indicating a strong interaction between the oxide and the phosphoryl group. The other modes are similar in shape and position to the corresponding gas-phase DMMP modes, indicating that no significant decomposition is observed. As observed with MgO, C-O modes at 1545 and 1396 cm^{-1} signal the growth of carbonate groups on the surface during exposure to DMMP.

B.3.6 Tb:Y_2O_3

Yttria particles were also prepared doped with 10% terbium. Such heterogenous systems could enhance reactivity due to the additional ion by increasing the number of reactive defect sites in a system. Upon DMMP exposure, the RAIR spectrum looked almost identical to that of Y_2O_3 with the exception that the P=O mode was not as greatly shifted (1217 cm^{-1}) from the gas phase value. Terbium doping, therefore, might have decreased the affinity of DMMP for the nanoparticle surface. Carbonate groups were observed to grow in and no indication for decomposition was observed.

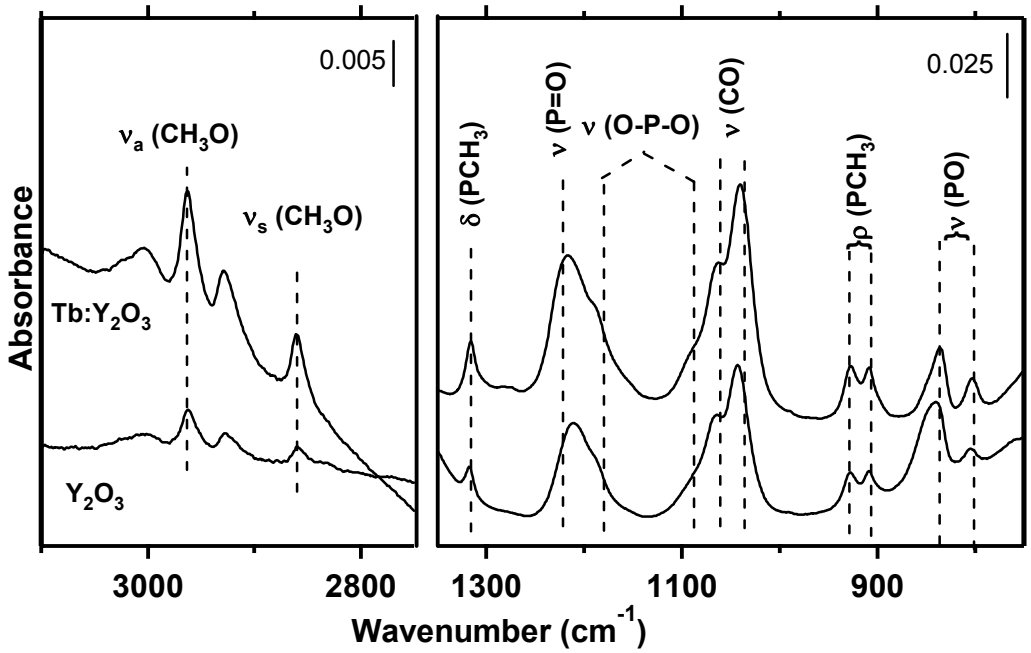

Figure B.4 RAIR spectra of Y_2O_3, and Tb: Y_2O_3 nanoparticle films exposed to a saturated DMMP vapor in air.

B.3.7 Er_2O_3

Er_2O_3 showed no initial evidence for decomposition of DMMP on the surface. RAIR spectra show that the P=O mode is shifted to 1222 cm^{-1} while other modes emulate the gas-phase DMMP spectrum. Several changes manifest themselves after the sample is allowed to sit for five days. After this period, the overall intensity of the DMMP peaks decreases by approximately 50%, indicating loss of adsorbed DMMP species. In addition, a new peak with an unknown origin appears at 1685 cm^{-1} and a broad mode appears with peaks at 1565 and 1407 cm^{-1} that are assigned to the C-O modes of a carbonate species. In the C-H stretching region, an unassigned mode grows in at 2879 cm^{-1} that may be due to some reaction of DMMP.

Even more intriguing are the changes that occur in the lower wavenumber region of the spectrum. The first change is a small red-shifted shoulder that grows in for the (P-CH_3) rocking mode. An apparent shift also occurs for the P=O stretch to 1215 cm^{-1}, while

intensity under the 1188 cm^{-1} mode increases and a new peak is observed at 1088 cm^{-1}. In addition, the relative intensity of the red-shifted P-CH_3 stretch at 908 cm^{-1} grows with respect to the 928 cm^{-1} mode while the intensity of the P-O stretch at 804 cm^{-1} increases relative to the (P-O)C stretch at 837 cm^{-1}. On Y_2O_3 (see Section 6.6.2), these changes were found to indicate the formation of an O-P-O bridging species on the surface by loss of a methoxy group from DMMP. Therefore, it is concluded that some dissociation of DMMP occurs on Er_2O_3 under ambient conditions over time.

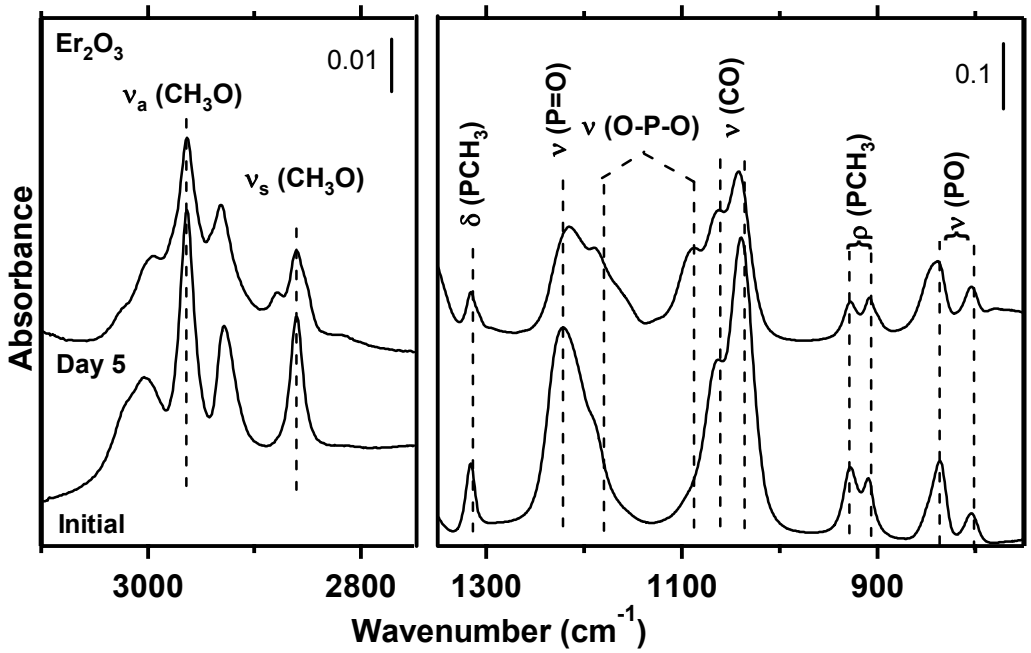

Figure B.5 RAIR spectra of a Er_2O_3 nanoparticle film (bottom) shortly after exposure to a saturated DMMP vapor in air after and (top) after five days sitting in an air-filled jar.

B.3.8 Gd_2O_3

As with several other metal-oxides studied in this survey, no clear evidence for reaction of DMMP on the surface is observed initially. Interaction of the simulant with the metal-oxide is shown by the shift in the P=O stretch to 1225 cm^{-1} with a red-shifted shoulder at 1190 cm^{-1}. After five days, changes are observed that indicate substantial

decomposition of DMMP on the surface. Red-shifting of part of the intensity of the asymmetric and symmetric $O(CH_3)$ stretches are clearly visible in the C-H stretching region. In the lower wavenumber region of the spectrum, the $P\text{-}CH_3$ deformation mode shifts from 1315 to 1309 cm^{-1} over the five days, and the intensity under the 1225 cm^{-1} P=O stretch decreases substantially while two modes grow at 1184 and 1096 cm^{-1}. As seen in the Er_2O_3 sample, the relative intensity of the red-shifted $P\text{-}CH_3$ rocking mode and the P-O stretches increase with respect to the blue-shifted $P\text{-}CH_3$ rocking and (P-O)C stretching modes. As observed on Fe_2O_3, a new mode grows in at 1263 cm^{-1} that could be assigned to a DMMP residue bound to the surface through the methoxy or methyl groups. These changes argue for a large amount of decomposition of DMMP to form an O-P-O bridging species on the surface.

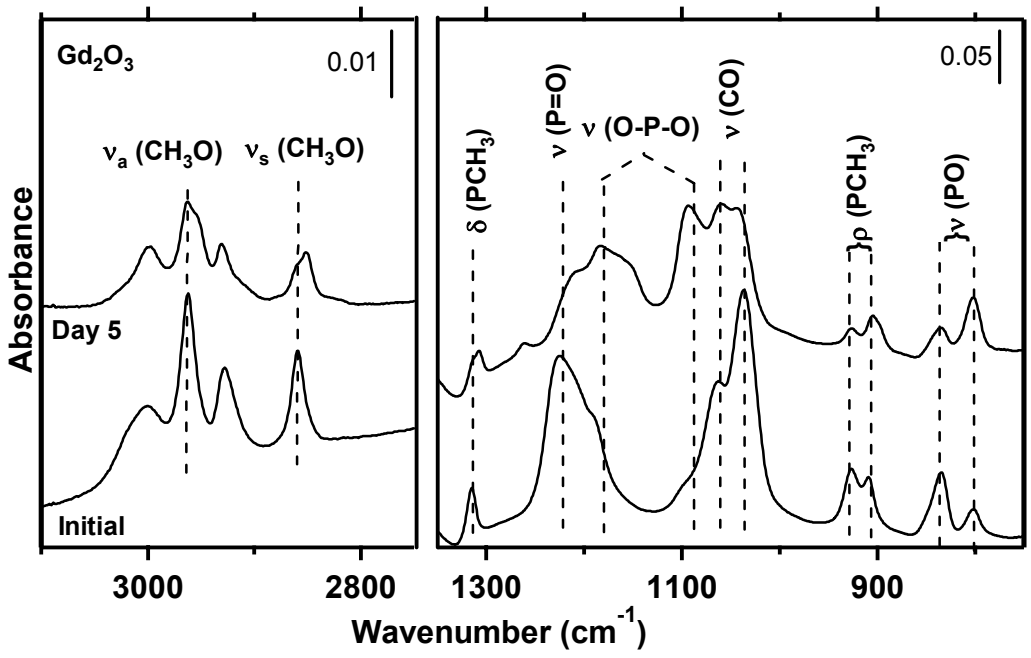

Figure B.6 RAIR spectra of a Gd_2O_3 nanoparticle film (bottom) shortly after exposure to a saturated DMMP vapor in air after and (top) after five days sitting in an air-filled jar.

B.3.9 HfO_2

HfO_2 shows interesting evidence for reactivity not seen on the metal-oxides discussed previously. In the C-H stretching region, a small stretching mode appears at 2810 cm^{-1} that can be assigned to the C-H stretch of a surface-bound methoxy group. Appearance of this mode provides evidence that some DMMP is dissociating to form a surface-bound methoxy group, also observed on Y_2O_3 as discussed in Section 6.6.2. In the lower wavenumber region, a broad band including the P=O mode has a peak at 1188 cm^{-1}, but the P=O stretch itself is probably located near 1212 cm^{-1}. A significant blue-shifted shoulder is observed on the C-O stretches, so it is proposed that the intensity of the bands at 1188 cm^{-1} and ~1095 cm^{-1} are due to the asymmetric and symmetric O-P-O stretches of a surface bridging species.

Four days after exposure, intensity is greatly reduced where the P=O stretching mode exists while the other bands are replaced with a large broad peak from ~1200 to ~1000 cm^{-1} with maximum intensity at 1063 cm^{-1}. In addition, the relative intensity of the red-shifted P-CH_3 rocking and the P-O stretching peaks increase with respect to the blue-shifted P-CH_3 rocking and (P-O)C stretching modes. In the C-H stretching region, it is noted that the 2810 cm^{-1} stretch has disappeared, so the surface bound methoxy group probably leaves as gas phase methanol. Other C-H stretching vibrations reduce in intensity, however the DMMP methoxy C-H stretching modes show a much greater relative decrease. These results implicate further decomposition of DMMP through cleavage of the P-OCH_3 bond. Surface-bound methoxy groups would be a product of this dissociation, which likely evolved from the surface as gas-phase methanol after reacting with surface hydroxyl groups, gas-phase water, or adsorbed water.[189]

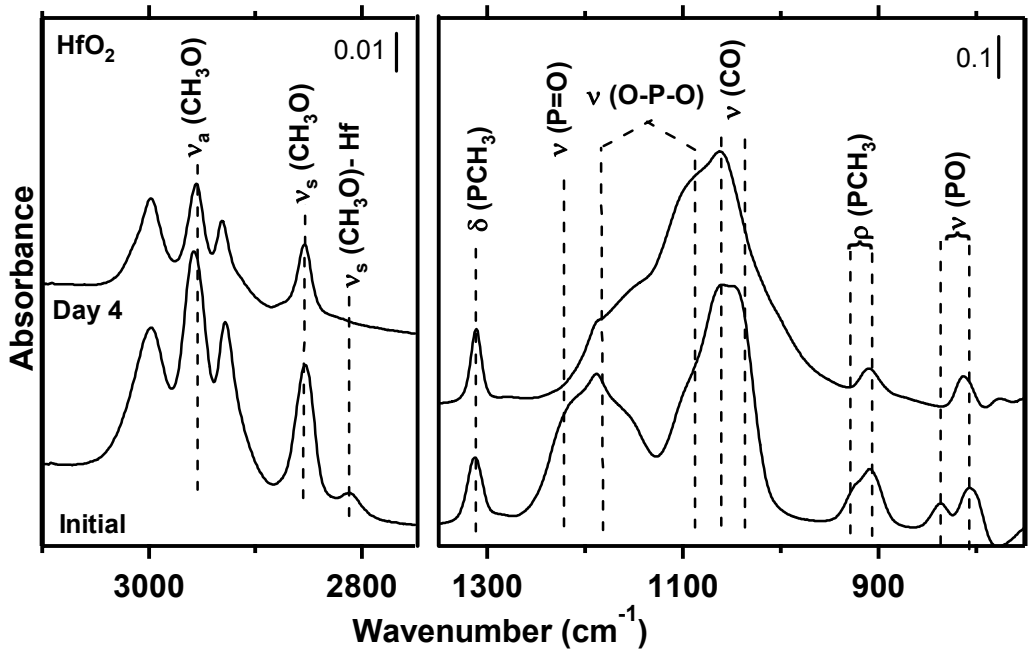

Figure B.7 RAIR spectra of a HfO_2 nanoparticle film (bottom) shortly after exposure to a saturated DMMP vapor in air after and (top) after four days sitting in an air-filled jar.

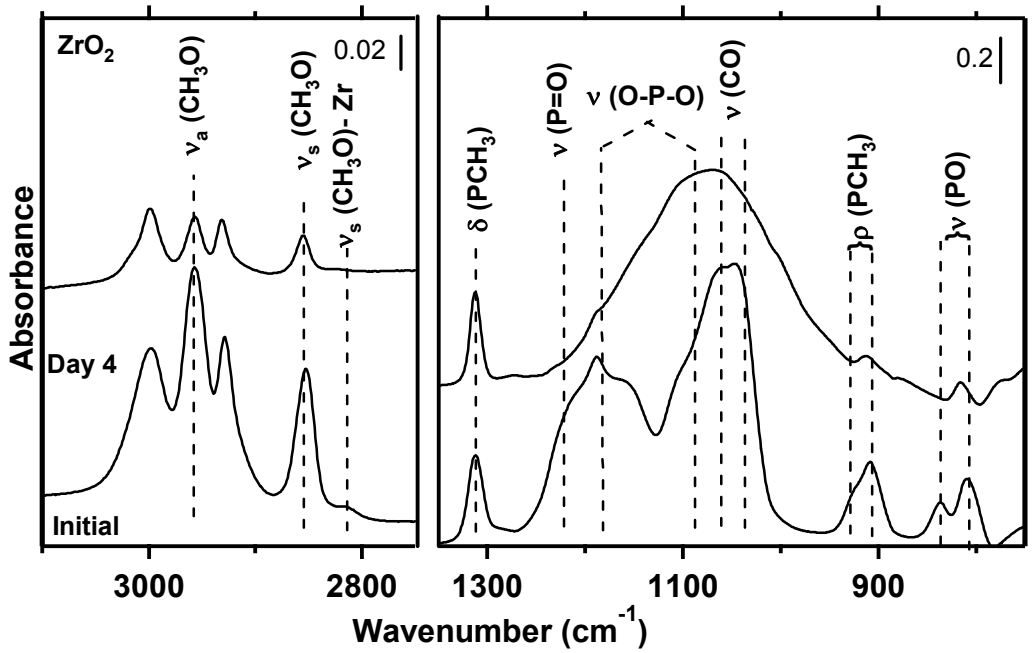

Figure B.8 RAIR spectra of a ZrO_2 nanoparticle film (bottom) shortly after exposure to a saturated DMMP vapor in air after and (top) after four days sitting in an air-filled jar.

B.3.10 ZrO_2

Results for ZrO_2 are almost identical for HfO_2. The surface-bound methoxy C-H stretch is visible at 2811 cm^{-1} and the P=O stretching peak (near 1214 cm^{-1}) is obscured by the intense (O-P-O) mode at 1188 cm^{-1}. After four days, the P=O stretch disappears into a large broad band from ~1180 to 990 cm^{-1} with a peak intensity at 1075 cm^{-1}. The changes in the P-CH_3 rocking modes and the P-O stretches are also indicative of DMMP reaction. In the C-H stretching region, the surface-bound methoxy C-H stretch disappears while the relative intensity of the asymmetric and symmetric DMMP methoxy C-H stretches decrease with respect to the methyl stretches, indicating loss of methoxy groups from DMMP, while surface-bound methoxy groups were likely eliminated to form gas-phase methanol. Based on the relative intensities of the C-H stretches, it is estimated that most of the adsorbed DMMP reacted to lose a methoxy group after four days in ambient conditions.

B.4 Conclusion: Survey Studies

It is clear from these results that DMMP readily adsorbs to various metal-oxide nanoparticles even when experiments are performed in air. Adsorption of DMMP can be monitored visually due to a change in the color of the particles (typically becoming whiter). This color change remained unaltered even when samples were stored in air for several days after exposure, raising the possibility of visible analysis of adsorption. Surface hydroxyl groups may be involved with this interaction, through the P=O group of DMMP, as reported on other metal-oxides in the literature.[1,199] HfO_2 and ZrO_2 show evidence for reaction within minutes of exposure to DMMP in air, while Gd_2O_3, FeO_x, and Er_2O_3 show strong evidence for further reaction and change of the DMMP species on

the surface over extended times. The other oxides show weaker evidence for reaction at longer times. This reaction most likely involves the cleavage (or hydrolysis) of the methoxy group of DMMP, leaving a surface-bound O-P-O species (methyl methylphosphonate) and a methoxy group that subsequently leaves the surface as gas-phase methanol. HfO_2 and ZrO_2 appear to be the most reactive, with evidence pointing to nearly complete dissociation of DMMP over a few days under ambient conditions.

These results show that many metal-oxide systems that have not been studied may indeed be useful for environmental protection and decontamination of chemical warfare agents in a real-world setting. These results also demonstrate that a more detailed study using UHV techniques would be valuable in determining the fate of DMMP on these metal-oxides. For this reason, a rigorous study of the interaction of DMMP with Y_2O_3 nanoparticles was performed as described in the remainder of this Chapter. Y_2O_3 was chosen because 1) the experience of the Tissue group with this material, and 2) the novel nature of using this oxide as a destructive adsorbent for CWA simulants.

Appendix C: Additional Y_2O_3 Nanoparticle Exposure Results

The following sections describe the results from experiments that were used to make vibrational mode assignments in the RAIR data for DMMP-exposed nanoparticles.

C.1 CO_2 Exposure

Figure C.1 shows the RAIR spectra of Y_2O_3 nanoparticles made under 1 Torr N_2 and exposed to ~1800 L of CO_2. The intensity of the C-O modes after this CO_2 exposure is approximately the same as the C-O modes of the "clean" nanoparticles, indicating that at least half of the sites for CO_2 adsorption are available once the sample is transferred into UHV conditions. IR absorption bands are seen at 1521 and 1400 cm^{-1} that are assigned to the asymmetric and symmetric C-O vibrations of a carbonate species.[197,202] The splitting of these two modes (121 cm^{-1}) and the band position is consistent with a unidentate carbonate species on yttrium, however some bidentate species probably exist on the surface.[204,252,253] In addition to the unidentate carbonate species, evidence for another species is seen with a C-O stretch mode at 1631 cm^{-1}. The assignment of this mode is not as straightforward, but might be attributed, along with the COH deformation mode at 1221 cm^{-1}, to a hydrogencarbonate species.[195] At low CO_2 exposures, the 1631 cm^{-1} peak dominated the spectrum, but as exposure continued the relative intensity of the 1521 cm^{-1} peak grew and eventually became more intense, indicating that the unidentate species is more stable on the surface. In addition, the 1631 cm^{-1} peak decreased in intensity after CO_2 dosing was halted, signaling depletion of that species.

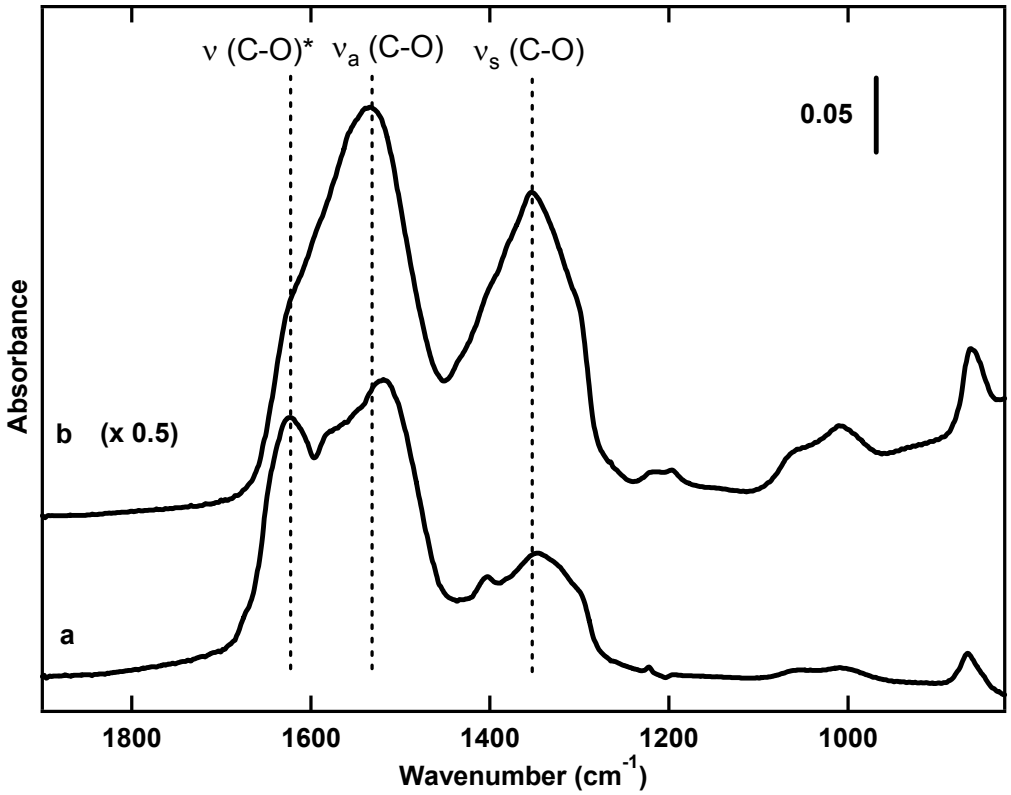

Figure C.1 a) Difference RAIR spectrum of Y_2O_3 nanoparticles after 1800 L CO_2 exposure. b) Direct RAIR spectrum of Y_2O_3 nanoparticles. Note the ν (C-O)* peak at 1631 cm^{-1}, which is assigned to an unstable carbonate species.

The 1631 cm^{-1} peak was not observed to be present with strong intensity in any as-prepared sample, so its associated species is not believed to be present in great amount on the nanoparticle surfaces that were tested. These results imply that the 1631 cm^{-1} peak can be attributed to an intermediate species that is a precursor for the unidentate carbonate species.

C.2 CO and O_2 Exposure

Another absorption seen in the spectra of freshly prepared yttria nanoparticles is a mode around 2185 cm^{-1}, which sometimes was observed with a shoulder at 2205 cm^{-1}. Similar infrared absorption peaks have been observed upon dosing of CO on copper oxide[254] and tetragonal zirconia,[255] therefore, this mode was assigned to a linear CO

surface species.[30] For confirmation, CO was dosed onto clean Y_2O_3 nanoparticles where a weak peak at 2185 cm^{-1} grew in. Further investigation demonstrated that, during heating, the intensity of the 2185 cm^{-1} mode grew in intensity, while simultaneously peaks associated with surface carbonate decreased. The mechanism for this reaction is unclear, but it appears that the linear CO species is formed as a product of carbonate decomposition. CO was introduced while the sample was heated, but no change in the 2185 cm^{-1} mode was observed. These results demonstrate that a CO linear species does form to a small degree on as-prepared samples, possibly due to CO_2 reacting at an oxygen vacancy.[203]

Y_2O_3 nanoparticles were also exposed to oxygen gas at room temperature to test for possible interaction and investigate the possibility of oxygen vacancies on the nanoparticle surface. After exposure to ~ 500 L of O_2 gas, no observable changes in the RAIR spectra of Y_2O_3 nanoparticles were detected at room temperature. This result implies that there are no oxygen defects on the particle surfaces when synthesized under nitrogen gas.

C.3 Isopropanol

Prior to exposure of the more toxic DMMP to nanoparticles, a trial experiment was run with isopropanol exposed to Y_2O_3 nanoparticles. Isopropanol was chosen because of its high vapor pressure and the existence of a study of decomposition of isopropanol on bulk Y_2O_3 at elevated temperatures.[197] Upon exposure, the difference spectra of Y_2O_3 nanoparticles showed characteristic stretches of adsorbed isopropanol that correlated well with the literature values for adsorbed alcohol on Y_2O_3. It is also noted that a large negative feature in the difference RAIR spectra at 3700 cm^{-1} is

indicative of depletion of isolated hydroxyl groups. No evidence for any reaction products was observed at room temperature, which is not surprising since isopropanol is not known to decompose over high surface area Y_2O_3 below 473 K.[197]

C.4 Methanol Exposure

Confirmation of the C-H stretching, OCH_3 rocking, and C-O modes of the proposed surface methoxy group is important to have confidence in the conclusion that DMMP dissociates on the yttria surface. Since the position of these peaks will be influenced by the nature of the oxide, assignment should be performed on this particular surface instead of comparing to other metal-oxides found in the literature. When methanol is exposed to a metal-oxide, it may react at a hydroxyl site to yield a surface methoxy group along with water or at metal-oxygen linkages to form methoxy groups and hydroxyl groups.[253,256] As seen in Figure C.2, methanol exposed to clean Y_2O_3 nanoparticles leads to loss of isolated hydroxyl groups and the growth of absorption peaks assigned to a surface methoxy group. No methanolic O-H stretch is observed, so these modes can be attributed to surface methoxy groups. The methoxy C-H stretches are observed at 2927 and 2804 cm^{-1}, while the surface-bound methoxy rocking and C-O stretching modes are observed at 1152 and 1074 cm^{-1}, respectively. These modes correlate with the absorbances that are attributed to the surface methoxy dissociation product of DMMP, confirming the assignment.

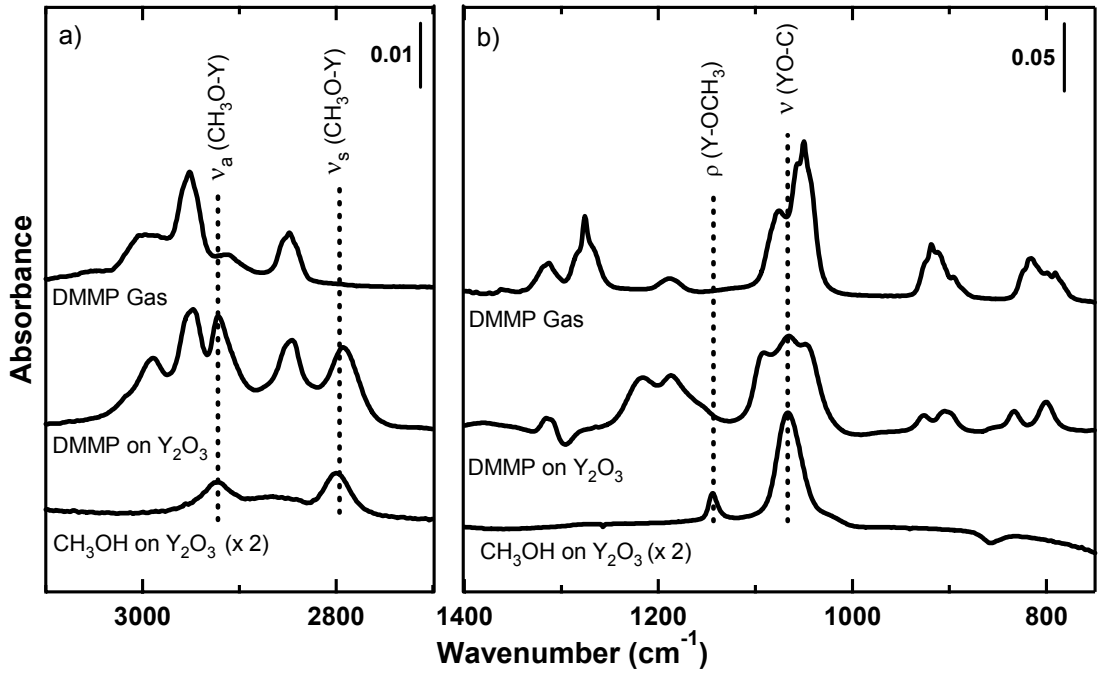

Figure C.2 RAIR spectra of methanol and DMMP exposed to Y_2O_3 nanoparticles in the a) high and b) low wavenumber regions. Peak assignments are all for surface bound methoxy groups, and the spectrum of gas-phase DMMP is included for reference.

C.5 TMP

C.5.1 Introduction

Trimethylphosphate is an analog of DMMP, with the replacement of the lone methyl group with a third methoxy group. Using this simulant, reactivity could be compared between the DMMP and TMP, in addition to eliminating the methyl C-H stretches to reveal the surface bound methoxy asymmetric C-H stretches. The gas and liquid phase vibrational spectra of TMP are known in the literature,[215,257,258] and the adsorption of TMP has been studied on MgO,[187,188,190,259] SiO_2,[186,191] WO_3,[178,179] and TiO_2.[178] Peak assignments below and shown in Figure C.3 were determined by observing difference RAIR spectra of TMP exposed to Y_2O_3 nanoparticles in consultation with the literature as well as changes noted in the difference spectra after exposure ended.

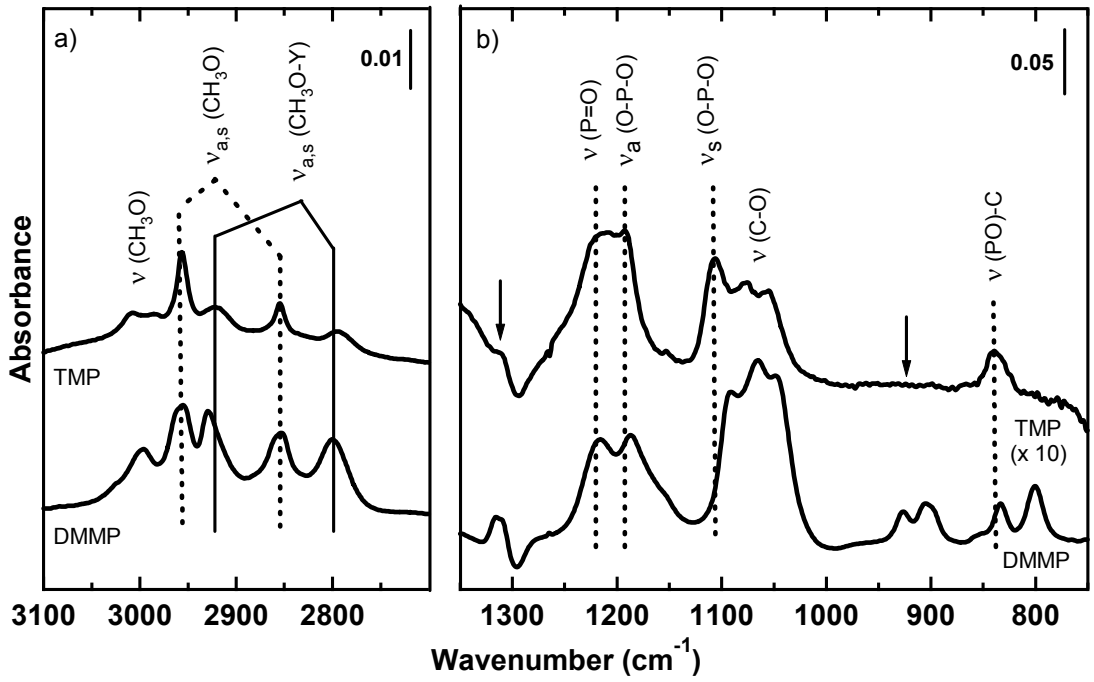

Figure C.3 RAIR spectra of the a) high and b) low wavenumber region for TMP and DMMP exposed to Y_2O_3 nanoparticles. Peak assignments are shown for adsorbed TMP. Note the lack of (P-C) modes as indicated by arrows.

C.5.2 High cm^{-1} Region Assignments

As is the case of DMMP, the spectrum of adsorbed TMP on yttria nanoparticles shows perturbation of the O-H stretches with a negative peak and shoulder at 3708 and 3672 cm^{-1}. Modes in the C-H stretching region at 3007 and 2985 cm^{-1} are very weak and are positioned higher in wavenumber than the expected for the methoxy C-H stretches. Kim et al. used ab initio calculations to determine that a mode at 3006 cm^{-1} is due to a C-H stretching mode of the methoxy group of TMP adsorbed on TiO_2.[178] Marsault-Herail similarly assigned two C-H stretching modes for TMP in the gas phase at 3022 and 2999 cm^{-1} with a splitting of 23 cm^{-1} while the splitting of peaks observed presently is 22 cm^{-1}.[215] This evidence allows the assignment of these peaks to these C-H stretching

modes and not to any impurity methyl C-H stretches. The peaks at 2956 and 2854 cm^{-1} are assigned to the asymmetric and symmetric methoxy C-H modes of molecularly adsorbed TMP. Like DMMP, difference RAIR spectra show that the blue-shifted component of these two modes originate from the molecularly adsorbed TMP while a red-shifted component results from the product bridging species. As with the spectra of DMMP adsorbed onto Y_2O_3, the peaks at 2923 and 2796 cm^{-1} are assigned to the C-H stretches of a surface bound methoxy group. The RAIR data indicates that TMP dissociates on the nanoparticle surface at room temperature and provide a less ambiguous assignment of the asymmetric C-H stretch of a surface bound methoxy group on yttria since there is no methyl C-H stretching mode overlapping this region.

C.5.3 Lower cm^{-1} Region Assignments

In the lower wavenumber region of the spectrum of adsorbed TMP, modes at 1467 and 1451 cm^{-1} are due to the asymmetric and symmetric deformation modes of the CH_3 groups while the 1240 cm^{-1} peak is assigned to the P=O group. The peak at 1217 cm^{-1} is due to the methoxy rock of molecularly adsorbed TMP while the 1194 peak is assigned to the asymmetric O-P-O stretch of the bridging species. At 1152 cm^{-1}, a shoulder is seen that is assigned to the OCH_3 rocking mode of the surface methoxy group. An 1106 cm^{-1} stretch is assigned to the symmetric O-P-O stretch of the bridging species while the C-O modes at 1074 and 1054 are assigned to the surface methoxy group and adsorbed TMP. The C-O stretch of the bridging product species is believed to be located between these two modes. Finally, overlapping modes for the PO stretches are observed at 868 and 839 cm^{-1}. The 868 cm^{-1} is assigned to the (PO)C stretch of adsorbed intact TMP, while the 839 cm^{-1} mode is assigned to PO product bridging species stretch.

C.5.4 Discussion: TMP Spectral Results

The data shows that TMP interacts with the yttria nanoparticles in an identical fashion to its analog DMMP. In comparing the results from the TMP exposure experiments, it should be noted that two conformations (C_{3V} and C_3) of TMP are known to exist in the gas phase that results in a splitting of the P=O band to modes at 1316 and 1291 cm^{-1}, respectively. The C_{3V} conformer features methoxy groups that are projected up and out along the P-O plane. On the other hand, the C_3 conformation features the methyl groups bending towards neighboring methoxy oxygens, and intramolecular H-bonding occurs between the alkyl hydrogens and the phosphoryl oxygen, resulting in the lower P=O stretching value.[257] Existence of two conformers may influence the spectral data that is discussed here. A small shift of the adsorbed TMP methoxy C-H stretches (2-3 cm^{-1}) combined with the large shift of the P=O mode (~ 64 cm^{-1}) from the gas phase is indicative of a strong interaction of the P=O moiety and the yttria. Depletion of the isolated hydroxyl species at 3708 and 3672 cm^{-1} demonstrates that a significant amount of the interaction of TMP with the metal-oxide is mediated through hydroxyl bonds.

Existence of surface-bound methoxy C-H stretching and rocking modes show that there is decomposition of adsorbed TMP to form a surface-bound methoxy group. In addition, the O-P-O stretches seen at 1194 and 1106 cm^{-1} (Δ = 88 cm^{-1}) confirm the presence of a bridging species similar to the one observed in the case of DMMP on yttria particles. Qualitatively, it is estimated that most of the TMP has adsorbed onto these small 2.8 nm particles has dissociated to form the product bridging species on this particle sample. This is due to the high relative intensity of the surface methoxy C-H stretches and the very low intensity of the P=O stretch.

C.5.5 Discussion: TMP vs. DMMP

There are a few differences observed in the spectra of TMP and DMMP on Y_2O_3 nanoparticles. The main difference is the blue shifted positions of corresponding peaks. This is most clear for the P=O and O-P-O stretches, but is visible throughout the spectrum. This blue-shift in wavenumber is attributed to the additional electronic contribution from the additional oxygen atom found in TMP by virtue of increased electron density in the bonds of the molecule. It is interesting to note is that the shift of the P=O mode from the gas-phase to the adsorbed molecule is similar for both TMP and DMMP at $\Delta \approx 65$ cm^{-1}, which is further indicative of a similar interaction. Another similarity that is observed with the TMP results is the changes occurring in the RAIR spectra after dosing is completed and dissociation continues. As observed with DMMP, the methoxy C-H stretches redshift while peaks are seen that correspond to the surface-bound methoxy C-H modes. Simultaneously, the P=O, lower wavenumber CO, and the (PO)-C stretches reduce in intensity while the O-P-O and the PO stretches increase signal. These results are consistent with those from the DMMP exposure and are indicative of continued reaction after dosing.

C.5.6 Discussion: TMP Comparison With Other Metal-Oxide Systems

The infrared spectra of TMP adsorbed to metal-oxides has been reported for TiO_2,[178] WO_3,[179] SiO_2,[186] and MgO.[188] To the author's knowledge, there is no report of decomposition of TMP on these metal-oxides at room temperature, however the published spectrum of TMP on TiO_2 shows evidence for surface-bound methoxy C-H stretches. This indicates that the 2.2 nm Y_2O_3 particles are highly reactive with TMP compared with the metal-oxide systems observed in the literature. The interaction of

TMP with the reported metal-oxides is similar with the exception of silica, where it was found that TMP will form hydrogen bonds through the methoxy groups with the oxide instead of through the P=O moiety. Further insight can be gained from observing the differences in the shift of the P=O stretch. On TiO_2, and MgO, the P=O mode is observed at 1266 and 1220 cm-1. On WO_3, three P=O stretching modes are reported at 1237, 1222, and 1206 cm^{-1}. These represent very strong shifts from the gas phase values of 1316-1291 cm^{-1} and are similar to the value found in this study, 1240 cm^{-1}.

C.5.7 TMP Summary

In summary, TMP interacts with yttria nanoparticles through the P=O moiety. It is believed that hydroxyl groups are involved to a strong degree with this interaction. Decomposition of TMP has been found to occur at room temperature over 2.2 nm particles, making this one of the more reactive metal oxide systems observed. TMP is believed to form the O-P-O bridging species that is observed with DMMP. Also like DMMP, TMP will continue to react on the surface after exposure is stopped. No clear evidence for further decomposition is observed.

C.6 DDMMP

Dimethyl methylphosphonate-d_6, (DDMMP, $O=P(OCD_3)_2(CH_3)$) is a valuable adsorbate to test on the system because the use of this compound will eliminate the asymmetric and symmetric $(CH_3)O$ stretches; as well as shift the $(CD_3O\text{-}Y)$ stretching and Y-OCD_3 rocking modes. DDMMP was synthesized as described in the experimental section above following the procedure published by Templeton.[199] The spectrum of DDMMP exposed to Y_2O_3 nanoparticles seen in Figure C.4 show peaks at 2996 and 2930 for the asymmetric and symmetric (PCH_3) C-H stretching modes and no other peaks in

the C-H stretching region, consistent with the assignments for adsorbed DMMP in that region. Evidence for H-D exchange or formation of surface O-D groups is seen with the observation of weak O-D stretching absorbances at 2730 and 2706 cm^{-1}. Asymmetric and symmetric (CD_3OP) C-D vibrations are visible at 2239 and 2081 cm^{-1} while the asymmetric and symmetric (CD_3OY) stretches of the surface deuterated methoxy group grow in at 2175 and 2040 cm^{-1}.

In the low wavenumber region, the symmetric (CH_3) deformation mode appears at 1310 cm^{-1} while the P=O stretching mode is visible at 1218 cm^{-1}. Corresponding to the DMMP spectrum, modes assigned to the O-P-O stretches are visible at 1186 and 1085 cm^{-1} while the modes at 1161, 1120, and 1030 cm^{-1} that are assigned to the surface d_3 methoxy group are visible. The C-O modes of DDMMP and the product species are observed at 1065 cm^{-1}. Finally, weak peaks assigned to the 896 cm^{-1} P-CH_3 rocking mode and the 791 cm^{-1} PO_2 stretch are seen. These peak assignments were performed in consultation with the literature,[199,214] and correlate well with the peak assignments of DMMP. DDMMP exposure further strengthens the assignments for DMMP, particularly in the (C-H) stretching region. The splitting between the two (O-P-O) modes is 100 cm^{-1}, in agreement with the literature.[212]

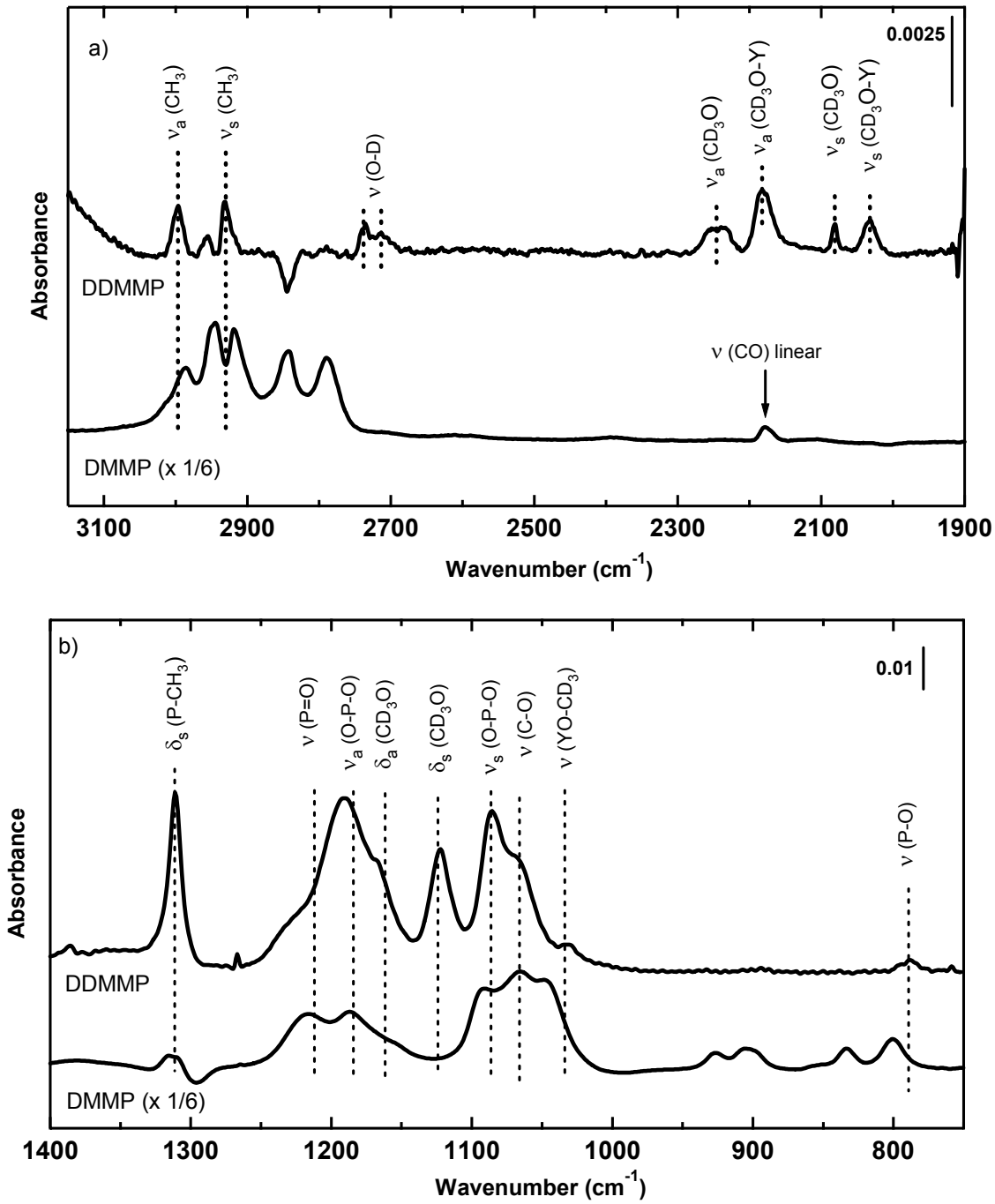

Figure C.4 a) high and b) low wavenumber regions of the RAIR spectra of Y_2O_3 exposed to DDMMP and DMMP. Note the overlapping peak for the linear C=O species for DMMP in a).

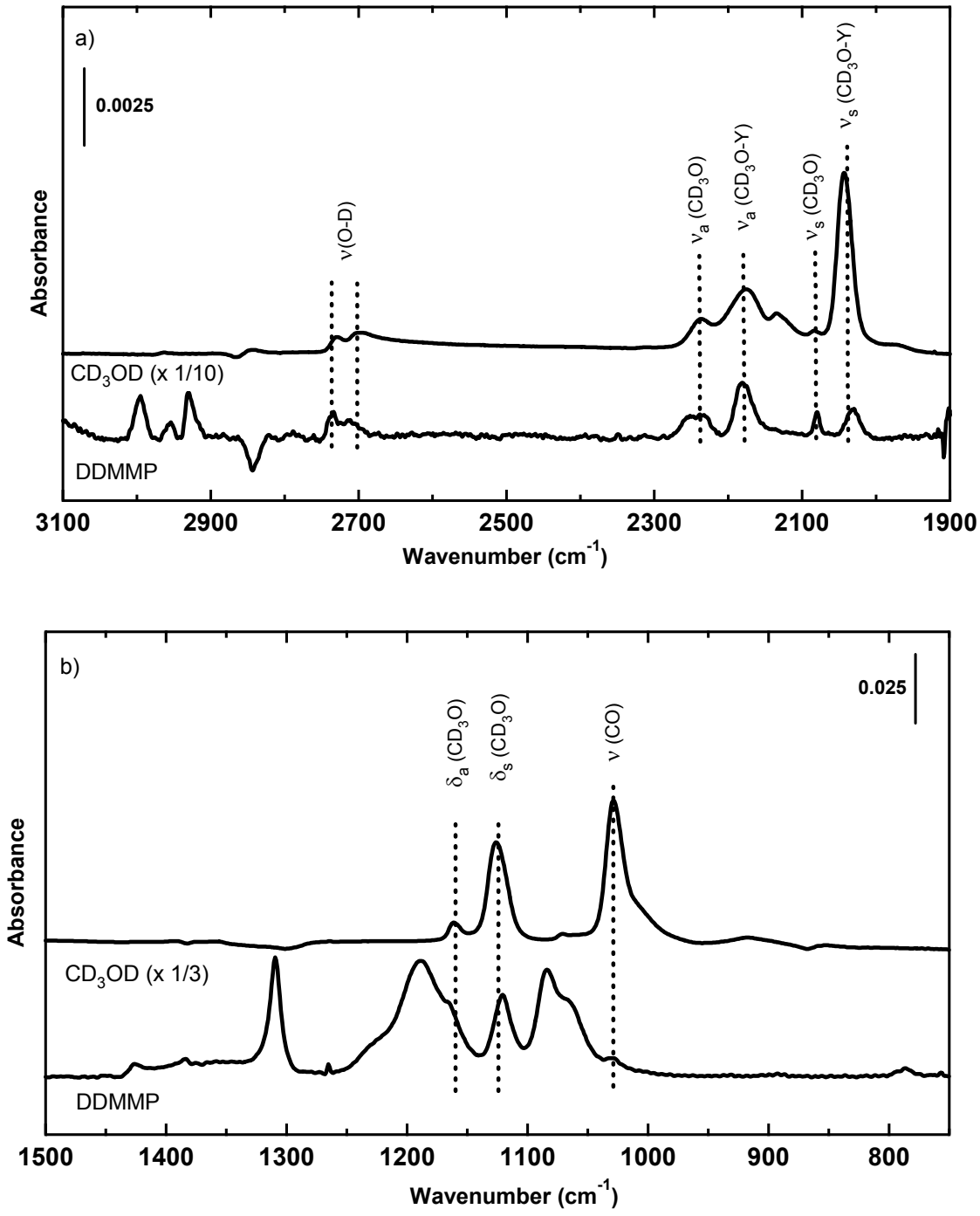

Figure C.5 RAIR spectra in the a) high and b) low wavenumber region of CD_3OD and DDMMP exposed to Y_2O_3 nanoparticles.

C.7 Deuterated Methanol Exposure

To assist in assignments of the DDMMP exposures, methanol-d_4 was adsorbed to clean yttria nanoparticles. As with methanol, the deuterated species loses its alcoholic deuterium and forms a surface bound Y-OCD_3 species. Adsorption of CD_3OD to yttria nanoparticles (see Figure C.5) leads to small modes growing in at 2729 and 2698 cm^{-1} due free O-D groups on the surface. These could result from H-D exchange with hydroxyl groups, but are more likely due to the reaction of the CD_3OD at the surface to form O-D species. In the C-D stretching region, peaks at 2175 and 2043 are assigned to the asymmetric and symmetric C-D stretches of the surface bound alkoxy species. Peaks at 1161, 1125, and 1028 cm^{-1} are attributed to the asymmetric and symmetric CD_3 deformations and the C-O stretching mode of the surface bound d_3 methoxide. Enhancement of the symmetric CD_3 deformation mode can be explained by strong Fermi resonance with the ν(C-O) mode.[260] Assignments were based on literature reports of –OCD_3 groups on a variety of surfaces.[216-218]

C.8 Heating Clean Nanoparticles

Several changes in yttria nanoparticles are observed in RAIRS upon heating the sample in vacuum as seen in Figure C.6. Initially, a decrease in the O-H stretching modes is observed at temperatures not much greater than room temperature. Intensity reduction in the broad mode at ~3600 cm^{-1} indicates that the associated hydroxyl groups are preferentially removed from the surface, but isolated hydroxyl groups desorbed as well. At temperatures around 575 K, the associated hydroxyl groups are mostly removed from the surface, as are a majority of the isolated hydroxyl groups. In addition, strong negative peaks in the carbonate C-O stretching region are indicative of removal of these groups

from the surface. Simultaneous growth of the linear carbonyl CO stretch at 2182 cm^{-1} is evidence for some decomposing carbonate forming a linear CO species on the surface. As temperatures are further elevated to 775 K, precise characterization of the sample becomes difficult due to thermal expansion and movement of the manipulator and gold slide. Experimental difficulties aside, it is clear that almost all of the associated hydroxyl groups are removed upon a few hours anneal at 775 K. Most isolated hydroxyl groups are also eliminated at this temperature. A large degree of the carbonate species have been removed from the surface, though it is likely that decomposed species also exist on the yttria nanoparticles even at 775 K.

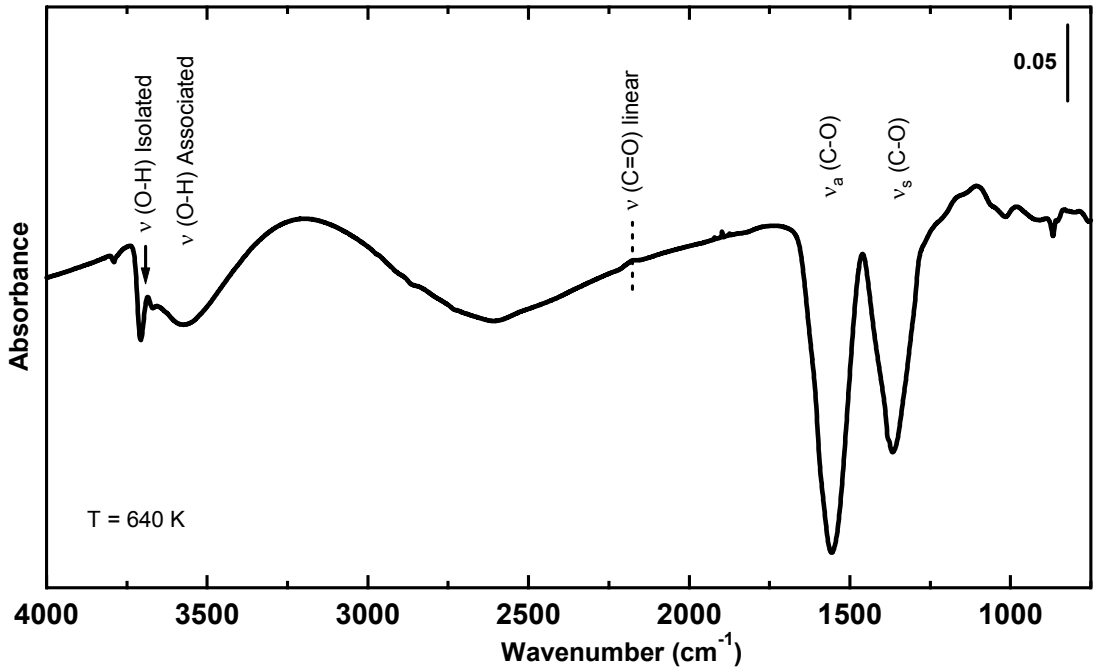

Figure C.6 Difference RAIR spectrum of Y_2O_3 nanoparticles after heating to 640 K. Most of the hydroxyl groups have been removed, as has a large amount of surface carbonate. Intensity of the linear C-O mode at 2185 cm^{-1} varied with sample and is often much greater than in this spectrum. Thermal expansion and movement is the likely cause for the broad feature centered at ~ 2600 cm^{-1}.

C.9 Cu^{2+} -COO^- Terminated SAM Exposure

One question about the assignment of the predominantly asymmetric O-P-O stretch at 1185 cm^{-1} for DMMP adsorbed to yttria nanoparticles is the overlap of this mode with the gas phase value of the OCH_3 rocking mode of molecularly adsorbed DMMP at 1188 cm^{-1}. Absorbance intensity for the mode attributed to the O-P-O stretch of the dissociation product species is relatively greater than the intensity of the OCH_3 rocking mode of gas-phase DMMP. While it is not expected that the intensity of this peak will be greatly modified upon adsorption of DMMP due to the bulk of the Y_2O_3-DMMP interaction involving the P=O moiety, modification of peak intensity is a possibility. Bertilsson et al. performed experiments adsorbing DMMP to CH_3, OH, and COOH terminated SAMs at 100K, and no modulation of the relative intensity of the OCH_3 rocking mode was observed.[261,262] Even with this literature precedence, an experiment was performed where DMMP is adsorbed to a surface that has been previously known in the literature to confirm no intensity change of the OCH_3 rock is seen with our experimental setup.

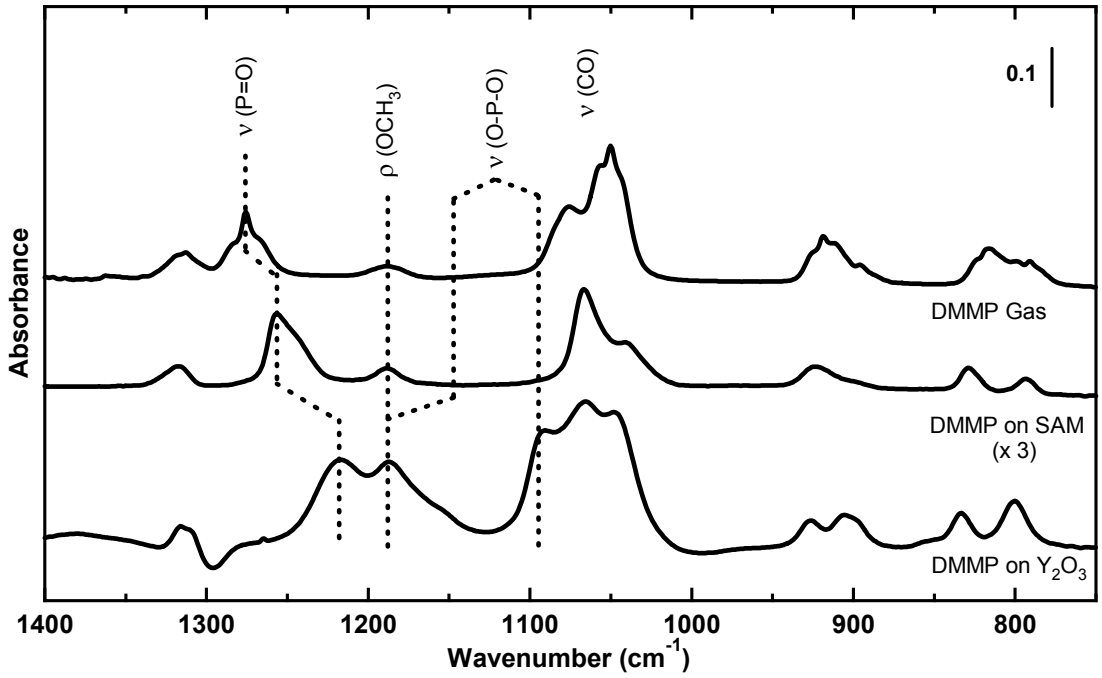

Figure C.7 RAIR spectra of (From top to bottom) DMMP in the gas-phase, adsorbed onto a Cu^{2+} - COO^--terminated SAM, and adsorbed onto Y_2O_3 nanoparticles. Note that the DMMP ρ (OCH_3) mode does not change significantly upon adsorption onto the SAM and the greater redshift for the ν(P=O) mode upon adsorption onto the nanoparticles.

Figure C.7 shows the difference RAIR spectrum of DMMP adsorbed to a copper ion-carboxylate complex terminated SAM at ~ 115 K. It is clear that DMMP adsorbs to the surface without decomposing under the experimental conditions. From this spectrum there are two important points to discuss. The first is downshift of the P=O stretching mode from 1276 cm^{-1} in the gas phase to 1257 cm^{-1} upon adsorption to the metal-ion-decorated surface. This shift of 19 cm^{-1} is weak compared to the shift observed of the same mode when DMMP is exposed to yttria nanoparticles (60 cm^{-1}), indicating a much stonger DMMP-nanoparticle interaction. More importantly, it is noted that the relative intensity of the OCH_3 rock, compared to the P=O and CO stretching modes, is at least a factor of 4 smaller than the relative intensity of the 1187 cm^{-1} mode observed for DMMP

adsorbed onto Y_2O_3 nanoparticles. These results combined with the literature results give us confidence that the relative intensity of the OCH_3 rocking mode does not greatly change upon adsorption, and therefore a majority of the intensity of the 1188 cm^{-1} mode on the yttria nanoparticles is due to the asymmetric O-P-O stretch of the product species.

C.10 XPS-induced Reactivity Monitored by RAIRS

As previously discussed, XPS was used to analyze nanoparticle films before and after exposure to DMMP. During XPS, the surface was typically bombarded with X-rays for 1 – 1.5 hours in order to produce photoelectrons. While all RAIR data was collected before X-ray exposure, it would be interesting if these high-energy photons induced reaction of any DMMP adsorbed onto the nanoparticle surface. In order to determine if these X-rays affected the species on the surface, RAIRS was used to compare the DMMP-exposed nanoparticles before and after XPS. Figure C.8 shows difference spectra of 5.8 nm Y_2O_3 nanoparticles before and after X-ray exposure. Intensity is dramatically reduced for the P=O, red-shifted C-O, blue-shifted rocking P-CH_3, and (PO)C stretching modes associated with adsorbed DMMP. Concurrently, an increase is noted for the Y-OCH_3 rocking mode as well as the O-P-O modes while OC-H_3 modes red-shift towards the value for the dissociated bridging species. Not surprisingly, the remaining intact DMMP dissociates on the surface after exposure to the X-ray radiation.

Investigation of the remainder of the spectrum reveals changes in the C-H stretching region as well as new vibrational modes growing in. It is first noted that the intensity of peaks assigned to the C-H stretches of surface-bound methoxy groups decrease while the intensity of the 2853 cm^{-1} peak dramatically increases. The 2853 cm^{-1} peak that is enlarged is in the region for the symmetric OC-H_3 stretch, however the fact

that the associated asymmetric stretch does not increase indicates that the growth is due to a new C-H containing species on the surface. In addition to the 2853 cm^{-1} peak changes, a weak new mode appears at 2727 cm^{-1}, a strong absorption appears at 1597 cm^{-1}, and two overlapping vibrations appear at 1381 and 1369 cm^{-1}. Finally, the intensity of the 2187 cm^{-1} stretch that is associated with the linear CO species doubles.

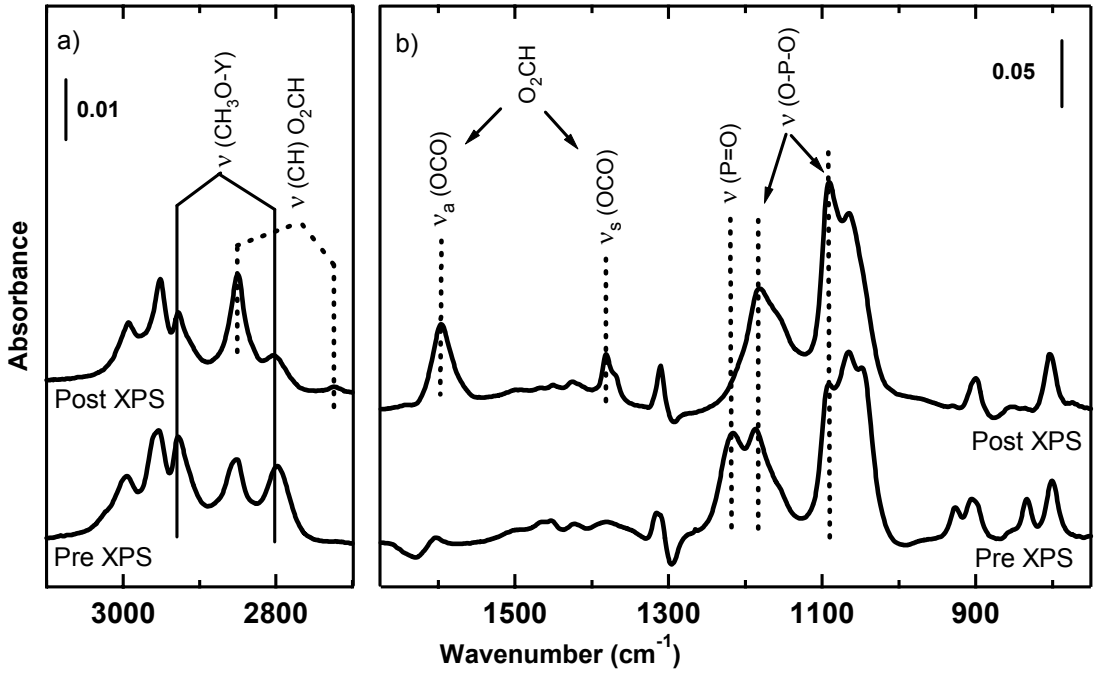

Figure C.8 Difference RAIR spectra of Y_2O_3 nanoparticles exposed to DMMP before (lower trace) and after (upper trace) XPS in the a) high wavenumber and b) low wavenumber regions.

These changes argue for a previously unseen species coupled with the loss of surface-bound methoxy groups. Upon comparison with the literature, the new modes are assigned to a surface bidentate formate that has been observed upon photocatalytic decomposition of DMMP on TiO_2[182,183] and upon adsorption onto Al_2O_3.[199] The bidentate species is proposed due to the lack of an observed C=O stretch. The modes at 2853 and 2727 cm^{-1} are assigned to the fundamental C-H stretch and a second C-H mode while the

1597 and 1369 cm^{-1} bands are associated with the OCO stretches[183,199] that match literature values for formic acid capped Y_2O_3 nanocrystals at 1592 and 1366 cm^{-1}.[263] The peak at 1381 cm^{-1} is assigned to the CH_3 deformation mode. Appearance of the linear CO stretch is probably unrelated to the reaction of DMMP but may result from carbon oxides (CO_x) being produced during oxidation of the methoxy groups[264] or from reaction of carbonate groups under X-ray radiation.

Results discussed above indicate that X-rays cause dissociation of DMMP on the surface of Y_2O_3 nanoparticles and induce the oxidation of surface methoxy groups to bidentate formate groups. Some desorption of DMMP is possible, but no clear evidence of this is detected in the RAIR data. Observation of this phenomenon reinforces the need for independent methods of analysis to fully characterize samples.

References

(1) Mitchell, M. B.; Sheinker, V. N.; Mintz, E. A. *Journal of Physical Chemistry B* **1997**, *101*, 11192-11203.

(2) Sciences, O. o. B. E. Nanoscale Science, Engineering and Technology Research Directions.

(3) Klabunde, K. J. In *Nanoscale Materials in Chemistry*; Klabunde, K. J., Ed.; Wiley-Interscience: New York, 2001, p 1-13.

(4) Bihari, B.; Eilers, H.; Tissue, B. M. *Journal of Luminescence* **1997**, *75*, 1-10.

(5) Matteazzi, P.; Alcala, M. *Materials Science & Engineering, A: Structural Materials: Properties, Microstructure and Processing* **1997**, *230*, 161-170.

(6) Shea, L. E.; McKittrick, J.; Lopez, O. A.; Sluzky, E. *Journal of the American Ceramic Society* **1996**, *79*, 3257-3265.

(7) Jiang, X. C.; Yan, C. H.; Sun, L. D.; Wei, Z. G.; Liao, C. S. *Journal of Solid State Chemistry* **2003**, *175*, 245-251.

(8) Levy, D.; Esquivias, L. *Advanced Materials (Weinheim, Federal Republic of Germany)* **1995**, *7*, 120-129.

(9) Kwon, M. S.; Kim, C. J.; Park, H. L.; Kim, T. W.; Lee, H. S. *Journal of Materials Science* **2005**, *40*, 4089-4091.

(10) Rulison, A. J.; Flagan, R. C. *Journal of the American Ceramic Society* **1994**, *77*, 3244-3250.

(11) Jain, S.; Skamser, D. J.; Kodas, T. T. *Aerosol Science and Technology* **1997**, *27*, 575-590.

(12) Swihart, M. T. *Current Opinion in Colloid and Interface Science* **2003**, *8*, 127-133.

(13) Hahn, H. *Nanostructured Materials* **1997**, *9*, 3-12.

(14) El-Shall, M. S.; Abdelsayed, V.; Pithawalla, Y. N.; Alsharach, E.; Deevi, S. C. *Journal of Physical Chemistry B* **2003**, *107*, 2282-2286.

(15) Vogt, G. J. *Proceedings - Electrochemical Society* **1988**, *88*, 572-583.

(16) Kiss, L. B.; Söderund, J.; Niklasson, G. A.; Granqvist, C. G. *Nanostructured Materials* **1999**, *12*, 327-332.

(17) Granqvist, C. G.; Buhrman, R. A. *Solid State Communications* **1976**, *18*, 123-126.

(18) Eilers, H.; Tissue, B. M. *Materials Letters* **1995**, *24*, 261-265.

(19) Hammond, C. *The Basics of Crystallography and Diffraction*; Oxford University Press: New York, NY, 1997.

(20) Jenkins, R.; Snyder, R. L. *Introduction to X-ray Powder Diffractometry*; Wiley-Interscience: New York, NY, 1996.

(21) Brunauer, S.; Emmett, P. H.; Teller, E. *Journal of the American Chemical Society* **1938**, *60*, 309-319.

(22) Nölte, J. *ICP Emission Spectrometry*; Wiley - VCH: Weinheim, Germany, 2003.

(23) Dean, J. R. *Practical Inductively Coupled Plasma Spectroscopy*; John Wiley & Sons: West Sussex, England, 2005.

(24) Goldstein, J. I.; Newbury, D. E.; Echlin, P.; Joy, D. C.; Lyman, C. E.; Lifshin, E.; Sawyer, L.; Michael, J. *Scanning Electron Microscopy and X-ray Microanalysis*; 3rd ed.; Kluwer Academic / Plenum Publishers: New York, NY, 2003.

(25) Cowley, J. M. In *High-Resolution Transmission Electron Microscopy and Associated Techniques*; Buseck, P., Cowley, J., Eyring, L., Eds.; Oxford University Press: New York, NY, 1988.

(26) Keyse, R. J.; Garratt-Reed, A. J.; Goodhew, P. J.; Lorimer, G. W. *Introduction to Scanning Transmission Electron Microscopy*; Spinger-Verlag: New York, NY, 1998.

(27) *SPM Training Notebook*; Revision E ed.; Veeco, 2003.

(28) Davis, G. M. M. S. Thesis, Virginia Polytechnic Institute and State University, 2003.

(29) Shuler, S. M. S. Thesis, Virginia Polytechnic Institute and State University, 2002.

(30) Urban, M. W. *Vibrational Spectroscopy of Molecules and Macromolecules on Surfaces*; Wiley-Interscience: New York, NY, 1993.

(31) Francis, S. A.; Ellison, A. H. *Journal of the Optical Society of America* **1959**, *49*, 131-138.

(32) Greenler, R. G. *The Journal of Chemical Physics* **1966**, *44*, 310-315.

(33) Greenler, R. G. *The Journal of Chemical Physics* **1969**, *50*, 1963-1968.

(34) Poling, G. W. *Journal of Colloid and Interface Science* **1970**, *34*, 365-374.

(35) Hollins, P.; Pritchard, J. In *Vibrational Spectroscopy of Adsorbates*; Willis, R. F., Ed.; Springer-Verlag: New York, NY, 1980, p 125-143.

(36) Minggin, W.; Xuehong, D. *Episodes from the History of the Rare Earth Elements*; Kluwer Academic Publishers: Pittsburg, PA, 1996; Vol. 15.

(37) Blasse, G. *Materials Chemistry and Physics* **1987**, *16*, 201-236.

(38) Henderson, B.; Imbusch, G. F. *Optical Spectroscopy of Inorganic Solids*; Oxford Science Publications: New York, NY, 1989.

(39) Dieke, G. H.; Crosswhite, H. M. *Applied Optics* **1963**, *2*, 675-686.

(40) Dieke, G. H. *Spectra and Energy Levels of Rare Earth Ions in Crystals*; Interscience Publishers: New York, NY, 1968.

(41) Williams, D. K.; Yuan, Y.; Tissue, B. *Journal of Luminescence* **1999**, *83-84*, 297-300.

(42) Riwotzki, K.; Haase, M. *Journal of Physical Chemistry B* **1998**, *102*, 10129-10135.

(43) Huignard, A.; Gacoin, T.; Boilot, J.-P. *Chemistry of Materials* **2000**, *12*, 1090-1094.

(44) Buissette, V.; Giume, D.; Gacoin, T.; Boilot, J.-P. *Journal of Materials Chemistry* **2006**, *16*.

(45) Meltzer, R. S.; Feofilov, S. P.; Tissue, B.; Yuan, H. B. *Physical Review B: Condensed Matter* **1999**, *60*, 14012.

(46) Ruan, X. L.; Kaviany, M. *Physical Review B: Condensed Matter* **2006**, *73*, 155422-1-155422-15.

(47) Ruan, X. L.; Kaviany, M. *Journal of Applied Physics* **2005**, *97*, 104331-1-104331-8.

(48) Cao, H. In *Optics & Photonics News* January 2005, p 24-29.

(49) Buissette, V.; Huignard, A.; Lahlil, K.; Gacoin, T.; Boilot, J.-P.; Franville, A.-C.; Mahiou, R. *Proceedings of SPIE - The International Society for Optical Engineering* **2003**, *5222*, 140-149.

(50) Chow, H. C.; Powell, R. C. *Physical Review B: Condensed Matter* **1980**, *21*, 3785-3792.

(51) Buijs, M., Utrecht University, 1987.

(52) Martín, I. R.; Rodríguez, V. D.; Rodríguez-Mendoza, U. R.; Lavín, V.; Montoya, E.; Jaque, D. *Journal of Chemical Physics* **1999**, *111*, 1191-1194.

(53) Cotton, S. *Lanthanides and Actinides*; Oxford University Press: New York, NY, 1991.

(54) Lakowicz, J. R. *Principles of Fluorescence Spectroscopy*; 2nd ed.; Kluwer Academic/Plenum Publishers: New York, NY, 1999.

(55) Joshi, B. C. *Journal of Non-Crystalline Solids* **1995**, *180*, 217-220.

(56) Ishizaka, T.; Nozaki, R.; Kurokawa, Y. *Journal of Physics and Chemistry of Solids* **2002**, *63*, 613-617.

(57) Li, Q.; Li, T.; Wu, J. *Journal of Physical Chemistry B* **2001**, *105*.

(58) Anh, T. K.; Ngoc, T.; Nga, P. T.; Bich, V. T.; Long, P.; Stręk, W. *Journal of Luminescence* **1988**, *39*, 215-221.

(59) Strohhöfer, C.; Kik, P. G.; Polman, A. *Journal of Applied Physics* **2000**, *88*, 4486-4490.

(60) Yang, J.; Zhang, L.; Wen, L.; Dai, S.; Hu, L.; Jiang, Z. *Chemical Physics Letters* **2004**, *384*, 295-298.

(61) Su, Q.; Barthous, C.; Denis, J. P.; Pelle, F.; Blanzat, B. *Journal of Luminescence* **1983**, *28*, 1-11.

(62) Nogami, M.; Enomoto, T.; Hayawaka, T. *Journal of Luminescence* **2002**, *97*, 147-152.

(63) Watanabe, K.; Fuji, M.; Hayashi, S. *Journal of Applied Physics* **2001**, *90*, 4761-4767.

(64) Fujii, M.; Yoshida, M.; Kanzawa, Y.; Hayashi, S.; Yamamoto, K. *Applied Physics Letters* **1997**, *71*, 1198-1200.

(65) Watanabe, K.; Tamaoka, H.; Fujii, M.; Moriwaki, K.; Hayashi, S. *Physica E* **2002**, *13*.

(66) Fujii, M.; Hayahsi, S.; Yamamoto, K. *Applied Physics Letters* **1998**, *73*, 3108-3110.

(67) Okamoto, S.; Kobayashi, M.; Kanemitsu, Y.; Kushida, T. *Physical Status Solidi B* **2002**, *229*, 481-484.

(68) Riwotzki, K.; Haase, M. *Journal of Physical Chemistry B* **2001**, *105*, 12709-12713.

(69) Hoekstra, H. R. *Inorganic Chemistry* **1966**, *5*, 754-757.

(70) Tissue, B. M.; Yuan, H. B. *Journal of Solid State Chemistry* **2003**, *171*, 12-18.

(71) Gordon, W. O.; Carter, J. A.; Tissue, B. M. *Journal of Luminescence* **2004**, *108*, 339-342.

(72) Park, J.-C.; Moon, H.-K.; Kim, D.-K.; Byeon, S.-H.; Kim, B.-C.; Suh, K.-S. *Applied Physics Letters* **2000**, *77*, 2162-2163.

(73) Shin, S. H.; Kang, J. H.; Jeon, D. Y.; Zang, D. S. *Journal of Luminescence* **2005**, *114*, 275-280.
(74) Heimer, T. A.; Meyer, G. J. *Journal of Luminescence* **1996**, *70*, 468-478.
(75) Greskovich, C.; Duclos, S. *Annual Review of Materials Science* **1997**, *27*, 69-88.
(76) Dosev, D.; Nichkova, M.; Liu, M.; Guo, B.; Liu, G.-y.; Hammock, B. D.; Kennedy, I. M. *Journal of Biomedical Optics* **2005**, *10*, 064006/1-064006/7.
(77) Flores-Gonzalez, M. A.; Louis, C.; Bazzi, R.; Ledoux, G.; Lebbou, K.; Roux, S.; Perriat, P.; Tillement, O. *Applied Physics A: Solids and Surfaces* **2005**, *81*, 1385-1391.
(78) Song, H.; Yu, L.; Yang, L.; Lu, S. *Journal of Nanoscience and Nanotechnology* **2005**, *5*, 1591-1531.
(79) Lei, Y.; Song, H.; Yang, L.; Yu, L.; Liu, Z.; Pan, G.; Bai, X.; Fan, L. *Journal of Chemical Physics* **2005**, *123*, 174710/1-174710/5.
(80) Liu, Q.; Quan, L. *Journal of Metastable and Nanocrystalline Materials* **2005**, *23*, 15-18.
(81) Kang, Y. C.; Roh, H. S.; Park, S. B.; Jung, K. Y. *Japanese Journal of Applied Physics, Part I: Regular Papers and Short Notes* **2004**, *43*, 5302-5306.
(82) Ledoux, G.; Mercier, B.; Louis, C.; Dujardin, C.; Tillement, O.; Perriat, P. *Radiation Measurements* **2004**, *38*, 763-766.
(83) Soukka, T.; Harma, H.; Paukkunen, J.; Lovgren, T. *Analytical Chemistry* **2001**, *73*, 2254.
(84) Hemmila, I.; Mukkala, V. M. *Critical Reviews in Clinical Laboratory Sciences* **2001**, *38*, 441.
(85) Niedbala, R. S.; Feindt, H.; Kardos, K.; Vail, T.; Burton, J.; Bielska, B.; Li, S.; Milunic, D.; Bourdelle, P.; Vallejo, R. *Analytical Biochemistry* **2001**, *293*, 22.
(86) McDonald, M. A., University of Illinois, 2004.
(87) Dujardin, C.; Le Luyer, C.; Martinet, C.; Garapon, C.; Mugnier, J.; Murrillo, A. G.; Pedrini, C.; Martin, T. *Nuclear Instruments & Methods in Physics Research, Section A: Accelerators, Spectrometers, Detectors, and Associated Equipment* **2005**, *537*, 237-241.
(88) Hüfner, S. *Optical Spectra of Transparent Rare Earth Compounds*; Academic Press: New York, NY, 1978.
(89) Zhou, Y.; Lin, J.; Wang, S. *Journal of Solid State Chemistry* **2003**, *171*, 391-395.
(90) Kim, E. J.; Kang, Y. C.; Park, H. D.; Ryu, S. K. *Han'guk Chaelyo Hakhoechi* **2002**, *12*, 771-775.
(91) Kang, Y. C.; Roh, H. S.; Kim, E. J.; Park, H. D. *Journal of the Electrochemical Society* **2003**, *150*, H93-H97.
(92) Eilers, H.; Tissue, B. M. *Materials Letters* **1995**, *24*, 261.
(93) Okumura, M.; Tamatani, M.; Albessard, A. K.; Matsuda, N. *Japanese Journal of Applied Physics* **1997**, *36*, 6411.
(94) Kulkarni, P.; Biswas, P. *Aerosol Science and Technology* **2004**, *38*, 541-554.
(95) Han, J.; Chang, H.; Lee, J.; Chang, H. *Aerosol Science and Technology* **2003**, *37*, 550-564.

(96) Kruis, F. E.; Fissan, H.; Peled, A. *Journal of Aerosol Science* **1998**, *29*, 511-535.
(97) Sánchez-López, J. C.; Fernández, A. *Acta Materialia* **2000**, *48*, 3761-3771.
(98) Xagas, A. P.; Androilaki, A.; Hiskia, A.; Falaras, P. *Thin Solid Films* **1999**, *357*, 173-178.
(99) Lin, M. Y.; Lindsay, H. M.; Weitz, D. A.; Ball, R. C.; Klein, R.; Meakin, P. *Physical Review A* **1990**, *41*, 2005-2020.
(100) Flagan, R. C.; Friedlander, S. K. In *Recent Developments in Aerosol Science*; Shaw, D. T., Ed.; Wiley: New York, NY, 1978, p 25-59.
(101) Onischuk, A. A.; di Stasio, S.; Karasev, V. V.; Baklanov, A. M.; Makhov, G. A.; Vlasenko, A. L.; Sadykova, A. R.; Shipovalov, A. V.; Panfilov, V. N. *Journal of Aerosol Science* **2003**, *34*, 383-403.
(102) Mandelbrot, B. B. *The Fractal Geometry of Nature*; Freeman: San Fransisco, CA, 1983.
(103) Filippov, A. V.; Zurita, M.; Rosner, D. E. *Journal of Colloid and Interface Science* **2000**, *229*, 261-273.
(104) Lee, T. G.; Hyun, J. E. *Chemosphere* **2006**, *62*, 26-33.
(105) Forrest, S. R.; T. A. Witten, J. *Journal of Physics A: Mathematical and General* **1979**, *12*, L109-L117.
(106) Zurita-Gotor, M.; Rosner, D. E. *Journal of Colloid and Interface Science* **2002**, *255*, 10-26.
(107) T. A. Witten, J.; Sander, L. M. *Physical Review Letters* **1981**, *47*, 1400-1403.
(108) Meakin, P. *Physical Review A* **1983**, *27*, 2616-2623.
(109) Meakin, P. *Physical Review B: Condensed Matter* **1984**, *30*, 4207-4214.
(110) Meakin, P. *Physical Review Letters* **1983**, *51*, 1119-1122.
(111) Kolb, M.; Botet, R.; Jullien, R. *Physical Review Letters* **1983**, *51*, 1123-1126.
(112) Jullien, R.; Kolb, M. *Journal of Physics A: Mathematical and General* **1985**, *17*, L639-L643.
(113) Fuchs, N. A. *The Mechanics of Aerosols*; Macmillan: New York, NY, 1964.
(114) Arunachalam, V.; Lucchese, R. R.; Marlow, W. H. *Physical Review E* **1999**, *60*, 2051-2064.
(115) Krinke, T. J.; Deppert, K.; Magnusson, M. H.; Schmidt, F.; Fissan, H. *Journal of Aerosol Science* **2002**, *33*, 1341-1359.
(116) Kulkarni, K.; Biswas, P. *Journal of Nanoparticle Research* **2003**, *5*, 259-268.
(117) Park, S. H.; Lee, K. W. *Journal of Colloid and Interface Science* **2002**, *246*, 85-91.
(118) Park, S. H.; Xiang, R.; Lee, K. W. *Journal of Colloid and Interface Science* **2000**, *231*, 129-135.
(119) Vold, M. J. *Journal of Colloid and Interface Science* **1963**, *18*, 684-695.
(120) Sutherland, D. N. *Journal of Colloid and Interface Science* **1966**, *22*, 300-302.

(121) Tassopoulos, M.; O'Brien, J. A.; Rosner, D. E. *AIChE Journal* **1989**, *35*, 967-980.
(122) Li, Z.; Wang, H. *Physical Review E* **2003**, *68*, 061206-1-061206-9.
(123) Li, Z.; Wang, H. *Physical Review Letters* **2005**, *95*, 014502-1-014502-4.
(124) Bandyopadhyaya, R.; Lall, A. A.; Friedlander, S. K. *Powder Technology* **2004**, *139*, 193-199.
(125) Lushnikov, A. A.; Negin, A. E.; Pakhomov, A. V. *Chemical Physics Letters* **1990**, *175*, 138-142.
(126) Geohegan, D. B.; Puretzky, A. A. *Applied Surface Science* **1996**, *96-98*, 131-138.
(127) Geohegan, D. B.; Puretzky, A. S.; Duscher, G.; Pennycook, S. J. *Applied Physics Letters* **1998**, *72*, 2987-2989.
(128) Geohegan, D. B.; Puretzky, A. S.; Duscher, G.; Pennycook, S. J. *Applied Physics Letters* **1998**, *73*, 438-440.
(129) Muramoto, J.; Inmaru, T.; Nakata, Y.; Okada, T.; Maeda, M. *Applied Physics Letters* **2000**, *77*, 2334-2336.
(130) Nakata, Y.; Muramoto, J.; Okada, T.; Maeda, M. *Journal of Applied Physics* **2002**, *91*, 1640-1643.
(131) Niklasson, G. A. *Physica Scripta* **1993**, *T49B*, 659-662.
(132) Friedlander, S. K. *Smoke, Dust, Haze*; Oxford University Press: New York, NY, 2000.
(133) Luk'yanchk, B. S.; Marine, W.; Anisimov, S. I.; Simakina, G. A. *Proceedings of SPIE - The International Society for Optical Engineering* **1999**, *3618*, 434-452.
(134) Kask, N. E.; Michurin, S. V.; Fedorov, G. M. *Quantum Electronics* **2003**, *33*, 57-68.
(135) Kask, N. E.; Leksina, E. G.; Michurin, S. V.; Fedorov, G. M.; Chopornyak, D. B. *Quantum Electronics* **2002**, *32*, 437-442.
(136) Guillou, N.; Nistor, L. C.; Fuess, H.; Hahn, H. *Nanostructured Materials* **1997**, *8*, 545-557.
(137) Huh, M.-Y.; Kim, J.-S.; Ahn, J.-P. *Powder Metallurgy* **2002**, *45*.
(138) Witten Jr., T. A.; Sander, L. M. *Physical Review Letters* **1981**, *47*, 1400-1403.
(139) Sánchez-López, J. C.; Justo, A.; Fernández, A. *Langmuir* **1999**, *15*, 7822-7828.
(140) Jang, H. D.; Friedlander, S. K. *Aerosol Science and Technology* **1998**, *29*, 81-91.
(141) Kim, S. Y.; Yu, J. H.; Lee, J. S. *Nanostructured Materials* **1999**, *12*, 471-474.
(142) Nakaso, K.; Shimada, M.; Okuyama, K.; Deppert, K. *Journal of Aerosol Science* **2002**, *33*, 1061-1074.
(143) Ohno, T. *Journal of Nanoparticle Research* **2002**, *4*, 255-260.
(144) Seto, T.; Shimada, M.; Okuyama, K. *Aerosol Science and Technology* **1995**, *28*, 183-200.
(145) Yang, G.; Biswas, P. *Aerosol Science and Technology* **1997**, *27*, 507-521.
(146) Katagiri, S.; Ishizawa, N.; Marumo, F. *Powder Diffraction* **1993**, *8*, 60.

(147) Lam, H. M.; Hong, M. H.; Yuan, S.; Chong, T. C. *Applied Physics A: Solids and Surfaces* **2004**, *79*, 2099-2102.
(148) Levoska, J.; Tyunina, M.; Leppävuori, S. *NanoStructured Materials* **1999**, *12*, 101-106.
(149) Lao, J. Y.; Huang, J. Y.; Wang, D. Z.; Ren, Z. F. *Journal of Materials Chemistry* **2004**, *14*, 770-773.
(150) Lao, J. Y.; Huang, J. Y.; Wang, D. Z.; Ren, Z. F. *Nano Letters* **2003**, *3*, 235-238.
(151) Pászti, Z.; Pet, G.; Horváth, Z. E.; Karacs, A. *Applied Surface Science* **2000**, *168*, 114-117.
(152) National Institute of Standards and Technology: 2005.
(153) Anisimov, S. I.; Luk'yanchuk, B. S.; Luches, A. *Applied Surface Science* **1996**, *96-98*, 24-32.
(154) Pithawalla, Y. B.; Deevi, S. C.; El-Shall, M. S. *Materials Science & Engineering, A: Structural Materials: Properties, Microstructure and Processing* **2002**, *A329-A331*, 92-98.
(155) Gonzalo, J.; Alfonso, C. N.; Pierrière, J. *Journal of Applied Physics* **1996**, *79*, 8042-8046.
(156) Lichtenwalner, D. J.; Auciello, O.; Dat, R.; Kingon, A. I. *Journal of Applied Physics* **1993**, *74*, 7497-7505.
(157) Amoruso, S.; Bruzzese, R.; Vitiello, M.; Nedialkov, N. N.; Atanasov, P. A. *Journal of applied Physics* **2005**, *98*, 044907/1-044907/7.
(158) Dyer, P. E.; Issa, A.; Key, P. H. *Applied Surface Science* **1990**, *46*, 89-95.
(159) Erhart, P.; Albe, K. *Applied Surface Science* **2004**, *226*, 12-18.
(160) Geohegan, D. B. *Applied Physics Letters* **1992**, *60*, 2732-2734.
(161) Coleman, K. *A History of Chemical Warfare*; Palgrave Macmillan: New York, NY, 2005.
(162) Ellison, D. H. *Handbook of Chemical and Biological Warfare Agents*; CRC Press: New York, NY, 2000.
(163) McPherson, M. K., Virginia Polytechnic Institute and State University, 2005.
(164) Yang, Y.-C.; Baker, J. A.; Ward, J. R. *Chemical Reviews* **1992**, *92*, 1729-1743.
(165) Yang, Y.-C. *Accounts of Chemical Research* **1999**, *32*, 109-115.
(166) Wagner, G. W.; Yang, Y.-C. *Industrial and Engineering Chemistry Research* **2002**, *41*, 1925-1928.
(167) Amos, D.; Leake, B. *Journal of Hazardous Materials* **1994**, *39*, 107-117.
(168) Prapas, D. K.; Silks, R. ₸Chem-Bio Defense Quarterly,ヤ JPEO-CBD, 2006.
(169) Braue, E. H., Jr.; Beocker, J. D.; Doxzon, B. F.; Hall, R. L.; Simons, R. T.; Nohe, T. L.; Stoemer, R. L.; Hobson, S. T. In *Defense Applications of Nanomaterials*; Miziolek, A. W., Ed.; American Chemical Society: Washington, D. C., 2005, p 153-169.
(170) Guo, X.; Yoshinobu, J.; Yates, J. T., Jr. *Journal of Physical Chemistry* **1990**, *94*, 6839-6842.
(171) Hegde, R. I.; Greenlief, C. M.; White, J. M. *Journal of Physical Chemistry* **1985**, *89*, 2886-2891.

(172) Henderson, M. A.; White, J. M. *Journal of the American Chemical Society* **1988**, *110*, 6939-6947.

(173) Wagner, G. W.; Bartram, P. W.; Koper, O.; Klabunde, K. J. *Journal of Physical Chemistry B* **1999**, *103*.

(174) Wagner, G. W.; Koper, O. B.; Lucas, E.; Decker, S.; Klabunde, K. J. *Journal of Physical Chemistry B* **2000**, *104*.

(175) Wagner, G. W.; Procell, L. R.; O'Connor, R. J.; Munavalli, S.; Carnes, C. L.; Kapoor, P. N.; Klabunde, K. J. *Journal of the American Chemical Society* **2001**, *123*, 1636-1644.

(176) Wagner, G. W.; Procell, L. R.; Koper, O. B.; Klabunde, K. J. In *Defense Applications of Nanomaterials*; 891 ed.; Miziolek, A. W., Ed.; American Chemistry Society: Washington, DC, 2005, p 139-152.

(177) Aurian-Blajeni, B.; Boucher, M. M. *Langmuir* **1989**, *5*, 170-174.

(178) Kim, C. S.; Lad, R. J.; Tripp, C. P. *Sensors and Actuators, B: Chemical Sensors and Materials* **2001**, *76*, 442-448.

(179) Kanan, S. M.; Lu, Z.; Tripp, C. P. *Journal of Physical Chemistry B* **2002**, *106*, 9576-9580.

(180) Moss, J. A.; Szczepankiewicz, S. H.; Park, E.; Hoffmann, M. R. *Journal of Physical Chemistry B* **2005**, *109*, 19779-19785.

(181) Zhou, J.; Varazo, K.; Reddic, J. E.; Myrick, M. L.; Chen, D. A. *Analytica Chimica Acta* **2003**, *496*, 289-300.

(182) Trubitsyn, D. A.; Vorontsov, A. V. *Journal of Physical Chemistry B* **2005**, *109*, 21884-21892.

(183) Rusu, C. N.; Yates, J. T. *Journal of Physical Chemistry B* **2000**, *104*, 12299-12305.

(184) Rusu, C. N.; Yates, J. T. *Journal of Physical Chemistry B* **2000**, *104*, 12292-12298.

(185) Henderson, M. A.; Jin, T.; White, J. M. *Journal of Physical Chemistry* **1986**, *90*, 4607-4611.

(186) Kanan, S. M.; Tripp, C. P. *Langmuir* **2001**, *17*, 2213-2218.

(187) Lin, S.-T.; Klabunde, K. J. *Langmuir* **1985**, *1*, 600-605.

(188) Li, Y.-X.; Schlup, J. R.; Klabunde, K. J. *Langmuir* **1991**, *7*, 1394-1399.

(189) Zhanpeisov, N. U.; Zhidomirov, G. M.; Yudanov, I. V.; Klabunde, K. J. *Journal of Physical Chemistry* **1994**, *98*, 10032-10035.

(190) Li, Y.-X.; Koper, O.; Atteya, M.; Klabunde, K. J. *Chemistry of Materials* **1992**, *4*, 323-330.

(191) Kanan, S. M.; Tripp, C. P. *Langmuir* **2002**, *18*, 722-728.

(192) Michalkova, A.; Ilchenko, M.; Gorb, L.; Leszczynski, J. *Journal of Physical Chemistry B* **2004**, *108*, 5294-5303.

(193) Richards, R.; Li, W.; Decker, S.; Davidson, C.; Koper, O.; Zaikovski, V.; Vologin, A.; Rieker, T.; Klabunde, K. J. *Journal of the American Chemical Society* **2000**, *122*, 4921-4925.

(194) Williams, D. K.; Bihari, B.; Tissue, B. M. *Journal of Physical Chemistry B* **1998**, *102*, 916-920.

(195) Morterra, C.; Cerrato, G.; Ferroni, L. *Journal of the Chemical Society, Faraday Transactions* **1995**, *91*, 125-132.

(196) Davis, B. H. *Journal of Catalysis* **1978**, *52*, 176-185.
(197) Hussein, G. A. M.; Gates, B. C. *Journal of Catalysis* **1998**, *176*, 395-404.
(198) Kuroda, Y.; Hamano, H.; Mori, T.; Yoshikawa, Y.; Nagao, M. *Langmuir* **2000**, *16*, 6937-6947.
(199) Templeton, M. K.; Weinberg, W. H. *Journal of the American Chemical Society* **1985**, *107*, 97-108.
(200) Crooks, R. M.; Yang, H. C.; McEllistrem, L. J.; Thomas, R. C.; Ricco, A. J. *Faraday Discussions* **1997**, *107*, 285-305.
(201) Li, Y.-X.; Klabunde, K. J. *Langmuir* **1991**, *7*, 1388-1393.
(202) Goldsmith, J. A.; Ross, S. D. *Spectrochimica Acta, Part A: Molecular Spectroscopy* **1967**, *23*, 1909-1915.
(203) Martin, D.; Duprez, D. *Journal of Molecular Catalysis A: Chemical* **1997**, *118*, 113-128.
(204) Seaverson, L. M.; Luo, S.-Q.; Chien, P.-L.; McClelland, J. F. *Journal of the American Ceramic Society* **1986**, *69*, 423-429.
(205) Dzurinskii, B. F.; Gati, D.; Sergushin, N. P.; Nefedov, V. I.; Salyn, Y. V. *Russian Journal of Inorganic Chemistry* **1975**, *20*, 2307-2314.
(206) Barr, T. L. *Journal of Physical Chemistry* **1978**, *82*, 1801-1810.
(207) Vasquez, R. P. *Journal of Electron Spectroscopy and Related Phenomena* **1990**, *50*, 167-170.
(208) Pelmenschikov, A. G.; Morosi, G.; Gamba, A.; Coluccia, S. *Journal of Physical Chemistry* **1995**, *99*, 15018-15022.
(209) Rusu, C. N.; John T. Yates, J. *J. Phys. Chem. B* **2000**, *104*, 12299-12305.
(210) Ferguson-McPherson, M. K.; Low, E. R.; Esker, A. R.; Morris, J. R. *Journal of Physical Chemistry B* **2005**, *109*, 18914-18920.
(211) Templeton, M. K.; Weinberg, W. H. *Journal of the American Chemical Society* **1985**, *107*, 774-779.
(212) Kuiper, A. E. T.; Bokhoven, J. J. G. M. V.; Medema, J. *Journal of Catalysis* **1976**, *43*, 154-167.
(213) Qi, H.; Gee, P. E.; Nguyen, T.; Hicks, R. F. *Surface Science* **1995**, *323*, 6-18.
(214) Moravie, R. M.; Froment, F.; Corset, J. *Spectrochimica Acta, Part A: Molecular Spectroscopy* **1989**, *45*, 1015-1024.
(215) Marsault-Herail, F. *Journal de Chimie Physique et de Physico-Chimie Biologique* **1971**, *68*, 274-286.
(216) Barros, R. B.; Garcia, A. R.; Ilharco, L. M. *Journal of Physical Chemistry B* **2001**, *105*, 11186-11193.
(217) Falk, M.; Whalley, E. *Journal of Chemical Physics* **1961**, *34*, 1554-1568.
(218) Bertie, J. E.; Zhang, S. L. *Journal of Chemical Physics* **1994**, *101*, 8364-8379.
(219) Stark, J. V.; Park, D. G.; Lagadic, I.; Klabunde, K. J. *Chemistry of Materials* **1996**, *8*, 1904-1912.
(220) Klabunde, K. J.; Stark, J.; Koper, O.; Mohs, C.; Park, D. G.; Decker, S.; Jiang, Y.; Lagadic, I.; Zhang, D. *Journal of Physical Chemistry* **1996**, *100*, 12142-12153.
(221) Decker, S.; Lagadic, I.; Klabunde, K. J.; Moscovic, J.; Michalowicz, A. *Chemistry of Materials* **1998**, *10*, 674-678.

(222) Rolison, D. R. *Science* **2003**, *299*, 1698-1701.
(223) Tanabe, K. *Materials Chemistry and Physics* **1985**, *13*, 347-364.
(224) Jung, K. T.; Bell, A. T. *Topics in Catalysis* **2002**, *20*, 97-105.
(225) Bensitel, M.; Saur, O.; Lavalley, J. C. *Materials Chemistry and Physics* **1987**, *17*, 249-258.
(226) Rhodes, M. D.; Pokrovski, K. A.; Bell, A. T. *Journal of Catalysis* **2005**, *233*, 210-220.
(227) Morterra, C.; Cerrato, G.; Ferroni, L.; Montanaro, L. *Materials Chemistry and Physics* **1994**, *37*, 243-257.
(228) Tsyganenko, A. A.; Filimonov, V. N. *Journal of Molecular Structure* **1973**, *19*, 579-589.
(229) Merle-Méjean, T.; Barberis, P.; Othmane, S. B.; Nardou, F.; Quintard, P. E. *Journal of the European Ceramic Society* **1998**, *18*, 1579-1586.
(230) Tesfai, T. M.; Sheinker, V. N.; Mitchell, M. B. *Journal of Physical Chemistry B* **1998**, *102*, 7299-7302.
(231) Rowland, A. P.; Peto, A.; Townsend, P. D.; Chandler, P. J.; Harmer, S.; Hole, D. E.; Olivares, J.; Randall, D. P. *Proceedings - Electrochemical Society* **1998**, *97*, 165-176.
(232) Vater, U.; Kuenzler, G.; Tews, W. *Journal of Fluorescence* **1994**, *4*, 79-82.
(233) Dexter, D. L. *Journal of Chemical Physics* **1953**, *21*, 836-850.
(234) Rostovshchikova, T. N.; Smirnov, V. V.; Kozhevin, V. M.; Yavsin, D. A.; Zabelin, M. A.; Yassievich, I. N.; Gurevich, S. A. *Applied Catalysis A: General* **2005**, *296*, 70-79.
(235) Milojevich, A.; Morris, J. R.; Virginia Tech: 2005.
(236) Zhou, W. P.; Lewera, A.; Larsen, R.; Masel, R. I.; Bagus, P. S.; Wieckowski, A. *Journal of Physical Chemistry B* **2006**, *110*, 13393-13398.
(237) Kell, A. J.; Donkers, R. L.; Workentin, M. S. *Langmuir* **2005**, *21*, 735-742.
(238) Santra, A. K.; Ghosh, S.; Rao, C. N. R. *Langmuir* **1994**, *10*, 3937-3939.
(239) Mayrhofer, K. J. J.; Blizanac, B. B.; Arenz, M.; Stamenkovic, V. R.; Ross, P. N.; Markovic, N. M. *Journal of Physical Chemistry B* **2005**, *109*, 14433-14440.
(240) Thompson, T. L.; John T. Yates, J. *Journal of Physical Chemistry B* **2005**, *109*, 18230-18236.
(241) Heiz, U.; Bullock, E. L. *Journal of Materials Chemistry* **2004**, *14*, 564-577.
(242) Nowakowski, M. J.; Vohs, J. M.; Bonnell, D. A. *Journal of the American Ceramic Society* **1993**, *76*, 279-283.
(243) Xu, C.; Goodman, D. W. *Chemical Physics Letters* **1997**, *265*.
(244) Zhou, X.-L.; Cowin, J. P. *Journal of Physical Chemistry* **1996**, *100*, 1055-1065.
(245) Pacchioni, G. *ChemPhysChem* **2003**, *4*, 1041-1047.
(246) Ma, S.; Zhou, J.; Kang, Y. C.; Reddic, J. E.; Chen, D. A. *Langmuir* **2004**, *20*, 9686-9694.
(247) Zhou, J.; Ma, S.; Kang, Y. C.; Chen, D. A. *Journal of Physical Chemistry B* **2004**, *108*, 11633-11644.

(248) Sheinker, V. N.; Mitchell, M. B. *Chemistry of Materials* **2002**, *14*, 1257-1268.
(249) Hegde, R. I.; White, J. M. *Applied Surface Science* **1987**, *28*, 1-10.
(250) Mitchell, M. B.; Sheinker, V. N.; Tesfamichael, A. B.; Gatimu, E. N.; Nunley, M. *Journal of Physical Chemistry B* **2003**, *107*, 580-586.
(251) Cao, L.; Segal, S. R.; Suib, S. L.; Tang, X.; Satyapal, S. *Journal of Catalysis* **2000**, *194*, 61-70.
(252) Nakamoto, K. In *Infrared Spectra of Inorganic and Coordination Compounds*; Wiley: New York, NY, 1963, p 159-163.
(253) Little, L. H. *Infrared Spectra of Adsorbed Species*; Academic Press: London, 1966.
(254) Busca, G. *Journal of Molecular Catalysis* **1987**, *43*, 225-236.
(255) Morterra, C.; Cerrato, G.; Ciero, S. D. *Applied Surface Science* **1998**, *126*, 107-128.
(256) Walrafen, G. E.; Hokmabadi, M. S.; Holmes, N. C.; Nellis, W. J.; Henning, S. *Journal of Chemical Physics* **1985**, *82*, 2472-2476.
(257) George, L.; Sankaran, K.; Viswanathan, K. S.; Mathews, C. K. *Applied Spectroscopy* **1994**, *48*, 7-12.
(258) Reva, I.; Simão, A.; Fausto, R. *Chemical Physics Letters* **2005**, *406*, 126-136.
(259) Atteya, M.; Klabunde, K. J. *Chemistry of Materials* **1991**, *3*, 182-187.
(260) Barros, R. B.; Garcia, A. R.; Ilharco, L. M. *Surface Science* **2003**, *532-535*, 185-190.
(261) Bertilsson, L.; Engquist, I.; Liedberg, B. *Journal of Physical Chemistry B* **1997**, *101*, 6021-6027.
(262) Bertilsson, L.; Potje-Kamloth, K.; Liess, H.-D.; Engquist, I.; Liedberg, B. *Journal of Physical Chemistry B* **1998**, *102*, 1260-1269.
(263) Pedersen, H.; Soderlind, F.; Jr., R. M. P.; Uvdal, K.; Kall, P.-O.; Ojamae, L. *Surface Science* **2005**, *592*, 124-140.
(264) Burcham, L. J.; Badlani, M.; Wachs, I. E. *Journal of Catalysis* **2001**, *203*, 104-141.

Vita

Wesley Odell Gordon was born to Jerry and Marilyn Gordon in May of 1979 in Salisbury, North Carolina, and was raised alongside his sister Amy and brother Blake in Winston-Salem, North Carolina. After graduating from Robert B. Glenn High School, he attended North Carolina State University to study Chemistry in 1997. After graduating with a Bachelor of Science degree, Wesley moved to Blacksburg, Virginia in August 2001 to begin graduate studies. At Virginia Tech, Wesley pursued his doctoral degree while studying the properties of metal oxide nanoparticles under the direction of Dr. Brian Tissue and Dr. John Morris. Upon completion of his studies at Virginia Tech, Wesley plans to join the Surface Science and Catalysis group at Oak Ridge National Laboratory as a postdoctoral fellow.